University of California
Santa Barbara

Mono- and Multivalent Ion Conduction in Solid Polymer Electrolytes

A dissertation submitted in partial satisfaction
of the requirements for the degree
Doctor of Philosophy
in
Materials

by

Nicole Sophie Michenfelder-Schauser

Committee in charge:

Professor Rachel A. Segalman, Co-Chair
Professor Ram Seshadri, Co-Chair
Professor Michael Chabinyc
Professor Songi Han

September 2020

The Dissertation of Nicole Sophie Michenfelder-Schauser is approved.

_____

Professor Michael Chabinyc

_____

Professor Songi Han

_____

Professor Ram Seshadri, Committee Co-Chair

_____

Professor Rachel A. Segalman, Committee Co-Chair

July 2020

Mono- and Multivalent Ion Conduction in Solid Polymer Electrolytes

by

Nicole Sophie Michenfelder-Schauser

To my family, for their unwavering support,

and to my mentors, for their guidance and inspiration

Acknowledgements

A PhD is by no means an individual achievement, and a long list of mentors, collaborators and friends deserve recognition and thanks. I would not have come this far without their guidance, direct help and indirect support.

First, I need to thank my advisors, Rachel and Ram. Rachel has provided incredible mentorship, and been an invaluable strong female role model in the field of science. Her leadership and caring have been key elements in making me feel at home in the group. I've also learned a lot about research project design, helping me become a better scientist. Lastly, I appreciate her efforts to provide me with some freedom in my research, enabling me to work on projects with diversity in research goals ranging from fundamental understanding to industry-diven performance improvements.

While my scientific projects have mostly all focused on polymers, Ram has always been an integral advisor and mentor. I admire his ability to critically analyze and understand aspects outside of his current core research avenues, providing insightful suggestions relevant to the science of the projects. More importantly, Ram has been instrumental in my personal and professional development. I appreciate his vocal attitude on ethics and morals, our random office musings, as well as our discussions about compassion and conflict. Ram is also incredibly selfless with his time and support, as I discovered my first year where he spent hours working on a poster draft with me for my first conference. Lastly, Ram always encouraged me to take the time to think critically and freely about science for the sake of science – while I admit I did not understand the practicality of this until rather late in my PhD, this is a lesson that will stick with me for the rest of my life, and one that I hope to take advantage of more in the future.

I would also like to thank my two other committee members: Michael and Songi.

Michael's ability to sit quietly in a meeting and then, seemingly out of the blue, say something extremely insightful amazes and surpirses me to this day. He has been an important source of critical discussions about understanding the assumptions inherent in specific models or experiments. I also appreciate the advice he's provided on making my next employment and life choices – his openness about my options and differences between industry, academic and other non-traditional paths have been quite helpful. Songi has been an important collaborator on the NMR and EPR aspects of some of my projects, but has also provided useful commentary about other aspects of polymer electrolyte experimental design in our weekly IRG-2 meetings. I particularly appreciate her ability to distill a question or discussion to the single most important or relevant point, enabling meetings to stay on track and discussions to be productive.

My time at UCSB was kickstarted by the mentorship and friendship of Gabriel Sanoja, and he certainly deserves significant credit in a large portion of the science included in this dissertation. As a senior grad student in the lab, he, along with a previous group member Chris Evans, designed the initial experiments and synthesis routes that ultimately led to the model polymer platform that became the cornerstone of my thesis. Through his guidance, I learned that it's possible to do amazing and rigorous science while still having incredible fun in the lab. In addition to learning synthesis from him, we had many discussions about science, politics, the future of society and life. I know he will be an amazing mentor and PI at UT Austin and wish him all the best!

The Segalman and Seshadri groups have also been incredible. I will miss Segalman dinners, summer workshop retreats, and the many conversations and friendships I've built with many of you. A few people deserve special mention. First and foremost Mikayla – thanks for the strong friendship we've been able to build over the years,

for our weekly dinners, being a great hiking buddy, and for our deep conversations. I'm so happy we were able to meet through Rachel's group! Thanks also to the Ionics sub-group past and present members, especially Seamus for stimulating science conversations, and support with synthesis and measurements, but also including Manny, Ethan, Keith, Josh B., Josh M., Segolene and Eiko. Thanks also to my beamline buddies, including Gabo, Beihang, Seamus, Anastasia, Scott and Segolene, for making beamtime more fun and sharing in on new experiences in New York. I also want to thank Dakota – I've really appreciated our conversations both about science and our futures, and it's been amazing to see all that you've accomplished in your quiet, unassuming but totally awesome way. Lastly, I want to acknowledge Anastasia, Emily, Reika and Elayne for being such strong female role models especially as I was still finding my footing in the lab.

As for the Seshadri group, thanks for being so supportive and friendly even though my research projects were so far afield from many of the rest of the group's. Thanks also for Burrito Fridays (when I was able to join), general Nano Cafe lunches and happy hours. Thanks to Kira, for our hiking, backpacking, diving, running and snowshoeing adventures, for some delicious dinners, for yoga and pottery, and for our continuing friendship. Thanks to Megan for meeting with me when I was first interested in joining Ram's group, and her initial help getting started in the lab. Emily L. was also instrumental in making me feel welcome, helping me with safety training, and I'm so happy we've built a lasting friendship. For her leadership in the battery lab, go-getting attitude, and continual support, I have to thank Molleigh. Emily S. – I couldn't have asked for a better person and friend to move through our PhDs together, and I'm so excited we're both about to move on to our next steps. To Josh, thanks for your awesome science and guidance on data mining, as well as our newly-found excitement for

birding – I'll miss that once you've moved to the UK. And to the other members who have made my time so enjoyable, including Doug for stimulating scientific (yay plastic crystals!) and political discussion, Kartik for NMR advice, Hayden for your humor, Joya (Great British Bake-Off!), and Rebecca.

Next I need to thank my undergraduate interns – I think you have all taught me more than I have taught you over the course of my time mentoring you. To Gabi, thanks for learning with me and being patient as I learned how to mentor and support an undergraduate researcher. Thanks also for your continual excitement, incredible motivation, independence in the lab, and hard work. Congrats on graduating and landing an awesome job – I can't wait to see where life takes you! Next to Linh: your willingness to learn, eagerness to continually improve, hard work and independence, and ability to critically reflect and innovate on our project were very inspiring. I'm so happy you've started on your own PhD journey here at UCSB, and I know you will be an amazing scientist! And lastly to Piper, I'm so glad you decided that polymers might be interesting even though they were so different from what you thought you might want to work on, and I admire your perserverence in the face of monotony even when I left for Germany for two months. I'm continually in awe of your energy, your openness, and your vision, and I hope you continue to explore all that life has to offer.

I'd also like to thank my past (and present) office mates: Emily L. for her friendship, mentorship and dog walks. Tigre, for being Luna's adoption-buddy, first doggy friend, and eternal crush. Victoria, for the opportunity to broaden my horizons through discussions about politics, communication, jobs, and more. Tyler, for stimulating conversations. And Rebecca, for our discussions about our past and future travel adventures.

The collaborative nature of research at UCSB makes it challenging to make sure I remember to thank all those who have influenced my experience during my PhD. Dur-

ing my first year, conversations with Brian Evanko and Galen Stucky helped widen my knowledge of energy storage options. Later, I had the opportunity to be involved with two large collaborative projects. The first – the Interdisciplinary Research Group (IRG) on polymeric ionic liquids – enabled a huge number of collaborations and expanded my knowledge significantly. I particularly appreciate my collaborations with Hui Nie – I will miss our research efforts and life conversations. Advice and mentorship from a number of professors resulted from this project, including Glenn Fredrickson, Javier Read de Alaniz, Craig Hawker, Chris Bates, and Todd Squires. Students involved in this IRG who I have had the pleasure of working with include Doug (for simulation support), Tarnuma (EPR), Sheetal (solid-state NMR), Angelique, Saejin, Jeff and Veronica.

Second, I have had the pleasure of working closely with Pete, Andrei, Professor Raphaele Clement, and Hengbin Wang on a project sponsored by Mitsubishi Chemical Corporation. Our energetic and highly productive collaborations and discussions have led to significant research output, as well as fun conversations and learning new science. I appreciate the opportunity to learn rigorous NMR principles from Pete and Raphaele, as well as collaborate with Andrei for the synthetic efforts.

I also need to acknowledge the mentorship of Professor Kay Saalwaechter and Anton Mordvinkin from the Martin-Luther University of Halle Wittenberg, for the opportunity to spend two months in Germany learning about multiple-quantum NMR. Kay's insights into both NMR and polymer physics are astounding, and Anton's willingness to mentor me even after defending his own thesis are much appreciated.

The work described in this thesis would never have been possible without all the help of some amazing staff at UCSB and synchrotron user facilities. First, those who work in the shared facilities were instrumental not only for their work keeping the instruments maintained and setting up trainings, but also for scientific discussions and

help with experimental design. Rachel Behrens (rheology, DSC, battery lab, GPC), Jerry Hu (NMR), Amanda Strom (TEMPO/TGA) and Youli Li (X-ray facility) were especially helpful, with additional support from Shamon, Jaya and Phillip. In addition to help with polymer characterization, Rachel inspired me to keep up with running and yoga through our talks of her amazing race adventures. I especially want to thank Masa Fukuto and Ruipeng Li from NSLS-II beamline 11-BM for their incredible dedication to user support, often staying late or coming in early to help us with our experiments.

The rest of the staff in the MRL and EngineeringII are equally integral to smooth research progress, as well as a sense of community and fun. The following is not a complete list, but represents a subest of the people who help behind the scenes to support the research we do: Mary McGuan for her help with purchases as well as conversations about life, Sylvia Vogel for her patience with all my reimbursement questions, Mike Best for EII-related lab and buliding services, Cynthia Rojo for coordinating Rachel's schedule and seminars, Samantha Crossno for her support with Mitsubishi-related expenses, Maki Donovan and Marisol Cedillo Dougherty for their work keeping our grant finances in order, Sara Sorensen for coordinating events including the annual Materials Research Outreach Program conference, and Fuzzy Rogers and George Crespo for help with IT and computing resources.

Outreach through the MRL was a highlight of my experience here at UCSB. For their continued efforts organizing local outreach events I'd like to thank Dotti Pak and Frank Kinnaman. For providing me with the opportunity to mentor a summer undergraduate, I'd like to thank Julie Standish. And for her work on scienceline, as well as her selfless efforts supporting graduate students like myself with her kind words and delicious tamales, I need to thank Claudia Gutierrez-Mazzotti.

I also need to thank my graduate student funding, from both the NSF Graduate

Research Fellowship Program and from the John and Fannie Hertz Foundation. The Hertz Foundation in particular was so much more than just a source of monetary support, with lasting inspiration and connections arising from the bi-annual workshops and continual mentorship and collaboration opportunities. The passion of the scholars involved in this community energizes and motivates me to strive to make an impact in society.

Mentors from my time as an undergraduate at UC Berkeley also deserve special recognition for helping set the foundation for a successful PhD. This includes Professor Nitash Balsara, whom I've been fortunate enough to continue to interact with at conferences – your passion for the beauty of science is both refreshing and inspiring. I also need to thank my graduate mentor at the time, Katherine Harry. Having now mentored undergraduates of my own I am so grateful for the support, advice, freedom and friendship that you provided.

Last, but certainly not least, I need to thank my family for their unwavering support. To my parents, your positive impact in my life can not be overstated. I appreciate the love for exploration and learning that you instilled in me since a young age, and your continuous support and belief in me that undoubtedly helped me reach the spot I'm at today. To my sister, thanks for being my best friend, my role model, my competitor, and my confidante. I continue to strive to match your selflessness and hard work, and always appreciate and admire your humor and adventurous nature. To Kevin: I can't ask for a better partner with whom to navigate through life's ups and downs. Thanks for your support, and for challenging me to continually grow and explore. I can't wait for our next adventure.

And of course, thanks to Luna, for reminding me to take it easy, go outside, and enjoy life.

Curriculum Vitæ

Nicole Sophie Michenfelder-Schauser

Education

Sep 2016 – July 2020 Ph.D. in Materials, University of California, Santa Barbara.
Co-advisors: Professor Rachel A. Segalman and Professor Ram Seshadri

Aug 2010 – May 2015 B.S. Materials Science and Engineering, University of California, Berkeley
Summa Cum Laude — Advisor: Professor Nitash Balsara

Publications

11. N. S. Schauser, G. A. Kliegle, P. Cooke, R. A. Segalman, and R. Seshadri. Data Visualization and Statistical Learning for Polymer Electrolyte Design. *[working title], in preparation.*
10. N. S. Schauser, P. M. Richardson, A. Nikolaev, P. Cooke, G. Kliegle, E. M. Susca, K. Johnson, J. Read de Alaniz, R. Fujita, H. Wang, R. Seshadri, R. J. Clement, and R. A. Segalman. Optimum in Ligand Density for Conductivity in Polymer Electrolytes. *[working title], in preparation.*
9. N. S. Schauser,* A. Nikolaev,* P. M. Richardson, K. Johnson, E. M. Susca, R. Fujita, H. Wang, R. Seshadri, R. J. Clement, J. Read de Alaniz, and R. A. Segalman. Dual Role of T_g and Ion Binding in Determining Conductivity and Lithium Transport in Polymer Electrolytes. *[working title], in preparation.* (*equal contribution)
8. Z. Geng, N. S. Schauser, J. Lee, R. P. Schmeller, S. M. Barbon, R. A. Segalman, N. A. Lynd, and C. J. Hawker. Role of Side-Chain Architecture in Poly(ethylene oxide)-Based Copolymers. *Macromolecules*, (2020). DOI: 10.1021/acs.macromol.0c01116
7. N. S. Schauser, D. J. Grzetic, T. Tabassum, G. A. Kliegle, M. L. Le, E. M. Susca, S. Antoine, T. J. Keller, K. T. Delaney, S. Han, R. Seshadri, G. H. Fredrickson, and R. A. Segalman. The Role of Backbone Polarity on Aggregation and Conduction of Ions in Polymer Electrolytes. *J. Am. Chem. Soc.*, 142, 7055 (2020). DOI: 10.1021/jacs.0c00587
6. H. Nie,* N. S. Schauser,* N. D. Dolinski, J. Hu, C. J. Hawker, R. A. Segalman, and J. Read de Alaniz. Light-Controllable Ionic Conductivity in a Polymeric Ionic Liquid. *Angew. Chemie Int. Ed.*, 59, 5123 (2020). DOI: 10.1002/anie.201912921 (*equal contribution)

5. N. S. Schauser, R. Seshadri, and R. A. Segalman. Multivalent Ion Conduction in Solid Polymer Systems. *Mol. Syst. Des. Eng.*, 4, 263 (2019). DOI: 10.1039/c8me00096d
4. N. S. Schauser,* G. E. Sanoja,* J. M. Bartels, S. K. Jain, J. G. Hu, S. Han, L. M. Walker, M. E. Helgeson, R. Seshadri, and R. A. Segalman. Decoupling Bulk Mechanics and Mono- and Multivalent Ion Transport in Polymers Based on Metal-Ligand Coordination. *Chem. Mater.*, 30, 5759 (2018). DOI: 10.1021/acs.chemmater.8b02633 (*equal contribution)
3. B. C. Popere, G. E. Sanoja, E. M. Thomas, N. S. Schauser, S. D. Jones, J. M. Bartels, M. E. Helgeson, M. L. Chabinyc, and R. A. Segalman. Photocrosslinking Polymeric Ionic Liquids via Anthracene Cycloaddition for Organic Electronics. *J. Mater. Chem. C*, 6, 8762 (2018). DOI: 10.1039/c8tc02561d
2. G. E. Sanoja,* N. S. Schauser,* J. M. Bartels, C. M. Evans, M. E. Helgeson, R. Seshadri, and R. A. Segalman. Ion Transport in Dynamic Polymer Networks Based on Metal-Ligand Coordination: Effect of Cross-Linker Concentration. *Macromolecules*, 51, 2017 (2018). DOI: 10.1021/acs.macromol.7b02141 (*equal contribution)
1. N. S. Schauser, K. J. Harry, D. Y. Parkinson, H. Watanabe, and N. P. Balsara. Lithium Dendrite Growth in Glassy and Rubbery Nanostructured Block Copolymer Electrolytes. *J. Electrochem. Soc.*, 162, A398 (2015). DOI: 10.1149/2.0511503jes

Abstract

Mono- and Multivalent Ion Conduction in Solid Polymer Electrolytes

by

Nicole Sophie Michenfelder-Schauser

Batteries are an integral component in society's technology revolution, enabling mobile phones, laptops, electric vehicles and renewable energy storage. The importance of electrochemical energy storage will continue to grow as we tackle critical and time-sensitive concerns surrounding fossil fuel use and climate change. One of the limitations of current battery technology is the electrolyte, which enables battery function by transporting ions between the anode and cathode electrodes. Current organic liquid electrolytes are highly flammable, and limit possible future battery chemistries. Polymer electrolytes are promising alternatives with improved safety, mechanical and electrochemical stability, and the potential to enable multivalent battery technology which can increase energy density. Critically, however, they suffer from low ionic conductivity, preventing their current use in applications.

This thesis explores design rules in a new family of polymer electrolytes based on metal-ligand coordination. Through the design of a model materials platform, we are able to examine the role of ion identity and concentration on polymer conductivity and mechanical properties, showing that these metal-ligand polymers decouple conductivity and mechanics through appropriate choice of metal ion. New insights on polymer dielectric properties and ion aggregation are also discussed, wherein we emphasize that additional design flexibility is achieved by tuning the polymer backbone separately from the ligand groups used to dissolve and interact with the metal salt.

Additionally, significant improvements in ionic conductivity are achieved by tuning the ligand density and linker chemistry of the imidazole ligand species used in this model platform; ligand density provides a 10-fold improvement in conductivity, while tuning linker chemistry enables a 100-fold increase in conductivity performance, along with improved Li^+ transport properties.

Lastly, we take a step back to explore how this series of studies fits into the larger body of work published on polymer electrolytes since their discovery in the 1970s. A data mining and visualization study reveals the continuing challenges in appropriate data reporting. Furthermore, the wide array of polymer chemistries studied show varying trends in the characteristics thought to influence ionic conductivity performance. Nevertheless, statistical learning techniques are able to corroborate the importance of polymer glass transition temperature, monomer solvating group electronegativity, and anion size on ionic conductivity.

Contents

List of Figures

List of Tables

Chapter 1

Introduction

1.1 Polymer electrolytes for energy applications

The development of lithium ion battery technology starting in the 1980s has enabled rapid advances in consumer electronics while delivering promise for applications such as grid storage and electrified transportation.[1, 2] For consumer electronics and transportation, the high energy density of lithium-ion batteries provides the performance necessary for powerful devices and vehicles with the acceleration and range needed to replace combustion engines. Batteries also enable the adoption of renewable energy technologies where intermittency is currently a critical limitation.

A battery is composed of two electrodes separated by an electrolyte (Figure 1.1). While the electrodes define the battery chemistry, operating voltage and capacity, the electrolyte is a critical component that enables battery operation. The electrolyte must physically separate the anode and cathode, prevent electrons from passing from one to

Reproduced in part with permission from [164]: N. S. Schauser, R. Seshadri, and R. A. Segalman. Multivalent Ion Conduction in Solid Polymer Systems. *Mol. Syst. Des. Eng.*, 4, 263 (2019). DOI: 10.1039/c8me00096d Copyright 2019 Royal Society of Chemistry.

the other internally, and conduct the ions relevant to the battery chemistry (e.g. Li^+ for a Li-ion battery). A sufficient electrolyte ionic conductivity is necessary for battery operation; low conductivity results in a significant voltage drop across the electrolyte, limiting both the total energy available to extract from the battery and the rate at which the energy can be extracted (power density). Additional characteristics that are required for an electrolyte include electrochemical stability, large transference number (fraction of current transported by the ion of interest), and safety. Conventional electrolytes are made from an organic liquid, such as ethylene carbonate, mixed with a lithium-based salt (for Li-ion batteries). Liquid electrolytes also require the use of a porous separator material which provides the mechnical stability to physically separate the two electrodes. While liquid electrolytes have high ionic conductivity, enabling good device performance, they are also generally volatile, highly flammable, and hazardous to human and environmental health.[1, 2]

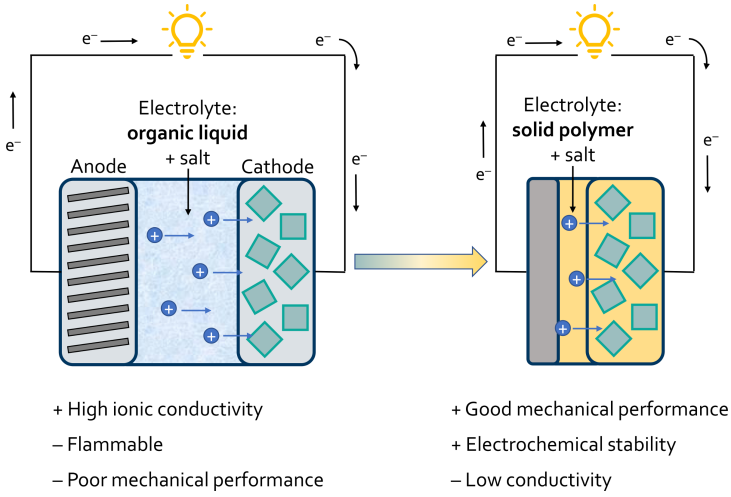

Figure 1.1: A battery is composed of an anode, an electrolyte+separator, and a cathode. Conventional electrolytes are organic liquids mixed with metal salts, which provide good conductivity but poor safety and mechanical performance. Replacing this with a polymer electrolyte reduces safety concerns and enables new battery chemistries, but suffers from low ionic conductivity.

Solid polymer electrolytes have mechanical and chemical stability advantages over their liquid counterparts, but suffer from low ionic conductivities. The discovery of ion conduction in polymers began in the early 1970s, with alkali salts mixed into poly(ethylene oxide) (PEO) [3]. Since then, countless researchers have studied the use of polymers for both Li^+ and other ion conduction applications, focusing both on fundamental understanding of the ion dissolution and transport mechanisms, as well as improving conductivity performance for practical application. The ubiquitous nature of polymers in both structural and functional applications world-wide speaks to their significant property tunability through varying polymer chemistry. Not only can one vary the monomer chemistry, but the architecture of the polymer can also be tuned to affect polymer properties. Linear, branched,[4, 5] brush,[6–8] dendrimer, star,[9] random- and block-copolymer,[7, 10–12] and cross-linked[13, 14] architectures are readily available for most polymer chemistries, providing an additional lever to change the mechanical and ion-conductivity response of a polymer electrolyte. Thus, polymers can be designed with sufficient mechanical rigidity to act as a robust separator between battery electrodes, while still enabling conformal contact between the electrodes and imparting a pathway for ion transport.

Polymer electrolytes may also enable new chemistries for both anode and cathode materials. On the anode side, it has been suggested that improved polymer electrochemical stability and mechanical rigidity could enable lithium metal, which would result in a nearly 10-fold improvement in theoretical energy density.[15, 16] However, many challenges remain in achieving safe device designs that effectively mitigate dendrite growth concerns.[14] Polymer electrolytes can also enable high-density cathodes such as lithium-sulfur and lithium-air chemistries.[17, 18] As will be discussed further below, polymer electrolytes are also being studied for use with multivalent battery

chemistries.

1.2 Mono- versus multivalent ion transport

While lithium boasts high gravimetric energy densities and a low reduction potential, safety and cost concerns and promises of higher energy densities motivate the development of new chemistry platforms. Multivalent batteries, such as those based on Mg^{2+}, Zn^{2+}, or Al^{3+} can dramatically reduce cost and improve device safety due to their increased abundance and reduced reactivity.[19–22] Further, multivalent batteries have higher volumetric energy density compared to lithium.[19] While metallic lithium anode batteries can obtain theoretic volumetric energy densities of 2062 mAh cm^{-3}, this is increased to 3833 mAh cm^{-3} for magnesium and 5851 mAh cm^{-3} for zinc.[19] This results from the larger charge to ionic radius ratio for many multivalent cations compared to Li^{+}. However, many challenges exist for multivalent battery chemistries, most importantly the low mobility of multivalent ions in both electrode and electrolyte materials due to the higher charge density of multivalent species leading to stronger interactions with the surrounding matrix.[23] Further, electrochemical compatibility presents a significant challenge because of the lack of understanding of how a solid-electrolyte interphase (SEI) would function in these materials. This is particularly true in magnesium batteries where stable Mg^{2+} stripping and plating is mostly limited to liquid electrolytes such as those based on Grignard reagents or oligoethers.[24, 25]

The enhanced mechanical and electrochemical stability of polymer electrolytes compared to organic liquids makes them advantageous for both lithium-ion and multivalent ion batteries. Their mechanical robustness facilitates device processability while

maintaining intimate contact with electrodes during battery cycling. Polymers can also function as both the electrolyte and separator material, potentially enabling higher energy density devices.[26] Further, the thermal and electrochemical stability of polymers enhances overall device safety and widens the operating voltage window, allowing for a broader range of cathode and anode chemistries[27] such as enabling reversible stripping and plating of magnesium metal anodes.[24] However, similar to the case of lithium transporting polyelectrolytes, multivalent ion transporting polyelectrolytes exhibit low ionic conductivities which limits their practicality for applications. While adequate conductivities of 10^{-3} S cm^{-1} are sometimes achievable at elevated temperatures, room temperature conductivities are generally at least an order of magnitude lower.[2] This deficit is exacerbated for most polymer electrolytes because these conductivities reflect total ion motion while only cations contribute to the battery function.[28, 29] The actual cation conductivity is usually a minority fraction of the total quoted ionic conductivity (transference numbers «1). High anion mobility also creates concentration gradients that may lead to uneven metal plating and stripping.[16]

Since a majority of published work on lithium-ion conducting electrolytes relates to Li^+ in PEO derivatives, the overall scope of design rules established is conflated to some degree with the specific attributes of PEO's interaction with Li^+. Recent work suggests that other polymer chemistries interact differently both with Li^+ and other battery-relevant ions.[30–32] For example, while ion-ion interactions still dominate performance, the effect of the T_g appears to be less important in governing ion mobility in non-polyether chemistries (see discussion in Chapter 7).

1.3 Mechanisms of ionic conductivity

Increased understanding of the mechanisms of ion transport in polymers can provide guidance for the design of polyelectrolytes optimized for mono- and multivalent ion transport. Conventional polymer electrolytes are formed by dissolving a salt into a polymer matrix. The interactions between the cation, anion, and polymer control the performance of the resulting electrolyte (Figure 1.2).

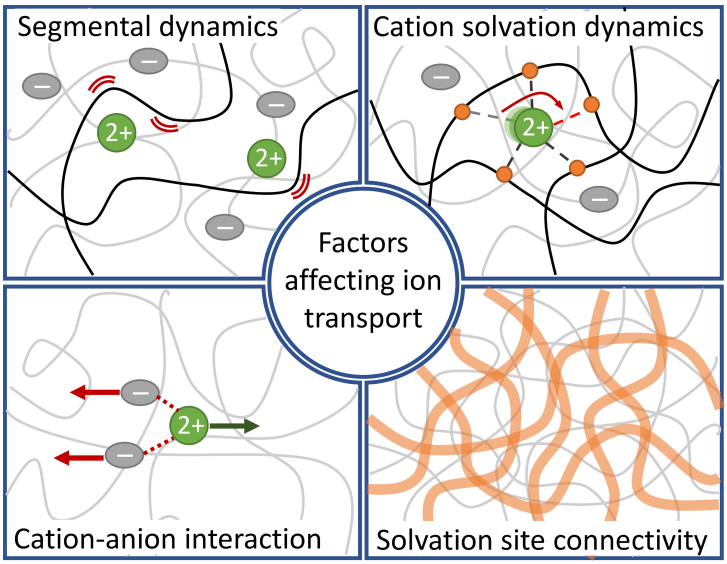

Figure 1.2: Overview of factors affecting the performance of multivalent ion transport in polymer electrolytes. These include the importance of segmental dynamics, the timescale for solvation site exchange, cation-anion interactions, and solvation site connectivity (i.e., percolation shown in orange) in determining ion mobility and the fraction of current transported by the cation of interest.

Ionic conductivity is broadly governed by two interconnected factors: ion concentration and ion mobility.[33] High ion concentration is achieved through the long-lived dissociation of a salt into its respective ions, without aggregation into pairs, triplets or other species which could impede ion motion. The extent of salt dissociation depends on the identity and concentration of the cation and anion as well as the interactions between the ions and the polymer matrix. Spontaneous dissolution of salt into a polymer

requires a negative Gibbs free energy, which results from a more negative solvation energy of the ions within the polymer compared to the lattice energy of the salt. Typically, cations rather than anions are solvated by the polymer, and thus interact more strongly with the polymer matrix. Since these are also the species of interest for conduction, there is an inherent trade-off between salt dissolution and subsequent cation mobility.

Optimizing the electrolyte requires a detailed understanding of how the polymer environment affects the structure and mobility of the dissolved salts. Typical ion conducting polymers have dielectric constants an order of magnitude lower than comparable liquid electrolytes, significantly reducing ion dissociation and increasing the importance of ion identity. The connectivity and chain architecture of polymers has been shown to affect the local dielectric environment around solvated ions, leading to further behavioral differences between polymers and liquid electrolytes.[34, 35] The use of more polarizable or larger counterions with smaller lattice energies should lead to higher dissociation rates and improved ionic conductivity.[36] Further, while increasing salt concentration should increase ion concentration, ion-ion interactions result in the formation of ion pairs or larger aggregates which reduce the ion concentration from its theoretical maximum value. These ion-ion interactions also reduce the mobility of ions due to coulombic drag forces and dynamic polymer crosslinking.[26] Experimental and theoretical studies suggest that increasing the dielectric constant of the polymer environment can reduce ion-ion interactions by improving screening between ion pairs, thus leading to enhanced dissociation and ion mobility.[37, 38]

Ion-polymer interactions also play a significant role in ion mobility. Polymer solvation sites, which stabilize the dissociation of a salt into its respective ions, generally interact more strongly with cationic species, which are also the ions of interest for most applications. Polymer segmental dynamics, generally tracked by the polymer glass

transition temperature, T_g, affect the mobility of ions and are commonly accounted for through a Vogel-Fulcher-Tamman (VFT) relationship of conductivity with temperature. The dynamics of the polymer-cation solvation interaction also govern ion mobility by determining the timescale for release of the cation species from relatively immobile solvation sites.[39]

Improving ionic conductivity in polymer electrolytes requires increasing ion concentration and mobility. Microscopically, ion mobility is achieved through successive ion hops from a current solvation site to a nearby open site.[26, 40, 41] The probability of a successful hop hinges on the proximity of a nearby open site and is mediated by local fluctuations in distance between sites (Figure 1.2). Thus, for polymers above their T_g, the motion of ions is generally related to the segmental dynamics of the polymer.[39, 42] Anion mobility is also loosely tied to the glass transition temperature, as anions require free volume or segmental rearrangement to move through the polymer matrix. Even for polymers at or below their T_g, conductivity behavior as a function of temperature can follow VFT scaling if the activation energy for ion hops changes as a function of temperature.[43] This convolution of effects can make it challenging to identify the fundamental mechanism of ion transport in a polymer electrolyte. It is clear, however, that in general for higher conduction the goal is to use salts with as low a lattice energy as possible for maximum dissociation and to design a polymer with labile cation interactions, or preferential anion interactions, to enhance cation mobility. For multivalent species, these requirements become more challenging, since charge densities increase, resulting in a larger salt lattice energy and stronger polymer-ion interactions. Thus, multivalent cations are expected to exhibit more ion pairing and aggregation as well as lower mobilities.

1.3.1 Total conductivity measurements

By far the most common method for measuring total ionic conductivity is using electrochemical impedance, or dielectric, spectroscopy (EIS) (Figure 1.3). EIS measures the response of a material to a frequency-varying stimulus.[44, 45] This technique applies a small-amplitude sinusoidal voltage (for potentiostatic EIS) or current (for galvanostatic EIS) to an electrolyte sandwiched between two paralell plate electrodes (current collectors), with precise control of the sample thickness, area and temperature. The frequency is swept from high to low, capturing the electrolyte's ability to couple to the input signal at varying timescales. At high frequency, only electronic polarizations can react to the quickly-varying electric field, resulting in a small signal response. As the frequency is decreased, other polarization mechanisms couple with the field, including atomic polarization, dipole re-orientation, and finally ion hopping.

All measurements in this thesis were performed using potentiostatic EIS. The current response is recorded as an amplitude (impedance, Z) and phase angle shift (ϕ). The data is generally plotted as a Nyquist plot, which is the in-phase (resistive response, Z') versus out-of-phase (capacitive response, Z'') impedance (Figure 1.3d). While impedance spectroscopy provides rich information about the timescales of various polarization responses in a sample, most analysis focuses on generating a 'DC conductivity'. This can either be done by fitting equivalent circuits or using known relations to calculate conductivity as a function of frequency.[46] The simplest equivalent circuit consists of a resistor and capacitor in parallel, which generates a semicircle on Nyquist plots. Importantly, EIS is an alternating current technique, meaning it is agnostic to the type of ion moving; thus all mobile ions are probed.

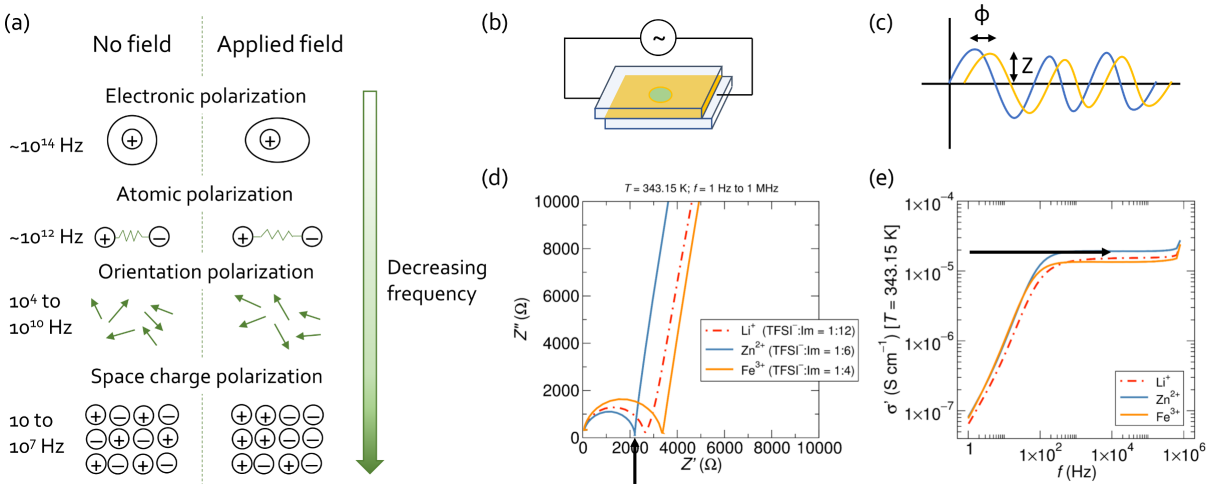

Figure 1.3: Electrochemical impedance spectroscopy measures a material's ability to couple with a sinusoidal electric field as a function of frequency. (a) The polarization mechanisms change as a function of frequency, with ion hopping only occurring at low frequency. (b) A typical sandwich cell set-up used in this dissertation. (c) The material's response is measured as a amplitude (Z) and phase(ϕ) shift from the input signal. The data can be represented in either (d) Nyquist format or (e) showing the real component of the conductivity as a function of frequency; the 'DC' conductivity is extracted from the touch-down or conductivity plateau in each respective representation.

1.4 Transport (and transference) number measurements

In addition to total ionic conductivity, the contribution from the ion of interest, typically the cation species, is extremely important for applications. There are two metrics of importance here, the first is the cation transport number, and the second is the transference number.[47] These metrics are tightly related and often used interchangeably, but measure slightly different electrolyte properties.

The transport number is defined for a single species, such as Li^+ or Zn^{2+}:

$$t_+ = \frac{\sigma_+}{\sigma_{total}} = \frac{\sigma_+}{\sigma_+ + \sigma_-} \tag{1.1}$$

where σ_+ is the contribution to the conductivity from the cation, and $\sigma_{total} = \sigma_+ + \sigma_-$ is the total ionic conductivity. The product of the cation transport number, t_+, and the total conductivity, σ_{total}, thus provides a measure of the cation conductivity.[48]

However, polymer electrolytes have significant amounts of ion pairing and clustering, resulting in the existence of other ionic species, such as $[M_2X]^+$ or $[MX_2]^-$, where M^+ is the cation species (monovalent in this case) and X^- is the anion. These species each have their own transport numbers, and the sum of all transport numbers relevant to a specific ion of interest is defined as the transference number (T_+):

$$T_+ = t_{M^+} + 2t_{[M_2X]^+} - t_{[MX_2]^-} + ... \tag{1.2}$$

Transport and transference number measurements are not straightforward in polymer electrolytes, with significant discussion arising over the past few decades on the appropriate experimental techniques to accurately capture the transport behavior of the cation. Electrochemical impedance spectroscopy (EIS), typically used for ionic con-

ductivity measurements, is an ac current technique and does not distinguish the species which contribute to the measured total ionic conductivity. Although several methods have been proposed for extracting transport/transference numbers, it is important to note that drawbacks for each of these methods arise in the case of lithium-ion conducting polymers[49–51] and seem to be exacerbated for multivalent ions due to their higher propensity to form ion aggregates, as well as their generally higher interfacial resistances with non-blocking electrodes of their corresponding metals.

1.4.1 Chronoamperometry

Chronoamperometry is the simplest and most common way of measuring the ion transport number but becomes inaccurate in systems with high interfacial impedance or with ion pairing.[52] In this method, a constant voltage is applied to a symmetric cell with non-blocking electrodes for the ion of interest, and the current is tracked as a function of time until steady-state is reached. The transport number is then calculated as

$$t_+ = \frac{I_{ss}(\Delta V - I_\Omega R_0)}{I_\Omega(\Delta V - I_{ss}R_{ss})} \tag{1.3}$$

where ΔV is the potential difference applied across the cell, I is the current and R is the interfacial resistance, and the subscript ss corresponds to measurements performed at steady-state while 0 corresponds to measurements at the beginning of the experiment prior to polarization.

This method has been used to report transport (mostly called transference in the literature) numbers for a variety of multivalent polymer electrolytes, with widely varying results. For Cu^{2+} in poly(ethylene oxide) (PEO), values range from 0.0832 to 0.24.[53]

Labile divalent species such as Hg^{2+} and Pb^{2+} exhibit high transport numbers of 0.25 and 0.6, respectively.[54] It was suggested that the known lability of Cu^{2+} and Hg^{2+} for metal−ligand water exchange rates correlates well with measures of higher contribution to the current from the cation species in PEO.[55] Transport numbers for Mg^{2+} with ClO_4^- counterions in PVA/PAN blends, are measured to be reasonably high, ranging from 0.27 to 0.33 even though Mg^{2+} is expected to have slow exchange rates as measured in aqueous solution.[55] It is possible that the addition of solvating groups distinct from ether oxygens, as well as the use of different anion species could be enhancing the cation transport in these systems; however, these values should be regarded with caution until a more systematic study is performed due to some challenges in implementing such measurements. First, the quoted transport number is highly dependent on the initial current reading, I_0, with a slower data acquisition speed resulting in a lower initial current and thus an improved transport number. This was recently addressed for lithium electrolytes, with the suggestion that the initial current be calculated from the initial impedance rather than the first recorded point in the chronoamperometry.[49] Further, to get enough current signal for accurate measurement, large cell polarizations are needed. This stems from the inherently low conductivity of polymer electrolytes as well as the large interfacial resistances commonly observed in symmetric cells containing multivalent metals. Strictly speaking, the theory mentioned above only holds for small potentials on the order of 10 mV, though many studies use 20 mV or even 100 mV for measurement without significant issue; applied voltages up to 1 V, however, are a significant departure from equilibrium and are too large for accurate application of this theory. Large changes of interfacial resistance over the course of the measurement also present a concern, as this suggests significant parasitic reactions and decomposition that could be contributing to the measured current.[56]

Lastly, the issue of ion pairing affecting the transport number measurement cannot be overlooked; in concentrated or otherwise non-ideal electrolytes where ion-ion interactions are most prevalent, the above relationship does not hold, and a more detailed understanding of the mobility of various species is needed for transference number analysis.[57, 58] This is especially relevant for multivalent electrolytes, which tend to have stronger ion-ion interactions, as discussed further below. Given the above complications with this technique, it is not surprising that transport number measurements for multivalent ions vary widely. At the very least these experiments suggest that divalent ions are indeed somewhat mobile in polymer electrolytes.

1.4.2 Pulsed-field gradient NMR

Nuclear magnetic resonance (NMR), specifically pulsed-field-gradient (PFG) NMR, has been used as an alternative strategy for measuring diffusion coefficients of ions of interest which can then be used to calculate transport/transference numbers. PFG NMR measures the diffusion coefficient of an NMR active nuclei, with the ability to both distinguish ion environments through chemical shift and measure multiple diffusion coefficients of nuclei within the same chemical shift environment.[59, 60] However, for many polymer systems, this technique cannot distinguish between the motion of unassociated single cations and those aggregated with other ions because PFG NMR measures diffusion over a length scale of a few micrometers. Ions hop through a polymer matrix in a series of association and dissociation events with both solvating units on the polymer and with their counterions. Over the time and length scale of a PFG NMR measurement, the ions being tracked have existed in a mix of environments ranging from mobile ions to immobile solvated ions to aggregates. The diffusion coefficient measured is thus an average diffusion coefficient weighted by the time spent in the var-

ious mobile and immobile environments. This exchange between environments over the PFG NMR measurement timescale makes it more difficult to identify the exact nature of the mobile nucleus of interest. However, it does allow for determination of whether the species is mobile at all. A PFG NMR transport number is defined, for a multivalent cation with monovalent anion salt, as

$$t_{+,NMR} = \frac{z_+ D_+}{z_+ D_+ + D_-} \tag{1.4}$$

where z_+ is the valency of the cation, and $D_\pm$ are the diffusion coefficients of the species containing the cation and anion as measured via PFG NMR. Thus, this measurement of transport includes the implicit assumption that all ions are perfectly dissociated and non-interacting over the course of the measurement.

A promising opportunity to begin to extract the diffusion coefficient of solely ionic species within polymer systems comes with electrophoretic PFG NMR, which measures the diffusion under an applied electric field and thus weights the diffusion of ionic species more heavily.[61, 62] This technique would allow for the measurement of the true transference number (T_+) rather than an assumed transport number. Electrophoretic NMR is not readily available, however, and has yet to be applied to polymer electrolytes.

While gaining prevalence in lithium-based conductors, we were the first to use PFG NMR for multivalent ion conductors due to the difficulty of finding appropriate multivalent nuclei for NMR (see Chapter 3).[5] While many divalent species are NMR-active, most have such low gyromagnetic ratios or abundance that direct detection, especially for diffusion measurements, is infeasible. This necessitates indirect confirmation of mobility through a comparison between the total ionic conductivity measured by EIS and

that calculated from diffusion coefficients measured via NMR. The ionic conductivity contribution that is expected from a set of i species based on their diffusion coefficients can be calculated as

$$\sigma = \frac{F^2}{RT} \sum z_i^2 c_i D_i \tag{1.5}$$

where F is Faraday's constant, R is the ideal gas constant, T is the absolute temperature, and z_i, c_i, and D_i are the valency, concentration, and diffusion coefficient of the i^{th} species.[33] This equation requires knowledge of the exact concentration of ions present as well as their diffusion coefficient; typically, it is assumed that the salt is fully dissociated and thus the relevant ion concentration is the initial concentration of salt added to the system. This assumption provides an upper bound on a species' conductivity contribution. If the conductivity contribution from the measured species is insufficient to recover the total ionic conductivity measured via EIS, then an additional species must be present in the system to contribute the remaining conductivity.

This technique was used in recent work on Zn^{2+} conductivity within a PEO-imidazole polymer system, discussed in Chapter 3.[5] The anion diffusion coefficient was measured using PFG NMR, and the ionic conductivity was calculated assuming no cation contribution. It was found that this conductivity underestimated that which was measured using EIS, indirectly suggesting a contribution from the Zn^{2+} cations within the system. Importantly, it should be noted that while the mobility of the divalent Zn^{2+} species was estimated to be slightly less than half of the corresponding Li^+ species in the equivalent polymer system, the contribution to the conductivity was comparable between the two ions ($t_+ = 0.18$ for Li^+ and $t_+ = 0.13$ for Zn^{2+}). This highlights the benefit of a multivalent as opposed to monovalent cation for conductivity: assuming the same cation concentration, a multivalent cation can have a diffusion coefficient

that is smaller by a factor of its valency and still contribute equivalently to the ionic conductivity.

Indirect measurements of transport number using PFG NMR do not work for all multivalent cations. For some multivalent species such as Cu^{2+}, unpaired electrons significantly increase the speed of NMR signal decay, making diffusion measurements of even the anion species impossible under most experimental conditions. Thus, this technique will be limited to either NMR-active nuclei, or at least NMR-friendly nuclei for indirect measurements of cation contributions to ionic conductivity.

1.4.3 Newman method

A more rigorous method for actual transference number determination stems from thermodynamic considerations but is limited by experimental complexity and propensity for propagating error.[58] The transference number can be calculated from separate measurements of potential versus concentration, restricted diffusion, and steady-state current. Unlike the previous two techniques, this method holds for concentrated and non-ideal solutions.[58] These measurements require non-blocking electrodes (e.g. metal foil) for the metal cation of interest and have been shown to result in negative transference numbers as low as -0.38 and -4.4 for Li^+ and Na^+, respectively, in PEO. [49, 58] This is in stark contrast to measurements using the steady-state or PFG NMR methods on the same systems, where the transference/transport number remained positive over the entire concentration range. The existence of ionic clusters can give rise to negative transference numbers, which means that current is primarily transported by negatively-charged aggregates, and thus cations move in the "wrong" direction within a cell.[49, 58] Unfortunately, this method is not popular, possibly due to the number of experiments that must be performed. One potential issue for these

measurements is that they can be influenced by the presence of a solid electrolyte interphase (SEI) that typically forms between the polymer and metal foil. This shortcoming has been acknowledged for lithium systems and could play a significant role for multivalent systems if a stable interface cannot be formed, or if the interfacial resistance becomes too large.[49] To our knowledge, this method has not yet been applied to multivalent electrolytes. Nonetheless, the use of this technique for multivalent electrolytes could provide critical information about the primary means of cation transport in such systems.

1.5 Polymer electrolyte mechanics

Multivalent ions within ion-conducting polymers may provide beneficial mechanical properties compared to their lithium counterparts. The use of polymer electrolytes in devices enables safer, simpler and more flexible device design if the polymer can act as both the separator and the electrolyte. This requires a robust polymer membrane. Most studies of multivalent polymer electrolytes have focused on ionic conductivity, but not on the mechanical properties of the resulting films.

1.5.1 Polymer rheology

Rheology is the study of the flow and deformation of materials, and is particularly useful for studying polymer mechanics. The analysis of polymer mechanics from rheological data is a highly active scientific field, and can provide rich information about local polymer interactions as well as bulk properties.[63–65] Polymers exhibit viscoelastic behavior, meaning their deformation response depends on both the force

and the rate of the applied force.[66] This is a combination of a fluid-like viscous response and a solid-like elastic response. Similar to EIS measurements, rotational rheology measures the frequency- (or temperature-)dependent polymer mechanical response to a sinusoidally-varying stimulus, in this case a shear force applied to a disk of polymer sandwiched between two parallel plates (see Figure 1.4a). The polymer mechanical response is typically represented by the shear modulus, G (shear stress divided by shear strain), as a function of frequency or temperature. The response is typically split into two metrics, the storage modulus, G', which measures the elastic or in-phase polymer response, and the loss modulus, G'', which measures the viscous or out-of-phase response (Figure 1.4b).

The nature of the response curve depends on the properties of the polymer (Figure 1.4c). All polymers start with a glassy plateau at high frequency/low temperature, transitioning through their T_g to a rubbery material. A low molecular weight polymer will quickly exhibit terminal flow at low frequency/high temperature where G' and G'' versus frequency on a log-log plot will have a slope of 2 and 1, respectively. As molecular weight increases, the transition to the terminal regime is delayed, resulting in a larger rubbery plateau which occurs due to entanglements and polymer-polymer interactions. A fully cross-linked polymer will not transition into terminal flow, showing frequency-independent behavior at low frequency. Ion-containing polymers typically show intermediate behavior between these two extremes since the ions within the polymer matrix interact dynamically with the polymer, leading to transient cross-links which create a solid-like response at high frequency but a liquid-like response at low frequency/long timescales.[63, 67] These curves are generally collected over many orders of magnitude in frequency, and often are completed using the principle of Time-Temperature Superposition (TTS), which states the equivalence between long

timescales and low temperatures. Many materials are rheologically complex, meaning that TTS should not hold over the entire range of responses of the material; however generally TTS holds reasonably well, enabling the creation of a master curve exhibiting the range of features described above.

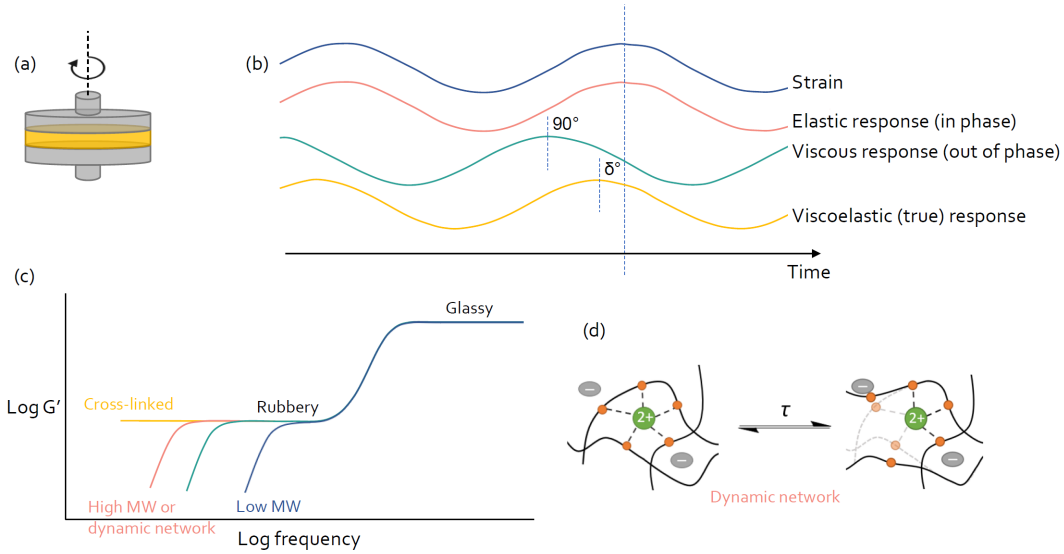

Figure 1.4: Polymer rheological response will change based on the nature of the polymer probed. (a) A schematic of the typical rheological set-up. (b) The viscoelastic response of polymers includes a solid-like elastic response and liquid-like viscous response. (c) The storage modulus response shows specific transitions as a function of frequency dependent on the polymer properties. (d) Mechanical properties of multivalent polymers can be tuned through the use of metal−ligand coordination

1.5.2 Tuning mechanical response

Multivalent ions are known to impart tailorable mechanical properties for polymer networks and gels. Specifically, multivalent ions such as Ni^{2+}, Cu^{2+}, Zn^{2+} and Fe^{3+} can be used as dynamic crosslinking agents for self-healing or stimuli-responsive polymer networks due to their multi-functional interactions with the polymeric host, [68–73] though the balance between transient cross-linking and ionic conductivity has not been

exploited (Figure 1.4d).

As will be discussed in detail in Chapter 2, we have shown that ion-conducting polymer networks form through the interaction of Ni^{2+} salts with imidazole ligand coordination sites on a polymer chain.[4] At all studied salt concentrations, a dynamically crosslinked network was formed, showing the typical rheological signature of a plateau in the storage modulus, followed by subsequent liquid-like relaxation at lower frequencies. The plateau modulus increases as a function of salt concentration but saturates at around eight times the original value of 1 MPa upon complete crosslinking of the gel. During the initial increase in plateau modulus, there is a concomitant improvement in ionic conductivity due to the higher ion concentration. At Ni^{2+} to imidazole ratios larger than 0.12, however, the ionic conductivity decreases due to dominant effects of an increasing T_g. The influence of the slower segmental dynamics is apparent when the temperature at which conductivity is measured is adjusted by the T_g at each salt concentration; the ionic conductivity then shows a monotonic increase with salt concentration. Thus, multivalent metal cations can act as dynamic cross-linking agents only at low concentrations, before slower segmental motion dominates the behavior and reduces ionic conductivity. Importantly, this initial study did not probe the extent to which the Ni^{2+} cation participates in ion conduction. While the labile nature of the metal−ligand coordination bond allows for cation conduction in such a system, the strong interaction between the Ni^{2+} and imidazole likely reduces cation mobility such that the anion conduction dominates as in most polymer electrolytes.

A follow-up study, which is the focus of Chapter 3, examined how a wider range of multivalent salts could be used to control polymer mechanical properties.[5] Li^{+}, Ni^{2+}, Cu^{2+}, Zn^{2+} and Fe^{3+} salts were mixed at a constant ratio of cation to imidazole of 0.1 into the same polymer matrix as before. The specific coordination chemistry

of the metal cation with imidazole results in dramatic tunability of the zero-frequency viscosity of the polymer systems, with over three-orders of magnitude change between the Li-PIGE polymer and the Ni-PIGE polymer. Interestingly, the ionic conductivity does not follow a specific trend and is much less sensitive to salt identity than the bulk mechanical properties. One likely contribution to this insensitivity is the invariant T_g as a function of metal cation identity; thus, while bulk viscosity can be altered by switching metal-ligand coordination strength, the local segmental dynamics remain essentially invariant, suggesting that ion mobility through the polymer matrix is likely not significantly affected. Such behavior has also been observed for covalent crosslinking in ion-conducting polymers with low crosslinking density and flexible crosslinkers.[74] Indeed, the PFG NMR diffusion coefficient of the $TFSI^-$ anion in the Li^+- and Zn^{2+}-containing polymers is identical once adjusting for the slight T_g change in the two polymers. This suggests that ion-ion interactions are minimal, as the identity of the cation and concentration of the anion do not play a role in the mobility of the anion species. In this study, PFG NMR suggests that the Zn^{2+} ions are mobile and contribute similarly to the ionic conductivity in the Zn-PIGE as the Li^+ ions do in Li-PIGE. These results motivate future studies to explore the ability of divalent species to both contribute to the ionic conductivity as well as impart beneficial mechanical properties to polymer electrolytes.

1.6 Polymer platform design and thesis outline

This thesis explores the design of ion conducting polymer electrolytes for both lithium and multivalent applications. A modular synthetic platform was designed for easy tunability of the various features hypothesized to impact ionic conductivity per-

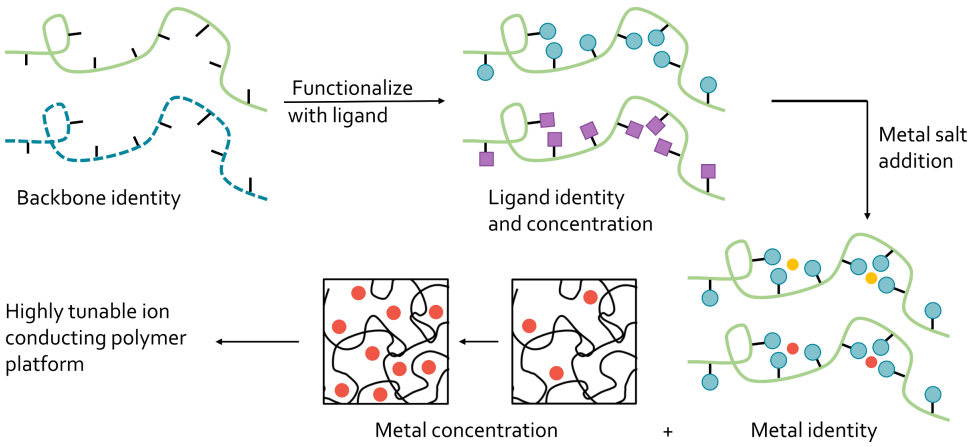

Figure 1.5: A modular synthetic platform based on thiol-ene click chemistry and metal salt addition was designed for maximum tunability of the factors hypothesized to control ionic conductivity.

formance and polymer mechanics (Figure 1.5). The polymer matrix is formed by functionalizing a variety of polymer backbone species with a range of ligands at varying concentrations. The polymer matrix is then mixed with metal salts, where the identity of the salt as well as the concentration can be altered.

The polymers studied in this work use metal–ligand coordination as the mechanism for salt solvation and ion transport (Figure 1.6). Metal–ligand interactions provide a nice framework for studying ion-polymer interactions because the interactions are well-defined, and highly tunable based on the identity of the metal and ligand species. A wide variety of ligands have been studied for self-healing [75, 76] and biologic applications [77], providing some pre-existing understanding of the interaction strengths and timescales. Most importantly, metal–ligand interactions are dynamic, though the timescale for breaking and re-forming a metal–ligand coordination interaction depends again on the metal and ligand species. The dynamic nature of the interaction enables cation conduction within these polymers, which is important for energy storage applications.

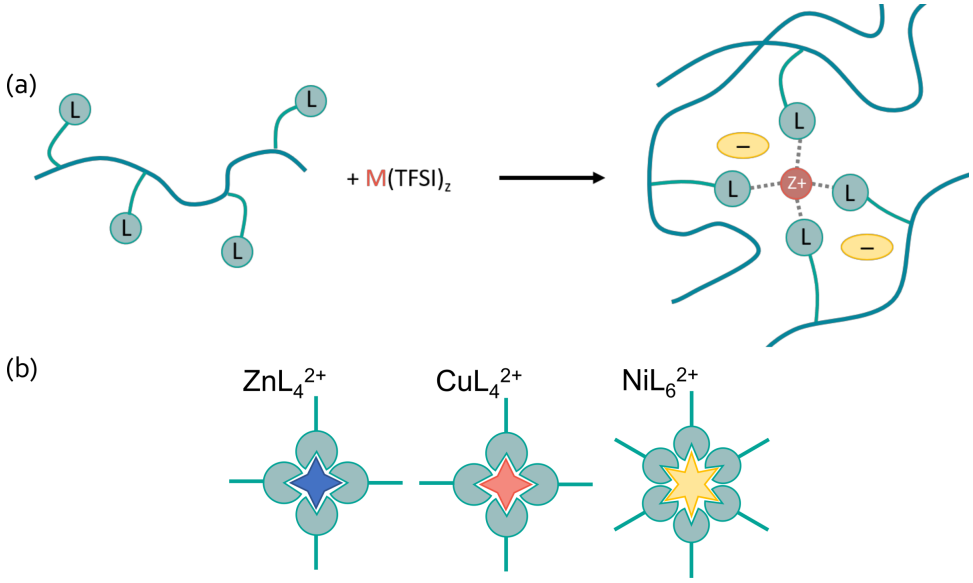

Figure 1.6: (a) Metal–ligand coordinating polymers dissolve salts through interaction of ligand species with metal cations. (b) These metal–ligand interactions are well-defined for most transition metal species. Importantly, these interactions are also dynamic, enabling cation transport through the polymer matrix.

The following chapters explore the various tunable handles of the synthetic platform shown in Figure 1.5. Chapter 2 identifies the role of Ni^{2+} concentration on the ionic conductivity and polymer mechanical response of an ether-imidazole based polymer. An optimum ion concentration was found to exist for conductivity performance due to the trade-off between ion mobility and polymer mechanical properties. This same polymer was studied with a variety of metal cations (Li^{+}, Zn^{2+}, Cu^{2+}, Ni^{2+}, and Fe^{3+}) in Chapter 3, revealing that while the polymer mechanics depend highly on metal identity, the total ionic conductivity does not. The cation transport properties were also measured using PFG NMR, and it was found that the divalent Zn^{2+} ion contributes almost equally to the ionic conductivity as a monovalent Li^{+}. Next, the role of polymer backbone identity was probed (see Chapter 4) - three backbones with varying polarity were synthesized and the conductivity and ion structure were compared. Surprisingly, while the backbone identity did influence the ion aggregation and local

metal−ligand environment, it did not alter the total conductivity performance. Field-theoretic simulations reveal that for all backbones, the ion aggregates are likely percolated and therefore the connectivity of the aggregates remains the same throughout the series. Chapter 5 explores the role of ligand density on the polymer conductivity performance, showing that reducing the imidazole ligand content can provide an order of magnitude improvement in ionic conduction. Lastly, the role of ligand linker chemistry was probed (Chapter 6), with the removal of an amide functionality providing a 100-fold improvement in ionic conductivity and a doubling of the Li^+ transference number. This highlights the importance of chemical design in optimizing polymer electrolyte performance.

Finally, this thesis provides a study of the overarching factors determining ionic conductivity performance of polymer electrolytes through a data-mining study which compiles and analyzes literature data published over the last half-century (Chapter 7). The visualization results of this study can be accessed and interacted with online (*website in progress*), and reveal that while individual controlled studies like those described in the preceeding chapters provide clues into polymer electrolyte performance, the aggregate performance of multiple classes of polymer electrolytes is more variable, and suffers from inconsistent processing conditions. Nevertheless, the importance of electrolyte T_g, salt concentration, polymer electronegative solvation sites and anion size are corroborated through the use of statistical learning techniques.

These chapters provide an overview of the relevant fundamental factors controlling polymer electrolyte performance, and guide future scientists in the design of high-performance electrolytes.

Chapter 2

Ion Transport in Dynamic Polymer Networks Based on Metal–Ligand Coordination: Effect of Cross-Linker Concentration

2.1 Abstract

The development of high-performance ion conducting polymers requires a comprehensive multiscale understanding of the connection between ion–polymer associations, ionic conductivity, and polymer mechanics. We present polymer networks based on dynamic metal–ligand coordination as model systems to illustrate this relationship.

Reproduced with permission from [4]: G. E. Sanoja,* N. S. Schauser,* J. M. Bartels, C. M. Evans, M. E. Helgeson, R. Seshadri, and R. A. Segalman. Ion Transport in Dynamic Polymer Networks Based on Metal-Ligand Coordination: Effect of Cross-Linker Concentration. *Macromolecules*, 51, 2017 (2018). DOI: 10.1021/acs.macromol.7b02141 (*equal contribution)

The molecular design of these materials allows for precise and independent control over the nature and concentration of ligand and metal, which are molecular properties critical for bulk ion conduction and polymer mechanics. The model system investigated, inspired by polymerized ionic liquids, is composed of poly(ethylene oxide) with tethered imidazole moieties that facilitate dissociation upon incorporation of nickel(II) bis(trifluoromethylsulfonyl)imide. Nickel−imidazole interactions physically cross-link the polymer, increase the number of elastically active strands, and dramatically enhance the modulus. In addition, a maximum in ionic conductivity is observed due to the competing effects of increasing ion concentration and decreasing ion mobility upon network formation. The simultaneous enhancement of conducting and mechanical properties within a specific concentration regime demonstrates a promising pathway for the development of mechanically robust ion conducting polymers.

2.2 Introduction

Polymer networks with dynamic junctions are an important class of materials based on noncovalent interactions such as hydrogen bonds,[78, 79] electrostatic forces,[80, 81] metal−ligand coordination,[82, 83] host−guest complexation,[84, 85] van der Waals forces,[86] and protein associations.[87] In contrast to their permanently cross-linked counterparts, dynamic polymer networks have physical associations with relatively weak binding energies (i.e., $\approx k_BT$) so that thermal fluctuations or external stimuli enable breakage and re-formation on time scales suitable for engineering materials.[64, 88] Dynamic polymer networks find numerous applications in energy conversion and storage,[89] thermoplastics,[90] and medicine[91] due to the toughness provided by the energy-dissipating physical associations.[92–94] Given that the

lability of physical associations is intimately coupled to the time-dependent bulk properties of dynamic polymer networks, it is essential to understand their role in polymer relaxation mechanisms on time scales relevant to the design of high-performance functional materials.

Dynamic polymer networks exhibit distinct viscoelastic behavior compared to polymer melts.[63, 64, 67] Under deformation these materials behave as elastic rubbers at times shorter than the lifetime of a physical cross-link, but exhibit liquid flow on longer time scales because of microscopic polymer chain diffusion enabled by the breakage of a few cross-links. The resulting linear viscoelastic response is characterized by longer terminal relaxation times and an increase in plateau modulus relative to polymer melts. Pioneering work on model poly(4-vinylpyridine) cross-linked with N,C,N-pincer Pd(II) and Pt(II) complexes demonstrates that the low strain, frequency-dependent dynamic moduli are dictated by the dissociation rate of physical associations as determined by NMR spectroscopy in dilute solution.[83, 95] This and complementary investigations on hydrogels with coiled-coils,[96] bis(histidine)$-Ni^{2+}$,[68, 71] and hydrazone[97] cross-links support the argument that the exchange rate of physical associations governs the relaxation dynamics of these materials as long as the time scale of exchange is faster than that of other competing processes (e.g., polymer diffusion). Nonetheless, elucidating the quantitative interconnection between the lifetime of the physical associations and the bulk viscoelastic properties of polymer networks still remains a challenge.[98] The lack of accurate quantitative prediction partially results from the approximation of the exchange rate of physical associations to the dissociation rate of small molecule complexes in dilute solution−a gross oversimplification that neglects important energetic and kinetic effects resulting from solvation, chain connectivity, and cooperativity. Groundbreaking investigations on model poly-(N,N-dimethylacrylamide)

functionalized with histidine and cross-linked with Ni^{2+} illustrate differences in the rates of dissociation and exchange of physical associations in polymer networks.[70] This motivates inspection not only of other time-dependent properties known to be coupled to polymer dynamics (e.g., ionic conductivity) but also of the cooperative and synergistic effects that arise on dynamic responses upon changes in network structure.

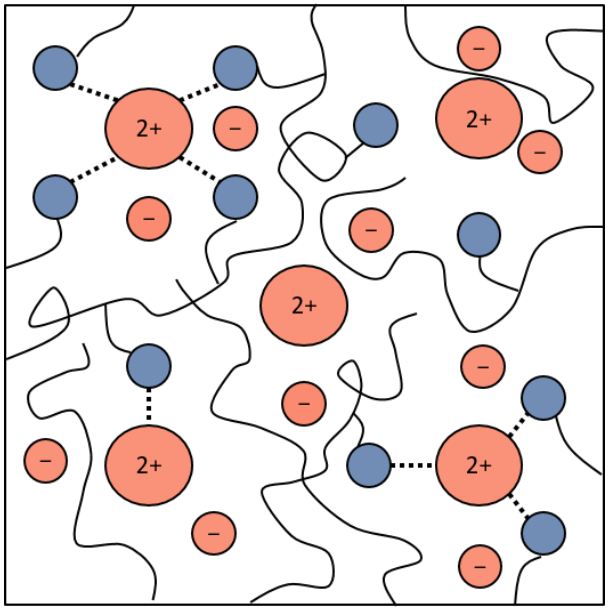

Figure 2.1: Salt solvation and metal−ligand coordination are coupled due to chemical equilibrium. Based on Le Chatelier's principle, metal−ligand coordination also promotes salt dissociation. This not only translates into a higher concentration of ions, but also on the formation of dynamic crosslinks with important consequences on polymer mechanics. The model system investigated is based on polymers with tethered imidazole ligands, nickel (II) cations (Ni^{2+}), and bis(trifluoromethylsulfonyl)imide anions ($TFSI^{-}$). The number of imidazole moieties coordinating the Ni^{2+} is defined as the coordination number (z). The geometries (z = 1 to 4) are only depicted for illustrative purposes. Figure prepared by Gabriel Sanoja.

Ion transport in polymers is influenced by ion–polymer associations (i.e., solvation) that reversibly break and form on time scales coupling conduction to polymer segmental dynamics. This results from excluded volume interactions requiring polymer segments to accommodate space upon ion motion.[99] The coupling between poly-

mer dynamics and ion transport is an essential feature which distinguishes ion conducting polymers from dilute liquid electrolytes. Because of the nucleophilic nature of conventional polymer electrolytes such as poly(ethylene oxide), long-range cation transport must involve dissociative steps that facilitate hoping between neighboring solvating sites, as polymer segmental motion arising from local reorientation enables only short-range motion within limited regions of space. Thus, only cations that form labile bonds with a polymer can have significant contributions to the ionic conductivity. The mechanism of ion conduction for anions is fundamentally different, as these do not form strong bonds with polymers so their motion depends primarily on local dynamics such as in concentrated liquid electrolytes[33] or multicomponent inert gases.[100] Dynamic polymer networks based on kinetically labile metal−ligand coordination serve as model systems to develop a multiscale picture between ion–polymer associations, ionic conductivity, and polymer mechanics. The nature and concentration of ligand and metal can be tuned in these materials to enable not only spanning a range of physical association energies, but also controlling the concentration of both elastically active strands and ions known to be critical in the bulk mechanical and conducting properties. In particular, polymers based on imidazole and histidine ligands are interesting due to a preexisting understanding of the reactivity[101] and interactions with transition metal ions in chemical and biological systems.[102] Investigations of these materials have primarily focused on quaternized imidazolium[103–109] and histammonium[110–112] ions (i.e., polymerized ionic liquids), yet imidazole and histidine moieties are capable of interacting with alkali, alkaline earth, and transition metal ions, thus promoting salt dissociation and influencing the ion conducting and mechanical properties (Figure 2.1). From a materials chemistry standpoint, these materials constitute macromolecular analogues of chelating ionic liquids, a set of concentrated electrolytes known to solubilize ions such as Zn^{2+} due to metal−ligand coordination.[113]

We present here an investigation of the ion conducting and mechanical properties of dynamic polymer networks based on metal−ligand coordination. A combination of ring-opening anionic copolymerization, thiol-ene click chemistry, and ligand chemistry is used to rationally design materials for elucidation of structure−property relationships. In particular, we focus on the effect of concentration of nickel(II) bis(trifluoromethylsulfonyl)imide salt on the ion conducting and mechanical properties of a poly(ethylene oxide) with tethered imidazole ligands. Upon physically cross-linking with Ni^{2+}, dynamic polymer networks exhibit an increase in elastic modulus of an order of magnitude, and a maximum in ionic conductivity presumably due to the trade-off between ion concentration and ion mobility. The demonstrated relationship between mechanics, ion conduction, and metal−ligand coordination illustrates design rules for the development of novel ion conducting polymers. As opposed to composites based on structural insulating agents (e.g., polymer nanocomposites or block copolymers),[114, 115] incorporation of transition metal ions into polymers with tethered ligand moieties allows for bulk mechanical reinforcement with beneficial effects on ion transport.

2.3 Experimental section

Materials. All materials were used as received from Sigma-Aldrich unless otherwise noted. $CDCl_3$ and methanol-d4 were purchased from Cambridge Isotope Laboratories; acetonitrile, hexanes, methanol, and isopropyl alcohol from BDH Chemicals; allyl glycidyl ether (AGE) from TCI America; and anhydrous nickel(II) bis(trifluoromethylsulfonyl-imide) from Alfa Aesar. Tetrahydrofuran (THF) was collected from a commercial J.C. Meyer dry solvent system and used immediately thereafter. AGE was dried over butylmagnesium chloride, degassed through three freeze−pump−thaw cycles, and further

distilled to a flame-dried receiving flask. Ethylene oxide (EO) was degassed through three freeze−pump−thaw cycles and further distilled to a flame-dried buret immersed in an ice bath until use. Potassium naphthalenide was prepared from potassium and naphthalene in THF (0.3 M) and stirred with a glass-coated stir bar for 24 h before use.

Synthesis of N-(2-(1H-Imidazol-1-yl)propyl)-4-mercaptobutanamide (Im-SH). The synthesis of Im-SH was adapted from Lundberg et al.[116] In a 250 mL round-bottom flask equipped with a Teflon-coated stir bar and a condenser, 1-(3-aminopropyl)imidazole (10.0 g, 79.9 mmol), γ-thiobutyrolactone (8.2 g, 80.2 mmol), and acetonitrile (135 mL) were added. The reaction was heated to 95 °C and allowed to proceed for 12 h. The reaction was cooled to room temperature, and the resulting pale yellow liquid isolated by evaporation in vacuo.

Synthesis of Poly[(ethylene oxide)-stat-(allyl glycidyl ether)] (PEO-stat-PAGE). The copolymerization of EO and AGE was adapted from Lee et al.[117] Separate burets containing THF and EO were connected to a thick-walled glass reactor fitted with Ace threads. The EO was connected by flexible stainless steel belows so that the buret could be immersed in an ice bath until use. The reactor assembly was flame-dried and then cycled between vacuum and positive argon pressure (5 psig) three times. The reactor was finally charged with an argon atmosphere and isolated from the Schlenk line. THF was added, and the temperature equilibrated at 0 °C. Based on the amount of purified EO (22.77 g, 517 mmol), a quantity of benzyl alcohol (166 μL, 1.60 mmol) was added through a gastight syringe. Potassium naphthalenide (0.3 M in THF) was added through a gastight syringe to titrate the benzyl alcohol until a pale green end point. EO was added by lifting the cold buret and allowing monomer to drain in the reactor while AGE (15 mL, 127 mmol) was simultaneously added via gastight syringe. The temperature was increased to 40 °C, and the polymerization allowed to proceed

for 24 h. After complete conversion of EO and AGE, degassed and acidified isopropyl alcohol was added to terminate the polymerization. The resulting PEO-stat-PAGE was precipitated into an excess of hexanes and dried for 48 h at 55 °C *in vacuo*. PEO-stat-PAGE was immediately transferred to a glovebox and stored in an inert nitrogen atmosphere to mitigate moisture uptake.

Synthesis of Imidazole Functionalized Copolymer (PEO-stat-PIGE). In a 250 mL round-bottom flask equipped with a Teflon-coated stir bar, PEO-stat-PAGE (3.00 g, 8.94 mmol of allyl groups), Im-SH (5.08 g, 22.35 mmol), 2,2-dimethoxy-2-phenylacetophenone (DMPA, 0.46 g, 1.79 mmol), and methanol (90 mL) were added. The solution was degassed sparging with nitrogen for 30 min and then allowed to react for 2 h under UV irradiation ($\lambda = 365$ nm). The resulting PEO-stat- PIGE was concentrated by rotary evaporation, purified by dialysis in methanol (4 times 4 L), and dried for 48 h at 55 °C *in vacuo* to yield a pale yellow viscoelastic liquid. PEO-stat-PIGE was immediately transferred to a glovebox and stored in an inert nitrogen atmosphere to mitigate moisture uptake.

Synthesis of Polymers Based on Imidazole−Nickel Coordination (PIGE-Ni^{2+}). In an inert atmosphere, stock solutions in anhydrous methanol of polymer (126 μL, 39.6 wt%, 88 μmol of imidazole) and nickel(II) bis(trifluoromethylsulfonyl)imide were mixed in 5 mL vials to yield materials with an appropriate molar ratio of nickel(II) to imidazole (i.e., r = [Ni^{2+}]:[Im]). The resulting ion conducting dynamic polymer networks were stored in the glovebox to mitigate moisture uptake.

Molecular Characterization. Gel permeation chromatography (GPC) was performed on a Waters instrument using a refractive index detector and Agilent PL gel 5 μm MiniMIX-D column. THF at 35 °C was used as the mobile phase with a flow rate of 1.0 mL min^{-1}. The polydispersity index (Đ) was determined against PEO narrow stan-

dards (Agilent). ^{1}H NMR spectra were collected on a Bruker Avance DMX 500 MHz. The molecular weight of the precursor PEO-stat-PAGE was determined using ^{1}H NMR end-group analysis. This spectrum is collected in $CDCl_3$ at a polymer concentration of 60 mg mL^{-1} with 128 scans and a pulse delay time of 5 s.

General Protocol for PIGE-Ni^{2+} Sample Preparation. *All Polymer Samples Were Kept Rigorously Dry Throughout the Described Experiments.* Polymer samples were prepared in an inert nitrogen atmosphere by casting solutions of PIGE-Ni^{2+} into standard substrates (e.g., aluminum pans, Teflon, and indium tin oxide) and drying in vacuo at 55 °C sequentially for 8 h in the glovebox (10^{-3} Torr) and 1 h in a high-vacuum oven (10^{-8} Torr). Traces of water and methanol in a representative PIGE-Ni^{2+} sample were below detection limits of both Karl Fischer titration and solid-state ^{1}H NMR.

Thermal Characterization. Polymer samples were cast as described above into standard aluminum pans. The samples were sealed and characterized with a PerkinElmer DSC 8000 to measure the glass transition temperature (T_g) on second heating at 20 °C min^{-1} using the onset method.

Mechanical Characterization. The rheology of the samples was characterized using 8 mm stainless steel parallel plates in a TA Instruments ARG2 rheometer operating under dry nitrogen flow. Sample thicknesses were approximately 200 μm. Dynamic frequency sweeps were performed over a range of temperature, frequency, and strain amplitude respectively of 5 °C to 70 °C, 0.1 rad s^{-1} to 100 rad s^{-1}, and 0.1% to 10%. Strain sweeps at 10 rad s^{-1} confirmed that measurements were performed in the linear viscoelastic regime. The reference temperature (T_{ref}) used for time−temperature superposition was either 30 °C or T_g, and master curves were generated using horizontal shift factors. The elastic modulus was defined as G' at the frequency at which G'' exhibits a local minimum (i.e., local maximum in $tan(\delta)$). The terminal relaxation time

was determined at the frequency at which the power-law fit of the complex viscosity intersects the zero-shear viscosity.

Electrochemical Impedance Spectroscopy. Polymer samples were prepared as described above by casting into 1/4 in. clean circular indium tin oxide (ITO) substrates top-coated with a 150 μm Kapton spacer. The samples were sealed with clean ITO substrates and characterized with a Biologic SP-200 potentiostat. Transparent ITO/-glass electrodes were used to ensure the absence of bubbles and proper interfacial contact during in situ conductivity measurements. A sinusoidal voltage with amplitude 100 mV was applied in the frequency range of 1 Hz to 1 MHz. Ionic conductivity, in the absence of concentration gradients, was determined from the real component of the complex conductivity at the peak frequency in tan(δ) arising from the conversion of complex impedance into dielectric storage and loss.[118] This method is equivalent to determining the ionic conductivity from the impedance at the abscissa intercept of a Nyquist plot. Note that the materials presented herein contain two types of mobile ions: bis(trifluoromethylsulfonyl)imide anions (i.e., $TFSI^-$) and Ni^{2+} cations, and the contributions to the current (i.e., transference number) from each of them will depend on the operating conditions of the electrochemical device.[33, 57]

2.4 Results and Discussion

2.4.1 Molecular Design

Ion transport in dynamic polymer networks based on metal−ligand coordination is anticipated to be intimately coupled to salt dissociation, ion–polymer associations, and polymer segmental dynamics (Figure 2.1). The incorporation of ligands in a polymer of

low dielectric constant promotes salt dissociation to enhance both the ionic conductivity and elastic modulus via formation of labile bonds that serve as dynamic cross-links. The relatively weak binding energies of these cross-links enable breakage and formation on time scales that not only hinder polymer diffusion but also affect ion transport. Although the bulk mechanical and ion conducting properties are influenced by the lifetime of metal−ligand bonds, the underlying molecular mechanisms associated with polymer diffusion and ion transport are different. The former requires the successive breaking of various cross-links to allow a polymer chain to diffuse,[63, 64, 67] whereas the latter appears to be a more convoluted effect between ion concentration, mobility, and solvation.[99]

To elucidate the relationship between ion conduction, mechanics, and metal−ligand coordination, we engineered a polymer with ligand moieties covalently bonded to the backbone and capable of facilitating salt dissociation by forming dynamic cross-links. The molecular properties that we sought to control are the nature and concentration of ligand and metal, as these dictate the lability and lifetime of the cross-links. This was achieved on a mixture of poly(ethylene oxide) with tethered imidazole moieties and nickel(II) bis(trifluoromethylsulfonyl)imide salt. The complexation between Ni^{2+} and imidazole is anticipated to be the primary interaction dictating the mechanical and ion conducting properties, since the formation of Ni^{2+}−imidazole complexes is thermodynamically favored relative to Ni^{2+}−crown ethers.[102, 119] The weak electrostatic interactions resulting from large and charge-delocalized ions resemble that of chelating ionic liquids, yielding “plasticized” and amorphous polymers which even at high concentrations exhibit low glass transition temperatures (i.e., T_g). These materials constitute the metal−ligand analogues of proton and hydroxide conducting polymers involving Brønsted acid–base pairs and are suitable to elucidate structure−property re-

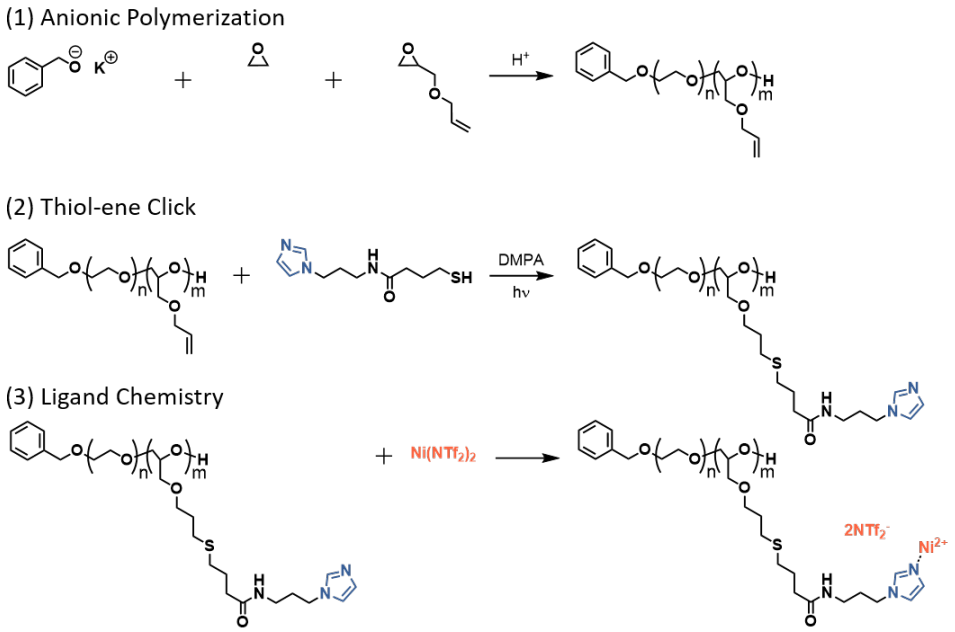

Figure 2.2: Molecular design strategy allows for fine and independent control over the properties expected to have an important effect on metal−ligand coordination, ion conduction, and polymer mechanics: ligand and metal concentration, and identity. This is respectively achieved by levering the relative amounts of co-monomers in anionic polymerization, the ratio of metal to ligand, the cation in the $TFSI^-$ salt, and the nucleophilicity of the aromatic ring of the thiol undergoing click chemistry. Figure prepared by Gabriel Sanoja.

lationships at high ion concentrations due to the thermal processability enabled by a subambient T_g.

The synthesis of ion conducting dynamic polymer networks is based on a combination of ionic copolymerization, click chemistry, and metal−ligand interactions (Figure 2.2). First, the imidazole-functionalized copolymer (i.e., PEO-stat-PIGE) was synthesized using epoxide ring-opening anionic copolymerization of ethylene oxide (EO) and allyl glycidyl ether (AGE), followed by UV activated thiol-ene click chemistry of N-(2-(1H-imidazol-4-yl)propyl)-4-mercaptobutanamide. PIGE was chosen because the nitrogen atom located in the aromatic ring can coordinate metal ions to facilitate salt dissociation and create dynamic cross-links. Next, the resulting PEO-stat-PIGE was

Polymer[a]	N_{EO}^{b}	N_{IGE}^{c}	$n_{Ni(TFSI)_2}^{d}$	r=[Ni^{2+}]:[Im][e]	wt%$_{Ni(TFSI)_2}$	T_g (°C)[f]
PIGE-Ni^{2+} 0.0	323	79	-	-	-	−33
PIGE-Ni^{2+} 3.7	323	79	2.9	0.037	4.2	−31
PIGE-Ni^{2+} 12.1	323	79	9.6	0.121	12.6	−29
PIGE-Ni^{2+} 14.9	323	79	11.8	0.149	15.1	−23
PIGE-Ni^{2+} 16.0	323	79	12.6	0.160	15.9	−12
PIGE-Ni^{2+} 19.5	323	79	15.4	0.195	18.8	−2

Table 2.1: Properties of ion conducting dynamic polymer networks based on metal−ligand coordination. [a]Polymers are labeled PIGE-Ni^{2+} X.X, where X.X is the mol% of Ni^{2+} relative to the imidazole ligands. [b,c]Degree of polymerization of EO and IGE in the statistical copolymer determined via ^{1}H NMR end-group analysis. [d]Determined via elemental analysis (see Appendix, Table 2.2). [e]Determined from the molar ratio of Ni^{2+} to imidazole ligands. This ion concentration nomenclature is analogous to that previously reported for Li^+-conducting PEO.[11] [f]Determined via DSC using the onset method.

mixed with $Ni(TFSI)_2$ to generate ion conducting PIGE-Ni^{2+}. Fine and independent control over the ligand and metal nature and concentration can be achieved by replacing the aromatic ring in the thiol or the metal ion and levering the relative amounts of EO and AGE and Ni^{2+} and IGE. Here, a series of PIGE-Ni^{2+} with variable molar ratio of Ni^{2+} to IGE (i.e., r = [Ni^{2+}]:[IGE] = [Ni^{2+}]:[Im]) were investigated. Well-defined and narrowly dispersed PEO-stat-PIGE (M_n = 40 kDa, Đ < 1.2) with a constant mole fraction of imidazole moieties (x_{IGE} = 0.17) was synthesized, as determined using a combination of GPC and ^{1}H NMR. DSC traces demonstrate the amorphous nature of the statistical copolymers, a result consistent with the suppression of PEO crystallization in an atactic backbone. The molecular properties and thermal transitions of the various PIGE-Ni^{2+} are summarized in Table 2.1.

2.4.2 Linear Viscoelastic Response

Metal−ligand coordination bonds between Ni^{2+} and imidazole cross-link the PIGE-Ni^{2+} and induce a dramatic change in the bulk mechanical properties. The linear vis-

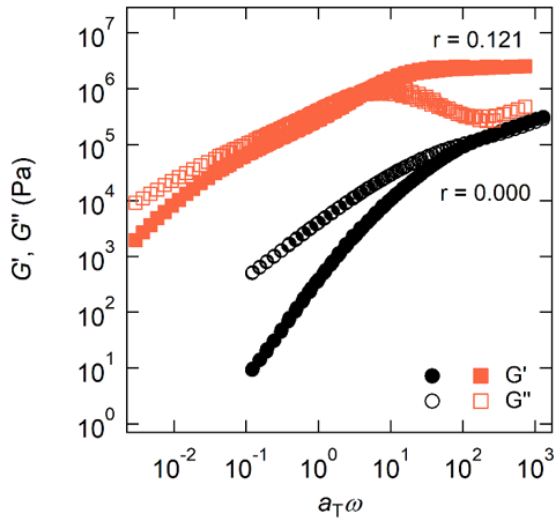

Figure 2.3: Viscoelastic response of dynamic polymer networks (T_{ref} = 30 °C) arises due to metal−ligand coordination between imidazole moieties tethered to the polymer backbone and Ni^{2+} cations resulting from salt dissociation. Rheology data collected on PIGE-N^{i2}+ under dry N_2 flow.

coelastic response of these materials is characteristic of associated polymers, with a significant increase in the terminal relaxation time (i.e., slower diffusion) and an enhancement in the plateau modulus relative to equivalent polymers without associating groups (Figure 2.3).[63, 64, 67] Associative polymers exhibit signature features in their dynamic mechanical moduli, including a plateau modulus at high frequencies, a crossover of the storage (G') and loss (G'') moduli, and terminal relaxation with scaling of $G' \sim \omega^2$ and $G'' \sim \omega$. Deviations from this liquid-like scaling observed in PIGE-Ni^{2+} ($G' \sim \omega^{0.9}$ and $G'' \sim \omega^{0.7}$) are attributed to a restricted experimentally accessible low frequency window and hindered polymer diffusion (i.e., sticky reptation). This terminal behavior is analogous to that of hydrogels based on histidine-functionalized poly(N,N-dimethylacrylamide) cross-linked with Ni^{2+} [120] and ionomers based on polyethers and sulfonated phthalates with sodium counterions.[65] The contributions of entanglements to the linear viscoelastic response are neglected due to the absence

of a rubbery plateau in neat PIGE. This assertion is further supported by the rheology master curves generated using T_g as the reference temperature (Appendix, Figure 2.8) where the mechanical spectra of the polymer melt and associated polymer networks with different r values fail to collapse − an observation consistent with differences in polymer topology and relaxation mechanisms governing the viscoelastic response. At high frequencies the network plateau modulus increases approximately 8-fold from 1.06 MPa to 7.93 MPa for r-concentrations respectively of 0.037 and 0.195 (Figure 2.4b). Moreover, the $G' - G$" crossover frequency ω_c decreases with increasing cross-linker concentration. For example, at 30 °C, ω_c is observed at 21.17 rad s^{-1} for PIGE-Ni^{2+} with $r = 0.037$ and decreases to 0.19 rad s^{-1} for $r = 0.257$.

The effect of Ni^{2+} on the elastic modulus can be explained by changes in polymer topology as a function of ion concentration. In particular, upon increasing the concentration of Ni^{2+} more metal−ligand complexes are formed which initially cross-link PIGE chains while inducing formation of independent network clusters. At a certain critical value of r known as the sol−gel transition (i.e., r_c), a space-spanning percolated network is formed that rapidly becomes more cross-linked with incorporation of additional Ni^{2+}. Here we approximate r_c to be that above which the linear viscoelastic response clearly resembles that of an associating polymer: $r_c \geq 0.121$. Comparisons of r_c with predictions from percolation theory are strictly not possible because the sol−gel transition is not defined for polymer networks with liquid-like terminal relaxation. Nonetheless, assuming PIGE-Ni^{2+} is a chemical network yields $r_c = 0.013$ (see Appendix). This combination of percolation theory and rheology serves to identify a clear criteria for network formation and is inspired by previous investigations on poly(4-vinylpyridine) cross-linked with N,C,N-pincer Pd(II) complexes.[121]

Enhancements in the elastic modulus above r_c are attributed to an increase in the

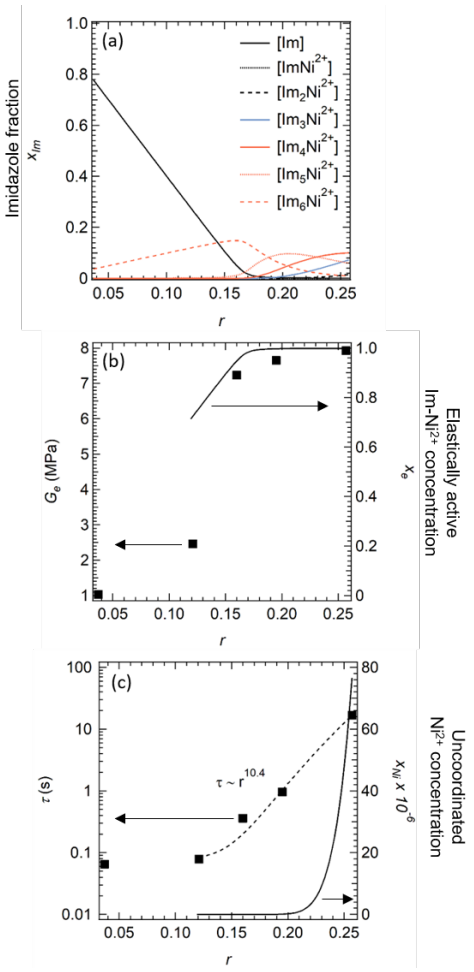

Figure 2.4: Mechanical properties depend strongly on the molar ratio of Ni^{2+} to imidazole ligands (r) (a) At the percolation threshold (i.e., $r_c \approx 0.121$) the majority crosslink species is Im_6Ni^{2+} with an average functionality of six. (b) The Im_nNi^{2+}crosslinks reinforce the material as revealed by an 8-fold increase in the plateau modulus G_e. Interestingly, the molar fraction of Im_nNi^{2+} species that contribute to the formation of elastically active strands, x_e, (–) and G_e plateau at approximately the same $r \approx 0.16$. This suggests that changes in coordination geometry have a negligible impact in the number of elastically active strands and in the polymer stiffness. (c) The terminal relaxation time, τ, increases due to larger friction resulting from ion–polymer interactions between the uncoordinated Ni^{2+} cation (–), poly(ethylene oxide) backbone, and imidazole moieties. The scaling experimentally obtained from a least-squares regression power-law fit is $\tau \sim r^{10.4}$. Analysis performed by Gabriel Sanoja.

number of elastically active strands upon addition of Ni^{2+}. Computation of the molar fraction of the various imidazole$-Ni^{2+}$ complexes in chemical equilibrium together with qualitative predictions from sticky-reptation theory support this assertion. Within this framework, only entropy contributes to the free energy, analogous to an ideal gas, and each elastically active strand provides an equal amount of stored energy (i.e., k_BT) to the modulus. Consequently, estimates of the fraction of imidazole$-Ni^{2+}$ complexes that yield elastically active strands provide quantitative insights into the concentration dependence of the modulus. We consider the following chemical equilibria for various Im_zNi^{2+} complexes with z tethered imidazoles coordinating Ni^{2+}:

$$Ni^{2+} + Im \overset{K_1}{\Longleftrightarrow} ImNi^{2+}$$

$$ImNi^{2+} + Im \overset{K_2}{\Longleftrightarrow} Im_2Ni^{2+}$$

$$Im_2Ni^{2+} + Im \overset{K_3}{\Longleftrightarrow} Im_3Ni^{2+}$$

$$Im_3Ni^{2+} + Im \overset{K_4}{\Longleftrightarrow} Im_4Ni^{2+}$$

$$Im_4Ni^{2+} + Im \overset{K_5}{\Longleftrightarrow} Im_5Ni^{2+}$$

$$Im_5Ni^{2+} + Im \overset{K_6}{\Longleftrightarrow} Im_6Ni^{2+}$$

and the corresponding material and charge balances:

$$[Im]_0 = [Im] + [ImNi^{2+}] + 2[Im_2Ni^{2+}] + 3[Im_3Ni^{2+}] + 4[Im_4Ni^{2+}] + 5[Im_5Ni^{2+}] + 6[Im_6Ni^{2+}]$$

$$[Ni^{2+}]_0 = [Ni^{2+}] + [ImNi^{2+}] + [Im_2Ni^{2+}] + [Im_3Ni^{2+}] + [Im_4Ni^{2+}] + [Im_5Ni^{2+}] + [Im_6Ni^{2+}]$$

$$2[TFSI^-]_0 = [Ni^{2+}]_0$$

For the purposes of this calculation, the equilibrium constants are assumed to be that of small molecule imidazole$-Ni^{2+}$ complexes in aqueous solution of potassium

nitrate:[102] $K_1 = 10^{3.03}\,\mathrm{M}^{-1}$, $K_2 = 10^{2.51}\,\mathrm{M}^{-1}$, $K_3 = 10^{2.01}\,\mathrm{M}^{-1}$, $K_4 = 10^{1.47}\,\mathrm{M}^{-1}$, $K_5 = 10^{1.10}\,\mathrm{M}^{-1}$, and $K_6 = 10^{0.51}\,\mathrm{M}^{-1}$. Evidently, this simplification neglects differences in physical and chemical environments between aqueous electrolytes and poly(ethylene oxide), yet the resulting equilibrium concentration trends are insensitive to the values of K_n as long as $K_1 \gg K_2 \gg K_3 \gg K_4 \gg K_5 \gg K_6 \gg [Im]_0^{-1}$. The calculated equilibrium mole fractions (Figure 2.4a) reveal critical features about metal−ligand coordination that influence the bulk mechanical properties such as (a) the average functionality of the cross-links at the percolation threshold is six, (b) there is a plateau in the concentration of imidazole−Ni^{2+} species (i.e., $x_e = \sum_n nIm_nNi^{2+}$) that contributes to the formation of elastically active strands at $r \approx 0.16$ (Figure 2.4b), and (c) at high $Ni(TFSI)_2$ concentrations there are uncoordinated Ni^{2+} ions ($[Ni^{2+}]$) (Figure 2.4c). An important underlying assumption behind these assertions is that intramolecular complexation reactions that yield network defects are negligible, an oversimplification that is rigorously not valid. However, this type of chemical equilibria analysis serves to simply illustrate changes in the distribution of metal−ligand complexes that govern the bulk properties of dynamic polymer networks. Note that although increasing the Ni^{2+} content in the polymer above $r \sim 0.16$ renders a change in coordination geometry, the modulus remains approximately constant due to inconsequential changes in the number of elastically active strands. Consequently, the initial order of magnitude enhancement in modulus upon cross-linking PIGE with Ni^{2+} plateaus upon saturation of imidazole, an observation that demonstrates mechanical stiffening of ion containing polymers via metal−ligand coordination.

Ni^{2+} ions that are not instantaneously coordinated by imidazole ligands or associated with $TFSI^-$ are solvated by the poly(ethylene oxide) backbone and can play a critical role in preventing bulk polymer flow. Incorporation of solvated Ni^{2+} in the PIGE

increases the friction force due to ion–polymer interactions and the terminal relaxation time (Figure 2.4). This effect is inverse to that previously reported on analogous acrylate copolymers cross-linked with Zn^{2+}, Cu^{2+}, or Co^{2+} where control of the mechanical properties is attained via incorporation of unbound free imidazole ligands.[69] Given that the probability of simultaneous dissociation of all imidazole−Ni^{2+} bonds on a polymer chain is negligible, the terminal relaxation signature for PIGE-Ni^{2+} networks presumably results from the partial and sequential release of the physical associations. PIGE-Ni^{2+} networks with a sufficient ion concentration (i.e., $r > 0.121$) exhibit a terminal relaxation time with a scaling $\tau \sim r^{10.4}$ experimentally obtained from a least-squares regression power-law fit. Attempts to compare this observation with theory are not straightforward due to the unknown number of physical associations in polymers based on metal−ligand coordination. This difficulty arises from the microstructure of materials with both ionic groups that can associate into clusters of various sizes and shapes[122] and metal−ligand complexes that can adopt a range of geometries with distinct lifetimes.[123] From a theoretical standpoint there are also important limitations, such as the inability to account for stress relaxation mechanisms beyond the formation and breakage of physical associations (e.g., solvation, fluctuations in tube length, and constraint release) in the calculation of the linear viscoelastic response.[66] Nonetheless, the reported increase in terminal relaxation time demonstrates control over the mechanical properties of polymer networks via incorporation of a transition metal ion cross-linker.

Overall, the network elasticity and terminal relaxation time are affected by the cross-linker concentration. While the former primarily depends on the instantaneous number density of elastically active strands, the latter results from polymer self-diffusion through a sequence of association and dissociation steps between the ions and the poly-

mer backbone. Polymer self-diffusion is hindered by a combination of solvation and metal−ligand interactions that create a friction force on the polymer chain and increase the terminal relaxation time. Nonetheless, the fast dynamics of solvating interactions prevent the formation of long-term associations capable of contributing to the network elasticity. Thus, polymer stiffness is solely dictated by metal−ligand coordination. This physical picture is qualitatively consistent with sticky-reptation dynamics of associating polymer networks.

2.4.3 Linear Dielectric Response

The incorporation of Ni^{2+} and $TFSI^{-}$ ions in PIGE generates a change in the bulk ion conducting properties. The linear dielectric response of these materials is characteristic of ion conducting polymers with a notable enhancement in the ionic conductivity relative to equivalent polymers without ions (Figure 2.5). The frequency-dependent conductivity exhibits a plateau ionic conductivity at high frequencies (σ_{dc}), a crossover in the real (σ') and imaginary (σ'') conductivity, and terminal relaxation associated with electrode polarization. Note that an important fraction of the electric dipoles are directly associated with the incorporated Ni^{2+} and $TFSI^{-}$ ions, but some result from either impurities or uneven electron density distributions in covalent bonds between carbon and heteroatoms. Thus, the presence of a σ_{dc} in neat PIGE is attributed to ionic impurities residual from the polymer synthesis (e.g., potassium naphthalenide). The effect on (σ_{dc} upon incorporation of $Ni(TFSI)_2$ demonstrates that mechanical reinforcement of polymers via metal−ligand coordination also has important consequences on functional material properties such as the ionic conductivity.

The maximum in ionic conductivity as a function of salt content reveals the trade-off between increasing ion concentration and decreasing ion mobility (Figure 2.6a).

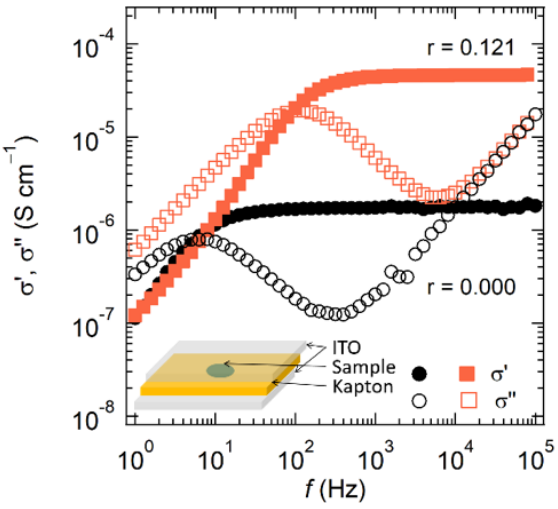

Figure 2.5: Dielectric response of dynamic polymer networks changes upon incorporation of Ni(TFSI)$_2$ due to salt dissociation. Real (σ') and imaginary (σ'') part of the complex conductivity as a function of frequency. The inset shows a schematic of the in situ conductivity measurement cell comprised of the polymer in between two ITO/glass transparent electrodes, separated by a Kapton spacer.

Upon incorporation of Ni(TFSI)$_2$, there is an enhancement in salt dissociation and an increase in the concentration of ions due to Le Chatelier's principle of chemical equilibrium. However, the formation of metal−ligand complexes also imposes restrictions on polymer segmental dynamics as measured by an increase in T_g (Table 2.1) − a change detrimental for the ion mobility because polymers need to accommodate space upon ion motion. Thus, upon normalization by T_g (i.e., evaluating the ionic conductivity at a fixed difference between temperature and the calorimetric T_g) there is a monotonic increase in the ionic conductivity with ion concentration (Figure 2.6b). This observation is consistent with that reported for chemically cross-linked ion-conducting networks generated from copolymerization of ionic liquid monomers with varying contents of multifunctional cross-linkers[124] and polymer electrolytes based on PEO and LiTFSI.[11] Although the complexation of Ni^{2+} by imidazole moieties couples ion transport to the polymer segmental dynamics, this does not translate into a single $TFSI^-$

conductor, such as polymerized ionic liquids based on imidazolium,[103–109] as the kinetically labile nature of metal−ligand coordination bonds allows for bond breakage and formation on time scales that could facilitate long-range Ni^{2+} transport as long as the operating temperature is above T_g. A more quantitative relationship between ion content and mobility is currently under investigation and outside the scope of this work. Nonetheless, the presented results demonstrate a competition between ion concentration and bulk (i.e., continuum) ion mobility.

The change in polymer segmental dynamics due to formation of dynamic cross-links has an influential but not determinant effect on the ionic conductivity. The different temperature dependence of the bulk ionic conductivity and fluidity (i.e., inverse of the zero-shear viscosity) for the series of PIGE+Ni^{2+} indicates a partial disconnect between ion and polymer segmental motion, as completely coupled dynamic properties are governed by the same shift factors and exhibit microscopic relaxation times with identical temperature dependences. Upon Williams-Landel-Ferry normalization ($T_{ref} = 30\,^{\circ}C$), the C_1 parameter is 30%−70% lower for bulk ion conduction than for polymer flow (Figure 2.7), with a statistically significant maximum at a r-concentration of 0.121. Assuming that the primary impediment to molecular motion is entropic in nature (i.e., there is space available to move) rather than energetic (i.e., there is thermal energy to overcome an activation barrier), this observation suggests (i) that the fractional free volume available for motion is 30%−40% larger for ions than for polymers and (ii) the maximum in ionic conductivity corresponds to the salt concentration at which there is a larger difference in fractional free volume for ion conduction and polymer flow. Although there is disagreement as to which of several different data analyses gives the best value for the free volume, the aforementioned observation qualitatively suggests that ion transport and polymer self-diffusion are molecularly governed by processes

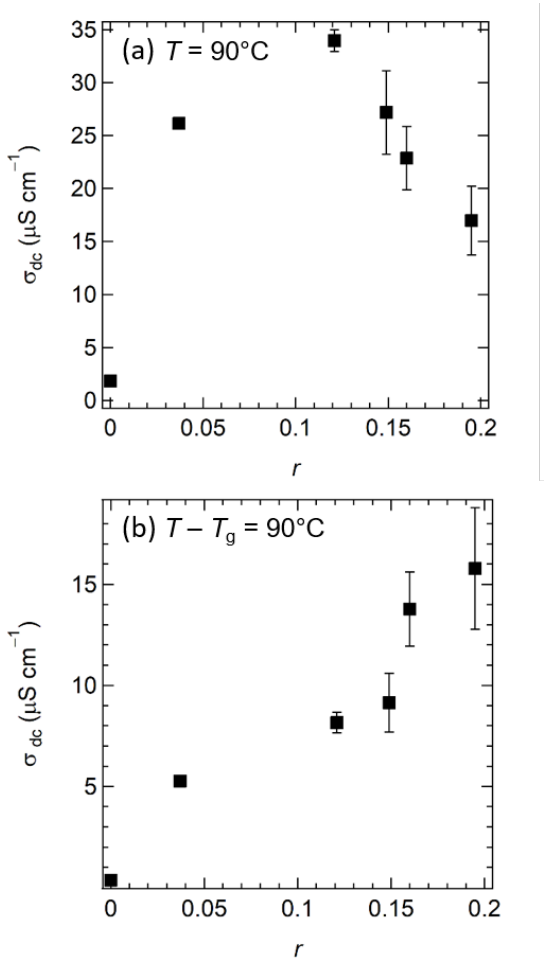

Figure 2.6: (a) Ion conducting dynamic polymer networks based on metal−ligand coordination exhibit a maximum in ionic conductivity due to a competition between ion concentration and ion mobility. The ionic conductivity as a function of Ni^{2+} concentration. Data collected at 90 °C. (b) Monotonic increase in the ionic conductivity due to normalization by the glass transition temperature ($T - T_g = 90°C$). Error bars represent 95% confidence intervals and when not depicted are smaller than the symbol.

with distinct relaxation times. The rigorous assessment of the extent of coupling between ion transport and polymer segmental dynamics requires evaluation of the ratio between the relaxation times,[125] yet the high frequency upturn in the real part of the conductivity is experimentally inaccessible (Figure 2.5). Further work is necessary not only to quantify the extent of coupling between ion and structural dynamics, but also to elucidate the molecular mechanisms of ion transport (i.e., hopping and molecular diffusion) that contribute to the conductivity and account for the observed differences in fractional free volume. Nonetheless, the illustrated discrepancy in the temperature dependence of the shift factors combined with a monotonic increase in the ionic conductivity upon normalization by T_g (Figure 2.6b) reasserts the trade-off between ion concentration and ion mobility which is critical to understand the relationship between metal−ligand coordination and bulk material properties.

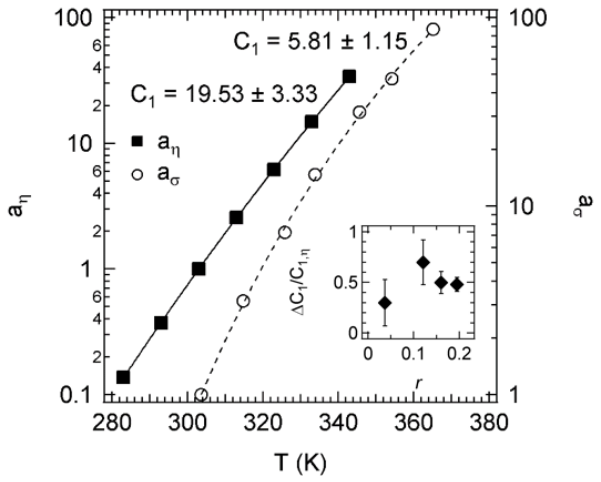

Figure 2.7: The temperature dependence of the shift factors for the ionic conductivity and fluidity of a representative dynamic polymer network based on metal−ligand coordination (r = 0.121) demonstrates incomplete coupling between ion and polymer segmental motion. The C_1 parameters obtained from a least-squares regression Williams-Landel-Ferry fit for the shift factors of the ionic conductivity and fluidity are respectively 5.81 ± 1.15 and 19.53 ± 3.33. The reference temperature was 30 °C. Figure prepared by Gabriel Sanoja.

2.5 Conclusions

The incorporation of transition metal ions into polymers with tethered ligand moieties constitutes a design strategy for mechanically reinforcing polymers with beneficial effects for ion transport, as opposed to the detriments arising from structural but insulating domains intrinsic to polymer nanocomposites[115] or block copolymers.[114] The presented molecular design for ion conducting dynamic polymer networks allows for independent control over the nature and concentration of metal and ligand and thus can be exploited to elucidate the interconnection between metal−ligand coordination, mechanics, and ion conduction. The formation of dynamic cross-links upon incorporation of transition metal ions in polymers with tethered ligand moieties increases the number of elastically active strands and enhances the plateau modulus by an order of magnitude. However, the associated restrictions in polymer segmental dynamics and ion mobility are detrimental for ion transport and yield a maximum in ionic conductivity. The different temperature dependence of the fluidity and ionic conductivity suggests that more fractional free volume is required for ion conduction than for polymer diffusion, yet further work is necessary to unravel the detailed mechanisms of ion and polymer motion that account for this observation. Nonetheless, the demonstrated structure−property relationship illustrates a rational design rule for novel functional polymers with applications ranging from energy storage and conversion to medicine.

2.6 Appendix

Elemental analysis results

Samples were sent out for elemental analysis to confirm nominal $Ni(TFSI)_2$ concen-

Polymer[a]	c_{Ni} (ppm)[b]	m (μg)[c]	n_{Ni} (mmol)[d]	n_{IGE} (mmol)[e]	r^f
PIGE-Ni^{2+} 3.7	3660	17.32	1.08	29.3	0.037
PIGE-Ni^{2+} 12.1	13200	3.96	0.89	5.99	0.149
PIGE-Ni^{2+} 14.9	11000	16.63	3.12	25.8	0.121
PIGE-Ni^{2+} 19.5	16600	20.79	5.88	30.1	0.195

Table 2.2: Elemental analysis of ion conducting dynamic polymer networks based on metal−ligand coordination. [a]Polymers are labeled PIGE-Ni^{2+}X.X, where X.X is the mol% of Ni^{2+} relative to the imidazole ligands. [b]Concentration of Ni^{2+}. [c]Mass of PIGE-Ni^{2+}X.X polymer. [d]Moles of Ni^{2+} contained in PIGE-Ni^{2+}X.X polymer. [e]Moles of IGE ligand in PIGE-Ni^{2+}X.X polymer. [f]Determined from the molar ratio of Ni^{2+} to imidazole ligands. This ion concentration nomenclature is analogous to that previously reported for Li^+ conducting PEO.

trations. The results are given in Table 2.2.

2.6.1 Linear viscoelastic Response

The contributions of entanglements to the linear viscoelastic response are neglected due to the absence of a rubbery plateau in the neat PIGE. This assertion is further supported by Figure 2.8, where the mechanical spectra of the polymer melt and associated polymer network fail to collapse at all frequencies; an observation consistent with differences in topology and relaxation mechanisms governing the mechanical properties of these materials.

2.6.2 Percolation Theory and the Sol-Gel Transition

PIGE-Ni^{2+} is a dynamic polymer network where chains are associated via physical interactions. Under a finite stress, the crosslinks eventually split, and the long-time behavior is always liquid-like. Thus, these materials do not have a strict sol-gel transition.

It is still interesting to consider PIGE-Ni^{2+} as chemical networks and evaluate the

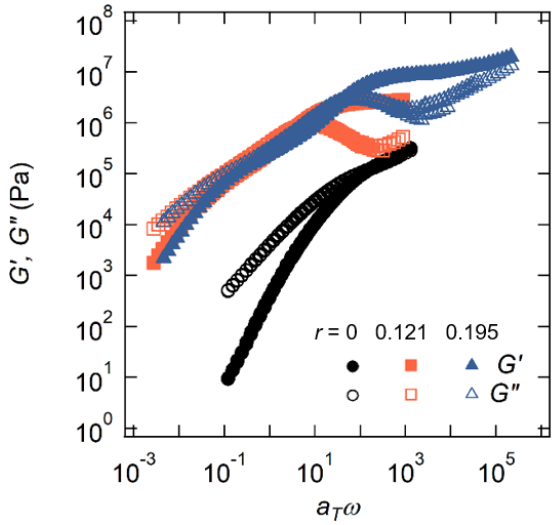

Figure 2.8: Viscoelastic response of PIGE-$^{2+}$ for r-concentrations of 0, 0.121, and 0.195 at $T_{ref} = T_g$ arises due to metal−ligand coordination between imidazole moieties tethered to the polymer backbone and Ni^{2+} cations resulting from salt dissociation.

sol-gel transition using percolation theory. In this case, we start from a dense system of linear chains (degree of polymerization $N = N_{EO} + N_{IGE} >> 1$) and we crosslink them. This is a similar scenario to the vulcanization of rubber.[126] In this situation, the functionality $z = N_{IGE}$ becomes very large because each IGE monomer is capable of participating in a crosslink. The sol-gel transition, corresponding to the concentration at which there is one interstrand crosslinker per polymer chain, is then given by $r_c = \frac{1}{(N_I GE-1)} \approx (N_{IGE})^{-1} \approx 0.013$. This prediction is below the ion concentration at which there is a stepwise increase in the elastic modulus ($r_c \approx 0.121$), an observation consistent with the existence of topological defects in the infinite cluster. The combinations of this prediction with the linear viscoelastic response of associated polymers serves as a criteria for network formation.

Percolation theory is a mean field theory that generally fails to describe the sol-gel transition of chemically crosslinked networks. The physical picture of this critical

phenomenon is based on a “tree approximation”, where topological defects such as loops or dangling chains arising from steric hindrances are neglected. This is evidently a gross oversimplification, as excluded volume interactions in a branched molecule are expected to be even stronger than in linear chains.

To understand why the theoretical prediction of the sol-gel transition of PIGE-Ni^{2+} can be considered accurate, it is convenient to follow the formalism elegantly discussed by de Gennes[127] and estimate the number (P) of chains which presumably crosslink directly with one given chain in the melt. The volume spanned by one particular chain C is of order $R_0^3 = N^{\frac{3}{2}} a^3$, and the number of chains per unit volume is $\frac{1}{Na^3}$. Any chain C’ which has a good overlap with the volume R_0^3 is certainly in direct contact at some points with C, the number of CC’ contacts being of order $\frac{N^2 a^3}{R_0^3} \sim N^{\frac{1}{2}}$. Thus, the total number of chains C’ probably attached to C is of order $P \approx \frac{1}{Na^3} R_0^3 \approx N^{\frac{1}{2}}$. Clearly, $P >> 1$ ensuring that all deviations from a mean field picture are weak and negligible.

Chapter 3

Decoupling Bulk Mechanics and Mono- and Multivalent Ion Transport in Polymers Based on Metal–Ligand Coordination

3.1 Abstract

Decoupling bulk mechanics and ion conduction in conventional ion conducting polymers is challenging due to their mutual dependence on segmental chain dynamics. Polymers based on dynamic metal–ligand coordination are promising materials toward this aim. This work examines the effect of the nature and concentration of

Reproduced with permission from [5]: N. S. Schauser,* G. E. Sanoja,* J. M. Bartels, S. K. Jain, J. G. Hu, S. Han, L. M. Walker, M. E. Helgeson, R. Seshadri, and R. A. Segalman. Decoupling Bulk Mechanics and Mono- and Multivalent Ion Transport in Polymers Based on Metal-Ligand Coordination. *Chem. Mater.*, 30, 5759 (2018). DOI: 10.1021/acs.chemmater.8b02633 (*equal contribution)

metal bis-(trifluoromethylsulfonyl)imide (MTFSI) salts on the mechanical properties and ionic conductivity of poly[(ethylene oxide)-stat-(allyl glycidyl ether)] functionalized with tethered imidazole ligands (PIGE). Varying the cation identity of metal salts mixed in PIGE enables dramatic tunability of the zero-frequency viscosity from 0.3 kPa s to 100 kPa s. The ionic conductivity remains comparable at approximately 16 μS cm^{-1} among mono-, di-, and trivalent salts at constant metal-to-ligand molar ratios due to negligible changes in glass transition temperatures at low ion concentrations. Thus, polymers based on metal−ligand coordination enable decoupling of polymer zero-frequency viscosity from ion conduction. Pulsed-field-gradient NMR on PIGE containing Li^+ or Zn^{2+} salts complement electrochemical impedance spectroscopy to demonstrate that both the anion and cation contribute to ionic conductivity.

3.2 Introduction

The outstanding mechanical properties of associating polymers have enabled novel functional materials for engineering,[78, 128] biomedicine,[129–131] and energy storage.[89, 132] Associating polymers can be formed from a variety of transient interactions including $\pi - \pi$ stacking,[133] Diels−Alder adducts,[134] electrostatic forces,[80] hydrogen bonds,[78, 135, 136] and metal−ligand (M−L) coordination.[75, 82, 83] M−L interactions are particularly interesting since they enable precise control of bulk properties through the nature and concentration of metal−ligand complexes with well-defined coordination geometry and large tunability in interaction time scale.[69, 95] While the effect of M−L interactions on the mechanics of associating polymers has been well-studied,[68, 70–73, 121, 137] the use of such systems as ion conducting polymers remains relatively unexplored. A recent investigation (see Chapter 2) on these materi-

als demonstrates that the zero-frequency viscosity and ionic conductivity are governed by processes with distinct relaxation times, suggesting that the transient nature of the M−L bonds plays a role in ion transport.[4]

The viscoelastic response of associating polymers is governed by the lifetime of the physical cross-links. Above the percolation threshold, these materials behave as elastic rubbers at shorter times and flow as liquids otherwise.[63, 64, 67] The time scale of breakage and re-formation of M−L coordination complexes depends on the nature and concentration of the metal and ligand, parameters that can be readily tuned without significant synthetic efforts[69, 83] This flexibility results from a strategy in which the polymer is first synthesized, postfunctionalized with a variety of ligands, and finally dynamically cross-linked with a transition metal salt. Seminal work on poly(4-vinylpyridine) based on Pd^{2+} or Pt^{2+} coordinated by N,C,N-pincer ligands illustrates that the linear mechanical response of polymers based on M−L interactions is universally described by the dissociation rate of model small-molecule coordination complexes.[83, 95] However, quantitative prediction of M−L polymer dynamic moduli using model small-molecule M−L complexes in solution remains limited, with discrepancies in behavior between the model compounds and their polymeric equivalents presumably arising as a result of chain connectivity, solvent concentration, and cooperativity.[70] Nevertheless, the bulk mechanical properties can be widely controlled based on the identity and concentration of metal and ligand, enabling the rational design of complex engineering materials.[76]

Polymer mechanics also plays an integral role in ion conduction due to the coupling between ion transport and local segmental dynamics.[99] Polymers containing solvating groups, such as ether oxygens in poly(ethylene oxide), facilitate salt dissociation by preferentially interacting with the cation while hindering its motion through the poly-

mer matrix.[3, 37, 138, 139] This issue is exacerbated for multivalent ions because of stronger interactions with solvating moieties that result in lower cation mobilities and ionic conductivities.[140–142] These ion−polymer interactions are at the core of the trade-off between ion concentration and mobility prompting the design of polymer electrolytes with low glass transition temperatures (T_g).[138, 143–145] However, low-T_g polymers are not mechanically robust at the temperatures required to operate many energy conversion and storage devices motivating the development of novel molecular designs for high-performance materials.[16]

Previous work to decouple the bulk mechanical and ion conducting properties has focused on the use of either nanostructured materials (e.g., block copolymers[10, 146] and polymer nanocomposites[147, 148]) or chemically cross-linked polymer networks.[14, 149] Although numerous studies on nanostructured materials have illustrated the role of structure on ionic conductivity, their bulk performance ultimately depends on the long-range ion transport enabled by the percolation of the conducting domains. Chemically cross-linked polymer networks are often tedious to optimize because their properties are extremely sensitive to synthetic conditions. More importantly, these materials exhibit reductions in the ionic conductivity upon cross-linking due to an increase in T_g with concomitant detrimental effects on segmental dynamics and ion mobility.

This study illustrates the connection between the mechanics and ionic conductivity of a series of polymers based on M−L coordination composed of mono-, di-, and trivalent metal bis(trifluoromethylsulfonyl)imide salts (MTFSI) incorporated in a poly(ethylene oxide) with tethered imidazole groups. As expected from previous investigations on analogous materials, the dynamic moduli and terminal relaxation time are dependent on the identity of the metal species.[69, 83, 95] However, in contrast to the dramatic tunability of the linear viscoelastic response, the ionic conductivity is rel-

atively independent of salt identity. The ability to control the terminal relaxation time separately from local segmental motion at low ion concentration potentially enables the decoupling of the bulk mechanical and ion conducting properties within a specific concentration regime. Comparisons between ^{7}Li and ^{19}F pulsed-field-gradient NMR with electrochemical impedance spectroscopy (EIS) in the polymer mixed with LiTFSI and $Zn(TFSI)_2$ reveal that the $TFSI^-$ anion is not the only species contributing to conductivity, suggesting that Li^+ and Zn^{2+} contribute to the ionic conductivity. While the ion-conducting polymers investigated here do not possess conductivities high enough for device application, the ability to decouple the polymer mechanical response from the ionic conductivity represents a promising route for future optimization.

3.3 Experimental Section

Synthesis of Imidazole-Functionalized Copolymer (PIGE). The synthesis of the imidazole-functionalized poly[(ethylene oxide)-*stat*-(allyl glycidyl ether)] (PIGE) polymer used in this study was previously reported by Sanoja et al. (Figure 3.1) and is based on a combination of ionic copolymerization and click chemistry.[4] First, the allyl-functionalized copolymer (PEO-*stat*-PAGE) was synthesized using epoxide ring-opening anionic copolymerization of ethylene oxide (EO) and allyl glycidyl ether (AGE), followed by UV (365 nm) activated thiol-ene click chemistry of N-(2-(1H-imidazol-1-yl)-propyl)-4-mercaptobutanamide (Im-SH). The resulting polymer was dried in vacuo at 55 °C and immediately transferred to a nitrogen glovebox to mitigate moisture uptake.

Synthesis of Polymers PEO-*stat*-PAGE and PIGE Containing Metal Salt. Samples of ion-conducting polymers were prepared in a nitrogen glovebox by mixing stock

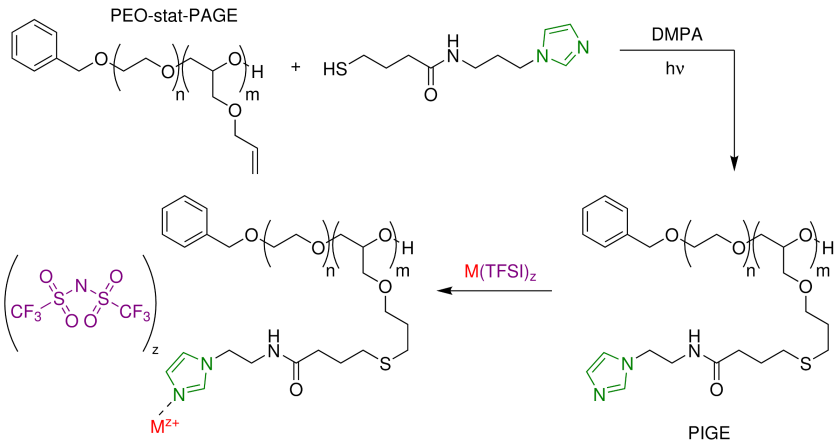

Figure 3.1: Synthesis of imidazole-functionalized PIGE copolymer and subsequent addition of metal salts allows for unique control of bulk properties. Various MTFSI salts (Li^+, Ni^{2+}, Cu^{2+}, Zn^{2+}, and Fe^{3+}) are added in controlled molar ratios of metal to imidazole ligand (r-ratios) to understand the role of M-L interactions and concentration on mechanical properties and ionic conductivity. The cations preferentially coordinate with the imidazole ligand, forming dynamic cross-links between polymer chains.

solutions of polymer and anhydrous metal salts (0.1 M) in anhydrous methanol. The metal salts used for this study were LiTFSI, $Ni(TFSI)_2$, and $Fe(TFSI)_3$ (anhydrous, Alfa Aesar) and $Zn(TFSI)_2$ and $Cu(TFSI)_2$ (anhydrous, Alfa Aesar and Solvionic). Salts from two manufacturers were acquired for Zn^{2+} and Cu^{2+}, with subtle differences detected throughout the measurements. Unless explicitly stated, the measurements reported here are for salts sourced from Alfa Aesar. Controlled ratios of metal cation (M^{z+}) to imidazole (Im) ligand ($r = [M^{z+}]$:[Im]), for PIGE, or equivalently of metal cation to AGE ($r = [M^{z+}]$:[AGE]) for PEO-*stat*-PAGE polymers, of $r = 0.05$, $r = 0.083$, and $r = 0.1$ were prepared by stoichiometrically mixing appropriate amounts of the polymer and salt solutions. The resulting solutions were stirred in the glovebox at 40 °C until they were homogeneously mixed.

Molecular Characterization. Size exclusion chromatography was performed on a Waters instrument using a refractive index detector and Agilent PL gel 5 μm MiniMIX-D

column. THF at 35 °C was used as the mobile phase with a flow rate of 1.0 mL min^{-1}. The polydispersity index (Đ) was determined against PEO narrow standards (Agilent). ^{1}H NMR spectra were collected on a Bruker Avance DMX 500 MHz. The molecular weight of the precursor PEO-*stat*-PAGE copolymer was determined using ^{1}H NMR end-group analysis. This spectrum was collected in $CDCl_3$ at a polymer concentration of 60 mg mL^{-1} with 128 scans and a pulse delay time of 5 s.

General Protocol for Sample Preparation. All polymer samples were handled in a nitrogen glovebox prior to characterization. Samples were drop-cast from solution onto substrates (Teflon, clean ITO-coated glass, or aluminum DSC pans) and dried in vacuo at 55 °C first for 8 h in a vacuum chamber in the glovebox (1×10^{-3} Torr) and then for 1 h in a high-vacuum oven (1×10^{-8} Torr).

Thermal Characterization. Polymer samples were drop-cast from solution into standard aluminum pans and dried as detailed above. The samples were briefly exposed to air between the final vacuum step and the sealing of the DSC pans. The glass transition temperature (T_g) was measured with a PerkinElmer DSC 8000 on second heating at 20 °C min^{-1} using the onset method.

Mechanical Characterization. Samples with a molar ratio $r = 0.1$ were drop-cast onto Teflon sheets, dried as described above, and transferred to a TA Instruments ARG2 rheometer operating under dry nitrogen flow. Samples were loaded onto a temperature-controlled platen and contacted with an 8 mm parallel top plate for measurement. Sample thicknesses were approximately 200 μm. Dynamic frequency sweeps were performed over a range of temperature, frequency, and strain amplitude of 5 °C to 70 °C, 100 rad s^{-1} to 0.1 rad s^{-1}, and 0.1% to 10%, respectively. Strain sweeps at 10 rad s^{-1} confirmed that measurements were performed in the linear viscoelastic regime. Time-temperature superposition (TTS) was performed using horizontal shift

factors with a reference temperature of 20 °C. TTS was not performed for the PEO-*stat*-PAGE samples, except for the $Ni(TFSI)_2$ in PEO-*stat*-PAGE.

^{1}H−^{7}Li 2D Heteronuclear Correlation NMR. A PIGE sample mixed with LiTFSI at a molar ratio $r = 0.083$ was drop-cast onto Teflon, dried as described above, and packed into a solid-state NMR Teflon 4 mm rotor insert. The insert was centrifuged to yield a uniform sample and subsequently sealed into a 4 mm rotor. 1D ^{1}H and 2D ^{1}H−^{7}Li heteronuclear correlation spectra were collected at a spinning frequency of 10 kHz at room temperature in a 11.7 T magnet. For the 2D experiment, 128 increments with 64 number of scans were used with an indirect dimension spectral width of 20 ppm for ^{1}H. A recycle delay of 3 s and cross-polarization (CP) contact time of 1.6 ms were used.

Ionic Conductivity Characterization. Ionic conductivity was measured using EIS on samples sandwiched between parallel ITO blocking electrodes. ITO electrodes on glass substrates were cleaned via subsequent sonications of 5 min with detergent, deionized water, acetone, and isopropyl alcohol followed by a 5 min UV/ozone treatment. A 1/8 or 3/16 in. hole was punched into 150 μm double-sided Kapton tape to define the cell surface area. Samples with a molar ratio $r = 0.05$ and $r = 0.1$ were drop-cast into the Kapton spacer placed on the ITO-coated glass and dried as described above. Samples were sealed with a second ITO electrode under an inert atmosphere, with sample thicknesses ranging from 150 μm to 200 μm. Transparent ITO-coated glass substrates were used to ensure complete contact of the sample to the electrodes. Both the Alfa Aesar and Solvionic Zn^{2+} and Cu^{2+} salts were investigated. The EIS measurements were performed using a Biologic SP-200 potentiostat in a nitrogen glovebox. A sinusoidal 100 mV signal was applied over a frequency range of 1 MHz to 1 Hz at temperatures ranging from 30 °C to 90 °C. The data were converted into dielectric storage and loss, and the ionic conductivities were determined from the real component of

conductivity at the maximum in tan(δ).[118] This method is equivalent to determining the ionic conductivity from the low-frequency intercept of the impedance with the real axis. At least two samples were measured for each composition.

Determination of Lithium Transference Number. The PIGE and PEO-*stat*-PAGE LiTFSI ion-conducting polymers at a molar ratio $r = 0.083$ were further characterized via dc polarization of symmetric lithium foil-polymer-lithium foil coin cells assembled in an argon glovebox. Samples were drop-cast on Teflon, dried as described above, and transferred to a 1/8 in. diameter hole within a 50 μm thick Kapton spacer on top of lithium foil. Coin cells were assembled, transferred to an oven set to 80 °C, and equilibrated for up to 48 h until the interfacial resistance, monitored via EIS, stabilized. This indicated the complete formation of a solid−electrolyte interphase (SEI) layer. Then, a 100 mV potential bias was applied and the resulting current measured as a function of time. EIS measurements were performed periodically to evaluate changes in the interfacial resistance. Lithium transference numbers were calculated following the method of Bruce and Vincent:[50, 52]

$$t_+ = \frac{I_{ss}(\Delta V - I_\Omega R_0)}{I_\Omega(\Delta V - I_{ss}R_{ss})} \tag{3.1}$$

Here, ΔV is the applied potential (100 mV), R_0 and R_{ss} are the initial and steady-state interfacial resistances, respectively, I_{ss} is the steady-state current, and I_Ω is the initial current determined from Ohm's law:

$$I_\Omega = \frac{\Delta V}{R_\Omega} \tag{3.2}$$

where R_Ω is the initial cell resistance (bulk and interfacial) measured by EIS. Using

I_Ω instead of the initial current eliminates measurement errors related to the speed at which the instrument can record the initial current.[150]

Pulsed-Field-Gradient (PFG) NMR. Samples at a molar ratio $r = 0.083$ were drop-cast onto Teflon and dried as described above. In a nitrogen glovebox, the polymers were packed with a spatula into thick-walled glass capillaries and centrifuged to yield uniform 4 cm long samples. The capillaries were centered in medium-walled NMR tubes and sealed with high-pressure caps before measurement. PFG NMR measurements were performed on a Bruker Avance III super-wide-bore spectrometer equipped with a Bruker DIFF50 diffusion probe tuned to ^{7}Li and ^{19}F nuclei with replaceable radio-frequency (RF) inserts. ^{19}F diffusion measurements of the $TFSI^-$ anion were performed on the Li^+ and Zn^{2+} PEO-*stat*-PAGE and PIGE samples at temperatures ranging from 30 °C to 80 °C. Diffusion measurements were not possible for the Ni^{2+}-, Cu^{2+}-, or Fe^{3+}-containing samples due to line broadening by the paramagnetic relaxation effects. ^{7}Li diffusion measurements were performed between 30 °C and 75 °C on the Li^+ PEO-*stat*-PAGE sample and at 80 °C on the Li^+ PIGE sample. Lower temperatures for the Li^+ PIGE could not be explored due to the low cation diffusion coefficient. Samples were equilibrated at each temperature for 15 min before measurement. A pulse sequence of stimulated echoes with bipolar pulses was used to measure diffusion coefficients. The attenuation of the echo (E) was fit to

$$E = exp\left[-\gamma^2 g^2 \delta^2 D\left(\Delta - \frac{\delta}{3}\right)\right] \tag{3.3}$$

where γ is the gyromagnetic ratio, g is the gradient strength, δ is the gradient pulse length, Δ is the interval between gradient pulses (diffusion time), and D is the diffusion coefficient. The intervals between gradient pulses used for the acquisitions ranged

from 20 ms to 40 ms for ^{7}Li and from 15 ms to 20 ms for ^{19}F. The pulse lengths used for acquisitions ranged from 4 ms to 5 ms for ^{7}Li and 1 ms to 4 ms for ^{19}F. For each diffusion measurement, 16 experiments of varying gradient strength up to a maximum of 2300 G cm^{-1} were performed. All measured attenuations were adequately fit with single-exponential decays. Two samples were measured for the PIGE polymers, while only one was measured for the PEO-*stat*-PAGE samples.

The PFG NMR experiments were analyzed in the context of dilute solution theory. Within this framework, an ionic conductivity can be calculated from the measured diffusion coefficients using the Nernst-Einstein equation[33]

$$\sigma = \frac{F^2}{RT}\left(z_+^2 c_+ D_+ + z_-^2 c_- D_-\right) \tag{3.4}$$

where F is Faraday's constant, R is the ideal gas constant, T is the absolute temperature, and $z_\pm$, $c_\pm$, and $D_\pm$ are the valency, concentration, and diffusion coefficient of the cation/anion, respectively. PFG NMR probes ion diffusion on a characteristic length scale $\sqrt{D\Delta}$ on the order of 1 μm to 10 μm. While the characteristic length scale probed by electrochemical impedance spectroscopy depends on more complex factors, it is generally assumed to be roughly equivalent to that of PFG NMR. Thus, a comparison of the conductivity extracted from each technique is reasonable, within the context of dilute solution theory. This theory neglects intermolecular interactions and assumes that the ionic species are completely dissociated.[33] Consequently, there might be discrepancies between the calculated and experimentally determined ionic conductivities, which could be due to either the diffusion coefficients measured via PFG NMR having contributions from a number of associated or aggregated species (inaccurate $D_\pm$ measurements) or incomplete salt dissociation (inaccurate estimation of $c_\pm$).[59, 60, 151]

In the binary electrolytes investigated in this study, the anion $TFSI^-$ concentration will equal z_+c_+ under the assumption of full salt dissociation. Thus, equation 3.4 reduces to

$$\sigma = \frac{F^2 c_+}{RT}\left(z_+^2 D_+ + z_+ D_-\right) \tag{3.5}$$

3.4 Results and Discussion

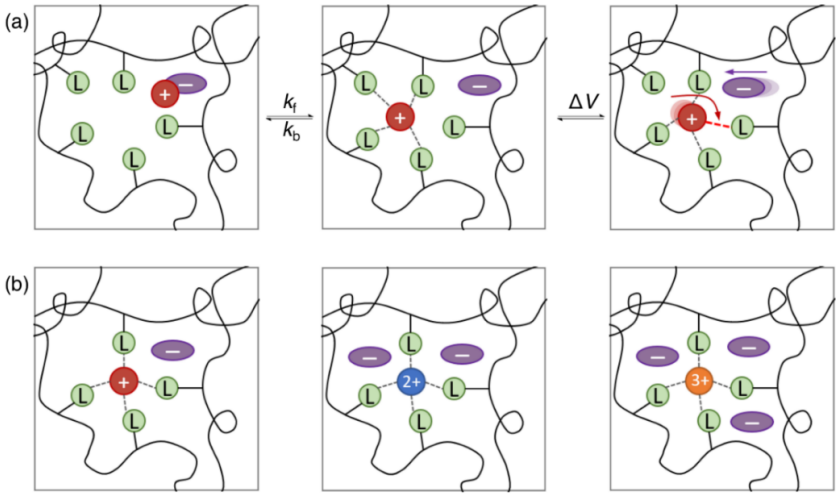

Figure 3.2: (a) Addition of metal salt to a polymer with tethered ligands results in an equilibrium between M−L coordination and salt dissociation. The application of an electric field allows for both ions to move, although the motion of coordinated cations is related to the timescale of metal−ligand coordination. (b) Addition of equal cation:ligand molar ratios (r) results in varying amounts of anions. In all figures, a fourfold coordination geometry is used for illustrative purposes.

To elucidate the effect of the nature and concentration of M−L bonds on the mechanical and ion conducting properties of polymers with tethered ligands, an array of mono- (Li^+), di-(Ni^{2+}, Zn^{2+}, Cu^{2+}), and trivalent (Fe^{3+}) MTFSI salts were incorporated into model PIGE at controlled molar ratios of metal cations to pendant imidazoles (r-

ratios). These neutral, nitrogen-linked, and pendant imidazoles (see Figure 3.1) lack mobile protons that might contribute to the ionic conductivity, while enabling M−L interactions between the metal cations and the non-aromatic lone pair of the nitrogen in the imidazole ring. Note that due to the stoichiometry of salt dissociation, there is an increase in the concentration of anions with metal valency at constant r-ratios (Figure 3.2b). Moreover, the fraction of cations coordinated by imidazole and part of a M−L crosslink will depend on the preferred complex geometry and is expected to range between 4 and 6.[69] The weak electrostatic interactions resulting from large and charge-delocalized $TFSI^-$ anions resemble that of ionic liquids, yielding 'plasticized' and amorphous polymers which even at high ion concentrations exhibit low T_gs. A PEO backbone was investigated because its relatively high dielectric constant potentially enables sufficient salt dissociation and hinders ion aggregation to enhance ionic conductivity. Although the extent of dissociation results from a balance between the salt lattice energy, ion solvation, and M−L coordination (Figure 3.2a), the latter is expected to be the primary interaction dictating the bulk polymer properties as the equilibrium constant for metal cation−imidazole complexation is significantly larger than that of metal cation−crown ether solvation.[102, 119, 137] In the case of LiTFSI salt in PIGE, this is substantiated by ^{1}H−^{7}Li 2D NMR heteronuclear correlation, which reveals the proximity of Li^+ to imidazole ligands (Figure 3.3). The peak intensities of the imidazole protons (6.1 ppm to 8.2 ppm) relative to the aliphatic protons on the PEO backbone (0 ppm to 5.8 ppm) is significantly higher in the heteronuclear correlation (HETCOR) spectrum of ^{1}H coupled to ^{7}Li compared to the direct 1D ^{1}H spectrum, as illustrated in Figure 3.3. In the 1D ^{1}H spectrum the ratio of the peak integrals of 6.1 ppm − 8.2 ppm to 0 ppm − 5.8 ppm peaks is ∼0.13, which increases to ∼1.32 in the HETCOR spectrum. This implies that the aliphatic protons are weakly coupled to the Li^+ whereas the imidazole protons have a relatively strong interaction to the Li^+ due

to spatial proximity. The other cation species are expected to follow similar behavior.

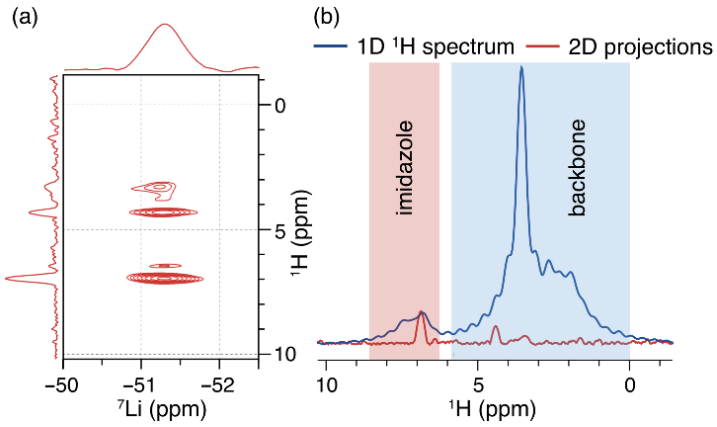

Figure 3.3: Solid-state NMR spectra demonstrate that cations interact preferentially with imidazole ligands. (a) 2D HETCOR ^{1}H−^{7}Li spectrum. (b) Comparison of 1D ^{1}H spectrum (red) with the projections of ^{1}H dimension (blue) from the 2D spectrum. This highlights the relative intensity changes of the ^{1}H peaks.

The dynamic nature of these M−L coordination bonds also allows for bond breakage and re-formation on time scales that facilitate long-range cation transport. This mechanism of ion conduction is fundamentally different from that of anions as these weakly interact with polymers and have motion primarily dependent on the local segmental dynamics. Cation conduction through these systems would be maximum with extremely labile M−L coordination bonds. This physical picture is similar to that of conventional polymer electrolytes (PEO) which are composed of nucleophilic polymer backbones that only solvate cations. The model PIGE is a statistical copolymer PEO_{323}-*stat*-$PIGE_{79}$ ($M_n = 40$ kDa, Đ < 1.2) with a constant mole fraction of imidazole moieties ($x_{IGE} = 0.17$) and was previously synthesized as described in Chapter 2.[4] DSC traces demonstrate its amorphous nature, a result consistent with the suppression of PEO crystallization in an atactic backbone. The molecular properties and thermal transitions of the various polymers are summarized in Table 3.1.

Polymer	r^a	wt% salt	T_g^b (°C)	σ (μS/cm) at 70 °C	σ (μS/cm) at $T - T_g = 90\,°C$
PIGE	0.0	0	−33	1.0 ±0.49	0.47 ±0.21
PIGE Li^+	0.1	4.8	−32	17 ±0.37	8.1 ±0.35
PIGE Ni^{2+}	0.1	9.8	−29	15 ±1.2	9.3 ±0.92
PIGE Cu^{2+} $^{(AA)}$	0.1	9.9	−31	20 ±1.8	10 ±0.73
PIGE Cu^{2+} $^{(S)}$	0.1	9.9	−25	13.6±1.6	10 ±1.1
PIGE Zn^{2+} $^{(AA)}$	0.1	9.9	−28	20 ±0.7	13 ±0.33
PIGE Zn^{2+} $^{(S)}$	0.1	9.9	−25	18 ±1.4	13 ±1.1
PIGE Fe^{3+}	0.1	13.6	−28	12 ±1.1	7.6 ±0.70

Table 3.1: Properties of ion-conducting polymers. All polymers are based on the same PIGE precursor synthesized in Chapter 2,[4] with a degree of polymerization of EO of 323 and of AGE of 79. ^{a} r = [M^{z+}:Imidazole]. ^{b} Determined via differential scanning calorimetry. $^{(AA)}$Salt acquired from Alfa Aesar. $^{(S)}$Salt acquired from Solvionic.

3.4.1 Linear Polymer Mechanics

M−L coordination dramatically changes the bulk mechanical properties, as evidenced by a shift in the linear viscoelastic response to higher modulus and lower frequency upon incorporation of various MTFSI salts into PIGE (Figure 3.4a,b). These materials mechanically respond as dynamic networks with a plateau in the storage modulus at high frequencies, a crossover of the storage (G') and loss modulus (G''), and terminal relaxation similar to that of liquids.[63, 64, 67] The neat PIGE polymer is expected to be weakly entangled based on the molecular weight of the PEO backbone, with small contributions to elasticity relative to M−L cross-linking.[152] At an r-ratio of 0.1, the rheological signature of polymers with Ni^{2+} and Fe^{3+} clearly show a plateau in G' and a peak in G'' while that of polymers with Li^+, Cu^{2+}, and Zn^{2+} only reveals a slight increase in G' and decrease in terminal relaxation time, indicating slower polymer dynamics. Although it is known that both Cu^{2+} and Zn^{2+} interact with imidazole to form dynamic cross-links,[69, 76] there is an almost inconsequential change in the mechanical response that presumably results from either a change in cross-link concen-

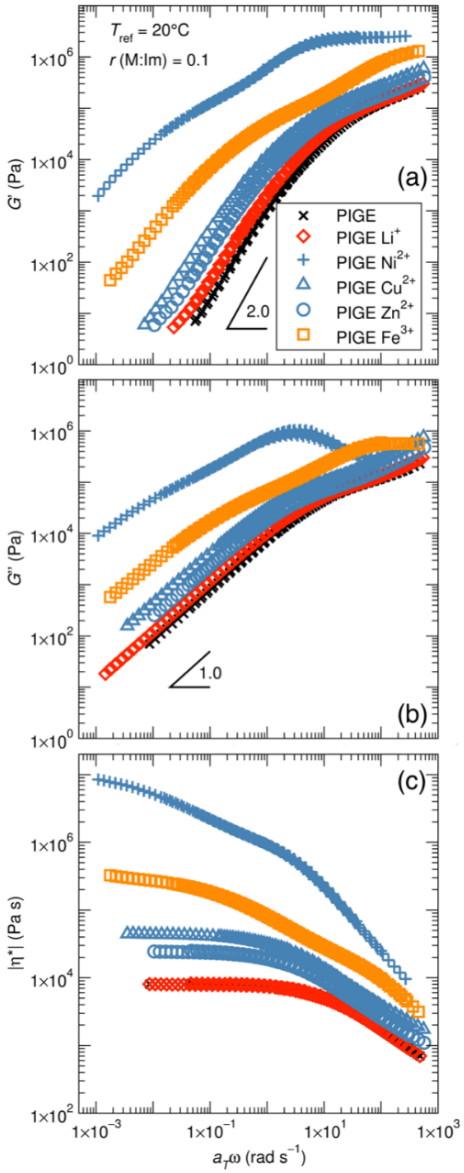

Figure 3.4: Mechanical properties of the polymer change drastically upon the addition of various metal salts. For the PIGE polymer containing covalently tethered ligands, Ni^{2+} and Fe^{3+} cations act as transient cross-linkers resulting in the appearance of a plateau in the storage modulus (a) and peak in the loss modulus (b) within the accessible frequency-temperature range. (c) A clearer effect of metal cross-linking can be seen from the complex viscosity, which increases dramatically with the addition of metal salts except for LiTFSI. Time-temperature superposition was successfully performed on all samples.

tration compared to the Ni^{2+} system or the similarity in time scale of M−L dissociation compared to relaxation of the entangled polymer melt. Additionally, all but the PIGE with Ni^{2+} and Fe^{3+} show liquid-like behavior at low frequency as evidenced by the scaling of $G' \sim \omega^2$ and $G'' \sim \omega$. The system based on Ni^{2+} yields the most dramatic change in the viscoelastic properties. Existing theories relate the modulus and terminal relaxation time scale with M−L ('sticker') binding kinetics.[63, 64] M−L dissociation kinetics trends for the equivalent small-molecule M−L system in aqueous solution do not match the experimental trend of characteristic relaxation time in this study (see the Appendix). As mentioned earlier, such discrepancies are perhaps expected since kinetic trends of M−L dissociation in aqueous solution neglect solvent cooperativity and polymer chain connectivity.[70] Further work is needed to determine the kinetics of M−L dissociation in polymer melts.

The effect of the MTFSI salts on the mechanical properties can be illustrated more clearly by inspecting the complex viscosity $|\eta^*| = \sqrt{(\eta')^2 + (i\eta'')^2}$, a property which describes the resistance of a fluid to undergo shear flow. More specifically, examination of its low-frequency plateau η_0 (zero-frequency complex viscosity) is more convenient as this accounts for changes in cross-link concentration, polymer structure, and relaxation times with dynamic M−L bonds.[67, 121] Figure 3.4c illustrates an increase in η_0 upon addition of MTFSI to PIGE for all metal cations except for Li^+. The rheological similarity between PIGE and PIGE mixed with LiTFSI suggests that either each Li^+ interacts with only one imidazole, thus not forming temporary cross-links, or the time scale for interaction between Li^+ and imidazole is short compared to polymer dynamics. Interestingly, the increase over 3 orders of magnitude in η_0 does not correlate with T_g (Table 3.1), as the polymer with Ni^{2+} is significantly more viscous than that with Cu^{2+} or Zn^{2+} even though they all have $T_g \sim -30°C$. This observation serves to demonstrate that

$T-T_g$	$\frac{1000}{T-T_g}$	$\frac{\sigma_{Ni}}{\sigma_{Li}}$	$\frac{\sigma_{Zn}^{(AA)}}{\sigma_{Li}}$	$\frac{\sigma_{Zn}^{(S)}}{\sigma_{Li}}$	$\frac{\sigma_{Cu}^{(AA)}}{\sigma_{Li}}$	$\frac{\sigma_{Cu}^{(S)}}{\sigma_{Li}}$	$\frac{\sigma_{Fe}}{\sigma_{Li}}$
111.1	9	1.0	1.4	1.6	1.2	1.3	0.8
83.3	12	1.2	1.6	1.8	1.3	1.3	1.0
66.7	15	1.4	1.9	1.9	1.3	1.4	1.2

Table 3.2: Ratios of the ionic conductivity of PIGE with di- and trivalent MTFSI salts to that of the same polymer con-taining monovalent LiTFSI. At three different reduced temperatures $T-T_g$ the ratios are very close to 1 indicating that the ionic conductivity does not scale with ion valency as predicted by dilute solution theory. Divalent salts were acquired from $^{(AA)}$Alfa Aesar and $^{(S)}$Solvionic.

the segmental dynamics, as expressed by T_g, and bulk polymer dynamics, as described by η_0, are decoupled, as the latter depends on the lability of M−L cross-links. As will be discussed shortly, this is the fundamental reason that enables independent control over the mechanical and ion conducting properties through the identity of the metal cation.

3.4.2 Ion Transport

The ionic conductivity of the PIGE-MTFSI is roughly independent of the identity of the metal cation (Figure 3.5, Tables 3.1 and 3.2). Its Vogel-Fulcher-Tamman (VFT) temperature dependence reveals the importance of entropy and free volume on ion motion. As previously noted, there is a minimal shift in T_g across the polymer series that indicates that local segmental dynamics are not greatly affected by cation valency, identity, or anion concentration. This is once again why this material design enables independent tunability over bulk mechanical and ion conducting properties.

The decoupling of the polymer zero-frequency viscosity from ionic conductivity upon the inclusion of metal salts provides a promising route to stiffening polymers without compromising ion transport. From a fundamental standpoint, this is a conse-

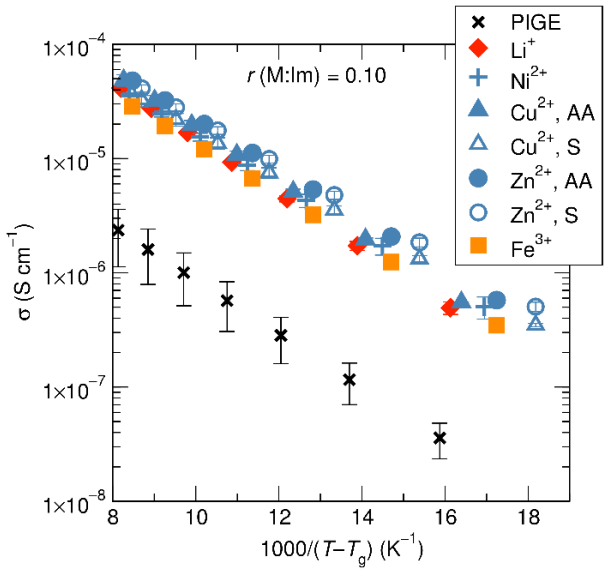

Figure 3.5: The ionic conductivity can be approximately normalized by the ratio of the concentration of metal to imidazole (r), regardless of ion valency or identity. Each data point results from an average of at least two different samples; error bars represent 68% confidence intervals.

quence of the molecular processes governing ion transport and bulk mechanics. While the former primarily depends on the local segmental dynamics as quantified by T_g, the latter results from polymer self-diffusion through a sequence of M−L association and dissociation steps. At $T = 70°C$, the total ionic conductivity of PIGE-MTFSI is approximately 16 μS cm^{-1} with no observable trend with the identity of the metal ion, while η_0 increases from 0.3 kPa s to 100 kPa s between Li^+ and Ni^{2+} (Figure 3.6). Again, the dramatic increase in η_0 is due to physical crosslinking and changes in the lifetime of M−L coordination. These observations complement our previous investigation on the effect of ion concentration on the bulk properties of polymers based on M−L coordination (Chapter 2)[4] and allow us to develop rational design rules for high-performance materials. In particular, there is an optimum ionic conductivity due to the competing effects of increasing ion concentration and decreasing ion mobility,[4] with further stiffening enabled by changing the identity of the metal cation without detrimental

effects to the ionic conductivity.

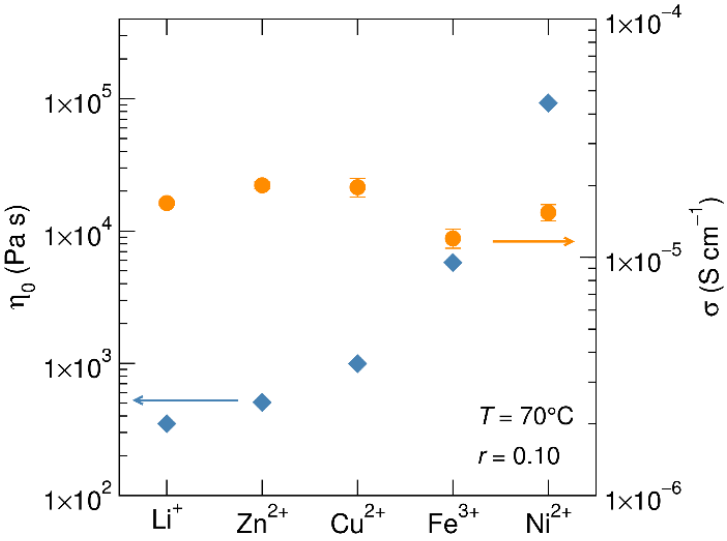

Figure 3.6: Polymers based on M−L coordination enable independent control over the mechanical and ion conducting properties. The zero-frequency viscosity of the material can be tuned over almost three orders of magnitude with minimal changes in the ionic conductivity. Error bars represent 68% confi-dence intervals.

Examination of the ionic conductivity within the framework of dilute solution theory not only demonstrates a complex trade-off between ion mobility, valency, and ion concentration on ion transport but also serves to further investigate the fundamental reason why the ionic conductivity is coupled to segmental dynamics. Normalization of the ionic conductivity by the r-ratio yields a universal curve, a scaling behavior that is inconsistent with equation 3.5, and vexing because the anion and overall ion concentration increase with metal valency. Assuming (1) full salt dissociation (strong electrolyte) and (2) that all metal cations have the same diffusion coefficient, it follows from equation 3.5 that the contributions to the ionic conductivity from the cation and anion should scale with z_+^2 and z_+, respectively.[33] These are presumably invalid assumptions, yet they serve as a starting point to explain ion transport in polymers based on M−L coordination. If the contribution to the ionic current would be predominantly

from the $TFSI^-$, a common feature in polymer electrolytes such as PEO/LiTFSI, the polymers with di- and trivalent salts would have a 2- or 3-fold increase in the ionic conductivity relative to their monovalent counterpart. Table 3.2 summarizes the ratio of the ionic conductivity of PIGE with di- and trivalent MTFSI salts to that of the same polymer containing monovalent LiTFSI. This ratio is evaluated at three different reduced temperatures ($T - T_g$) to account for differences in segmental dynamics among the polymers investigated, though this correction is inconsequential due to the negligible change in T_g with the identity of the MTFSI salts. Only at the lowest reduced temperature ($T - T_g = 66.67$ K), the PIGE based on Zn^{2+} is approximately twice as conductive as that based on Li^+, but for all other temperatures and metal cations the theoretical scaling does not hold. Similar results are observed for an r-ratio of 0.05 (see Appendix, Figure 3.10). This motivates a thorough reassessment of the comparison between measured ionic conductivity and predictions from dilute solution theory and suggests that changes in diffusion coefficient or incomplete salt dissociation likely dominate the behavior of the M−L polymers studied here.

3.4.3 Ion Diffusion Coefficients and Dilute Solution Theory

The deviation from dilute solution theory of the ionic conductivity suggests a change in either the ion mobility or extent of dissociation with metal identity. Pulsed-field-gradient (PFG) NMR provides a powerful tool to investigate the role of ion mobility on conduction by probing the self-diffusion coefficients of NMR-active nuclei on a micrometer length scale.[59, 60, 153] This technique does not distinguish between ions and aggregates composed of an NMR-active species unless their diffusion coefficients or chemical shifts are distinguishable over the experimental time scale (i.e., in the absence of fast exchange between ion and aggregate states). Previous investigations on

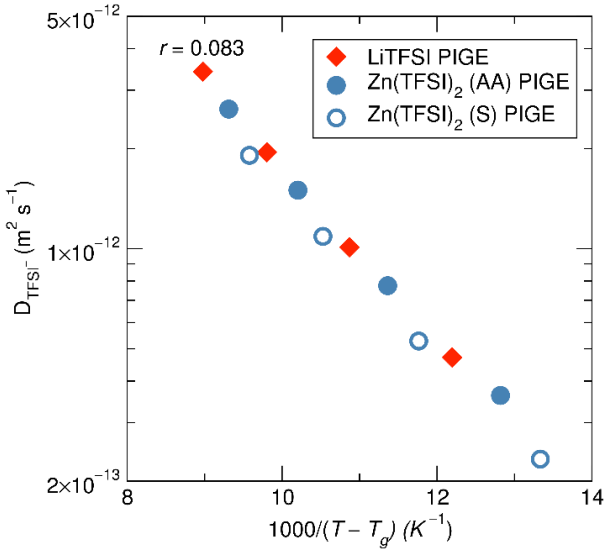

Figure 3.7: ^{19}F diffusion measurements reveal the nature of the cation and concentration of the anion do not play a role in the anion diffusivity in polymers based on M−L coordination. Although PIGE with Zn^{2+} has twice as much $TFSI^-$, the anion is just as mobile as in PIGE with Li^+ after accounting for differences in T_g. (AA) and (S) refer to salt sourced from Alfa Aesar and Solvionic, respectively.

PEO−LiTFSI have demonstrated that the ion diffusion coefficients decrease with ion concentration,[60] an observation attributed to an increase in either polymer viscosity due to solvation or ion drag force from ion−ion interactions. If local chain dynamics are critical in the ion mobility of PIGE−MTFSI, a VFT normalization of the diffusion coefficient by T_g should yield a universal master curve irrespective of metal identity. This is indeed the case when examining the diffusion coefficient of $TFSI^-$ in PIGE with Li^+ and Zn^{2+} (Figure 3.7). The only subtle differences in diffusion coefficient implies not only that the metal identity and the anion concentration are only relevant insofar as they affect the polymer segmental dynamics but also that these salts probably do not form significant aggregation, as changes in polymer viscosity are enough to account for the difference in diffusion coefficient of the salts. A similar comparison between the diffusion coefficient of $TFSI^-$ in PEO-*stat*-PAGE with Li^+ and Zn^{2+} does not yield

the same universal scaling after normalizing for T_g (Appendix, Figure 3.11). As will be discussed later, this is presumably due to incomplete dissociation of the MTFSI salts within the PEO-*stat*-PAGE, causing ion−ion interactions to affect the anion diffusion coefficient. Thus, we hypothesize that metal−imidazole coordination in the Li^+ and Zn^{2+} PIGE effectively screens the electrostatic interactions such that the cation identity and anion concentration do not play a key role on anion mobility.

The anion diffuses faster than the cation in polymers based on M−L coordination, consistent with previous investigations on PEO−LiTFSI and presumably due to interactions of the cation with the polyether backbone or imidazole ligands.[138] ^{7}Li PFG NMR experiments on PIGE (see Appendix, Figure 3.12) enable measurement of the Li^+ diffusion coefficient and further calculation of the transference number within the context of dilute solution theory

$$t_+ = \frac{z_+ D_+}{z_+ D_+ + D_-} \tag{3.6}$$

where z_+ is the valency of the cation, and $D_\pm$ are the diffusion coefficients of the cation and anion. This analysis reveals that the Li^+ transference number in PIGE (0.19, at 80 °C) is slightly higher than that of the corresponding PEO-*stat*-PAGE system (0.15, at 75 °C). While this small difference could be attributed to temperature effects, the higher transference number in PIGE could also result from weaker Li^+-polymer interactions in the presence of imidazole. Whereas the Li^+ ions in the PEO-*stat*-PAGE polymer are solvated by ether oxygens and thus tightly wrapped by the polymer backbone, the Li^+ in the PIGE interact primarily with the imidazole, as demonstrated with ^{1}H−^{7}Li 2D heteronuclear correlation in Figure 3.3. This likely facilitates hopping between adjacent sites in the PIGE. These results are further supported by comparisons

of the transference number with that determined via conventional chronoamperometry (equation 3.1) in symmetric lithium foil−polymer electrolyte−lithium foil coin cells (0.18 at 80 °C).[52] The agreement demonstrates that the diffusion coefficients measured by PFG NMR do not have an important contribution from ion aggregates.

Comparison of the ionic conductivity with predictions from dilute solution theory indicates that the Li^+ and Zn^{2+} are mobile in PIGE (Figure 3.8). In PEO-*stat*-PAGE with Li^+, the ionic conductivity calculated with equation 3.5 overestimates that experimentally determined with EIS, especially when accounting for contributions from both ions. This observation indirectly suggests incomplete dissociation or aggregation of LiTFSI in PEO-*stat*-PAGE. A similar analysis on PIGE with Li^+ reveals that contributions of both the Li^+ and $TFSI^-$ are required to adequately capture the experimentally measured conductivity. The addition of the imidazole ligands presumably enhances salt dissociation such that the Nernst-Einstein relation in equation 3.5 adequately describes the ionic conductivity. This comparison between theory and experiment becomes useful when analyzing the ionic conductivity and diffusivities of polymers based on Zn^{2+}.

In particular, incomplete dissociation is even more apparent in the PEO-*stat*-PAGE for $Zn(TFSI)_2$ than for LiTFSI. Though a Zn^{2+} diffusion coefficient cannot be measured with NMR, the ionic conductivity estimated with equation 3.5 assuming a single-ion $TFSI^-$ conductor ($D_+ = 0$) already overestimates the measured conductivity value. The Zn^{2+} PIGE system, however, underestimates the conductivity when only taking $TFSI^-$ diffusion into account (Figure 3.8). This suggests either the presence of an additional mobile ion or that the $TFSI^-$ diffusion coefficient measured via PFG NMR does not adequately capture the true behavior of the ion. A combination of XRF, ^1H and ^{19}F NMR, and Karl Fischer (KF) titration corroborated the high purity (>99%) of the $Zn(TFSI)_2$ salt, indicating that the residual conductivity is likely due to mobile Zn^{2+} within the

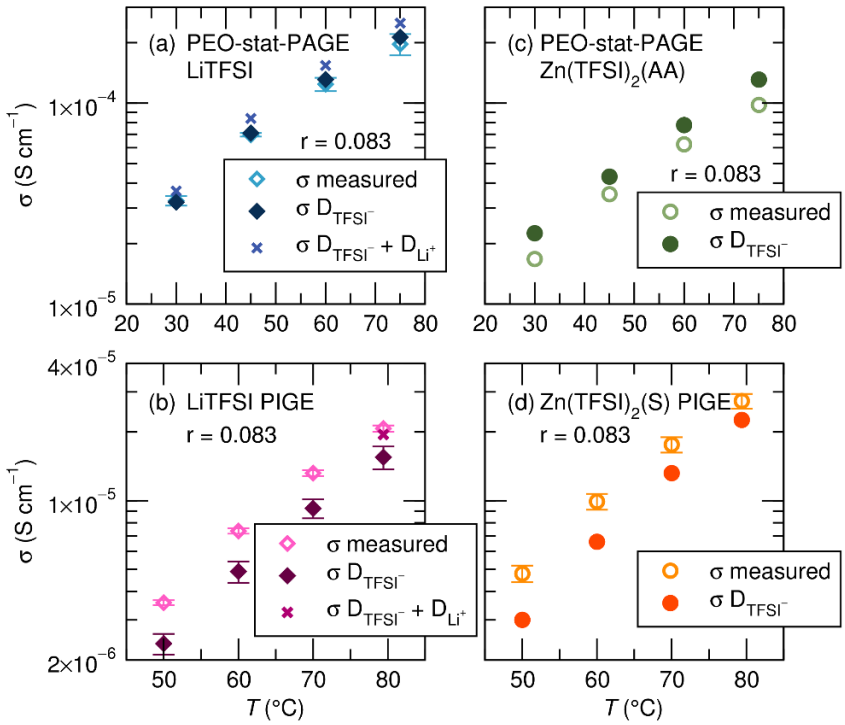

Figure 3.8: The comparison of measured conductivity values with calculated conductivity suggest incomplete salt dissociation for the PEO-*stat*-PAGE, and cation contribution to the conductivity for the PIGE. Conductivity is calculated using diffusion coefficients measured from pulsed-field-gradient NMR using the Nernst-Einstein equation assuming full salt dissociation. First only anion ($TFSI^-$) participation in ion conductivity is accounted for, and then for the lithium-containing polymers full participation from both Li^+ and $TFSI^-$ is assumed. In the PEO-*stat*-PAGE samples (a, c), an overestimation of conductivity compared to the measured conductivity indicates incomplete salt dissociation, while in the PIGE samples (b, d) $TFSI^-$ diffusion underestimates the observed conductivity. Lithium diffusion adequately accounts for the remaining difference in LiTFSI PIGE (b), suggesting the possibility that zinc might account for the remaining difference in the $Zn(TFSI)_2$ PIGE (d). $Zn(TFSI)_2$ from Alfa Aesar was used for the PEO-*stat*-PAGE measurement, while the Solvionic salt was used for the PIGE measurement.

sample. Assuming all Zn^{2+} are dissociated and mobile, one can estimate with equation 3.5 the diffusion coefficient that would be required to obtain the experimentally measured conductivity value. This analysis provides a lower bound of a diffusion coefficient of Zn^{2+} in PIGE of around 3×10^{-9} cm^2 s^{-1} at 80 °C, which would correspond to a transference number of 0.13 (see the Appendix). Although the Zn^{2+} diffusion coefficient is about 35% that of Li^+, its higher valency provides leeway for an equivalent contribution to the ionic conductivity at slower ion motion.

3.5 Conclusion

The introduction of metal salts into a polymer matrix containing covalently tethered imidazole ligands enables the decoupling of mechanical properties from ionic conductivity. Polymers based on M−L coordination exhibit higher zero-frequency viscosities compared to the neat entangled polymer melt, with high sensitivity toward the identity of the metal cation due to the formation of dynamic M−L cross-links. In contrast, the ionic conductivity of these materials is relatively insensitive to the metal cation identity and seems instead to be a function of cation to ligand ratio. Ion mobility in polymers is dictated to a significant extent by the local segmental dynamics, which remain largely unchanged with metal cation identity but depend more strongly on salt concentration. These results enable orders-of-magnitude changes in polymer zero-frequency viscosity with negligible changes in ionic conductivity. PFG NMR diffusion measurements performed on polymers based on Li^+ and Zn^{2+} demonstrate that $TFSI^-$ diffusion is insensitive to cation identity or anion concentration and only depends on polymer T_g. Interestingly this result only holds for the imidazole-containing polymer and not the PEO-*stat*-PAGE precursor. Whether this is a function of the extent of dissociation of

the metal salt or is due to the nature of the M−L interaction with pendant imidazole groups merits further analysis. Lastly, diffusion measurements can be used to estimate an ionic conductivity assuming full salt dissociation. While it is known that impedance spectroscopy and PFG NMR probe different time scales, this analysis for the PIGE with Zn^{2+} suggests that, in addition to the $TFSI^-$, Zn^{2+} ions contribute to the ionic conductivity measured by EIS. While Zn^{2+} ions appear to have lower diffusion coefficients than Li^+, their higher valence ensures that their contribution to the overall conductivity is significant, even comparable to what is seen in the case of Li^+ in PIGE. This work paves the way for future studies on polymers based on M−L coordination, suggesting multivalent systems can be designed with beneficial mechanical properties and no detriment to total ionic conductivity compared with monovalent salt species.

3.6 Appendix

3.6.1 Connection of observed trend in η_0 and M−L dissociation kinetics

The observed trend in zero-frequency viscosity as a function of metal identity should be described by either the "sticky" Rouse or "sticky" reptation models which suggest the terminal relaxation time scale and zero-frequency viscosity increase as the dissociation rate of the M−L coordination decreases. Dissociation kinetics for Li^+, Ni^{2+}, Cu^{2+}, Zn^{2+} and Fe^{3+} with ligand moieties in aqueous solution have been found to be roughly independent of ligand identity, as the rate-determining step is considered to be the interaction of the M−L complex with water (i.e. a solvent-assisted mechanism).[154, 155] It is thus perhaps not surprising that the trend in dissociation kinetics in aqueous solu-

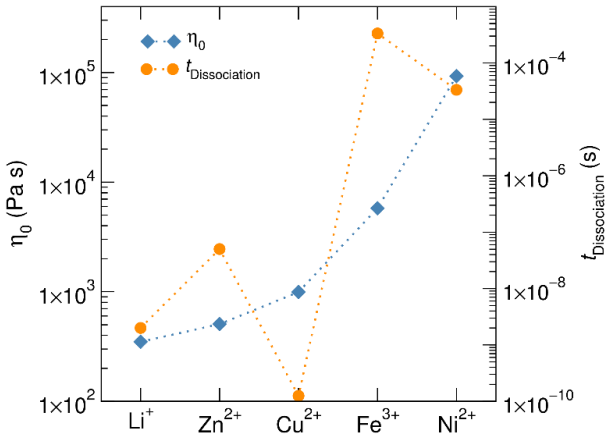

Figure 3.9: Zero-frequency viscosity trends as a function of cation identity do not follow M−L dissociation kinetics trends ($t_{Dissociation} = \frac{1}{(Dissociation\,rate}$) for the given metal ions in aqueous solution.

tion ($Li^+ \sim Cu^{2+} > Zn^{2+} > Ni^{2+} > Fe^{3+}$) does not correspond to that in zero-frequency viscosity ($Li^+ < Zn^{2+} < Cu^{2+} < Fe^{3+} < Ni^{2+}$) as shown in Figure 3.9. Data for dissociation kinetics for M−L exchange in bulk polymer melts or even organic solvents is not available for a majority of metal ions and ligands.

3.6.2 Ionic Conductivity

The impedance data collected was manipulated to calculate the DC ionic conductivity plateau of the data. This was achieved by calculating the real conductivity at the maximum in tan(δ)[118]:

$$C_0 = \frac{\epsilon_0\, Area}{thickness} \tag{3.7}$$

$$\epsilon' = \frac{Z''}{(Z''^2 + Z'^2)\,\omega C_0} \tag{3.8}$$

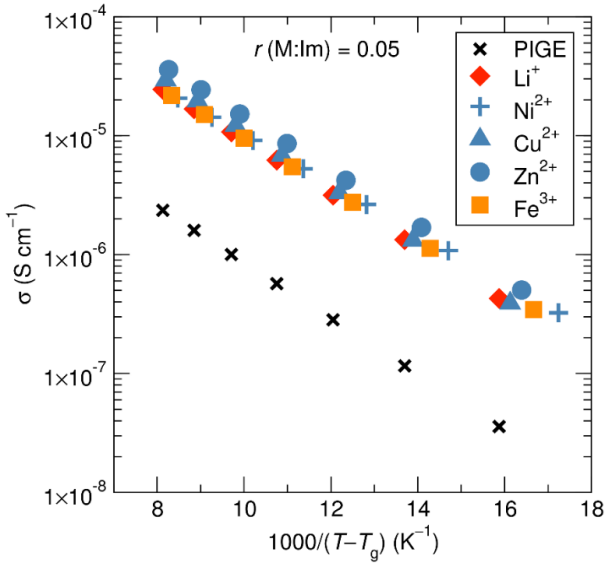

Figure 3.10: Ionic conductivity as a function of reduced temperature at a molar ratio of metal:imidazole of $r = 0.05$. The data can be approximately normalized by r-ratio.

$$\epsilon'' = \frac{Z'}{(Z''^2 + Z'^2)\,\omega C_0} \tag{3.9}$$

$$\sigma' = \omega \epsilon'' \epsilon_0 \tag{3.10}$$

$$tan\,(\delta) = \frac{\epsilon''}{\epsilon'} \tag{3.11}$$

$$\sigma_{DC} = \sigma'\,(max\,(tan\,(\delta))) \tag{3.12}$$

3.6.3 PFG NMR

Calculation of Zn^{2+} diffusion coefficient and transference number

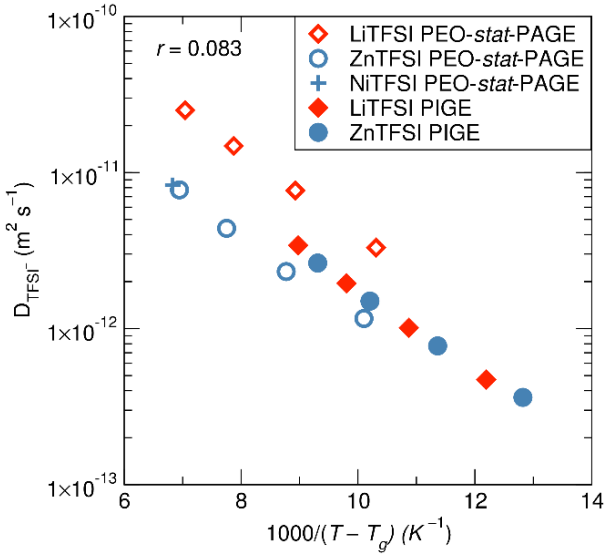

Figure 3.11: ^{19}F PFG NMR diffusion data as a function of temperature in both PIGE and PEO-*stat*-PAGE polymers. When adjusting for T_g, the $TFSI^-$ diffusion aligns for the Li and Zn PIGE samples, as well as for the Zn and Ni PEO-*stat*-PAGE samples.

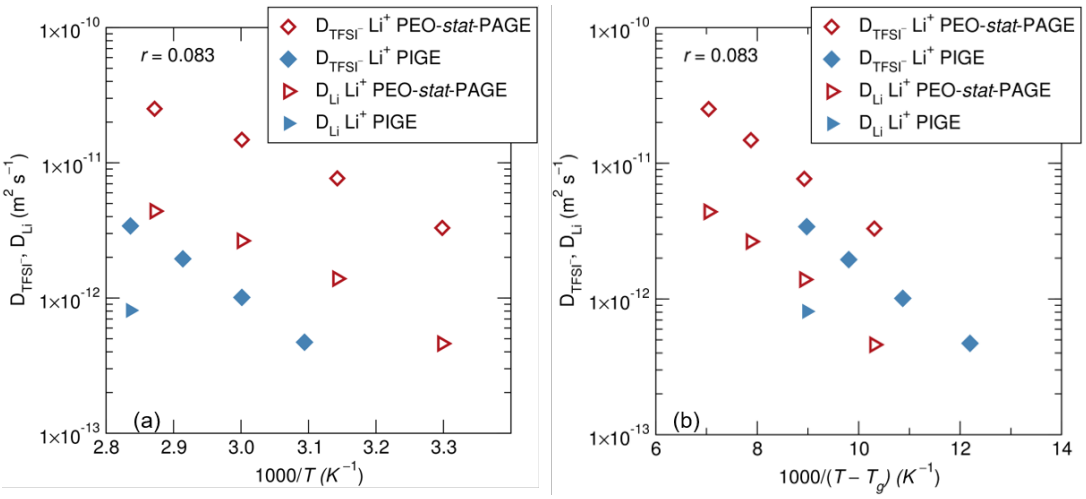

Figure 3.12: ^{7}Li diffusion (triangles) as measured via PFG NMR is slower than TFSI diffusion (diamonds) for both the PEO-*stat*-PAGE (red open symbols) and PIGE (blue filled symbols) polymers.

$T\,(°C)$	σ_{EIS} (S cm^{-1})	D_{TFSI^-} (cm^2 s^{-1})	σ_{TFSI^-} (S cm^{-1})	$\sigma_{Zn^{2+}}$ (S cm^{-1})	$D_{Zn^{2+}}$ (cm^2 s^{-1})	t_+ (Zn^{2+})
50	4.39×10^{-6}	2.33×10^{-9}	3.00×10^{-6}	1.38×10^{-6}	5.36×10^{-10}	0.32
60	9.12×10^{-6}	5.28×10^{-9}	6.60×10^{-6}	2.52×10^{-6}	1.00×10^{-9}	0.28
70	1.62×10^{-5}	1.09×10^{-8}	1.32×10^{-5}	3.01×10^{-6}	1.24×10^{-9}	0.19
80	2.59×10^{-5}	1.91×10^{-8}	2.26×10^{-5}	3.32×10^{-6}	1.40×10^{-9}	0.13

Table 3.3: Measured values of EIS conductivity, $TFSI^-$ diffusion coefficient, calculated $TFSI^-$ conductivity, calculated Zn^{2+} conductivity, and calculated Zn^{2+} diffusion coefficient at temperatures between 50 °C and 80 °C. The cation concentration is estimated as 0.186 mMol cm^{-3} assuming a polymer density of 1.06 g cm^{-3}.

From the difference in conductivity measured via impedance spectroscopy (σ_{EIS}) and that calculated from PFG-NMR assuming only $TFSI^-$ mobility (σ_{TFSI^-}), one can estimate the contribution to the conductivity from the Zn^{2+} ions. The diffusion coefficient of the Zn^{2+} ions can then be calculated as follows (results in Table 3.3):

$$\sigma_{TFSI^-} = \frac{F^2 c_+}{RT}\left(z_+ D_-\right) \tag{3.13}$$

$$\sigma_{Zn^{2+}} = \sigma_{EIS} - \sigma_{TFSI^-} \tag{3.14}$$

$$D_{Zn^{2+}} = \frac{\sigma_{Zn^{2+}} RT}{F^2 c_+ z_+^2} \tag{3.15}$$

$$t_+ = \frac{z_+ D_+}{z_+ D_+ + D_-} \tag{3.16}$$

Chapter 4

The Role of Backbone Polarity on Aggregation and Conduction of Ions in Polymer Electrolytes

4.1 Abstract

The usual understanding in polymer electrolyte design is that increasing the polymer dielectric constant results in reduced ion aggregation and therefore increased ionic conductivity. We demonstrate here that in a class of polymers with extensive metal−ligand coordination and tunable dielectric properties, the extent of ionic aggregation is delinked from the ionic conductivity. The polymer systems considered here comprise ether, butadiene, and siloxane backbones with grafted imidazole side-chains,

Reproduced with permission from [215]: N. S. Schauser, D. J. Grzetic, T. Tabassum, G. A. Kliegle, M. L. Le, E. M. Susca, S. Antoine, T. J. Keller, K. T. Delaney, S. Han, R. Seshadri, G. H. Fredrickson, and R. A. Segalman. The Role of Backbone Polarity on Aggregation and Conduction of Ions in Polymer Electrolytes. *J. Am. Chem. Soc.*, 142, 7055 (2020). DOI: 10.1021/jacs.0c00587

with dissolved Li^+, Cu^{2+}, or Zn^{2+} salts. The nature of ion aggregation is probed using a combination of X-ray scattering, electron paramagnetic resonance (in the case where the metal cation is Cu^{2+}), and polymer field theory-based simulations. Polymers with less polar backbones (butadiene, and siloxane) show stronger ion aggregation in X-ray scattering compared to those with the more polar ether backbone. The T_g-normalized ionic conductivities were however unaffected by extent of aggregation. The results are explained on the basis of simulations which indicate that polymer backbone polarizability does impact the microstructure and the extent of ion aggregation, but does not impact percolation, leading to similar ionic conductivity regardless of the extent of ion aggregation. The results emphasize the ability to design for low polymer T_g through backbone modulation, separately from controlling ion-polymer interaction dynamics through ligand choice.

4.2 Introduction

Ion conducting polymers show great potential as electrolytes in energy storage devices because they promise increased safety, mechanical robustness, and voltage stability.[1, 27] Higher ionic conductivity than is currently obtainable is still a requirement for practical applications.[2] A fundamental understanding of the design principles for high-conductivity solvent-free polymer electrolytes remains elusive, although significant progress has been made both experimentally[14, 138, 156–158] and computationally.[138, 159, 160]

Ionic conductivity in polymer electrolytes is dependent on the concentration and diffusion coefficient of the ionic species present.[33] Many factors influence these quantities, including polymer dielectric constant,[105, 161–163] glass transition tempera-

ture, T_g,[26, 39, 42] solvation chemistry,[32, 164, 165] ion aggregation,[166, 167] and molecular architecture and morphology (Figure 4.1).[8, 9, 168, 169] A current challenge is to design systems that enable these factors to be separated in order to identify their respective impacts. This is difficult as many of these factors are interconnected, an example being polymer polarity and T_g.[170]

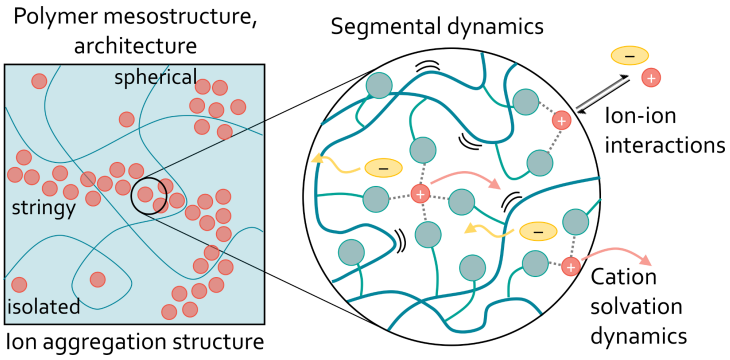

Figure 4.1: Polymer electrolytes often dissolve salt incompletely due to a low dielectric constant, with ion-ion interactions resulting in aggregation. On a molecular level, the solvation site identity, polymer architecture, segmental dynamics, and salt identity affect ion motion.

The extent of ion aggregation or clustering remains relatively unexplored for many reported polymer electrolytes. The lower dielectric constant of polymer electrolytes compared to organic liquid electrolytes results in incomplete salt dissociation and clustering of ionic species added to the polymer. Conflicting literature exists on whether ion clustering and aggregation negatively impact conductivity performance. Some studies have suggested that reducing ion aggregation leads to higher ionic conductivity. For example, for a poly(ethylene oxide) (PEO)-based Li^+ single-ion conductor, a decrease in the polymer dielectric constant with increasing temperature led to increased ion aggregation. This clustering of ions resulted in a low mobile Li^+ content and low conductivity.[171, 172] Ionic conductivity for this PEO-based single-ion conductor was improved upon the addition of a poly(ethylene glycol) plasticizer, due to both a lower

T_g and decreased ion aggregation from charge-shielding.[173] Furthermore, molecular dynamics simulations on polyether electrolytes suggest that increasing their dielectric constant results in decreased ion aggregation and increased ionic conductivity.[37]

There are, however, other studies suggesting that aggregation can enhance ionic conductivity. Sinha and Maranas showed that for single-ion conductors based on Li^+, Cs^+, or Na^+, the aggregation state varied with ion identity but the ionic conductivity did not; they attributed this to an invariance of the local dynamics with ion identity as measured via quasielastic neutron scattering.[174] Separately, molecular dynamics simulations for single-ion anion conductors suggest that percolation of ion aggregate domains may enhance anion motion by decoupling it from polymer segmental dynamics.[175] Additionally, proton conductivity has shown to be dramatically improved in comb polymers that form aggregated nanochannels compared with similar polymers without nanoscale organization.[176] Similar trends are seen in precise ionomers forming nanoscale proton transport layers.[177] Lastly, a recent study probing the effect of linker polarity in polymeric ionic liquid networks suggested that both ion aggregation and ionic conductivity near T_g are promoted with the use of a lower polarity linker.[178]

It is very likely that ion aggregate morphology determines the impact of aggregation on ionic conductivity behavior. Ion aggregates that form into discrete clusters, whether spherical, cylindrical, or ramified, might show poor conductivity performance compared to aggregates that form percolated domains through the bulk of the electrolyte.[167, 179] This was suggested to be the cause of the improved conductivity seen in an imidazolium polymer with ions placed along the backbone rather than pendant to the backbone; changing the placement of ion groups within polymers affects the aggregation morphology, with percolated morphologies leading to improved con-

ductivity behavior.[38, 108, 180] Aggregation morphology is challenging to measure experimentally, however, as X-ray scattering and Raman can indicate the existence but not the morphology of aggregates.[38] Some groups have obtained real-space aggregate images using electron microscopy.[181–183] However, aggregate shape is generally identified from computation rather than experiment.[38, 184]

This work analyzes the impact of aggregation on conductivity for imidazole-containing polymers with a range of polymer backbone chemistries and both mono- and multivalent salts. We have employed a versatile synthetic platform using thiol-ene click chemistry to post-functionalize polymers containing pendant vinyl groups. This enables us to study the effect of segmental dynamics and dielectric constant on ion aggregation and conductivity without changing the solvating species. We find that the backbone identity controls the dielectric constant and thus the extent of ion aggregation as probed via X-ray scattering and field-theoretic simulations.

Importantly, ion aggregation and salt identity do not correlate with ionic conductivity performance, and instead, only the glass transition temperature plays a major role in determining conductivity. This study shows how polymer electrolyte design can be optimized by controlling segmental dynamics of the polymer matrix through polymer backbone choice, separately from the choice of the pendant solvating unit.

4.3 Experimental and Theoretical Methods

Synthesis of Polymer Backbones. Poly(allyl glycidyl ether) (PAGE) was synthesized via anionic ring-opening polymerization of allyl glycidyl ether using benzyl alcohol deprotonated by potassium naphthalenide as an initiator as previously reported in the literature by Lee *et al.*[117] The reaction was performed at 45 °C under argon

atmosphere for 24 h. The resulting PAGE was purified by precipitation in hexane and dried under vacuum at 45 °C for 10 h. Poly(vinyl methyl siloxane) (PVMS) was synthesized by anionic polymerization using standard Schlenk line techniques. A 40 mL portion of uninhibited and dry THF was further purified by distillation over n-butyl lithium and dried by the addition of 200 μL of sec-butyl lithium at 0 °C, after which the solution was allowed to warm to room temperature. The monomer, 1,3,5-trivinyl-1,3,5-trimethyl-cyclotrisiloxane (Gelest), was degassed by three freeze-pump-thaw cycles and used without additional purification. A 200 μL portion of sec-butyl lithium was added to THF at 0 °C as initiator, followed by the addition of 3 mL of degassed monomer. The reaction was allowed to proceed for 3 h at 0 °C before termination with degassed methanol. The solution was concentrated and precipitated in methanol three times. Size exclusion chromatography (SEC) was performed on a Waters Alliance HPLC instrument using a refractive index detector and Agilent PLgel 5 μm MiniMIX-D column at 35 °C with THF as the eluent. Dispersity index (Đ) was determined against polystyrene calibration standards (Agilent Technologies). The PVMS molecular weight was estimated from SEC, while the PAGE molecular weight was determined using ^{1}H NMR end-group analysis. Poly(1,2-butadiene) (PBD) with >95% 1,2 addition, M_n = 9.5 kDa, and Đ= 1.04 was purchased from Polymer Source, Inc. and used without further purification. ^{1}H NMR spectra were collected on a Varian 600 MHz spectrometer in $CDCl_3$ or DMSO-d6.

Synthesis of Imidazole-Functionalized Polymers. N-(2-(1HImidazol-1-yl)propyl)-4-mercaptobutanamide (Im-SH) was synthesized as discussed in Chapter 2.[4] The vinyl-containing polymers were fully functionalized by UV (365 nm) activated thiolene click chemistry in methanol for PAGE or methanol/THF (20/80) for PBD and PVMS. The resulting polymers (PAGE-Im, PBD-Im, and PVMS-Im) were purified either through

dialysis in methanol (SnakeSkin dialysis tubing with a 3.5 kDa MW cutoff, and solvent exchange every 12 h for a total of 5-7 times) or precipitation in acetonitrile, drying in vacuo at 55 °C in the presence of phosphorus pentoxide, and immediate transfer to a nitrogen glovebox to mitigate moisture uptake.

Preparation of Metal Salt-Containing Polymers. Polymers were dissolved in anhydrous methanol and drop-cast onto Teflon boats on a hot plate at 60 °C in a nitrogen atmosphere glovebox. Stock solutions (0.05 M) of Li^+ (Alfa Aesar), Cu^{2+} (Solvionic), and Zn^{2+} (Solvionic) bis(trifluoromethylsulfonyl)imide ($TFSI^-$) salts in anhydrous methanol were added to the Teflon boats in appropriate amounts to reach nominal metal cation-to-imidazole molar ratios, *r*, of 0.03, 0.08, and 0.12. Nominal molar ratios for the PAGE-Im polymer were slightly lower, at 0.028, 0.073, and 0.11. The samples were dried in vacuo at 60 °C overnight in a vacuum chamber in the glovebox (1×10^{-3} Torr) and then at 60 °C for 5 h in a high vacuum oven (4×10^{-8} Torr) to ensure complete removal of solvent. The samples were then transferred into a nitrogen glovebox for storage and measurement. The divalent salts caused uneven gelation and precipitation of polymer, requiring further homogenization after drying by pressing the samples between Teflon sheets in a hand press at 90 °C.

Thermal Characterization. Standard aluminum DSC pans were loaded with polymer samples in a nitrogen glovebox. The samples were briefly exposed to air during the sealing of the pans and then transferred directly into the DSC. The glass transition temperature (T_g) of each sample was measured using a PerkinElmer DSC 8000 on second heating at 20 °C min^{-1} at the midpoint of the step transition. The T_g of the PAGE and PVMS before functionalization were measured on a TA Instruments Q2000 DSC on second heating at 20 °C min^{-1} using the midpoint method. The T_g of PBD before functionalization was taken from literature.[185] T_g values are shown with error bars

of $\pm 2.5\,^{\circ}$C, due to the expected uncertainty of the measurement technique.

Ionic Conductivity Characterization. Total ionic conductivity was measured as a function of temperature on samples sandwiched between parallel ITO blocking electrodes using electrochemical impedance spectroscopy (EIS). The ITO-coated glass electrodes (Thin Film Devices) were cleaned by sonication for 5 min each in detergent, DI water, acetone, and isopropyl alcohol, followed by a 5 min UV/ozone treatment. The electrode thicknesses were measured using a micrometer, after which a double-sided Kapton tape spacer with a 1/8" hole was added to one electrode. Polymer samples were loaded into the hole in the Kapton spacer in a nitrogen glovebox. Samples were heated to about 30 °C above their T_g before being sealed with a second ITO electrode. All samples were then heated to 110 °C and pressed in a hand press. The final stack thickness was measured using a micrometer, and the sample thickness was determined by subtracting the electrode thicknesses. EIS was measured with a Biologic SP-200 potentiostat using a sinusoidal 100 mV signal from 1 MHz to 1 Hz at temperatures ranging from 30 °C to 110 °C. The data was converted into dielectric storage and loss, and the ionic conductivities were determined from the real component of conductivity at the maximum in tan(δ).[118] Three samples were measured for each composition, with errors reported as standard deviations from the mean.

Dielectric Constant Measurement. Dielectric constant measurements were performed using a Biologic VSP-300 and parallel ITO blocking electrodes. ITO electrodes were cleaned as mentioned above. Conductive copper tape was adhered to the back (glass) side of each electrode, and silver paste was used to make contact between the front ITO electrode and the copper tape. Two 1 mm $\times$ 6 mm double-sided Kapton tape spacers were added to the electrode surface. Dielectric spectra were measured inside a temperature-controlled INSTEC stage with a sinusoidal 100 mV voltage sig-

nal from 1 MHz to 100 Hz. For fluid samples (PVMS, PAGE, and PBD), the top ITO electrode was sealed first, and the material was then added into the cell inside a nitrogen glovebox using capillary action. More viscous samples (PAGE-Im, PBD-Im, and PVMS-Im) were spread onto the ITO electrode with Kapton spacers using a spatula, heated on a hot plate inside a nitrogen glovebox to allow the sample to flow, and then sealed with another ITO electrode. The static dielectric constant was extracted from the frequency-dependent spectra at a frequency of 1 MHz and a temperature of $-20\,^{\circ}\mathrm{C}$, where all samples exhibited a phase of around -90° which indicates a purely capacitive response.

X-ray Scattering. Polymer samples were loaded into metal washers in a nitrogen glovebox and covered with Kapton tape to prevent moisture uptake during measurement. X-ray scattering measurements were performed as a function of temperature at the National Synchrotron Light Source II (NSLS-II, beamline 11-BM, Brookhaven National Laboratory), with an X-ray energy of 13.5 keV, and at the Advanced Light Source (ALS, beamline 7.3.3, Lawrence Berkeley National Laboratory), with an X-ray energy of 10 keV. Samples were equilibrated for 15 min at each temperature before collecting exposures. Data processing, including detector distance calibration using a silver behenate standard, reduction of 2D raw SAXS images into 1D intensity versus q curves, and corrections for empty cell scattering were performed using the Nika package for Igor Pro for data taken at the ALS, and using the SciAnalysis software for NSLS-II data.[186, 187]

Electron Paramagnetic Resonance. Pulse EPR experiments at Q-band (34 GHz) were performed on an ELEXYS 580 Bruker spectrometer equipped with a liquid helium cryostat from Oxford Inc. and a 300 W TWT amplifier. Samples were packed into capillaries in a nitrogen glovebox, inserted into 3 mm EPR tubes, and sealed with a

cap and parafilm to prevent moisture uptake. The samples were quenched from room temperature to 20 K for the EPR measurements; thus, the structure surrounding the Cu^{2+} is expected to be representative of the polymers at room temperature.

Electron-Spin-Echo (ESE) Detected EPR. The experiments were carried out with the pulse sequence: $\pi/2 - \tau - \pi - \tau - echo$, mw pulse lengths $t_{\pi/2} = 16$ ns and $t_\pi = 32$ ns, and a τ value of 150 ns were used.

Hyperfine Sublevel Correlation (HYSCORE). The experiments were carried out with the pulse sequence $\pi/2 - \tau - \pi/2 - t_1 - \pi - t_2 - \pi/2 - \tau - echo$. The parameters were: mw pulses of lengths $t_{\pi/2} = t_\pi = 16$ ns, starting times 40 ns for t_1 and t_2 and incremented by 6 ns. Spectra with a τ value of 150 ns were recorded at 20 K. A shot repetition rate of 1.25 kHz was used, and a 16-step phase cycle was used to remove unwanted echoes. The time traces of the HYSCORE spectra were baseline corrected with a third-order polynomial, apodized with a Hamming window, and zero filled. After two dimensional Fourier transformation, the absolute value spectra were calculated. EPR and HYSCORE spectra were simulated using the MATLAB Easyspin package using the "saffron" function, with details provided in the Appendix.[188]

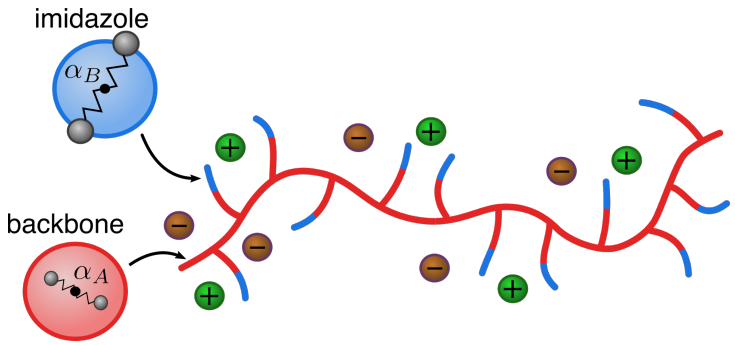

Figure 4.2: Schematic of the molecular model for the metal salt-coordinating polymer. The backbone monomeric species is shown as red, and the imidazole side chain block is shown as blue, with polarizability volumes α_A and α_B, respectively. Figure created by Dr. Douglas Grzetic.

Field-Theoretic Simulations. Our molecular model for the metal salt-coordinating polymer is constructed out of two species of monomeric beads (denoted *A* and *B*) and two small-molecule salt ion species (denoted + and −). The *A*- and *B*-type beads have equal statistical segment lengths *b* and are linked into continuous Gaussian chains with a backbone of species *A* having degree of polymerization N_{bb} = 100, with n_{sc} = 19 equally spaced symmetric diblock side-chains each with lengths N_{sc} = 2, and with the *B* block at the end of the side chain. The charge and bead densities for all species are Gaussian-distributed with a characteristic radius of $a = b/\sqrt{6}$. The short end *B*-block of the side chains models the pendant imidazole, as indicated in the schematic of this molecular model presented in Figure 4.2. The dielectric properties of the polymer are incorporated using embedded Drude oscillators; this polarizable-bead approach is amenable to the transformation to a statistical equilibrium field theory as outlined in previous work by some of us.[189–192] The backbone monomer is granted polarizability volume $\alpha_v^{(A)}$, which is a parameter that we adjust in this study to control the backbone dielectric constant. For monomeric species *B* (the imidazole), we set $\alpha_v^{(B)} = 0.541b^3$; we provide justification for this parameter choice in the Appendix. For simplicity, we restrict ourselves to monovalent, unpolarizable salt ions in this work and fix the background (vacuum) Bjerrum length to $l_b^{(0)} = 32.5b$ and the average density of the system to $\rho_0 = 7.35b^{-3}$, following previous work.[192] We model the metal−ligand interaction phenomenologically using a Flory interaction parameter $\chi_{B+} = -20$ between species B and the cation, a common approach in models of salt-polymer complexation.[42, 193, 194] We also include short-range repulsions for all beads via an excluded volume parameter $\beta_{u0} = \rho_0^{-1} = 0.136b^3$ which sets a weak system compressibility, and Flory parameters $\chi_{AB} = \chi_{+-} = 0.2$ between species *A* and *B*, and between the cations and anions (in addition to full electrostatic interactions). Further details on the model and parameter choices are discussed in the Appendix. Using

standard techniques, the field-theoretic canonical partition function takes the form

$$Z = Z_0 \int D\{\omega\} D\phi e^{-H[\{\omega\},\phi]} \tag{4.1}$$

where the $\{\omega\}$ is a set of fluctuating chemical potential and pressure fields that mediate the contact (nonelectrostatic) interactions, and ϕ is a fluctuating electrostatic potential field, which mediates the ion-ion, ion-dipole, and dipole-dipole interactions in the system.

Traditional simplifying (e.g., mean-field) approximations to polymer field theories are typically not appropriate for charged systems due to the importance of electrostatic field fluctuations and charge correlations. Our interest in ion aggregation in this work makes it particularly critical to capture the effect of charge correlations. The complex Langevin sampling technique allows us to perform field-theoretic simulations (FTS) of the model described above without any approximations. The details of the approach are well described in the literature.[195–198]

4.4 Results and Discussion

The goal of this study is to ascertain the impact of polymer backbone polarity on ionic conductivities of both mono and multivalent metal ions. A modular synthetic strategy was employed based on thiol-ene click chemistry which allows the polymer backbone to be altered while keeping the solvating unit, in this case, imidazole, constant for all polymers (see Figure 4.3). This requires a set of polymer backbones which have pendant vinyl functional handles. Thus, PAGE, 1,2-PBD, and PVMS were chosen, as they all have vinyl pendant groups on every monomer. These backbones have vary-

Polymers	BB[a] M_n (kDa)	BB Đ	BB dielectric constant[e]	Functionalized dielectric constant[e]	BB Tg (°C)[f]	Functionalized Tg (°C)[f]
PAGE-Im	8.1[b]	1.17[d]	6.0	9.4	-73 ± 2.5	-15 ± 2.5
PVMS-Im	29.5[c]	1.23[d]	2.9	4.7	-115 ± 2.5	-8 ± 2.5
PBD-Im	9.5	1.04	2.3	3.7	-20 ± 2.5[185]	9 ± 2.5

Table 4.1: Properties of the polymers in this study. [a] BB denotes 'backbone'. [b] M_n measured using NMR end-group analysis. [c] M_n measured via GPC with PS standard. [d] Đmeasured using GPF with PS standard. [e] Dielectric constants measured at $-20\,^{\circ}C$ at a frequency of 1 MHz. [f] T_g measured using DSC upon second heating.

ing dielectric constants and T_g's (see Table 5.1), both of which are expected to affect salt dissociation and ionic conductivity. The larger molecular weight of the PVMS polymer compared to the PAGE or PBD is not expected to impact the results, since polymer properties such as conductivity and T_g plateau at high molecular weights.[143] PAGE has the highest dielectric constant, at 6.0, while PBD has the lowest dielectric constant at 2.3. Functionalization with the imidazole ligand increases both the dielectric constant and T_g of each polymer, with the largest effect on T_g for the siloxane backbone. We also note that the imidazole-thiol chosen for functionalization incorporates an amide group, which likely plays a role in modifying the dielectric environment and interacting with cations. However, since this functional group combination is present in all polymer samples, its effect is intrinsically included in the experimental measurements.

Salt addition increases T_g for all polymer systems as shown in Figure 4.4. Small amounts of salt result in similar T_g changes for both the monovalent LiTFSI as well as divalent $Zn(TFSI)_2$ and $Cu(TFSI)_2$, while at larger salt concentrations, the T_g for the divalent salts increases more significantly than for the monovalent one. This is likely due to the dynamic cross-linking which results upon metal coordination within these polymers.[4] The similar behavior for all three backbone identities suggests metal$-$ligand interactions between the pendant imidazole and the salt dominate the T_g trend.[5]

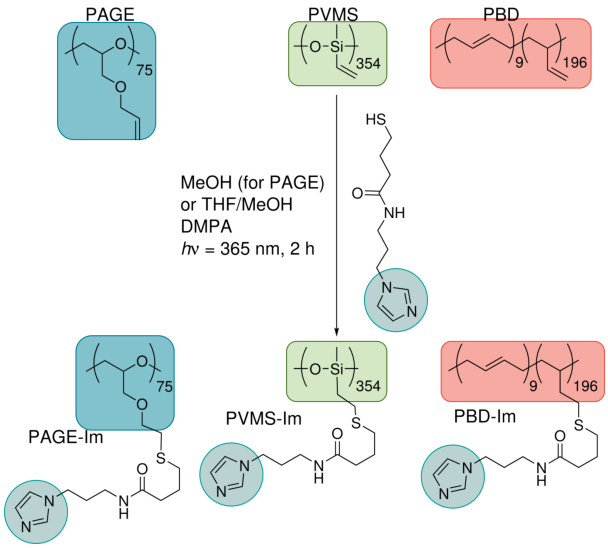

Figure 4.3: Synthesis of Imidazole-Functionalized Polymers Proceeds via UV-Activated Thiol-ene Click Chemistry in Methanol for PAGE or Methanol/THF (20/80) Mixtures for PVMS and PBD

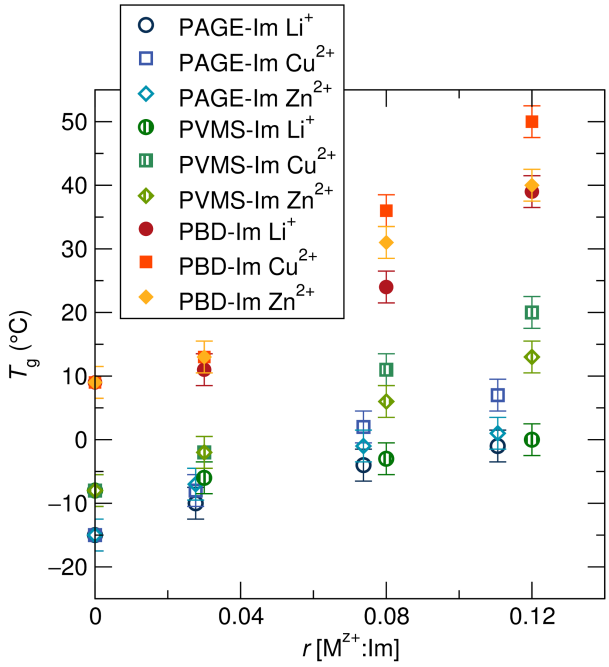

Figure 4.4: Electrolyte glass transition temperature, T_g, (°C) as a function of salt concentration given in molar ratio of metal cation to imidazole ligand (r) for the three polymer systems studied. T_g increases with salt concentration due to dynamic cross-linking interactions between the polymer and the cations. Error bars show uncertainty of ± 2.5 °C.

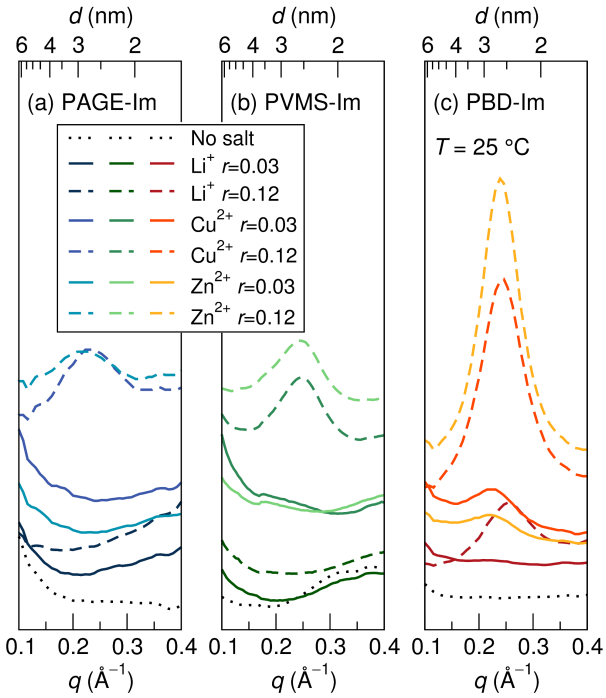

Figure 4.5: X-ray scattering profiles for the (a) PAGE-Im, (b) PVMS-Im, and (c) PBD-Im polymers as a function of salt identity and concentration. Peaks in the scattering profile indicate ion aggregation.

While the T_g behavior is similar for all three polymers, X-ray scattering analysis shows varying amounts of ion clustering or aggregation dependent on the polymer backbone polarity. X-ray scattering profiles taken at 25 °C for a narrow q-range are shown in Figure 4.5. All three polymer precursors show no correlation peak in the q-range of interest; upon addition of varying concentrations of metal salts, a correlation peak appears for some polymers around 0.15 $Å^{-1}$ to 0.3 $Å^{-1}$ (4 nm to 2 nm). These distances are on the same order of magnitude for separation expected for evenly distributed cations/anions at the low salt concentrations probed in this study (see Table 4.3). However, since the peaks do not shift to higher q (smaller distances) with increasing salt concentration, it is likely that the correlation peak corresponds to spacings between domains of high salt density (i.e., ion aggregation), rather than distances between individual ions. Further evidence for this assignment will be provided with the EPR analysis below. For the PAGE-Im and PVMS-Im polymers, this correlation peak is only visible at a higher salt concentration of $r = 0.12$, while the PBD-Im polymer exhibits ion aggregation even at the lowest salt concentration of $r = 0.03$.

The intensity of the peaks changes as a function of both backbone identity and metal salt identity. Samples containing $Zn(TFSI)_2$ have the strongest ion aggregation peaks, followed by $Cu(TFSI)_2$. X-ray scattering shows correlation lengths due to differences in electron contrast but does not provide information as to the identity of the species providing that contrast. Thus, it is unclear whether the weaker scattering seen for polymers containing LiTFSI is due to the monovalent nature of Li^+ or the much weaker scattering power of Li^+ compared to those of Zn^{2+} and Cu^{2+}. Nevertheless, clear signatures of aggregation in the LiTFSI-containing PBD-Im polymer are observed at a Li^+ to imidazole ratio of $r = 0.12$. It is expected that the lower polarity of the PBD backbone in PBD-Im results in the enhanced ion aggregation in this polymer compared with

those of the PVMS or PAGE systems. The effect of temperature on ion aggregation was also probed, showing a slight decrease in peak intensity with increasing temperature. This suggests the aggregates become slightly more diffuse as temperature increases but remain present through the entire temperature range of interest.

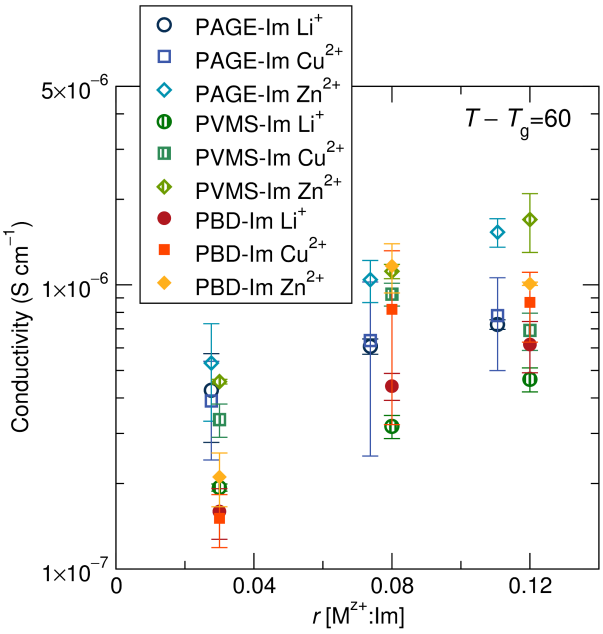

Figure 4.6: Ionic conductivity is relatively invariant with polymer backbone and salt identity when normalized by the T_g of each system, suggesting ion aggregation plays a minimal role in affecting conductivity.

Surprisingly, while the three polymers show dramatic differences in ion aggregation as probed via X-ray scattering, these effects are not manifested in the ionic conductivity behavior. Figure 4.6 shows the ionic conductivity plotted as a function of salt concentration for all the polymers studied, at a temperature 60 °C above the glass transition temperature for each system. This representation removes effects of changes in T_g with polymer identity, salt identity, or salt concentration which were discussed previously (see Figure 4.4). A temperature of 60 °C above T_g was chosen because this temperature ranged from 49 °C to 110 °C for the various samples, which was directly measurable.

Ion aggregation was visible in the X-ray scattering data throughout this temperature range. No clear trend in conductivity exists as a function of polymer backbone or salt identity. Since the PAGE-Im backbone exhibited the least ion aggregation, especially for the LiTFSI salt, one might have expected the highest conductivities for this system. However, the PBD-Im and PVMS-Im polymers show comparable conductivities for all salts at all concentrations. This suggests that ion aggregation, as measured via X-ray scattering, does not significantly affect conductivity behavior. Instead, as Figure 4.7, which plots ionic conductivity at an absolute temperature of 60 °C for each system, shows, the glass transition temperature is the strongest indicator for conductivity performance in these systems.

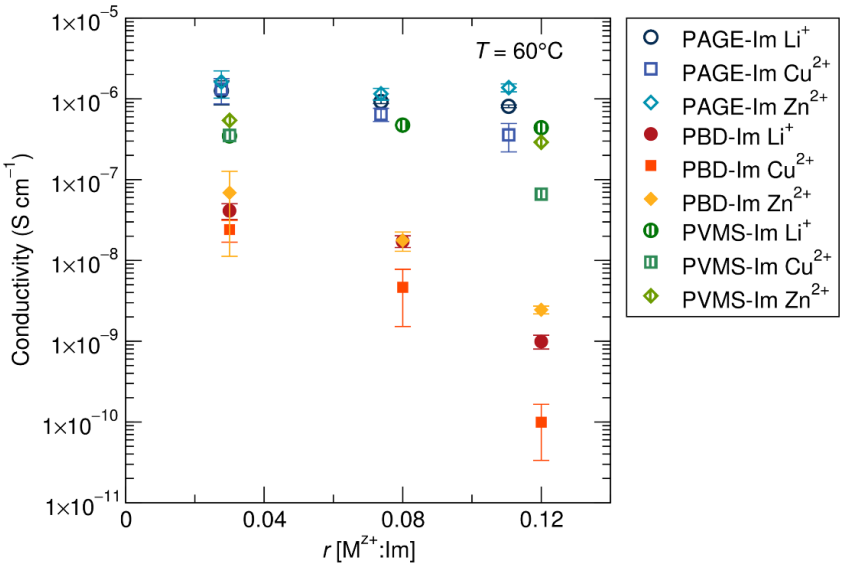

Figure 4.7: Ionic conductivity as a function of salt content at a constant temperature of 60 °C. Conductivity decreases with increasing salt content due to an increase in T_g. This is especially stark for the PBD backbone due to the proximity to T_g, which reaches 50 °C for the PBD-Im Cu^{2+} $r = 0.12$ sample.

Understanding how the backbone identity affects the ion aggregate microstructure and ion-ion correlations without significantly impacting ionic conductivity requires us to investigate the nature of the microstructure and correlations in these systems. To

this end, we turn to electron paramagnetic resonance (EPR) to probe local ion environments and field-theoretic simulations to identify ion aggregation morphology and characteristics.

While X-ray scattering shows bulk changes in ion aggregation as a function of polymer identity, EPR can be used to identify local changes in the environment of paramagnetic metals. Here, we exploited the EPR properties of Cu^{2+} with an electron configuration of d^9, and hence, one unpaired electron in its d-orbital. The copper nucleus itself has two magnetically active isotopes (^{63}Cu 69.13%; ^{65}Cu 30.83%) with nuclear spin $I = 3/2$, thus resulting in hyperfine interactions between the electron and the nuclear spins. The strong spin-orbit coupling and electron-ligand field interactions give rise to significant anisotropy of the g and hyperfine values, both of which are sensitive to the local environment of the Cu^{2+}. Thus, Cu^{2+} was used as a local probe to identify whether the environment around the metal atom is affected by the polymer backbone. Since the largest changes in ion aggregation were observed for the PAGE-Im and PBD-Im polymers, these two systems were chosen for the EPR study. A concentration of $r = 0.03$ was used to probe systems where the ion aggregation as probed via X-ray scattering differed between the two polymers, with the PAGE-Im polymer showing no ion aggregation but the PBD-Im polymer exhibiting signs of ion aggregation.

Field-Swept Echo (FSE) spectra acquired for PAGE-Im Cu^{2+} and PBD-Im Cu^{2+} at 20 K, shown in Figure 4.8a, indicate the presence of local ion-ion interactions in both polymers. While the axial Cu^{2+} lineshapes for each of the backbones show subtle differences, both display significant broadening contributions. The spectra show an envelope of the different orientations of the Cu^{2+} spins. Simulation of the line shape allows us to model the differences in interactions that result from differences in structural nuances between the two backbones (Figure 4.8b). The EPR parameters extracted from the

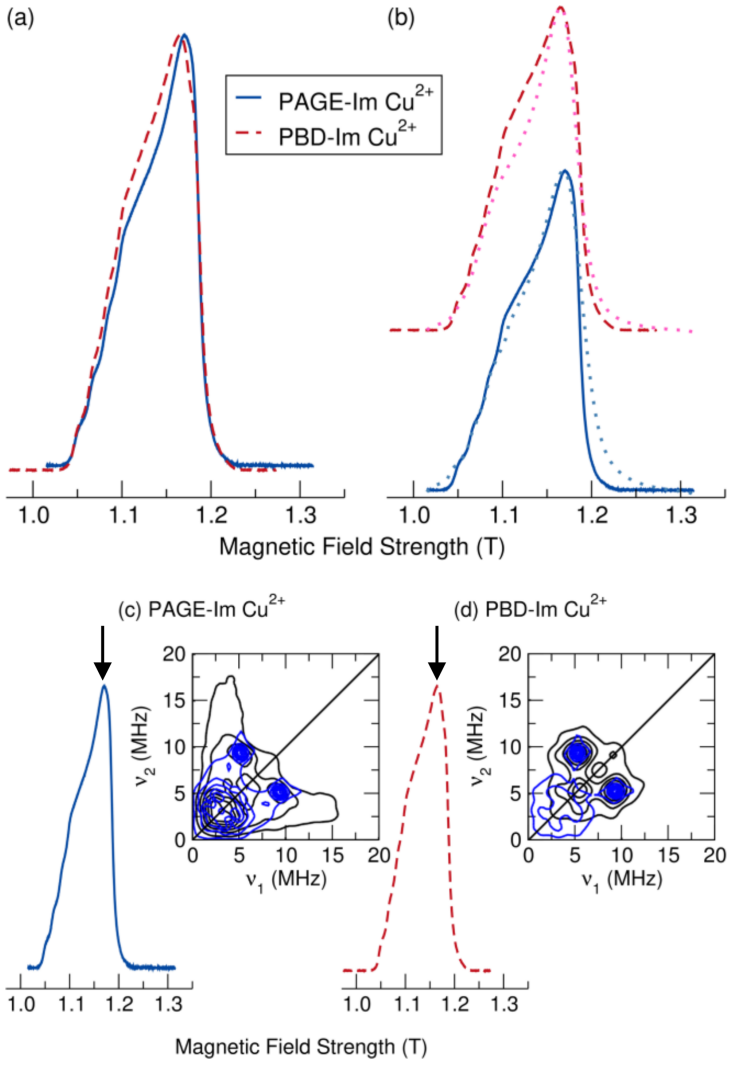

Figure 4.8: (a) FSE of the two polymers with different backbones, recorded at 20 K. (b) Comparison of experimental (solid/dashed lines) and simulated spectra (dotted lines) for each polymer. PBD spectra are shifted vertically for clarity. Experimental (black) and simulated (blue) HYSCORE spectra of (c) Cu-PAGE-Im and (d) Cu-PBD-Im at the maximum observer field position at 20 K. Data collected and analyzed by Tarnuma Tabassum.

simulations are summarized in Table 4.2. The lineshapes for the PBD-Im and PAGE-Im can only be simulated considering a two-component system of (i) resolved, isolated, Cu^{2+} ions with an axially elongated tetragonal ligand field ($g_{||} > g_{\perp}$) and (ii) a broad, unresolved component, corresponding to clusters of ions, hinting toward ion aggregation even at such low concentrations (Appendix, Figure 4.12). The broad component accounts for a significant proportion of EPR active species within the spectrum (∼75%) for both polymers. Dipolar coupling is expected to occur in EPR when the Cu^{2+} are within about 1.5 nm from each other.[199, 200] A minimum Cu^{2+} concentration for dipolar interaction without aggregation can be calculated, assuming dipolar broadening occurs at separation distances below 15 Å and between evenly spaced random close packed Cu^{2+} ions. This corresponds to a Cu^{2+} density of around one Cu^{2+} per 170 $Å^3$ (see Appendix for calculation). Meanwhile, a molar ratio of $r = 0.03$ as probed here corresponds to a Cu^{2+} concentration of around one Cu^{2+} per 2 nm^3 (see Appendix for calculation). The contribution of 75% EPR active species to a broadened signal is significantly higher than would be expected from a random distribution of Cu^{2+} ions within the polymer, suggesting that the broad signal indeed comes from aggregated Cu^{2+}. While we are unable to see ion aggregation peaks for such concentrations of Cu^{2+} on the X-ray scattering profiles for the PAGE backbone, X-ray scattering only detects correlations between aggregate clusters rather than between individual ions within an aggregate. In contrast, EPR provides a more sensitive local probe suggesting that multiple Cu^{2+} ions are in close proximity in both backbones, regardless of whether larger scale clustering of ion aggregates occurs or not. Experimentally derived $g_{||}$ and $g_{\perp}$ values listed in Table 4.2 are typical of Cu^{2+}-imidazole systems, hinting toward binding of the Cu^{2+} and imidazole ligand in both polymers. Strikingly, the hyperfine interactions, both $A_{||}$ and $A_{\perp}$, between the unpaired electron and the copper nuclei are larger than generally observed values for Cu^{2+}-imidazole systems ($A_{||}$ = 426 MHz to 615 MHz and

	$g_{\|\|}$ ($\pm$0.005)	$g_{\perp}$ ($\pm$0.005)	$A_{\|\|}$($\pm$10) (MHz)	$A_{\perp}$($\pm$10) (MHz)	%
PAGE-Im Cu^{2+} (I)	2.245	2.045	616	112	25
PAGE-Im Cu^{2+} (II)	2.245	2.045	-	-	75
PBD-Im Cu^{2+} (I)	2.250	2.050	686	224	25
PBD-Im Cu^{2+} (II)	2.250	2.050	-	-	75

Table 4.2: Experimentally derived g and A parameters and contributions from narrow and broad components for both polymer backbones.

$A_{\perp}$ = 39 MHz to 50 MHz).[201] The stronger hyperfine interactions suggest greater elongation along both the z-axis and the x-y plane, possibly due to increased steric hindrance from the imidazole tethered to a polymer backbone. The PBD backbone in fact shows even greater hyperfine coupling for both hyperfine components, indicating that the identity of the backbone alters the local environment of the Cu^{2+} metal ion itself. This can be correlated with the backbone's lower polarity, consequently resulting in greater distortion of the environment of the Cu^{2+}, leading to the observance of the ion aggregation peak in the X-ray scattering profile.

Lineshape analysis of the Cu^{2+} spectra revealed signatures of the local environment of Cu^{2+}. However, to probe the interactions between the Cu^{2+} center with the polymer sidechains and the effect of the backbone, we can rely on resolving hyperfine interactions to the ^{14}N nuclei. The question is whether there is differential interaction between Cu^{2+} and ^{14}N when the backbone is altered. In the field-swept echo (FSE) spectra for both polymers, the hyperfine coupling between Cu^{2+} and ^{14}N is hidden within the larger hyperfine interactions between the unpaired electron spins of Cu^{2+} and the ^{63}Cu or ^{65}Cu nuclear spins and hence not resolved. To closely inspect differences in interaction between Cu^{2+} and imidazole, we used two-dimensional hyperfine sublevel correlation (HYSCORE) spectroscopy, a well-established technique that provides correlations between nuclear frequencies of different spin manifolds that interact

with the unpaired electron.[202] The representative HYSCORE spectra collected for the two backbone polymers (Figure 4.8c,d) show direct interaction of Cu^{2+} and ^{14}N on the imidazole ligand, as expected. The presence of characteristic *dq* cross-peaks at approximately [5.05, 9.10] MHz and [9.10, 5.05] MHz in the strong coupling regime ($A > \frac{\nu_{^{14}N}}{2}$) shows direct coordination of ^{14}N species to the unpaired electrons in Cu^{2+} in both polymer backbones. In addition, a broad anisotropic peak appears in the lower frequency regime centered around [3.6, 3.6] MHz for PAGE-Im Cu^{2+}, but not for PDB-Im Cu^{2+}.

Simulations of the HYSCORE data and estimation of the ^{14}N parameters suggest slight differences in Cu^{2+}-imidazole environments between the two backbones. While a single component was successfully fit to the PBD-Im spectra, a second ^{14}N component was required to produce a reasonable fit for the PAGE-Im Cu^{2+} system (Table 4.4). This second component still corresponds to an imidazole ligand (see Appendix) but shows slightly less electron delocalization and slightly higher symmetry. Overall, for the PAGE backbone, the EPR analysis suggests that the coordination environment of imidazole bound ligands is more heterogeneous due to the presence of different ^{14}N imidazole species, which coordinate to the Cu^{2+} center differently. We cannot exclude the possibility of an interaction between the Cu^{2+} with the ether oxygens of the backbone in this polymer. ^{16}O has a nuclear spin $I = 0$ and therefore cannot be detected by hyperfine techniques. This would result in a decreased interaction with the imidazole ligand. It should also be noted that cross-suppression of peaks is an effect in HYSCORE, where strongly coupled nuclei can suppress weaker couplings with other nuclei.[203] In other words, interactions with weakly coupled ^{14}N in the amide linkages of the side chains may be suppressed due to stronger interactions between Cu^{2+} and the imidazole.

The EPR results suggest both polymer backbones exhibit local Cu^{2+}-Cu^{2+} interac-

tions, but differ in their Cu^{2+}-imidazole interactions. The general similarity in local ion-ion interactions is perhaps surprising given the difference observed in extent of aggregation according to X-ray scattering and in backbone polarity. However, both polymers have generally low dielectric constants and could be expected to promote ion clustering at a local level, as detected by FSE EPR. The HYSCORE data indicates some inhomogeneity of Cu^{2+}-imidazole interactions in the two backbone systems; changes in solvation behavior, which may impact ion screening, might result in more diffuse ion aggregation which is not detected in X-ray scattering because of the breadth of any resulting peak. Importantly, while EPR confirms the presence of ion aggregates in both polymers, it gives no indication of the morphology or connectivity of the ion aggregates, which likely also plays a large role in ionic conductivity behavior.

Field theoretic simulations examine not only the ion-ion correlations but also visualize the ion densities and thus infer structural information directly. Within our statistical field theory approach, we cannot probe instantaneous density configurations, since instantaneous density field operators are complex-valued. Instead, structures are extracted from time-averages over a finite sampling interval for which the averages of the imaginary parts of the field operators have diminished. The choice of sampling interval is a balance between inaccurate structures at too small averaging windows and total loss of structure for too large windows as the full configuration space for the system (including the ion aggregates) is explored.

An examination of the ion-ion correlations in field-theoretic simulations of the model reveals the presence of a correlation peak, a well-known signature of ion aggregation, consistent with both the X-ray scattering and EPR results above. Figure 4.9 shows the cation-cation structure factor from FTS for a range of salt-loading and for low and high backbone dielectric constants (referred to as PBD-Im-like and PAGE-Im-

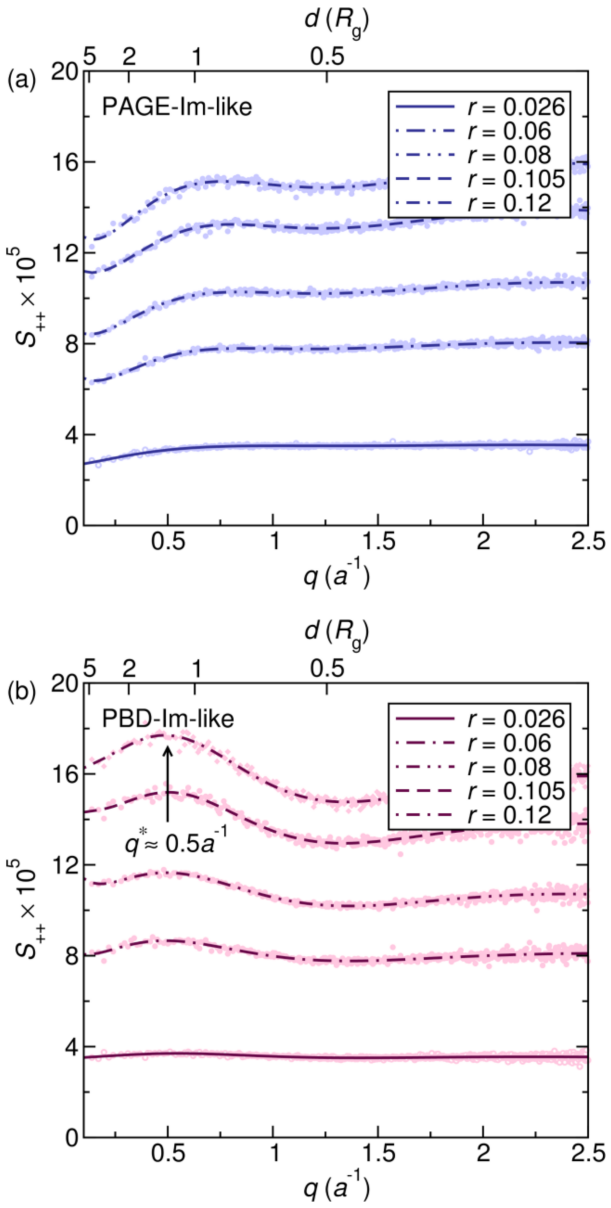

Figure 4.9: Cation-cation structure factor profiles from simulations of the field-theoretic model for (a) PAGE-Im-like and (b) PBD-Im-like polymers for a range of salt concentrations (r = 0.026 to 0.12). The points are raw data from field-theoretic simulations, and the lines are visual guides generated via a nonlinear curve fit of the raw data. Simulations performed by Dr. Douglas Grzetic.

like polymers). A peak in the ion-ion structure factor emerges for high salt-loading ($r > 0.026$), significantly stronger for a low backbone dielectric constant ($\epsilon = 2$) than for a high dielectric constant ($\epsilon = 10$). No peak is observed for the low salt-loading cases, in agreement with the trends seen via X-ray scattering of the lithium salt-doped systems. The peak in FTS occurs at a wavevector $q^* \approx 0.5a^{-1}$, which may be converted to units of Å^{-1} by estimating the statistical segment length $b \approx 0.5\,\text{nm}$ to give $q^* \approx 0.25\,\text{Å}^{-1}$, in good agreement with the positions of the experimentally observed scattering peaks (Figure 4.10). However, the peak is significantly broader than that seen in the X-ray scattering; we attribute this to the coarse-grained nature of our model, which produces weaker ion-ion correlations due to the soft (Gaussian) nature of the ions.

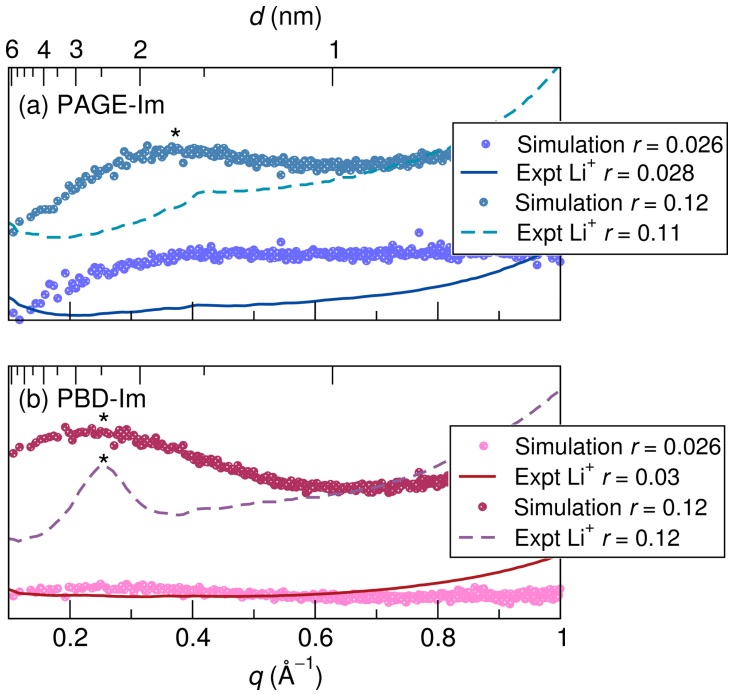

Figure 4.10: Comparison of experimental X-ray scattering data with FTS cation-cation structure factors for (a) the PAGE-Im polymer and (b) the PBD-Im polymer mixed with LiTFSI. Experimental and simulation data have been scaled vertically for comparison. Peak maxima are indicated by a *. Simulations performed by Dr. Douglas Grzetic.

The cation-cation structure factors in Figure 4.9 establish that the field-theoretic model exhibits ion correlations that are consistent with the X-ray scattering results, as shown more clearly in Figure 4.10: the dependence of structure factors on backbone dielectric constant and salt concentration are in qualitative agreement, and the location of the correlation peak is in quantitative agreement for the PBD-Im polymer. The temporally averaged cation densities from field-theoretic simulations are shown in Figure 4.11a for $r = 0.105$, for which the structure factor profiles in Figure 4.9 indicate significant differences in the extent of ion aggregation for the PAGE-Im-like and PBD-Im-like polymers. Visually, the difference between the cation densities for those cases does not appear to be so great, but the histograms of the cation density reveal a measurable difference. Although for strongly segregated ion channels a bimodal ion density distribution is expected, due to high ion concentration in the ion channels and concomitant low ion concentration in the surrounding matrix, in Figure 4.11a, the cation density is distributed *unimodally* for both cases. This indicates that when averaging over the rearranging ion aggregates, the resulting ion structure can be understood as fluctuations about the bulk ion density, with a characteristic length-scale and a magnitude that depends on the length of the averaging window used. There is a dependence of the magnitude of these fluctuations on the polymer identity (i.e., backbone polarity); that is, the magnitude of the fluctuations is stronger for the PBD-Im-like (low polarity) polymer than for the PAGE-Im-like (high polarity) polymer, as can be seen in the width of the cation density distributions of Figure 4.11a. This is a manifestation of the same ion aggregation effects that produce the difference in the structure factors in Figure 4.9.

A rudimentary percolation analysis of the averaged ion morphologies reveals that any differences in the magnitude of the ion density in these channels, due to the differ-

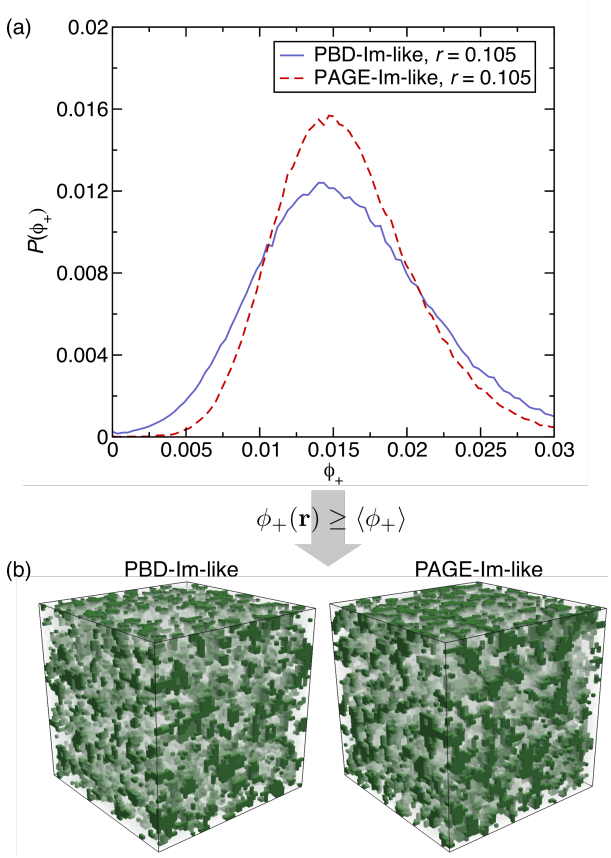

Figure 4.11: (a) Histograms of the thermally averaged cation density from FTS for the $r = 0.105$ cases. (b) Ion channels, identified by the criterion $\phi_+(r) \geq < \phi_+ >$, form a percolating network for both polymers. Simulations performed by Dr. Douglas Grzetic.

ence in polymer backbone polarity, is not sufficient to lead to a substantial difference in their percolation properties. We identify "ion channels" as those for which the cation volume fraction $\phi_+(r)$ is greater than its bulk value (in this case, $r = 0.105$ corresponds to $< \phi_+ > \approx 0.014$). The resulting channels, which are visualized in Figure 4.11b, are analyzed to determine whether or not they percolate through the simulation box. In all directions, the channels, as defined by the threshold value $\phi_+ \approx 0.014$, form a completely percolating network; that is, the ratio of the volume of percolating ion channels to the total volume of ion channels is greater than 0.99. Since the ionic conductivity stems from both cation and anion contributions, it is relevant to confirm that the anion-anion structure factor likewise shows behavior similar to the cation-cation structure factor. Indeed, as can be seen in Figure 4.13 in the Appendix, the anion structure factor and percolation behavior are the same as those for the cation.

These results indicate that it is possible for changes in backbone dielectric properties to affect ion aggregation, in a way that would produce differences in the scattering profiles but would not produce differences in the percolation properties of the ion channels/network, and thus might not correlate with the ionic conductivity, as was seen in Figure 4.6.

4.5 Conclusion

Ionic conductivity in a series of imidazole-tethered graft polymers has been shown to be insensitive to backbone polarity, despite the extent of ion aggregation being greater in the systems with less polar backbones. EPR results reveal that low concentrations of $Cu(TFSI)_2$ in the butadiene and ether-based polymers show similar Cu^{2+}-Cu^{2+} local interactions, indicating that local ion-ion interactions may still be prevalent in all

samples even when not visible in X-ray scattering. Field-theoretic simulations suggest ionic aggregates in both the low and high-dielectric backbone systems are percolated, despite a dependence of the extent of ion aggregation on the backbone dielectric constant, further supporting the similar conductivity performance in these systems when normalized by T_g. These results underscore that ion aggregation is not necessarily detrimental to ionic conductivity, especially in systems where such aggregates form percolating domains with high local mobility. The results emphasize the much larger experimental synthetic space, such as focusing on low T_g and non-interacting backbones, that may be accessible in the search for higher performance ion-conducting polymers, than was previously considered viable.

4.6 Appendix

4.6.1 X-ray Scattering Characterization

Separation distance for evenly dispersed ions.

For a molar ratio of Li^+, Cu^{2+}, or Zn^{2+} to imidazole of $r = 0.03$, and assuming a polymer density of around $1\,g\,cm^{-3}$, and a monomer molar mass of 341.5 g/mol (PAGE-Im), we calculate a concentration of M^{z+} in the polymer as follows ('imid' = imidazole):

$$\frac{1g}{cm^3}\times\frac{cm^3}{10^{21}\,nm^3}\times\frac{1mol\,polym}{341.5g}\times\frac{1mol\,imid}{1mol\,polym}\times\frac{0.03mol\,M^{z+}}{1mol\,imid}\times\frac{6.02\times10^{23}\,ions}{1mol\,M^{z+}}=0.05\frac{M^{z+}}{nm^3} \tag{4.2}$$

This corresponds to one metal ion in $20\,nm^3$, or an average separation distance of $20^{1/3}$ nm or 2.7 nm. A similar calculation can be performed for the other salt concen-

Polymer	$r = 0.03$	$r = 0.08$	$r = 0.12$
PAGE-Im	2.7 nm	1.9 nm	1.7 nm
PVMS-Im	2.6 nm	1.9 nm	1.6 nm
PBD-Im	2.5 nm	1.8 nm	1.6 nm

Table 4.3: Approximate cation separation distances expected for evenly dispersed ions for the three polymers and three concentrations studied.

trations and polymers, with the results listed in Table 4.3 below.

4.6.2 Electron Paramagnetic Resonance

Field-Swept Echo (FSE)

The FSE spectra for PBD-Im and PAGE-Im were simulated with two components: i) resolved, isolated, Cu^{2+} ions with an axially elongated tetragonal ligand field ($g_{||} > g_{\perp}$) and ii) a very broad, unresolved component.

Cu^{2+} calculations for dipolar broadening.

A minimum concentration of Cu^{2+} ions that would cause dipolar broadening even in the absence of aggregation can be calculated assuming random close packing of Cu^{2+} spheres where the diameter of the Cu^{2+} sphere is the maximum separation distance that would cause dipolar broadening. Estimating this distance as $d = 15$ Å provides an easy baseline. Then, the volume of a Cu^{2+} sphere is $V_{Cu} = \frac{4}{3}\pi\left(\frac{3}{2}\right)^2 = 235.6\,\text{Å}^3$

The packing density for a randomly close packed system of spheres is around 62.5%; thus, the total volume associated with a single Cu^{2+} ion (occupied volume and free volume) is $V_{total} = V_{Cu} \times \frac{100}{62.5} = 377\,\text{Å}^3$

Thus, there must be at least one Cu^{2+} in a volume of 377 Å^3 to observe dipolar broadening without ion aggregation. For a molar ratio of Cu^{2+} to imidazole of $r = 0.03$,

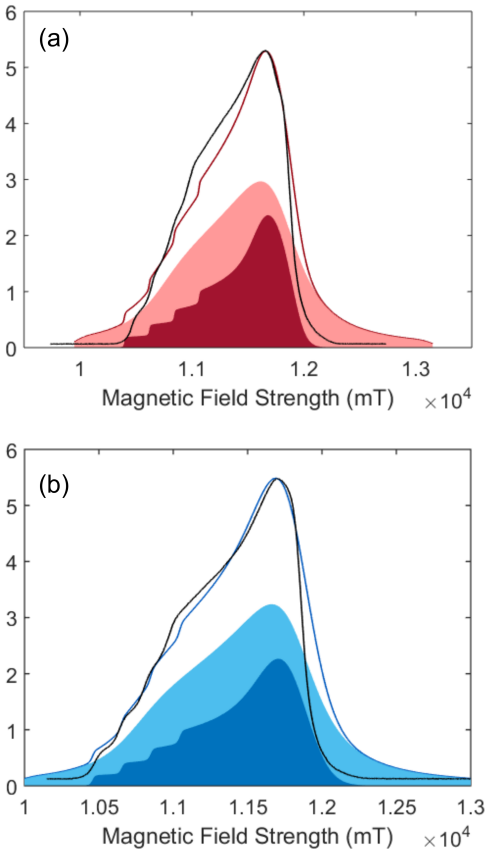

Figure 4.12: FSE spectra of a) PBD-Im Cu^{2+} and b) PAGE-Im Cu^{2+} and the individual spectral contributions from the narrow (isolated) and broad (aggregated) components. Data collected and analyzed by Tarnuma Tabassum.

and assuming a polymer density of around $1\,\mathrm{g\,cm^{-3}}$, and a monomer molar mass of 341.5 g/mol (PAGE-Im), we calculate a concentration of Cu^{2+} in the polymer as follows:

$$\frac{1g}{cm^3} \times \frac{cm^3}{10^{21}\,nm^3} \times \frac{1mol\,polymer}{341.5g} \times \frac{1mol\,imidazole}{1mol\,polymer} \times \frac{0.03mol\,Cu^{z+}}{1mol\,imidazole} \times \frac{6.02\times10^{23}\,ions}{1mol\,M^{z+}} = 0.05\frac{Cu^{z+}}{nm^3} = 0.02\frac{Cu^{z+}}{0.377nm^3}$$

Thus, there is a much lower Cu^{2+} concentration in the polymer than what would be required to reach dipolar broadening without ion aggregation.

Hyperfine Sublevel Correlation Spectroscopy (HYSCORE)

Two-dimensional hyperfine sublevel correlation (HYSCORE) spectroscopy is a well-established technique that provides correlations between nuclear frequencies of different spin manifolds that interact with the unpaired electron.[202] In other words, it shows the NMR transitions of magnetically active nuclei interacting with the electron spin. The ^{14}N nucleus is magnetically active, having a nuclear spin $I = 1$, in principle should result in six nuclear transitions if it interacts with an unpaired electron, three from each electron spin manifold, $m_s = \pm\frac{1}{2}$. For a disordered system such as PAGE-Im and PBD-Im, we expect complicated spectra, with large anisotropy leading to broadened peaks on the HYSCORE spectrum. These peaks contain information about the strength and nature of the hyperfine interaction between the unpaired spin in the Cu^{2+} nucleus and ^{14}N. The hyperfine interaction consists of two components, a_{iso} and T. a_{iso}, the isotropic hyperfine coupling, is the Fermi contact term, which measures the spin density on the nucleus; while T, the dipolar coupling term, is inversely proportional to the distance between the electron and the nuclear spins ($T \propto \frac{1}{r^3}$). In addition, since ^{14}N is a spin $> \frac{1}{2}$ (I=1) nucleus, it has a quadrupole moment that interacts with the electric field gradient (EFG) around the nucleus. The EFG tensor consists of 3 components.

Polymer	a_{iso} (MHz)	T (MHz)	K	η	$B(^\circ)$
PBD-Im Cu^{2+}	2	0.15	1.8	0.8	80
PAGE-Im $Cu^{2+}(I)$	1.5	0.2	1.5	0.8	0
PAGE-Im Cu^{2+} (II)	2	0.15	1.8	0.8	80

Table 4.4: Estimated ^{14}N HYSCORE parameters from simulations of experimental data

This EFG tensor can be fully described using two parameters, the nuclear quadrupole coupling constant, $K = e^2 q_{zz} Q/h$, where e is the charge of the electron and Q is the nuclear electric quadrupole moment of the ^{14}N nucleus, and the asymmetry parameter, η. K measures the strength of interaction between the nuclear quadrupole moment and the EFG at the nucleus due to anisotropic distribution of charges. On the other hand, η measures the deviation of the distribution of charges from axial symmetry. K and η, along with a_{iso}, are used as signatures to identify the chemical environment around the ^{14}N nucleus, allowing its characterization. Extensive studies on Cu^{2+} and its interactions with the remote ^{14}N of the imidazole have allowed the elucidation of characteristic parameters for these systems.[204–208] Q-Band frequencies (35 GHz) were chosen in these experiments because the HYSCORE spectra are greatly simplified and only exhibit a single pair of cross-peaks of the v_{dq} transitions.[209]

The experimental parameters, such as magnetic field, excitation frequency, number of points, dwell time, pulse width, and pulse delay, were taken directly from the HYSCORE experiments. Simulations of the spectra were iteratively done until a set of parameters was obtained that could reproduce the general features of the experimental spectra. The fit was performed using one type of ^{14}N species, where each of the five parameters (a_{iso}, T, K, η and β) were varied until a reasonable fit was observed for PBD-Im Cu^{2+} and fell within expected values for imidazole ligands (Table 4.4). The estimated a_{iso} value of 2 MHz corresponds to an unpaired spin density in the ^{14}N 2s orbital of $\sim 1 \times 10^{-3}$ arising from the coordination of the imidazole ligand. The dipolar

coupling term is not dominant for imidazole ^{14}N (0.15 MHz), while the K and η terms equal 1.8 MHz and 0.8 respectively. On the other hand, spectra for PAGE-Im Cu^{2+} could not be reproduced with the same parameters, especially at the low frequency region. Another ^{14}N component was therefore introduced to obtain a reasonable fit between the experimental and simulated spectra. The estimated parameters for this ^{14}N component also fall within the range of values that correspond to imidazole ligands, albeit with smaller a_{iso} (1.5 MHz) and K (1.5 MHz) values. The a_{iso} value describes the delocalization of electrons in the imidazole ring, therefore hinting towards slightly less delocalization for one of the imidazole environments. In addition, the K value is also smaller, suggesting a more symmetric environment. Finally, the orientation of this second imidazole, obtained from the Euler angle of the nuclear quadrupole tensor is almost perpendicular to that of the first. The principal axes system (PAS) specific to a molecule is used as the molecular frame reference. The PAS for Cu-imidazole complexes is typically the g parallel axis/symmetry axis. An estimation of the orientation of the hyperfine and the quadrupole coupling tensor (from the ^{14}N of the imidazole) can be found from the Euler angle (α, β, γ) because that angle can be thought of as a rotation angle to the molecular frame reference. In these simulations, the hyperfine angles did not significantly change the spectrum. However, varying the β angle of the quadrupole tensor played a role in the appearance of the peaks.

4.6.3 Field-theoretic (complex Langevin) simulations

Species polarizabilities in field-theoretic simulations

In our field-theoretic model, bead species A is either PBD-like or PAGE-like and species B is imidazole-like (Im-like). The PBD and PAGE backbones in the experimental section of this work have measured dielectric constants of $\epsilon_{PBD} = 2.3$ and $\epsilon_{PAGE} = 6.0$,

as reported in Table 5.1. The dielectric constant of liquid 1-methylimidazole (MeIm) has been reported to be as large as $\epsilon_{MeIm} \approx 40$.[210] We note that fluid dielectric constants are typically sensitive to temperature, pressure, and other variables such as chain connectivity and addition of salt, so we do not attempt to achieve quantitative agreement with literature or reported values. Rather, we grant these beads molecular polarizabilities such that they have qualitatively correct emergent dielectric properties: most importantly, that $\epsilon_{PBD-like} < \epsilon_{PAGE-like} < \epsilon_{Im-like}$ for pure fluid phases of the respective bead types, and that the dielectric constants have a reasonable magnitude when compared to the above reported and measured values. To estimate the emergent dielectric properties of the beads in our model, we can use the mean-field expression for the dielectric constant in the polarizable field theory

$$\epsilon_{MF} = 1 + 4\pi\rho_0\alpha_\nu \tag{4.3}$$

where α_ν is the polarizability volume. We note that the true dielectric constant in field-theoretic simulations (FTS) will differ somewhat from the above mean-field expression, due to correlation effects that mean-field theory does not capture. In this work we use $\alpha_\nu^{PBD-like} = 0.011b^3$, $\alpha_\nu^{PAGE-like} = 0.108b^3$, and $\alpha_\nu^{Im-like} = 0.541b^3$. The pure-fluid dielectric constants, which correspond to the dielectric function at k=0, are roughly $\epsilon_{PBD-like} \approx 2$, $\epsilon_{PAGE-like} \approx 10$, and $\epsilon_{Im-like} \approx 47$.

Anion-anion structure factor

Figure 4.13 shows the comparison between the anion-anion structure factor and cation-cation structure factor for the PBD-like polymer.

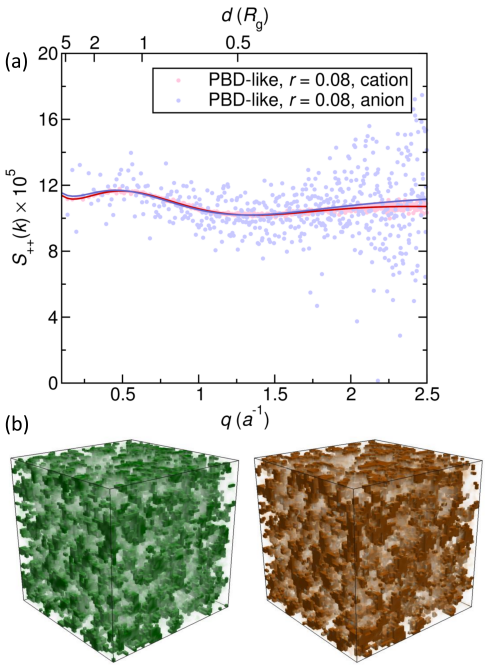

Figure 4.13: (a) Cation-cation and anion-anion structure factors show similar behavior with a peak indicating ion aggregation. (b) Ion channels, identified by the criterion $\phi_{\pm}(r) \geq < \phi_{\pm} > \approx 0.014$, form a percolating network for both cations and anions. Simulations performed by Dr. Douglas Grzetic.

Chapter 5

Optimum in Ligand Density for Conductivity in Polymer Electrolytes

5.1 Abstract

Current design rules for ion conducting polymers suggest that fast segmental dynamics and high solvation site density are important for high performance. In this study, we explore the interplay between solvation site density, segmental dynamics, and ionic conductivity in a family of imidazole side chain grafted siloxane polymer electrolytes containing LiTFSI. By replacing the imidazole side chains with non-solvating ethane or bulky phenyl groups, the effects of solvation site density and polymer segmental dynamics were deconvoluted. Lowering the imidazole content in the ethane-imidazole series leads to a 10-fold increase in conductivity, while conductivity decreases for the phenyl-imidazole series due to differences in steric bulk. Normalizing conductivity by T_g reveals a threshold ligand density above which increased solvation sites do not improve conductivity, but below which the conduction gradually decreases. NMR spec-

troscopy shows the high temperature Li^+ transference number increases slightly with increasing grafting density, from around 0.17 to 0.27. NMR $T_{1\rho}$ relaxation reveals that the Li^+ ions are present in two environments with distinct dynamics within the polymer, matching X-ray scattering and PFG results which suggest ion aggregation exists in these polymers. These results emphasize the importance of local re-arrangements in facilitating ion transport at low solvation site density, confirming the role of dynamimc percolation, and suggest that an optimum ligand density exists for improved charge transport.

5.2 Introduction

Ion-conducting polymers have been proposed as safe, mechanically robust and electrochemically stable alternatives to organic liquid electrolytes for energy storage devices.[26, 27] Critically, while polymers have many advantages over their liquid counterparts, they continue to suffer from low ionic conductivity.[2] Polymers form a relatively translationally-immobile matrix compared to liquids, requiring design rules emphasizing labile ion-solvation interactions.[5, 211, 212]

To dissolve and conduct ions, polymers must contain solvation groups which interact favorably with ions to promote their dissociation, without immobilizing the ions within the polymer framework. The competition between effective salt dissolution and labile ion-polymer interactions results in necessary tradeoffs in electrolyte design and performance. For example, both intermediate polymer polarity[170] and salt concentration[4, 11, 213] seem to provide maximum conductivity performance due to the complex interplay between ion-polymer interactions, segmental dynamics, and ion mobility. Most polymer electrolytes contain at least two mobile ions, the cation

and anion, which both contribute to the total conductivity. Salt dissolution is generally achieved by coordination with the cationic species. For cation motion, these same coordination sites must be dynamic and allow the ion to hop through the matrix by breaking and reforming coordination bonds on a reasonable timescale. Anions typically interact less strongly with the polymer, but still rely on free volume or local polymer re-arrangement, which is in turn generally coupled to cation-polymer interactions since these interactions dynamically cross-link the polymer matrix and result in increases in polymer glass transition temperature (T_g). While energy storage applications require cation transport, most electrolytes exhibit higher anion than cation mobility, underscoring a current challenge for these materials.[49] Polymer design thus requires the incorporation of functional solvation groups which provide strong yet dynamic interactions between the polymer and ions to enable higher cation mobility.

One class of materials with labile ion-polymer interactions is metal-ligand coordination polymers,[214] which we have previously shown to dissolve and conduct a range of metal salts relevant for energy storage.[4, 5] This family of polymers offers advantages in tunability through the wide range of possible combinations of polymer backbone[215] and ligand choices which enables optimization of additional unexplored features for improving performance.

One promising route towards improving ionic conductivity is to increase the segmental mobility of the electrolyte. This can be achieved through the choice of a polymer matrix with inherently low T_g. The lowest T_g polymers generally do not contain the necessary solvation sites for dissolving ions, requiring the introduction of tethered species for ion solvation. One effective way to introduce such solvating groups is by adding side-chains to a low T_g polymer backbone. This has been successfully demonstrated for siloxane [156, 215, 216], phosphazene [217], acrylate [218–221] and aliphatic[215]

backbones. However, the attachment of side-chains to a low T_g polymer backbone generally increases the T_g of the electrolyte.[216, 222, 223] Thus, there is a trade-off between the inclusion of the necessary solvation sites for ion conduction and keeping a low T_g. Ideally, a minimal concentration of solvation sites would be added to a low T_g polymer backbone to achieve ion dissolution and conduction without increasing the T_g to a detrimental level.

Tuning the grafting density of solvating side chains can provide the desired T_g control, but also influences the density of solvation sites and extent of ion aggregation within the polymer. A recent computational study on ether-based electrolytes suggested that the connectivity of solvation sites within an electrolyte can play a critical role in conductivity performance.[160, 224] It is therefore expected that as the grafting density of solvation sites decreases, the efficacy of ion transport through the electrolyte decreases as well, resulting in reduced conductivity performance. Unfortunately, predicting the distribution of solvation sites within a polymer electrolyte can be challenging; experimental methods such as X-ray scattering may observe correlation peaks suggesting some amount of aggregation, but cannot determine the shape of any aggregate features.[184] Furthermore, uniformly distributed coordination sites would not show any features in X-ray scattering at all, but may have significantly different connectivity. Computational tools can aid in this understanding by providing information about aggregate morphology and connectivity.[38, 184, 215]

Since segmental dynamics play such an important role in determining conductivity behavior, a static view of the solvation site and ion aggregate connectivity in these systems is unwarranted.[225] Most electrolyte conductivity is measured significantly above the polymer T_g, suggesting local fluctuations are important for aiding in ion transport. Of particular relevance is the timescale for solvation site re-arrangement rel-

ative to the timescale for ion motion. The importance of the timescale for solvation site re-arrangement was suggested by Druger, Nitzan and Ratner through the development of a dynamic percolation theory.[226–229] This theory has two key timescales – the rate of ion hopping that would be present in a static matrix, and the rate of solvation site re-arrangement. In a system where ion hopping is much faster than solvation site re-arrangement, we recover the static percolation limit, which suggests there is a critical density of solvation sites required to enable ion conduction. However, in the limit where the solvation site re-arrangement is much faster than ion hopping, this percolation threshold disappears entirely, and ion conduction is predicted even for electrolytes with dilute solvation sites. Most electrolyte systems fall intermediate to these two limits, suggesting that both the rate of ion hopping, dictated by ion-solvation site dynamics, and the rate of solvation site re-arrangement, dictated by segmental dynamics, are important for ion transport.[160] Indeed, this explains why T_g is an important lever for increasing conductivity, but that there is still a spread of conductivity performance between systems that have essentially the same T_g but different chemistries.[32]

For energy storage applications, maximizing the Li^+ contribution to the total conductivity is important, and is quantified by the transference number (t_+). Typically, a large Li^+ t_+ reduces the concentration polarization during battery operation, yielding higher power densities.[29] However, the determination of the transference number is challenging for polymer electrolytes systems.[164] Several electrochemical techniques exist for extracting transference number values, although all come with drawbacks. Chronoamperometry, for instance, becomes inaccurate in systems with high interfacial impedance or ion pairing, and for polymeric systems which require large cell polarizations.[51, 52, 57] More rigorous methods for the determination of transference numbers stem from thermodynamic considerations, but are limited by experimental

complexity and propensity for propagation error, and are influenced by the solid electrolyte interphase that typically forms between the polymer and Li metal foil.[49, 58] Here, we use ^{7}Li and ^{19}F pulsed-field gradient nuclear magnetic resonance (PFG-NMR) to determine the diffusion coefficients of the ions of interest, Li^{+} and $TFSI^{-}$.[151] PFG-NMR typically measures the diffusion coefficient over a length-scale of a few micrometers, which means that the diffusion coefficient is therefore an average diffusion coefficient weighted by the time spent in the various mobile and immobile environments in the polymer.

In this work, the role of ligand density on T_g, total ionic conductivity and Li^{+} t_{+} is explored for a series of sidechain grafted polymer electrolytes. A library of polymers was synthesized from a poly(vinyl methyl siloxane) backbone functionalized with varying ratios of imidazole ligands and 'spacer' side chains, chosen to remove residual vinyl reactive groups and to test for the role of spacer steric bulk on the electrolyte properties. It is shown that replacing the imidazole ligands with small ethane spacers enables a reduction in the polymer T_g of over 80 °C, and a concomitant 10-fold conductivity increase. Interestingly, the use of phenyl spacers likewise results in dramatic decreases in T_g of about 60 °C, yet leads to a decrease in the conductivity performance of the polymer electrolyte. After normalization of the conductivity data by the corresponding values of T_g, both polymers show a decrease in conductivity at low grafting density, though the conductivity of the ethane-imidazole series is insensitive to imidazole grafting density at grafting percentages above 30% imidazole. These results are examined based on approximations of molar volume of imidazole and salt concentration, which suggests that reducing the imidazole molar concentration below a certain threshold leads to reduced conductivity performance. Importantly, there is not a strict threshold of imidazole concentration which results in zero ionic conductivity, suggesting that

static percolation theories indeed do not hold, and solvation site re-arrangement recovers some performance for even extremely low imidazole contents. The Li^+ transference behavior of the ethane-imidazole series was also studied using PFG-NMR and relaxometry. The Li^+ t_+ decreases from 0.27 to 0.17 as the imidazole content is reduced to 30% of side chains. Thus, a maximum in cation conductivity exists, emphasizing the need to consider t_+ for ligand density optimization.

5.3 Experimental

Polymer synthesis. Two batches of poly(vinyl methyl siloxane) (PVMS) were synthesized by anionic polymerization using standard Schlenk line techniques. For the first, 200 mL of uninhibited and dry THF was further purified by distillation over n-butyl lithium and dried by the addition of 260 μL of sec-butyl lithium at 0 °C, after which the solution was allowed to warm to room temperature. The monomer, 1,3,5-trivinyl-1,3,5-trimethyl-cyclotrisiloxane (Gelest), was degassed by four freeze-pump-thaw cycles and used without additional purification. 260 μL of sec-butyl lithium was added to THF at 0 °C as initiator, followed by the addition of 15.5 mL of degassed monomer. The reaction was allowed to proceed for 10 min at 0 °C before termination with degassed methanol. The solution was concentrated and precipitated in methanol three times. The second batch followed a similar synthesis procedure. 75 mL of uninhibited and dry THF from a solvent purification still underwent three freeze−pump−thaw cycles before the addition of 5 mL n-butyl lithium. 50 mL of this THF was distilled into a second two-neck round bottom flask, cooled to 0 °C and dried with the addition of 400 μL sec-butyl lithium. 8.5 mL degassed monomer was initiated with 75 μL n-butyl lithium. The reaction was allowed to proceed for 3 h at 0 °C before termination with degassed

methanol. The polymer was purified through dissolution in hexanes, separation in water (3X), a 2 day dialysis in THF, and filtering through a 20 μm PTFE plug. Size exclusion chromatography (SEC) was performed on a Waters Alliance HPLC instrument using a refractive index detector and Agilent PLgel 5 μm MiniMIX-D column at 35 °C with THF as the eluent. Dispersity index (Đ) was determined against polystyrene calibration standards (Agilent Technologies). The PVMS molecular weight was estimated from SEC using Polystyrene standards.

Phenyl thiol (Ph-SH) synthesis. To an oven dried round bottom flask equipped with a magnetic stir bar was added NaSH (1.1 equiv.) followed by a 0.35 M solution of (7-bromoheptyl)-benzene in degassed absolute DMF at 0 °C. This solution was stirred for one hour at ambient temperature under dinitrogen atmosphere. Upon completion, the reaction was diluted with DCM and extracted with brine 4X, dried with Na_2SO_4 and concentrated in vacuo. The 7-phenylheptane-1-thiol was isolated in 93% yield and used for the next step without further purification. The ^{1}HNMR data matched that of previously reported structure.[230]

Polymer functionalization. N-(2-(1H-Imidazol-1-yl)propyl)-4-mercaptobutanamide (Im-SH) was synthesized as previously reported by Sanoja et al.[4] Ethane thiol was purchased from Sigma Aldrich and used as-received. The PVMS polymer was dissolved in THF and added to a round bottom flask containing 2,2-Dimethoxy-2-phenylacetophenone (0.2 mol% with respect to vinyl functional handle). An appropriate mass of Im-SH was dissolved in methanol and added to the flask to vary the imidazole grafting density. For the ethane-imidazole series, an appropriate amount of ethane thiol was added volumetrically using a syringe. For the phenyl-imidazole series, the Ph-SH was dissolved in THF and added into the flask. The total thiol to vinyl ratio was kept constant at 1.75:1. The final methanol/THF solvent ratio was adjusted to be 20/80 to maintain solubility

during all reactions. The reaction was degassed with nitrogen for 30 min, after which the reaction was allowed to proceed under UV (365 nm) light for 2 h. The polymers were purified either by precipitation in acetonitrile, methanol or water, or through dialysis in methanol/THF (50/50) solutions (SnakeSkin dialysis tubing with a 3.5kDa MW cutoff, and solvent exchange every 12 h for a total of 5 to 7 times). The polymers were then dried *in vacuo* at 55 °C in the presence of phosphorous pentoxide and immediately transferred to a nitrogen glove box. The imidazole content of the resulting polymers was analyzed using NMR (DMSO-d6 or $CDCl_3$).

Salt Addition. Polymers were weighed into 7 mL vials and dissolved in anhydrous methanol or anhydrous THF (for low imidazole content polymers) inside a nitrogen glove box. Stock solutions of lithium bis(trifluoromethylsulfonyl)imide (LiTFSI, Alfa Aesar) ranging from 0.1 M to 1 M were prepared using anhydrous methanol. Appropriate volumes of LiTFSI stock solution were added to each polymer vial to achieve nominal molar ratios of Li^+ to imidazole of 0.1, or Li^+ to monomer of 0.1 or 0.05 (see Table 5.1 for concentrations used for each polymer). The sample vials were sealed, removed from the glovebox and frozen in LN_2 before being opened and quickly transferred to a vacuum oven and dried *in vacuo* (1×10^{-3} Torr) at room temperature overnight, and then at 60 °C for 24 h. The samples were then transferred to a high vacuum oven (3×10^{-8} Torr) at 60 °C for 24 h to ensure complete removal of solvent. Finally, the samples were transferred into a nitrogen glove box for storage and measurement.

Ionic Conductivity Measurement. Total ionic conductivity was measured as a function of temperature on samples sandwiched between parallel ITO blocking electrodes using electrochemical impedance spectroscopy (EIS). The ITO-coated glass electrodes (Thin Film Devices) were cleaned by sonication for 5 min each in detergent, DI water, acetone and isopropyl alcohol, followed by a 5 min UV/ozone treatment. The

electrode thicknesses were measured using a micrometer, after which a double-sided Kapton tape spacer with a 1/8" hole was added to one electrode. Polymer samples were loaded into the hole in the Kapton spacer in a nitrogen filled glove box. Samples were heated to about 30 °C above their T_g before being sealed with a second ITO electrode. All samples were then heated to 110 °C and pressed in a hand press. The final stack thickness was measured using a micrometer, and the sample thickness was determined by subtracting the electrode thicknesses. EIS was measured with a Biologic SP-200 potentiostat using a sinusoidal 100 mV signal from 1 MHz to 1 Hz at temperatures ranging from 30 °C to 110 °C. The data was converted into dielectric storage and loss, and the ionic conductivities determined from the real component of conductivity at the maximum in tan(δ).[118] One to three samples were measured for each composition, with errors (where applicable) reported as standard deviations from the mean.

Thermal Characterization. Aluminum DSC pans were loaded with polymer samples in a nitrogen filled glove box and briefly exposed to air during sealing of the pans. The glass transition temperature (T_g) of each sample was measured using a Perkin Elmer DSC 8000 or TA Instruments Q2000 DSC on second heating at 20 °C min^{-1} at the midpoint of the step transition.

X-ray Scattering. X-ray scattering was performed as a function of temperature at the National Synchrotron Light Source II (NSLS-II, beamline 11-BM, Brookhaven National Laboratory) with an X-ray energy of 13.5 keV. Samples were packed into metal washers in a nitrogen glove box and covered on both sides with Kapton tape to prevent moisture uptake during measurement. Samples were equilibrated for 15 min at each temperature before collecting exposures. Data processing, including detector distance calibration using a silver behenate standard, reduction of 2D raw SAXS images into 1D intensity versus q curves and corrections for empty cell scattering were performed

using the SciAnalysis software.[187]

NMR. All ^{7}Li and ^{19}F solid-state NMR experiments were performed on either a 4 mm double resonance (HX) magic angle spinning (MAS) probe or a Diff50 probe fitted with either a 10 mm ^{19}F or ^{7}Li coil. All measurements were done on a 300 MHz (7.05 T) SWB Bruker NMR spectrometer. The polymer samples were packed into 4 mm MAS rotors by adding small amounts of polymer and centrifuging the sample down at 10 kHz for around 2 min each time, until the rotor was full. The rotor was packed inside a nitrogen or argon filled glovebox. The packed NMR rotor was then either used directly inside the 4 mm MAS probe or placed inside a 5 mm NMR tube equipped with a valve which kept an inert atmosphere around the sample. In both instances the sample was then temperature controlled by a flow of N_2 gas at a rate of 800 L hr^{-1} which ensured an inert atmosphere. The temperature for each probe was calibrated using dry methanol and dry ethylene glycol at sub-ambient and elevated temperatures, respectively.

The power level used for the ^{7}Li on the Diff50 probe was either 100 W or 200 W with a 90° pulse duration of around 16 μs (15.6 kHz) or 11 μs (22.7 kHz) respectively. The power level used for the ^{7}Li on the 4 mm MAS probe was 76 W with a 90° pulse duration of around 3.3 μs (75.8 kHz). The power level used for the ^{19}F insert on the Diff50 probe was 50 W with a 90° pulse duration of around 11 μs (22 kHz). For all measurements, a recycle delay of around $5T_1$ was applied before each scan when signal averaging, to allow full relaxation. The ^{7}Li chemical shift was calibrated using a 1 M LiCl aqueous solution (single peak at 0 ppm) while the ^{19}F chemical shift was referenced against a neat PF_6 sample exhibiting a doublet centered around 71.7 ppm.

The T_1 relaxation times were measured using a saturation recovery or inversion recovery sequence. The $T_{1\rho}$ experiments were measured by applying a spin-locking pulse during evolution of the spins following an initial 90° excitation pulse. The spin-

locking frequency chosen here was 10 kHz for all samples. The PFG-NMR experiments used a diffusion sequence which includes a stimulated echo to protect the signal from T_2 relaxation, which is typically very short in these polymer systems. The diffusion was measured using a variable magnetic field gradient strength sequence, where the maximum gradient available was 2800 G cm^{-1}. The selection of gradient strength, along with the gradient duration (δ) and diffusion time (Δ) were chosen for each measurement to ensure an appropriate window on the decay curve was acquired. The value of δ and diffusion time Δ never exceeded 10 ms and 100 ms respectively and were kept as low as possible while using the strongest gradient strength possible in order to achieve the greatest possible signal to noise.

To determine the Li^+ t_+ for these polymer systems, diffusion constants can be measured for the Li^+ (D_{Li^+}) and $TFSI^-$ (D_{TFSI^-}) ions using ^{7}Li and ^{19}F NMR, respectively. The transference number is then defined as the proportion of the conductivity which arises from the Li^+ ions only. If the relative concentration of anions and cations are equal, then the transference number can be determined as follows:

$$t_+ = \frac{\sigma_+}{\sigma_+ + \sigma_-} = \frac{D_{Li^+}}{D_{Li^+} + D_{TFSI^-}} \tag{5.1}$$

The transference numbers, along with the diffusion coefficients, for three different imidazole grafting density polymer samples ranging from 29% up to fully grafted (100%) with ethane spacer units have been measured. These data were collected at 72.7 °C and 81.4 °C only as the conductivity levels for these polymers are relatively low, which in turn causes short NMR spin-spin (T_2) relaxation times limiting the diffusion measurements at ambient temperatures.

Spin-spin relaxation time (T_2) measurements can distinguish between multiple en-

vironments by fitting multiple exponents to the data. However, for the solid polymer systems of interest to this study, the T_2 values are prohibitively short to be measured with accuracy. $T_{1\rho}$ measurements are analogous to T_2 measurements, in that they are sensitive to multiple environments, with the additional benefit that the timescales are controllable through the choice of spin-lock frequency. Specifically, the $T_{1\rho}$ experiment measures T_1 in the xy plane using a low power spin-lock pulse applied during the duration of the evolution period of the sequence. There are limitations to the spin-lock frequencies that can be used due to heating effects, as the pulse power and duration are limited to prevent damage of the NMR probe. Here, a spin-locking frequency of 10 kHz (0.1 ms) was used for all samples, to establish whether multiple environments are present.

5.4 Results and discussion

The two polymer series were designed to identify the role of the concentration of solvation sites (imidazole ligands) on both segmental dynamics and ion conduction (Figure 6.1). Imidazole ligands are attached to a poly(vinyl methyl siloxane) backbone using thiol-ene click chemistry (Figure 5.2). The remaining active vinyl functional groups are reacted with either ethane-thiol or phenyl-thiol. Ethane thiol was chosen as a small spacer unit to remove the residual vinyl functional groups and eliminate the possibility of unwanted reactions or cross-linking occurring in these polymers during processing or characterization. The phenyl-thiol spacers were chosen to maintain similar steric bulk to the imidazole ligand, while still removing the active coordination sites from the polymer. LiTFSI salt was then added to the polymer series at a few concentrations. The first concentration kept the molar ratio of Li^+ to monomer

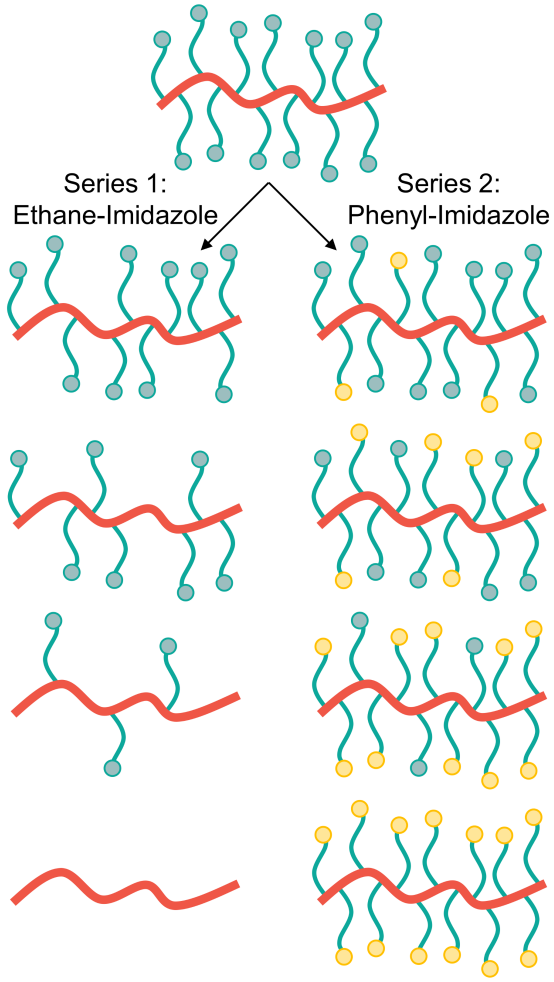

Figure 5.1: Schematic representation of the polymer series synthesized for this study. Series 1 changes the imidazole grafting density by replacing imidazole with a non-bulky ethane spacer, while Series 2 replaces the imidazole with a phenyl spacer to maintain similar steric bulk.

repeat unit constant at 0.1. For the phenyl-imidazole system, this roughly also keeps the weight percent of salt constant (Table 5.1), while for the ethane-imidazole series, the weight percent changes due to the significant difference in molar mass between ethane-thiol and imidazole-thiol. The second salt concentration, explored only for the ethane-imidazole series, kept the molar ratio of Li^+ to imidazole constant. This series tests the hypothesis that the salt dissociation is governed by the imidazole content. The total salt concentration added to the polymer varied more dramatically throughout the grafting density series for constant Li:imidazole (Table 5.1).

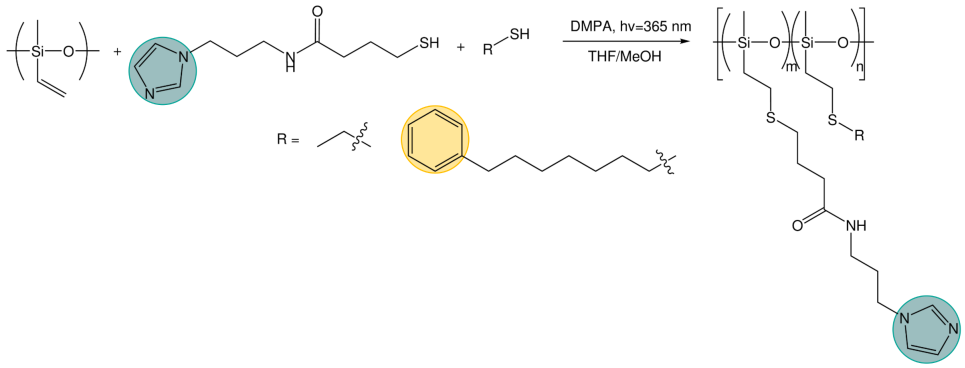

Figure 5.2: Synthesis of the polymer grafting series was achieved using thiol-ene click chemistry to attach various ratios of imidazole thiol and either ethane thiol or phenyl thiol to a poly(vinyl methyl siloxane) backbone.

Wide-angle X-ray scattering (WAXS) shows changes in polymer structure with lower grafting density for the ethane-imidazole polymer series but no change for the phenyl-imidazole series (Figure 5.3). In addition to a broad amorphous halo peak around 0.4 nm, a shoulder peak emerges at about 1 nm as imidazole content within the ethane-imidazole polymers is reduced. This peak is the most intense when no imidazole is present in the polymer, signifying the ethane spacer is responsible for this added structure. The phenyl-imidazole polymers do not show the same feature in X-ray scattering, suggesting that the bulk of the phenyl spacer may be effectively preventing this aggre-

Name	% Imidazole (NMR)	Polymer Molar Mass (g/-mol)	mmol Imidazole per Gram Polymer	Li: Monomer	Li: Imidazole	Salt Concentration (mmol/cm^3)	Salt wt%
VPc	0%	294	0	0.1	N/A	0.340	8.9
VPcI_14	14%	296.72	0.472	0.1	0.714	0.337	8.82
VPcI_40	40%	301.76	1.326	0.1	0.25	0.331	8.69
VPcI_72	72%	307.97	2.338	0.1	0.139	0.325	8.53
VE	0%	148	0	0.1	N/A	0.676	16.25
VEI_7	7%	159.58	0.439	0.1	1.429	0.627	15.25
	7%	159.58	0.439	0.05	0.714	0.313	8.25
	7%	159.58	0.439	0.007	0.1	0.044	1.24
VEI_20	20%	181.08	1.104	0.1	0.5	0.552	13.68
VEI_29	29%	195.97	1.48	0.1	0.345	0.510	12.78
VEI_33	33%	202.58	1.629	0.1	0.303	0.494	12.41
	33%	202.58	1.629	0.033	0.1	0.163	4.47
VEI_49	49%	229.05	2.139	0.1	0.204	0.437	11.14
	49%	229.05	2.139	0.049	0.1	0.214	5.79
VEI_71	71%	265.43	2.675	0.1	0.141	0.377	9.76
	71%	265.43	2.675	0.071	0.1	0.267	7.13
VI	100%	313.4	3.191	0.1	0.1	0.319	8.39

Table 5.1: Polymer characteristics. Polymer name corresponds to PVMS backbone ('V'), with phenyl-carbon ('Pc') or ethane ('E') spacers used to tune the grafting density of imidazole ('I') ligands. The percentage of imidazole grafting density as determined by NMR is given as a number following the name.

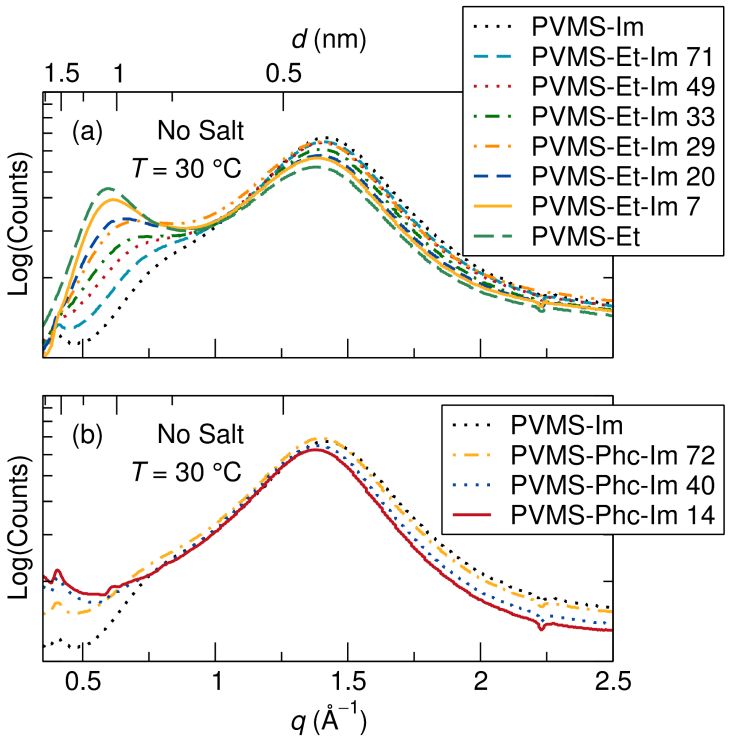

Figure 5.3: WAXS data for the (a) ethane-imidazole and (b) phenyl-imidazole polymer series without salt shows additional structure arising in the ethane-imidazole system through the appearance of a shoulder peak around 0.8 nm to 1.2 nm which grows in intensity and shifts to larger d-spacing as the imidazole content decreases. Such additional structure is not present for the phenyl-imidazole series.

gation. Importantly, the structure determined from X-ray scattering only provides an averaged, static snapshot of these polymers. Since the ion conduction properties are measured at temperatures above the glass transition temperature, these polymers are highly mobile locally, and any aggregation or phase segregation undergoes significant fluctuations with time. These fluctuations likely reduce the importance of this polymer structure on the ion conduction results.

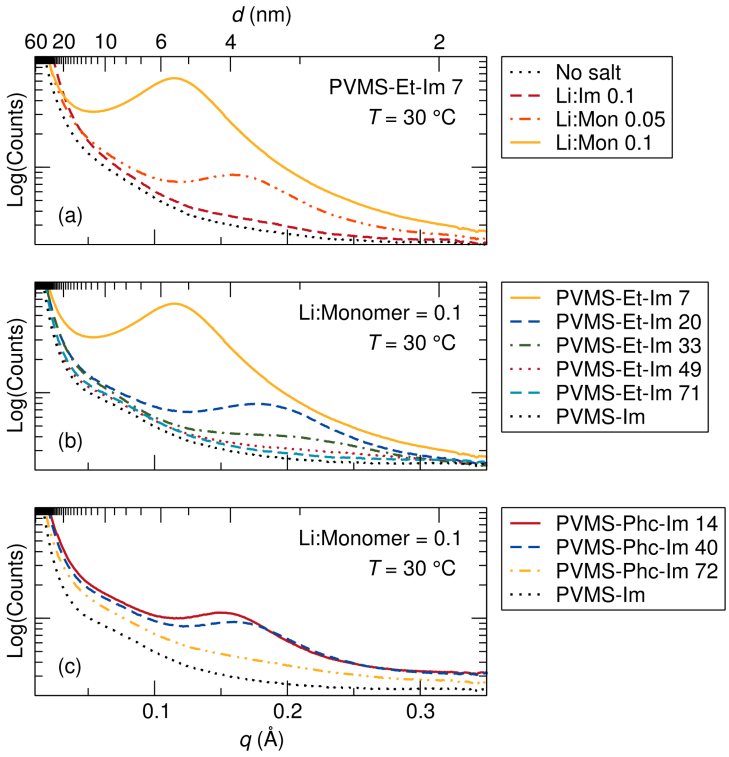

Figure 5.4: SAXS shows change in aggregation peak location and intensity with (a) salt concentration in the ethane-imidazole polymer containing 7% imidazole, and with imidazole grafting density at a constant Li^+ to monomer molar ratio of 0.1 for the (b) ethane-imidazole and (c) phenyl-imidazole polymer series.

Salt addition to the polymers often results in the emergence of an 'ion aggregation' peak at length scales between 3 nm and 6 nm, as probed via small-angle X-ray scattering (SAXS). The interpretation of this aggregate peak is challenging, but is generally believed to arise from scattering between discrete aggregates, or, for stringy or per-

colated aggregates, both inter- and intra-aggregate scattering.[184] Thus, for discrete aggregates it measures the spacing between aggregates, while for stringy or percolated aggregates it can also measure the distance between various segments of a single aggregate.

As salt concentration is increased in the VEI-7 polymer, the aggregate peak grows in intensity and shifts to larger lengthscales, suggesting increased spacing between aggregated domains (Figure 5.4a). A very low salt concentration does not result in ion aggregation in this polymer. The increase in peak intensity follows from the increase in ion concentration, and indicates that a larger number of ions aggregate as the concentration is increased. The increase in spacing between aggregates is less intuitive, as one might expect the aggregates to become larger and more numerous, which would lead to smaller inter-aggregate spacings. However, it is likely that the aggregates formed in these side-chain grafted imidazole systems are stringy or even percolated[215]. In that case, higher salt concentrations may be elongating aggregate domains in such a way to increase the spacing between the closest distance between neighboring aggregates, or between parts of an individual aggregate. Interestingly, salt addition does not change the intermediate structure probed in the WAXS regime.

Increasing imidazole content for the ethane-imidazole polymer series at a constant Li^+ to monomer ratio of 0.1 results in a smaller aggregation peak intensity and a shift in the correlation distance to smaller length scales (Figure 5.4b). The reduction in peak intensity is likely a result of two factors. First, the higher imidazole grafting percentages result in a lower overall salt concentration, due to the increase in polymer volume from the imidazole spacer compared to the ethane spacer (see Table 1). Second, as the imidazole content increases the dielectric constant of the polymer matrix is expected to increase, which results in larger debye screening lengths and therefore

less ion aggregation. The shift in peak position to smaller lengthscales with increasing imidazole content might result from the decreased spacing between imidazoles. Since the salt interacts most strongly with the imidazole ligands in the polymer, it likely segregates to regions of higher imidazole density, resulting in ion aggregate clusters that are spaced closer together as imidazole content increases.

A similar trend of decreasing aggregate correlation distance with increasing imidazole content at a constant Li^+ to monomer ratio of 0.1 exists for the imidazole-phenyl series (Figure 5.4c). Compared to the ethane-imidazole polymer series, the aggregation scattering peak for the phenyl-imidazole is less intense, and is shifted to smaller length scales for a similar imidazole grafting percentage. The additional steric bulk of the phenyl group results in a lower density of imidazole functional groups for the phenyl-imidazole series at the same grafting percentage relative to the ethane-imidazole series (Table 5.1), which could be a contributing factor to the intensity of the peaks. The smaller aggregate peak distance in the phenyl system might be a result of the extra bulk of the phenyl spacers which more effectively prevents ion-imidazole clusters from forming and results in aggregate clusters spaced farther apart instead.

In addition to affecting polymer structure and propensity for ion aggregation, a lower grafting density of imidazole ligands results in significant decrease of the polymer T_g, as seen in Figure 5.5. Before the addition of LiTFSI salt, the ethane-imidazole polymer series T_g ranges from $-8\,^{\circ}$C for fully imidazole-functionalized to $-90\,^{\circ}$C for fully ethane-functionalized (Figure 5.5a). The T_g decrease for the phenyl-imidazole series is slightly smaller, with a drop to $-68\,^{\circ}$C for a fully phenyl-functionalized polymer (Figure 5.5b). Expected T_g values for copolymers can be estimated using the Fox equation,[231] but consistently underestimate the measured T_g for both series. The changing concentration of hydrogen-bonding amide functionality is likely playing a

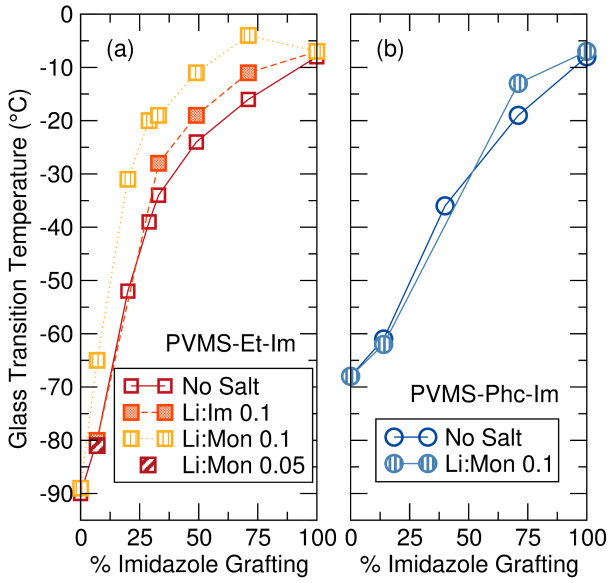

Figure 5.5: Polymer glass transition temperature (T_g) versus grafting density for the (a) ethane-imidazole and (b) phenyl-imidazole polymer grafting series. A lower imidazole content results in lower T_g due to the removal of the polar and hydrogen-bonding groups. The lower steric bulk of the ethane spacer unit results in a lower T_g ($-90\,^{\circ}$C) than the fully phenyl-functionalized polymer ($-68\,^{\circ}$C).

large role (see Chapter 6). It is also possible that microphase separation or clustering of the polar imidazole side-chains away from the non-polar spacer units (as suggested by the X-ray scattering profiles for the ethane-imidazole polymer series) could be driving additional T_g increases for the copolymer series.

The significant decrease in T_g with lower imidazole content for both the ethane- and phenyl-imidazole series suggests that two effects contribute to the polymer T_g. First, the removal of the imidazole side chain eliminates both the polar imidazole group and the amide functional group, which is expected to participate in hydrogen bonding and dynamic cross-linking of the polymer. Elimination of hydrogen bonding and polar groups results in a $-60\,^{\circ}$C drop in T_g as measured for the phenyl-imidazole series. The ethane-imidazole series further eliminates the steric bulk of the phenyl unit, replacing it with a small ethane cap instead. The smaller side chain reduces steric crowding of

the polymer backbone, and results in a further $-20\,^{\circ}\mathrm{C}$ drop of the polymer T_g.

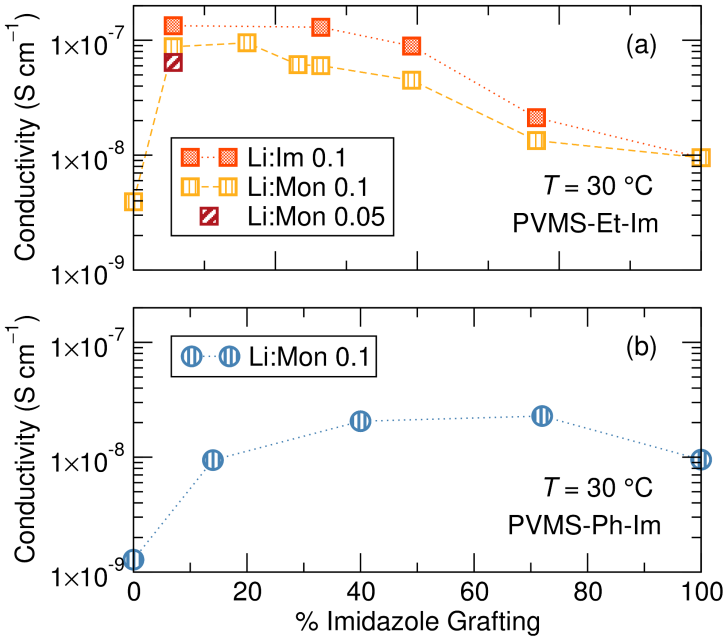

Figure 5.6: Total ionic conductivity for the (a) ethane-imidazole and (b) phenyl-imidazole series as a function of the percentage of monomers containing an imidazole sidechain.

While the ethane- and phenyl-imidazole series show similar T_g behavior, they differ remarkedly in their conductivity trend with changing grafting density at a constant temperature of $30\,^{\circ}\mathrm{C}$, likely due to the difference in steric bulk of the phenyl versus ethane spacer. The ethane-imidazole polymer series undergoes a steady increase of about an order of magnitude in ionic conductivity as the imidazole grafting density is reduced from 100% to around 30% (Figure 6.4a). This conductivity increase reaches a plateau at imidazole contents less than 30%, until all the imidazole is removed from the polymer, which results in a significant drop in conductivity due to the poor solvation and conduction properties of the siloxane backbone and thioether functional group. Interestingly, for the phenyl-imidazole series, the conductivity peaks at a relatively high grafting density of 72%, and subsequently decreases with lower imidazole

content (Figure 6.4b). The maximum conductivity increase is also only approximately a factor of 2. The non-monotonic evolution of the conductivity with grafting density differs from the continually decreasing T_g trend. This result highlights that T_g is not the only important factor in controlling ionic conductivity. Instead, the difference in steric bulk of the phenyl group in comparison to the ethane spacer might be playing a role in determining the conductivity performance.

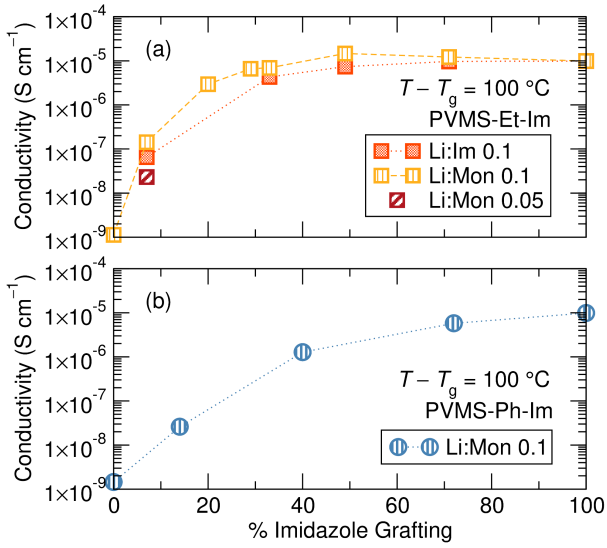

Figure 5.7: T_g-normalized total ionic conductivity versus grafting density for the (a) ethane-imidazole and (b) phenyl-imidazole polymer series. Conductivity values are plotted at a constant $T - T_g = 100$. The conductivity remains flat until around 30% imidazole functionalization for the ethane-imidazole series, while the phenyl-imidazole series shows an immediate decline with reduced imidazole content.

Analyzing conductivity at a constant temperature relative to T_g reveals a threshold grafting density above which extra imidazole is unimportant for the conductivity mechanism. Figure 6.5 shows conductivity as a function of imidazole grafting percentage for both series at $T - T_g = 100$, which was chosen because this temperature was accessible for conductivity measurements for all the samples within both series. Eliminating the contribution due to changing T_g within each series isolates the role of spacer concentration and identity on conductivity performance. This representation shows a

significantly different picture to the un-normalized conductivity data shown in Figure 6.4.

The ethane-imidazole exhibits a plateau in ionic conductivity at imidazole grafting densities above ∼30%, suggesting that at these imidazole concentrations the conductivity is unaffected by a change in the imidazole content. This is an important design rule, as it indicates that increasing the concentration of solvating groups does not always result in improved ion transport. The phenyl-imidazole series, on the other hand, shows a continuous decline in conductivity with lower imidazole content, though the initial decrease in imidazole content to 72% only has minimal effect.

Below a grafting density threshold, which differs between the two series, the conductivity begins to decline more steeply, but also does not immediately reduce to zero. While it is tempting to discuss this decline in terms of a percolation threshold, static percolation theory does not hold in polymer electrolytes significantly above their T_g.[226, 232] In these polymers, significant segmental motion occurs, and solvation site re-arrangement likely plays an important role in determining conductivity performance at lower grafting densities.

Instead, these results can be understood in terms of dynamic percolation theory, which suggests ion conductivity depends on both the rate of solvation site re-arrangement and the rate of ion hopping. The T_g-normalized conductivity representation eliminates differences in solvation site re-arrangement between the polymer electrolytes, enabling understanding of the impact of imidazole content on ion hopping rates. Figure 6.5 shows that ion hopping rates are invariant at high imidazole contents, especially for the ethane-imidazole series, but drop steadily below a threshold imidazole density. High imidazole contents likely form a percolated network of solvation sites, resulting constant solvation site connectivity and thus invariant ion hopping rates. When the ligand

concentration drops below a threshold, the distribution and connectivity of solvation sites changes with imidazole content, resulting in decreasing ion hopping rates and thus lower T_g-normalized conductivity. The role of solvation site distribution on ion hopping rates was previously discussed in Webb *et al.*[160] Note, this T_g-normalized conductivity representation eliminates differences in solvation site re-arrangement, but does not eliminate the overall importance of such re-arrangement, as the conductivites here are 100 degrees above T_g. This is why the conductivity declines but does not reduce to zero after the threshold imidazole content.

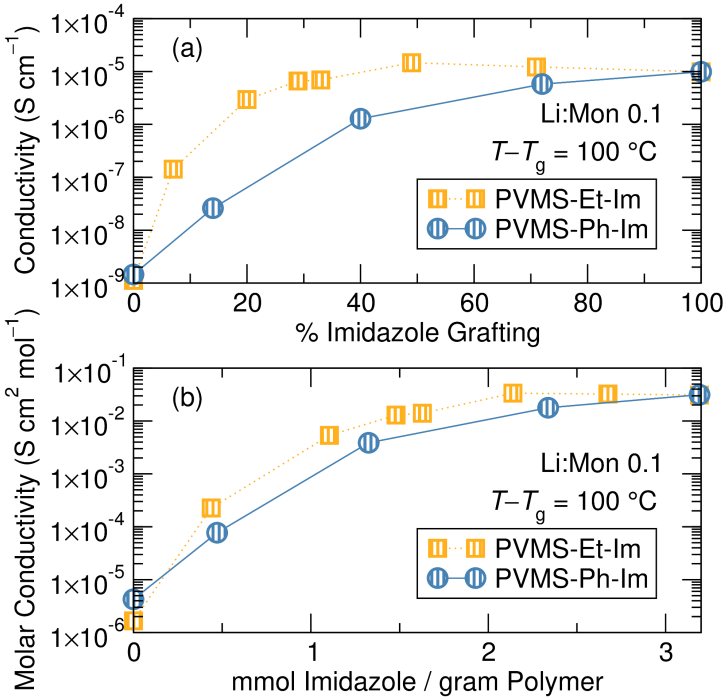

Figure 5.8: (a) T_g-normalized total ion conductivity versus grafting density for the ethane-imidazole and phenyl-imidazole polymer series at a Li^+:monomer ratio of 0.1. (b) The T_g-normalized conductivity can be approximately normalized by salt concentration (to obtain molar conductivity) and plotted against the mmol of imidazole per gram polymer which acts as a proxy for imidazole molar volume. This data now shows a very similar trend between the ethane and phenyl series.

The difference in grafting percentage below which a conductivity drop is seen in the two series likely results from the significantly different steric bulk, or volume, of

the ethane versus the phenyl spacer units used in this study. To compare the phenyl-imidazole and ethane-imidazole series directly, the T_g-normalized conductivity is first plotted on the same graph in Figure 5.8a. This more clearly shows the faster drop in conductivity of the phenyl-imidazole series compared to the ethane-imidazole series. It is possible to convert the imidazole grafting percentage into a mass-normalized imidazole concentration by calculating the mmol of imidazole per gram of each polymer. If the densities of the polymers within the series does not appreciably change, then this mmol imidazole per gram polymer should translate directly into a volumetric concentration (mmol cm^{-3}) of imidazole. To better compare the two series, the conductivity is also normalized into an approximate molar conductivity. This requires assuming full salt dissociation and a constant polymer density (here taken as 1 g cm^{-3}) for all polymers. This form of normalization is commonly applied to both liquid and polymer electrolytes to aid in comparability between studies.[157, 162, 233, 234] Figure 5.8 shows the comparison between the un-normalized conductivity data for the ethane- and phenyl-imidazole series with a Li:monomer ratio of 0.1 and the scaled conductivity behavior (Figure 5.8b). This approximate normalization scheme provides much stronger agreement between the two series in terms of the threshold imidazole content that results in a drop in conductivity performance.

Unlike the total (cation + anion) conductivity, which decreases with increasing imidazole content at a fixed temperature, the Li^+ transference number increases with increasing grafting density when measured at 72.7 °C, suggesting lithium mobility is preferentially enhanced over the $TFSI^-$ at higher imidazole densities. This could be due to shorter distances between imidazole sites, potentially reducing the energy barrier for lithium hopping compared with anion motion. For the 29% and 71% imidazole grafted samples the transference number was observed to increase with temperature. Con-

Grafting Density (%)	$D_{^7Li}$ ($m^2\,s^{-1}$)	$D_{^{19}F}$ ($m^2\,s^{-1}$)	t^+ (%)	σ_+, $\times10^6$ ($S\,cm^{-1}$)	σ_-, $\times10^6$ ($S\,cm^{-1}$)	σ_{total}, $\times10^6$ ($S\,cm^{-1}$)	$\sigma_{measured}$, $\times10^6$ ($S\,cm^{-1}$)
29	6.17×10^{-14}	2.87×10^{-13}	17.7	1.02	4.74	5.76	3.66
71	5.26×10^{-14}	1.91×10^{-13}	21.6	0.642	2.33	2.97	2.69
100	1.03×10^{-13}	3.29×10^{-13}	23.9	1.06	3.04	4.46	2.31

Table 5.2: Li^+ (D_{Li^+}) and $TFSI^-$ (D_{TFSI^-}) self-diffusion constants, as well as transference numbers, calculated conductivity arising from the Li^+ (σ_+) and $TFSI^-$ (σ_-), as well as the total calculated conductivity (σ_{total}) for the four PVMS-Et-Im polymers with varying imidazole grafting density, all with a 0.1 Li:monomer LiTFSI salt added and measured at 72.7 °C.

versely, the 100% grafted sample was independent of the limited temperature range accessible for these systems. The diffusion and transference number values for all samples at 72.7 °C are displayed in Table 6.2.

Comparing the total ionic conductivity measured by impedance spectroscopy with the expected conductivity calculated from PFG diffusion measurements reveals that not all ions participate in the conductivity. The conductivity is calculated using the Nernst-Einstein equation:

$$\sigma = \frac{N_a e^2 C}{k_B T}\left(D_+ + D_-\right) \tag{5.2}$$

where N_a is Avogadro's number, e is the charge on an electron, C is the concentration of ions in the system, k_B is Boltzmann's constant and T is the temperature of the measurement, in Kelvin. The ion concentration has been estimated assuming a polymer density of 1 $g\,cm^{-3}$ and complete salt dissociation. The calculated conductivities from each ion (σ_+ and σ_-) as well as the total calculated conductivity are also presented in Table 6.2.

One possible explanation for the over-estimation of the calculated conductivity is

incomplete salt dissociation, which would result in neutral ion pairs that do not contribute to the overall conductivity or larger aggregates that reduce the total ion concentration. While SAXS (Figure 5.4) does not indicate significant ion aggregation at this salt concentration for the 71% and 100% imidazole grafting density, this does not preclude the existence of ion pairing or small-scale aggregates not detectable in X-ray scattering. The ratio of the measured to calculated conductivity for each sample provides an estimate of the percentage of conducting ions compared to full salt dissociation. These are 63.5%, 90.6% and 51.8% for the 29%, 71% and 100% imidazole grafted samples. It is also possible that a second slow-moving Li^+ component is filtered out in the diffusion sequence, leading to an overestimation of the Li^+ diffusion.

NMR line-width analysis enables a comparison of local ion dynamics at lower temperatures, and reveals that while local dynamics of both the Li^+ and $TFSI^-$ are similar for the entire grafting series at elevated temperature, the ion mobility is progressively impeded with increasing grafting density at ambient temperatures (Figure 5.9). The NMR line-width is inversely proportional to the spin-spin relaxation time (T_2) which in turn depends on the mobility of the species under investigation. As ion dynamics become slower, for instance at lower temperatures, the T_2 value decreases and tends to zero, while the NMR signal becomes broader. The similar linewidths between polymer samples at elevated temperatures is consistent with the high-temperature convergence of the diffusion coefficients measured by PFG-NMR, although the line-width is a more local dynamics probe compared to PFG. At lower temperatures, the 29% imidazole grafted polymer has a significantly narrower line-shape than the 71% polymer, which implies that Li^+ ions are more locally mobile in the former compared to the latter polymer at room temperature. The data in Figure 5.9a can be fit to a standard Arrhenius equation, yielding activation energies of 56.5 kJ mol^{-1} and 60.0 kJ mol^{-1} for the 29%

and 71% grafted polymers, respectively. As discussed below, there is a second, broader component in the ^{7}Li NMR data which unfortunately can not be fitted with accuracy and is not considered in this linewidth analysis. Analogous to the ^{7}Li data, the width of the ^{19}F peaks converge at higher temperatures for all of the samples suggesting similar dynamics, although differences between samples are clearly observed at ambient temperatures. The activation energies derived from Figure 5.9b are 59.3 kJ mol^{-1}, 62.7 kJ mol^{-1} and 80.3 kJ mol^{-1} for the 29%, 71% and 100% imidazole grafted samples, respectively.

Additional information can be obtained from NMR relaxometry measurements. Two relaxation times were studied here, the spin-lattice relaxation (T_1) and the spin-lattice relaxation in the rotating frame of reference ($T_{1\rho}$). T_1 is used to monitor the short-range dynamics (typically 1 ns to 100 ns) of Li^+ (^{7}Li) and $TFSI^-$ (^{19}F) ions independently, and subsequently determine activation energies which relate to the very short range motion, such as the polymer chain dynamics. On the other hand, $T_{1\rho}$ can be used to probe much longer range dynamics on the order of 10 μs to 1 ms, depending on the spin-locking frequency used, and thus, in some instances is comparable to the timescale of the self-diffusion measurements (ms). $T_{1\rho}$ has the added benefit of providing site-specific information on the dynamics of the ionic species of interest.

The observed activation energies for the T_1 measurements (detailed in the Appendix, see Figure 5.11) are significantly smaller than the corresponding values measured for the diffusion process. Discrepancies between the activation energies obtained from the T_1 relaxation data and diffusion measurements can be explained by the fact that T_1 measurements probe very fast dynamics, on the order of 10 ns, whereas the diffusion experiments probe much longer timescales, on the order of ms. Therefore, T_1 is sensitive to other more local dynamics, such as local vibrations, rotations and

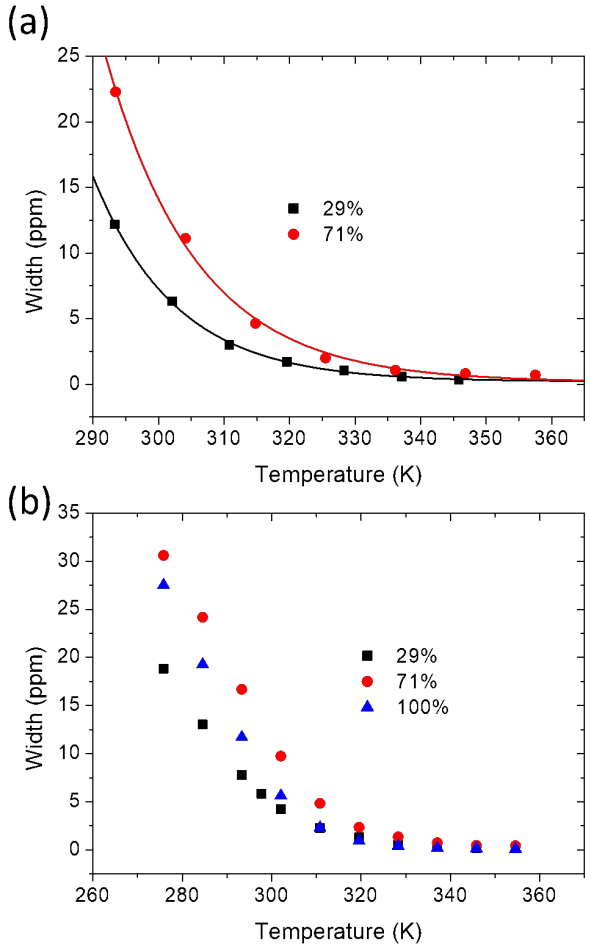

Figure 5.9: (a) ^{7}Li NMR and (b) ^{19}F NMR peak width, as a function of temperature. All samples consist in a 0.1 Li:monomer ratio of LiTFSI added to the polymer. NMR collected and analyzed by Dr. Peter Richardson.

tumbling, which are associated with low activation energies.

Additional $T_{1\rho}$ measurements (as well as chemical shift analysis, see Appendix Figure 5.12) reveals the presence of two ^{7}Li environments, regardless of the imidazole grafting density. Figure 6.6a shows an example $T_{1\rho}$ decay curve for the 71% imidazole grafted sample measured at 63 °C using a spin-locking frequency of 10 kHz. The $T_{1\rho}$ intensity (S) decay curves as a function of time (t) are fitted to an exponential decay function in the form of Equation 5.3 for a single exponential fit and Equation 5.4 for a biexponential (two component) fit. It can be clearly observed from Figure 6.6a that a second component is needed to fit the data well.

$$S = S_0 exp\left(\frac{-t}{T_{1\rho}}\right) \tag{5.3}$$

$$S = S_1 exp\left(\frac{-t}{T_{1\rho,1}}\right) + S_2 exp\left(\frac{-t}{T_{1\rho,2}}\right) \tag{5.4}$$

It is difficult to ascertain the origins of these two ^{7}Li components. One possibility is that the two components correspond to Li^{+} ions bound to the imidazole and in the unbound state ('free' in solution). Another possibility is that the multiple components correspond to Li^{+} ions bound to varying numbers of imidazole moieties. It is unlikely that the second environment is related to binding to the amide group present on the polymer side-chain as two environments were also noted in similar polymer systems which do not contain the amide functionality (see Chapter 6).

The ratio of the two environments is constant with temperature, but changes slightly with grafting density, suggesting imidazole content affects the lithium environment somewhat. The relative occupation of each environment can be determined by com-

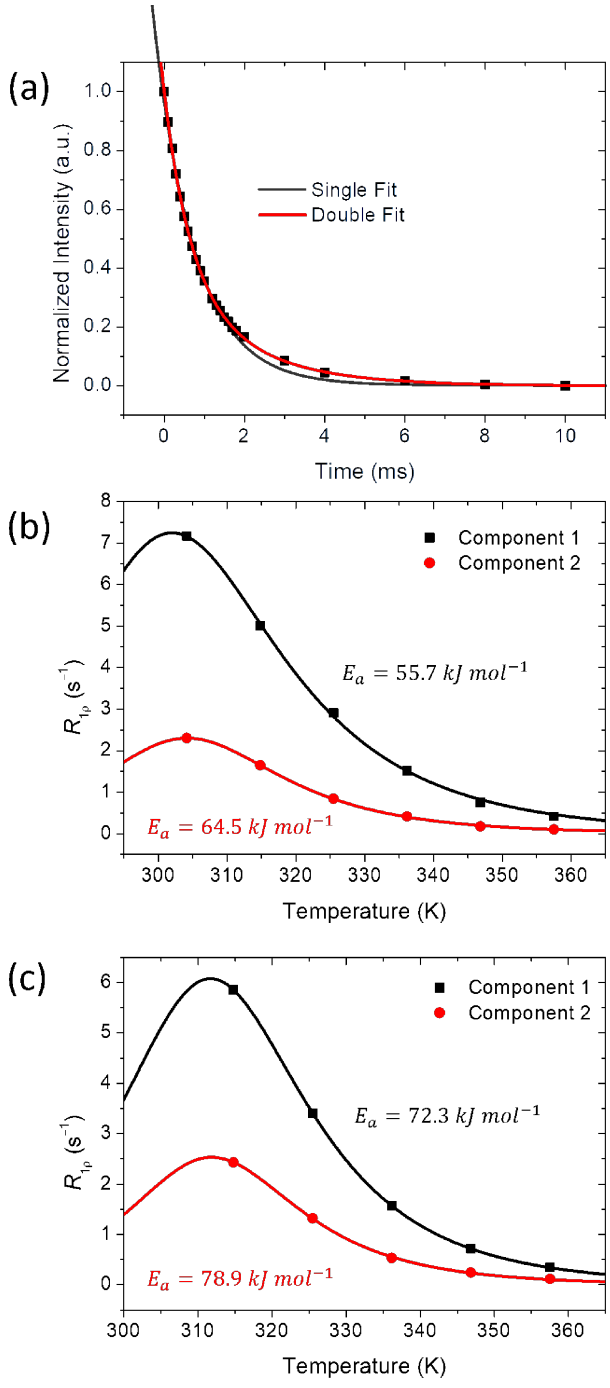

Figure 5.10: (a) ^{7}Li example $T_{1\rho}$ decay curve for the 71% imidazole grafted polymer sample with ethane spacers with 0.1 Li:monomer LiTFSI added, measured at 63 °C, with 10 kHz spin-locking frequency. Two components found for all samples and shown as a function of temperature for the (b) 29% grafted sample and (c) 71% grafted polymer electrolyte. NMR collected and analyzed by Dr. Peter Richardson.

paring the S_1 and S_2 pre-exponential terms. Interestingly, the values of S_1 and S_2 do not seem to be dependent on temperature. The values of S_1 (component 1) are determined to be 0.67±0.01 and 0.61±0.01 for the 29% and 71% imidazole grafting density polymers, suggesting that component 1 becomes slightly more dominant upon increasing the imidazole grafting density. Importantly, while the ratio between the two environments shifts slightly, it does not scale proportionally with the change in imidazole content between the two polymers, which emphasizes that the role of the imidazole on affecting lithium environment is indirect.

The more prevalent lithium environment (component 1) is also more mobile, as revealed by the lower activation energy obtained from fits to the temperature-dependent relaxation rate $R_{1\rho}$ (Figure 6.6b,c). The data were fitted to the theoretical equation for the dipole-dipole relaxation ($R_{1\rho,DD} = \frac{1}{T_{1\rho,DD}}$), which is dependent on the spin-lock frequency (ω_1), the Larmor frequency (ω_0), an arbitrary constant (k) and the rotational correlation time (τ_c), and is expressed in Equation 5.5.

$$R_{1\rho,DD} = \frac{1}{T_{1\rho,DD}} = k\left(\frac{3\tau_c}{1+4\omega_0^2\tau_c^2} + \frac{5\tau_c}{1+\omega_0^2\tau_c^2} + \frac{2\tau_c}{1+4\omega_0^2\tau_c^2}\right) \tag{5.5}$$

In order to relate Equation 5.5 to the temperature study in Figure 6.6 the correlation time is assumed Arrhenius in nature and Equation 5.6 is substituted into Equation 5.5.

$$\tau_c = \tau_0 exp\left(\frac{E_a}{RT}\right) \tag{5.6}$$

The fit shown in Figure 6.6b for the 29% grafting density polymer allows activation energies to be determined for the two components, namely 55.7 kJ mol^{-1} and 64.5 kJ mol^{-1} for component 1 and 2, respectively. Therefore, component 1 is the faster diffusing environment and is also the dominant component. The 71% grafted sample, displayed

in Figure 6.6c, exhibits very similar trends with component 1 as the faster, and dominant environment. However, both components are less mobile for the 71% grafted polymer sample as the activation energies of component 1 and 2 are 72.3 kJ mol^{-1} and 78.9 kJ mol^{-1}, respectively.

This study demonstrates the use of $T_{1\rho}$ measurements to determine the number of environments for the different ions and to assess the dynamics of each component individually. These insights are not readily available using any other technique, suggesting that $T_{1\rho}$ measurements coupled with PFG-NMR yield unique information on the ion dynamics of polymer systems and can be used to predict dynamics at lower temperatures, where diffusion measurements are not easily acquired.

5.5 Conclusion

Tuning the ligand grafting density of an imidazole side-chain siloxane polymer electrolyte doped with LiTFSI enables dramatic tunability over polymer glass transition temperature and total ionic conductivity. The choice of spacer unit, either ethane thiol or phenyl thiol, has significant impact on the ionic conductivity behavior, with the less bulky ethane spacer enabling an order of magnitude improvement in the total ionic conductivity. The T_g-normalized conductivity is shown to be constant at high imidazole grafting density, and decreases below a threshold imidazole content that can be correlated with an approximate volume fraction of imidazole. PFG-NMR enables measurement of Li^+ transference numbers, which decrease slightly with decreasing imidazole content, likely due to poorer connectivity between neighboring coordination sites. These measurements also suggest ion pairing or incomplete salt dissociation. Relaxation NMR measurements indicate the existence of at least two ion environments, and

prove useful for estimating t_+ at lower temperatures not accessible to PFG-NMR. This system presents further opportunities for tuning polymer electrolyte conductivity performance by reducing, rather than increasing, the total ligand content to a value that optimizes polymer T_g, ionic conductivity, and Li^+ t_+.

5.6 Appendix

5.6.1 T_1 Relaxation Experiments

Spin-lattice NMR relaxation (T_1) values were determined as a function of temperature by using a saturation recovery sequence for the four grafting density samples discussed in the main text. The theoretical equation that governs the spin-lattice relaxation rate ($R_1 = \frac{1}{T_1}$) depends on the rotational correlation time (τ_c), the resonant frequency of the nuclei under investigation (ω_0) and a constant (k), which is governed by several fundamental constants:

$$\frac{1}{T_1} = R_1 = k\left(\frac{\tau_c}{1+\omega_0^2\tau_c^2} + \frac{4\tau_c}{1+4\omega_0^2\tau_c^2}\right) \tag{5.7}$$

Equation 5.7 does not have an explicit term included for temperature dependence, but the τ_c parameter depends on temperature and is related to ion dynamics. If we assume that the correlation time follows an Arrhenius-type behavior then Equation 5.6 can be used to define the temperature-dependent correlation time in order to determine an activation energy for this relaxation (E_a):

T_1 measurements suggest that increasing grafting density results in slower local Li^+ and faster local $TFSI^-$ dynamics. Figure 5.11 shows the T_1 values as a function of tem-

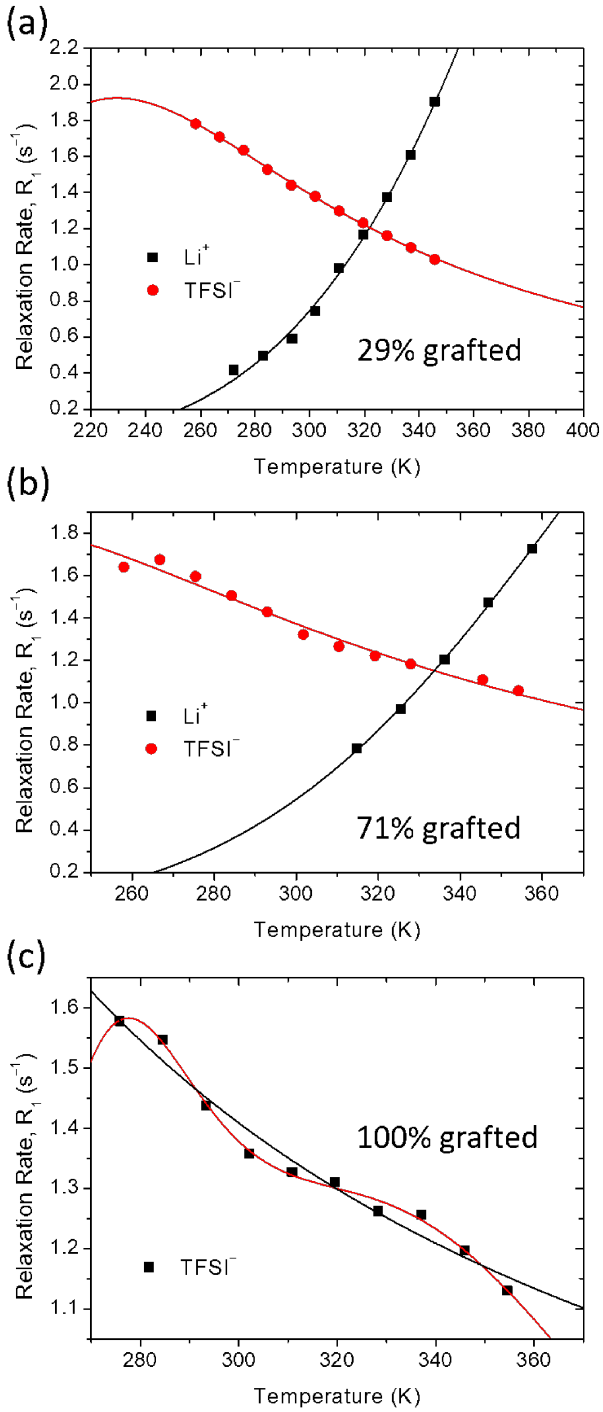

Figure 5.11: T_1 values as a function of temperature for the (a) 29 %, (b) 71 % and (c) 100 % imidazole grafting density polymer electrolyte samples all with 0.1 Li:monomer LiTFSI salt, for both the Li^+ (^7Li) and $TFSI^-$ (^{19}F) ions. NMR collected and analyzed by Dr. Peter Richardson.

perature for the 29%, 71% and 100% imidazole grafting density polymer electrolyte samples all with 0.1 Li:monomer LiTFSI salt, for both the Li^+ (^{7}Li) and $TFSI^-$ (^{19}F) ions. The data were fitted using a combination of Equations 5.7 and 5.6 to extract activation energies (E_a). When inferring ionic mobility from T_1 data, it is important to use activation energy values rather than overall relaxation times, as these can be dependent on local environment as well as ion dynamics. The ^{7}Li activation energies obtained from Figure 5.11 are 17.6 kJ mol^{-1} and 19.2 kJ mol^{-1} for the 29% and 71% grafted samples respectively. The ^{19}F activation energies obtained from Figure 5.11 are 7.36 kJ mol^{-1}, 6.14 kJ mol^{-1} and 3.25 kJ mol^{-1} for the 29%, 71% and 100% imidazole grafted polymers. The activation energies are significantly smaller than the corresponding energies obtained for the diffusion process. T_1 experiments probe typically ns timescale dynamics, which are orders of magnitude shorter than that of diffusion, and therefore probe very local dynamics, such as reorientation and reptation. It is for this reason that the activation energy obtained is much smaller than the activation energy obtained from that of the diffusion process.

5.6.2 Chemical Shift Analysis

An example 1D ^{7}Li NMR spectra is shown for VEI-71 in Figure 5.12, exhibiting both a narrow and broad component.

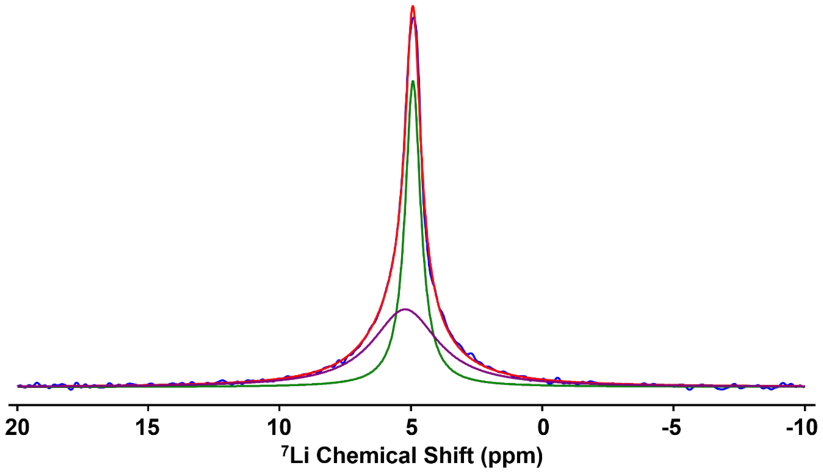

Figure 5.12: ^{7}Li NMR spectrum of the 71% imidazole grafting density polymer with 0.1 Li:monomer LiTFSI salt concentration at 72.7 °C. The data (blue line) has been fitted with two components (green and purple lines) and also shows the overall fit (red line). NMR collected and analyzed by Dr. Peter Richardson.

Chapter 6

Dual Role of T_g and Ion Binding in Determining Conductivity and Lithium Transport in Polymer Electrolytes

6.1 Abstract

High Li^+ conductivity polymer electrolytes provide a route towards improved safety and performance of lithium-ion batteries. However, most polymer electrolytes suffer from low ionic conduction, and even lower lithium ion contribution to the conductivity (transference number, t_+), with the anion typically transporting over 80% of the charge. Here, we show that undetected associations within a polymer electrolyte can entrain both the anion and the cation. When removed, the conductivity performance of the electrolyte can be improved by two orders of magnitude. Importantly, while about half of this improvement can be attributed to the lower T_g of the newly-designed polymer, the amide functional group removal also reduces the polymer interaction with

the Li^+ cation, thus increasing the Li^+ t_+ by a factor of two to 0.46, as measured using pulsed-field-gradient NMR. This work highlights the importance of strategic synthetic design and emphasizes the dual role of T_g and ion binding for the development of new polymer electrolytes with higher ionic conductivity performance.

6.2 Introduction

High energy density lithium-ion (Li-ion) batteries have revolutionized both consumer electronics and electrified transportation.[1] However, current Li-ion technology based on organic liquid electrolytes suffers from low chemical, thermal and mechanical stability, leading to substantial safety concerns.[1, 235, 236] Ion-conducting polymers form chemically stable, easily processable and mechanically robust films and could lead to safer and higher performing batteries.[27, 235, 236] Currently, however, polymer electrolytes lack the ionic conductivity performance required for their use in applications.[2] Significant effort has focused on polymers based on poly(ethylene oxide), and while a few polymers have reached ionic conductivities on the order of 10^{-4} S cm^{-1},[156] some studies suggest that the Li^+ ion only contributes a small fraction of this conductivity (cation transference number, t_+).[49] In fact, both liquid and polymer electrolytes usually transport anions better than cations, with t_+ ranging from -4.5 to 0.2 for standard monovalent salt-in-polymer electrolytes.[5, 32, 49, 58, 237] This cation entrapment is a result of the specific solvation mechanism of most polymer electrolytes wherein it is challenging to separate the solvation and conduction functions. Thus, finding different polymer classes that enable tuning of polymer-ion interactions for both high ionic conductivity and high t_+ is critical for further advancement in polymer electrolyte performance.

Metal-ligand coordination polymers enable tunable dynamic interactions between cations and ligands tethered to a polymer backbone[68, 75, 214, 238] and promote salt dissociation even with low polarity polymer backbones,[215] providing a large library of polymers for optimizing conductivity performance.[4, 5, 215] Ion conduction in polymer electrolytes is achieved through the dissolution of a metallic salt and subsequent transport of the metal cation and organic anion.[3, 26, 43] Polymer electrolytes must therefore contain solvating groups that interact with ions (typically the cation) to stabilize ionic species but still allow for ion mobility. [5, 32, 239] Careful choice of the solvating group is warranted, as a strong tradeoff exists between good solvation resulting in effective salt dissolution and slow cation-polymer binding leading to low t_+. We have previously demonstrated the dynamic metal−ligand coordination of imidazole-containing polymers towards lithium and other metal ions, suggesting this class of materials satisfies these requirements.[4, 5, 215]

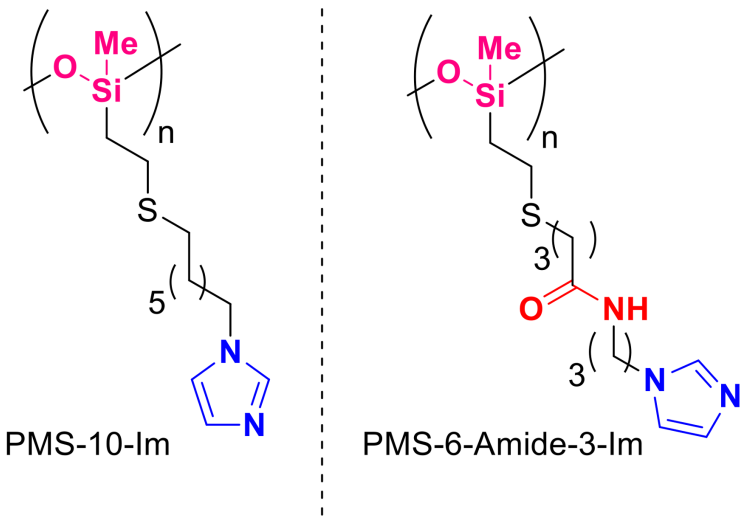

Figure 6.1: Structure comparison between the amide-free (PMS-10-Im) and the amide-containing (PMS-6-Amide-3-Im) polymers. Both polymers are based on a low T_g siloxane backbone and grafted imidazole ligand, but differ in their linker chemistry.

In this chapter, we show how rational polymer design can result in dramatic improvements in both total ionic conductivity and Li^+ t_+. We functionalize a low T_g siloxane polymer backbone with an imidazole-based ligand, but change the linker identity from a more easily synthesized amide-containing linker (forming PMS-6-Amide-3-Im) to an aliphatic chain (forming PMS-10-Im, Figure 6.1). This improves room temperature ionic conductivity by two orders of magnitude, and Li^+ t_+ by a factor of two due to the removal of the hydrogen bonding and Li^+-coordinating amide group. This work highlights the role of both intended and unintended ion binding sites within a polymer in controlling both T_g and ion mobility.

6.3 Experimental

Polymer synthesis. Two batches of poly(vinyl methyl siloxane) (PVMS) were synthesized by anionic polymerization using standard Schlenk line techniques. For the first, 200 mL of uninhibited and dry THF was further purified by distillation over n-butyl lithium and dried by the addition of 260 μL of sec-butyl lithium at 0 °C, after which the solution was allowed to warm to room temperature. The monomer, 1,3,5-trivinyl-1,3,5-trimethyl-cyclotrisiloxane (Gelest), was degassed by four freeze-pump-thaw cycles and used without additional purification. 260 μL of sec-butyl lithium was added to THF at 0 °C as initiator, followed by the addition of 15.5 mL of degassed monomer. The reaction was allowed to proceed for 10 min at 0 °C before termination with degassed methanol. The solution was concentrated and precipitated in methanol three times. The second batch followed a similar synthesis procedure. 75 mL of uninhibited and dry THF from a solvent purification still underwent three freeze−pump−thaw cycles before the addition of 5 mL n-butyl lithium. 50 mL of this THF was distilled into a sec-

ond two-neck round bottom flask, cooled to 0 °C and dried with the addition of 400 μL sec-butyl lithium. 8.5 mL degassed monomer was initiated with 75 μL n-butyl lithium. The reaction was allowed to proceed for 3 h at 0 °C before termination with degassed methanol. The polymer was purified through dissolution in hexanes, separation in water (3X), a 2 day dialysis in THF, and filtering through a 20 μm PTFE plug. Size exclusion chromatography (SEC) was performed on a Waters Alliance HPLC instrument using a refractive index detector and Agilent PLgel 5 μm MiniMIX-D column at 35 °C with THF as the eluent. Dispersity index (Đ) was determined against polystyrene calibration standards (Agilent Technologies). The PVMS molecular weight was estimated from SEC using Polystyrene standards.

Carbon-linked imidazole synthesis. To an oven dried round bottom flask equipped with a magnetic stir bar, imidazole (1.1 equiv.) and half the total volume of THF was added 1.1 equiv. of 2.5 M nBuLi in hexane at ambient temperature. This solution was stirred for 30 minutes at ambient temperature under dinitrogen atmosphere. To this reaction was added a solution of 1-bromo-7-chloroheptane in THF to a final concentration of 0.3 M in imidazole. This reaction mixture was placed in an oil bath preheated to 40 °C and stirred for 22 hours. Upon completion, the reaction was filtered through a pad of silica and concentrated in vacuo. The 1-(7-chloroheptyl)-1H-imidazole was isolated in 85% yield and used for the next step without further purification. The ^{1}H-NMR data matched that of previously reported structure.[240]

To an oven dried round bottom flask equipped with a magnetic stir bar was added NaSH (1.4 equiv.) followed by a 0.35 M solution of 1-(7-chloroheptyl)-1H-imidazole in deoxygenated absolute MeOH at ambient temperature. This reaction mixture was placed in an oil bath preheated to 65 °C and stirred for 19 hours. Upon completion, the reaction was filtered through a pad of silica and concentrated in vacuo. The 7-

(1H-imidazol-1-yl)heptane-1-thiol was isolated in 78% yield and used for the next step without further purification.

Polymer functionalization.

Amide-containing PMS-6-Amide-3-Im. N-(2-(1H-Imidazol-1-yl)propyl)-4-mercaptobutanamide (Im-SH) was synthesized as previously reported by Sanoja et al.[4] Dried PVMS was weighed out and dissolved in THF. An appropriate mass of Im-SH was dissolved in methanol and added to the flask to achieve a thiol to vinyl ratio of 1.75:1. DMPA (2,2-Dimethoxy-2-phenylacetophenone) was added at a initiator to vinyl ratio of 0.2:1. The final methanol/THF solvent ratio was adjusted to be 20/80 to maintain solubility during reaction, with a 0.1 M PVMS concentration. The reaction was degassed with nitrogen for 30 min, after which the reaction was allowed to proceed under UV (365 nm) light for 2 h with continuous stirring. The polymer was purified by precipitation in acetonitrile, then dried *in vacuo* at 55 °C in the presence of phosphorous pentoxide and immediately transferred to a nitrogen glove box.

Amide-free PMS-10-Im. To an oven dried round bottom flask equipped with a magnetic stir bar was added 7-(1H-imidazol-1-yl)heptane-1-thiol (3.0 equiv.), PVMS, DMPA (2,2-dimethoxy-2-phenylacetophenone) (10 mol%) followed by deoxygenated absolute DCM to a concentration of 0.1 M in PVMS. This reaction mixture was irradiated with 365 nm light for 20 hours. Upon completion, the crude mixture was concentrated *in vacuo*. The polymer was purified by precipitation in THF, then dried under high vacuum and immediately transferred to a nitrogen filled glove box.

Salt Addition. Polymers were weighed into 7 mL vials and dissolved in anhydrous methanol inside a nitrogen glove box. Stock solutions of lithium bis(trifluoromethylsulfonyl)-imide (LiTFSI, Alfa Aesar) ranging from 0.1 M to 1 M were prepared using anhydrous methanol. Appropriate volumes of LiTFSI stock solution were added to each polymer

vial to achieve nominal molar ratios of Li^+ to imidazole of 0.03, 0.1, or 0.3. The sample vials were sealed, removed from the glovebox and frozen in LN_2 before being opened and quickly transferred to a vacuum oven and dried *in vacuo* (1×10^{-3} Torr) at room temperature overnight, and then at 60 °C for 24 h. The samples were then transferred to a high vacuum oven (3×10^{-8} Torr) at 60 °C for 24 h to ensure complete removal of solvent. Finally, the samples were transferred into a nitrogen glove box for storage and measurement.

Ionic Conductivity Measurement. Total ionic conductivity was measured as a function of temperature on samples sandwiched between parallel ITO blocking electrodes using electrochemical impedance spectroscopy (EIS). The ITO-coated glass electrodes (Thin Film Devices) were cleaned by sonication for 5 min each in detergent, DI water, acetone and isopropyl alcohol, followed by a 5 min UV/ozone treatment. The electrode thicknesses were measured using a micrometer, after which a double-sided Kapton tape spacer with a 1/8" hole was added to one electrode. Polymer samples were loaded into the hole in the Kapton spacer in a nitrogen filled glove box. Samples were heated to about 30 °C above their T_g before being sealed with a second ITO electrode. All samples were then heated to 110 °C and pressed in a hand press. The final stack thickness was measured using a micrometer, and the sample thickness was determined by subtracting the electrode thicknesses. EIS was measured with a Biologic SP-200 potentiostat using a sinusoidal 100 mV signal from 1 MHz to 1 Hz at temperatures ranging from 30 °C to 110 °C. The data was converted into dielectric storage and loss, and the ionic conductivities determined from the real component of conductivity at the maximum in tan(δ).[118] One sample was measured for each composition.

Thermal Characterization. Aluminum DSC pans were loaded with polymer samples in a nitrogen filled glove box and briefly exposed to air during sealing of the pans.

The glass transition temperature (T_g) of each sample was measured using a Perkin Elmer DSC 8000 on second heating at 20 °C min^{-1} at the midpoint of the step transition.

NMR. All ^{7}Li and ^{19}F solid-state NMR experiments were performed on either a 4 mm double resonance (HX) magic angle spinning (MAS) probe or a Diff50 probe fitted with either a 10 mm ^{19}F or ^{7}Li coil. All measurements were done on a 300 MHz (7.05 T) SWB Bruker NMR spectrometer. The polymer samples were packed into 4 mm MAS rotors by adding small amounts of polymer and centrifuging the sample down at 10 kHz for around 2 min each time, until the rotor was full. The rotor was packed inside a nitrogen or argon filled glovebox. The packed NMR rotor was then either used directly inside the 4 mm MAS probe or placed inside a 5 mm NMR tube equipped with a valve which kept an inert atmosphere around the sample. In both instances the sample was then temperature controlled by a flow of N_2 gas at a rate of 800 L hr^{-1} which ensured an inert atmosphere. The temperature for each probe was calibrated using dry methanol and dry ethylene glycol at sub-ambient and elevated temperatures, respectively.

The power level used for the ^{7}Li on the Diff50 probe was either 100 W or 200 W with a 90° pulse duration of around 16 μs (15.6 kHz) or 11 μs (22.7 kHz) respectively. The power level used for the ^{7}Li on the 4 mm MAS probe was 76 W with a 90° pulse duration of around 3.3 μs (75.8 kHz). The power level used for the ^{19}F insert on the Diff50 probe was 50 W with a 90° pulse duration of around 11 μs (22 kHz). For all measurements, a recycle delay of around $5T_1$ was applied before each scan when signal averaging, to allow full relaxation. The ^{7}Li chemical shift was calibrated using a 1 M LiCl aqueous solution (single peak at 0 ppm) while the ^{19}F chemical shift was referenced against a neat PF_6 sample exhibiting a doublet centered around 71.7 ppm.

The T_1 relaxation times were measured using a saturation recovery or inversion recovery sequence. The $T_{1\rho}$ experiments were measured by applying a spin-locking pulse during evolution of the spins following an initial 90° excitation pulse. The spin-locking frequency chosen here was 10 kHz for all samples. The PFG-NMR experiments used a diffusion sequence which includes a stimulated echo to protect the signal from T_2 relaxation, which is typically very short in these polymer systems. The diffusion was measured using a variable magnetic field gradient strength sequence, where the maximum gradient available was 2800 G cm^{-1}. The selection of gradient strength, along with the gradient duration (δ) and diffusion time (Δ) were chosen for each measurement to ensure an appropriate window on the decay curve was acquired. The value of δ and diffusion time Δ never exceeded 10 ms and 100 ms respectively and were kept as low as possible while using the strongest gradient strength possible in order to achieve the greatest possible signal to noise.

6.4 Results and Discussion

The PMS-10-Im polymer was designed to reduce polymer T_g and eliminate unwanted ion-polymer interactions through the removal of unnecessary polar functional groups. The ionic conductivity of most polymer electrolytes is governed by Vogel-Fulcher-Tamman temperature dependence, where free volume and segmental dynamics (as measured by glass transition temperature, T_g) strongly affect ion mobility.[39, 157, 211] Thus, low T_g polymer electrolytes are favorable for higher conductivity performance. In Chapter 4, we showed that backbone polarity is unimportant for ion conductivity performance, emphasizing that backbone choice should focus on T_g rather than polarity.[215] Therefore, poly(methylsiloxane) was chosen for this study because

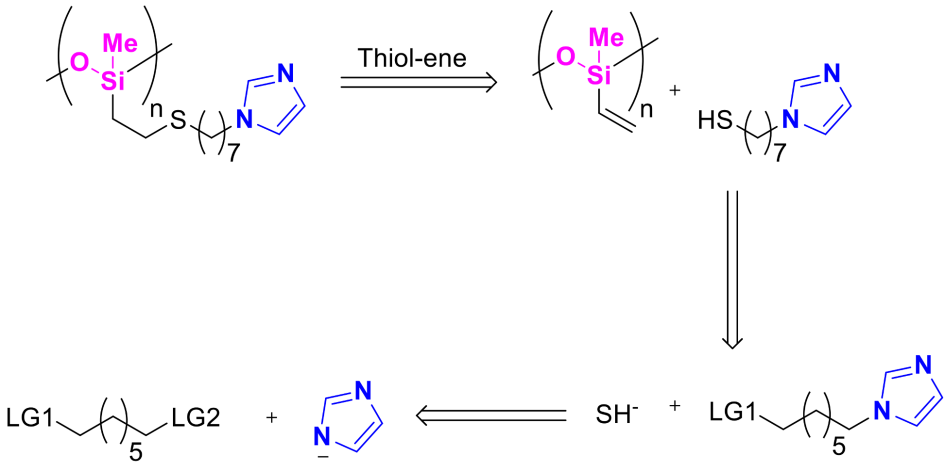

Figure 6.2: Retrosynthetic analysis for synthesizing the amide-free imidazole-containing polymer. Amide-free imidazole thiol synthesized by Dr. Andrei Nikolaev.

it is non-coordinating and possesses low T_g.[156, 215] While the siloxane backbone itself shows low T_g, the T_g increases by over 100 °C upon functionalization with the first-generation imidazole ligand.[215] We hypothesized the hydrogen-bonding capability of the amide functional group might be contributing substantially to this increase.

To assist in synthetic planning for the amide-free imidazole-containing polymer we turned to retrosynthetic analysis (Figure 6.2). Attaching an amide-free imidazole-containing sidechain onto the poly(methylsiloxane) backbone can be readily accomplished using alkene hydrothiolation reaction (thiol-ene) between poly(vinylmethylsiloxane) (PVMS) and thiol-alkyl-imidazole.[4] We envisioned that synthesis of a thiol-alkyl-imidazole sidechain could be achieved through sequential substitution reactions. Using an alkyl chain bearing a leaving group (LG1 and LG2 in Figure 6.2) at each terminal carbon allowed for two sequential substitution reactions, first with an imidazole then with an SH^- source.

The amide-free imidazole-grafted siloxane polymer (PMS-10-Im) was compared to the previously reported[215] amide-containing version (PMS-6-Amide-3-Im) to iden-

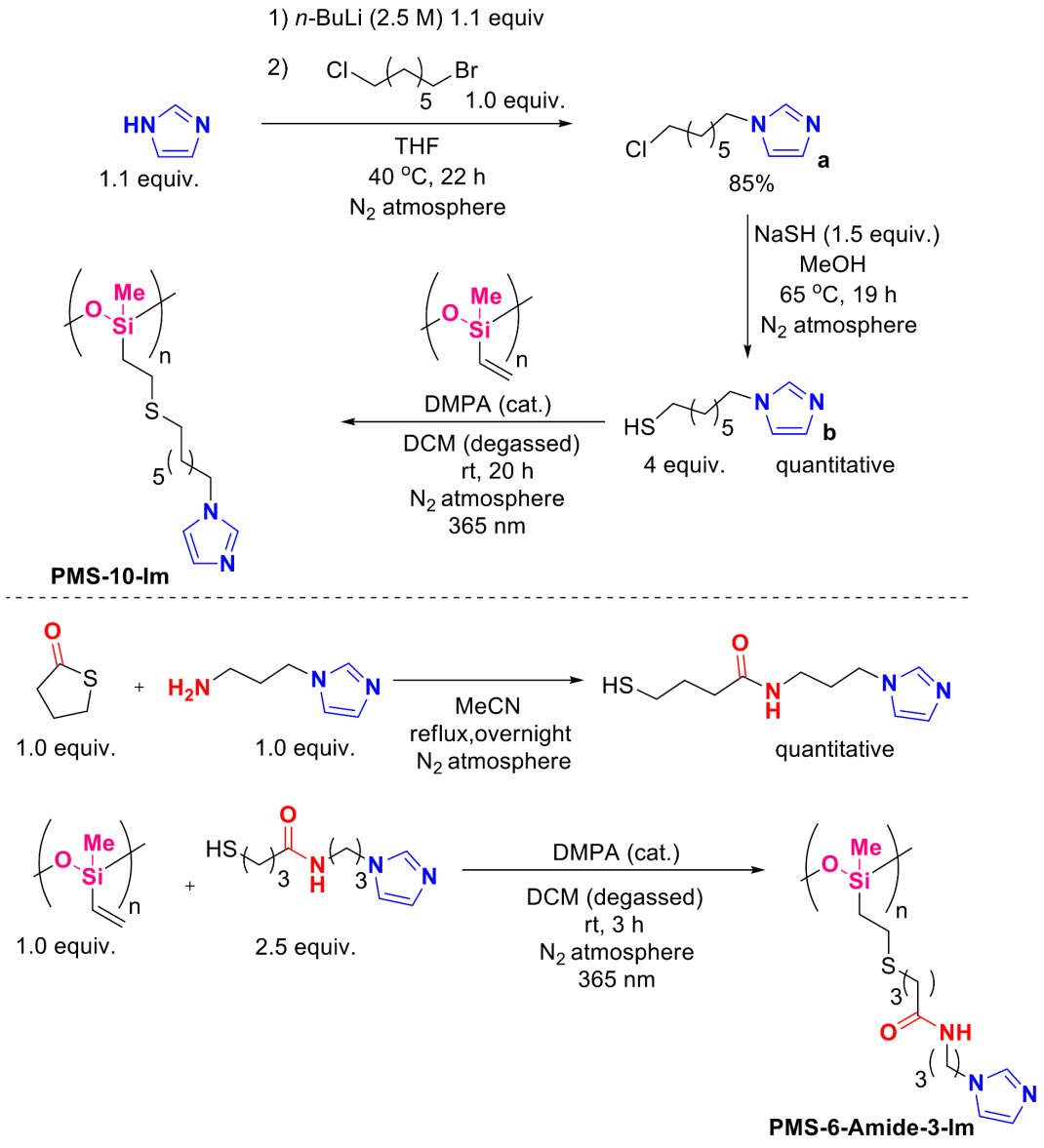

Figure 6.3: Synthesis of the amide and amide-free imidazole-containing polymers.

Polymer	PVMS backbone M_n (kDa)	Đ	T_g (°C)	T_g at $r = 0.03$ (°C)	T_g at $r = 0.3$ (°C)
PMS-6-Amide-3-Im	29	1.60	− 8	− 6	13
PMS-10-Im	19	1.29	− 44	− 22	7

Table 6.1: Polymer backbone characteristics (M_n, Đ), as well as T_g once functionalized, and after salt addition.

tify the result of targeted functional group removal. The two-step synthesis of PMS-6-Amide-3-Im polymer commenced with an addition reaction between γ-thiobutyrolactone and 1-(3-aminopropyl)imidazole to yield the corresponding thiol-containing product. In the next step, this thiol-containing side chain was readily introduced onto PVMS through hydrothiolation reaction under continuous irradiation with 365 nm light. The three-step synthesis of PMS-10-Im began with a substitution reaction between 1-lithio-1H-imidazole (generated in situ from imidazole and *n*-BuLi) and 1-bromo-7-chloroheptane to yield the corresponding product **a** (Figure 6.3). In the second step, a substitution reaction between **a** and sodium hydrogen sulfide (NaSH) furnished the corresponding thiol product **b** (Figure 6.3). Utilizing light-driven hydrothiolation reaction between thiol **b** and PVMS allows access to the amide-free imidazole-containing target polymer PMS-10-Im (Figure 6.3). The successful synthesis of an amide-free imidazole grafted polymer resulted in a decrease in polymer T_g from − 8 °C to − 44 °C (Table 6.1), suggesting the amide was indeed detrimentally increasing T_g.

The total ionic conductivity performance of these two polymers mixed with lithium bis(trifluoromethanesulfonly)imide (LiTFSI) salt was compared using impedance spectroscopy. Figure 6.4 shows over two orders of magnitude improvement in the ionic conductivity of the amide-free polymer electrolyte at room temperature, with the improvement decreasing to about an order of magnitude at 90 °C. This is a dramatic in-

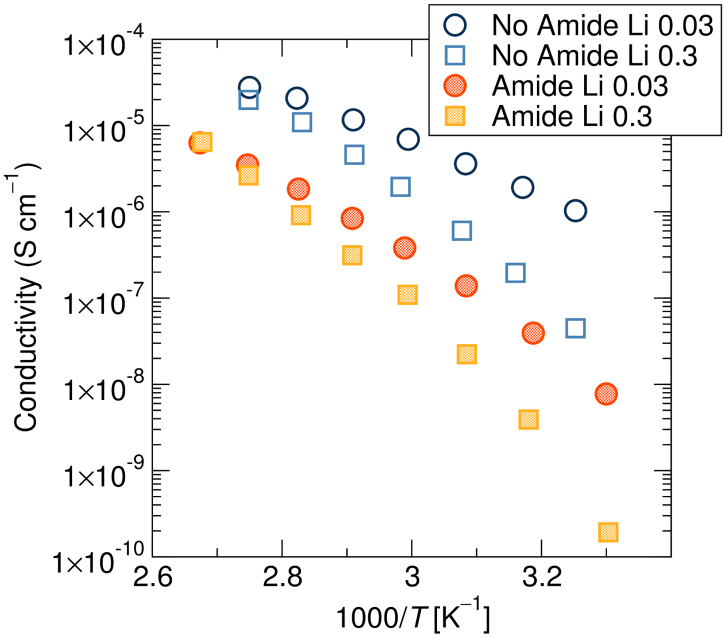

Figure 6.4: Ionic conductivity as a function of temperature, showing about two orders of magnitude improvement in room-temperature conductivity through the removal of the amide functional group.

crease in conductivity solely driven by the removal of the polar and hydrogen-bonding amide functional group from the sidechains of the polymer electrolyte. This confirms that targeted removal of unnecessary functional groups can greatly increase the total conductivity performance. The curved nature of the conductivity data plotted in an Arrhenius fashion suggests the influence of segmental dynamics on conductivity. To ascertain the extent to which T_g plays a role in conductivity improvement, the conductivity data can be normalized by T_g.

The removal of the amide functional group, PMS-10-Im, still results in a 10-fold increase in conductivity over PMS-6-Amide-3-Im after normalization by the T_g of each sample (Figure 6.5). This T_g-normalized representation highlights that T_g only accounts for a little less than half of the conductivity improvement of the amide-free polymer. Importantly, this suggests that the amide was also participating in ion solva-

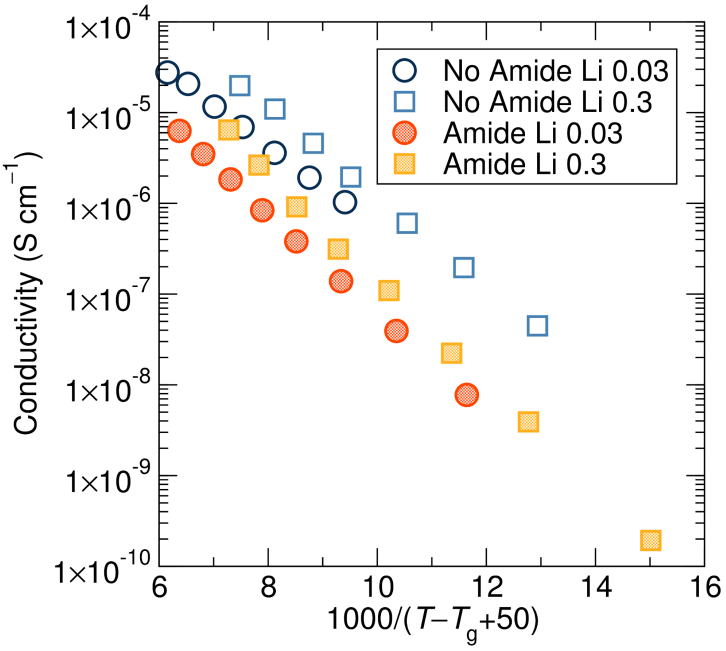

Figure 6.5: T_g-normalized ionic conductivity still shows over a magnitude improvement in the conductivity through the removal of the amide functional group, suggesting that the conductivity increase is not solely governed by T_g effects.

tion and conduction.

Total conductivity as measured using impedance spectroscopy does not provide information on which ions contribute to the ionic conductivity. It is therefore unclear from these measurements alone whether the amide interacts more strongly with the Li^+ cation or $TFSI^-$ anion. To probe individual ion mobilities in each electrolyte more closely, these polymers were studied further using pulsed-field-gradient (PFG) and relaxometry NMR.

PFG experiments reveal an increase in the Li^+ t_+ from 23.8% for the amide-containing polymer to 45.8% for the amide-free polymer at 72.7 °C (Table 6.2). This arises from a clear increase in the Li^+ diffusion constant for the amide-free polymer compared to the amide-containing polymer. Conversely, the two polymers have roughly comparable $TFSI^-$ diffution constants, as expected since the $TFSI^-$ ions do not interact significantly

	Diffusion Constants ($\times 10^{-13}$ m^2 s^{-1})			Conductivity ($\times 10^{-5}$ S cm^{-1})			
Temp (°C)	D_+	D_-	t^+ (%)	σ_+	σ_-	σ_{total}	$\sigma_{measured}$
Amide-Free ($r = 0.3$)							
72.7	1.68	1.98	45.82	0.573	0.677	1.25	0.605
81.4	3.06	4.22	42.02	1.02	1.41	2.43	1.17
Amide-Containing ($r = 0.1$)							
72.7	1.03	3.29	23.84	0.106	0.340	0.446	0.231
81.4	1.92	6.19	23.67	0.193	0.624	0.817	0.538

Table 6.2: Li^+ (D_+) and $TFSI^-$ (D_-) self-diffusion constants, Li^+ transference numbers, calculated conductivity arising from the Li^+ (σ_+) and $TFSI^-$ (σ_-), as well as the total calculated conductivity (σ_{total}) and interpolated measured conductivity as a function of temperature for an amide-free polymer with Li:monomer = 0.3 and amide-containing polymer with Li:monomer = 0.1.

with the polymer. The slightly faster dynamics of the amide-containing polymer are likely due to the lower salt concentration.

Li^+ t_+ measurements confirm that the amide group slows down the dynamics of the Li^+ ions, which aligns with the conductivity data. Unlike the $TFSI^-$ ions, the Li^+ ions are expected to interact with the polymer side-chains, with definite interactions with the nitrogen site of the imidazole[5, 215] and likely interaction with the amide site. Therefore, the observed increase in conductivity through the removal of the amide group can be attributed to a combination of decreased T_g and selective enhancement of the Li^+ dynamics.

PFG NMR also suggests that the fraction of ions not participating in the conduction process is roughly equal for both polymers. This can be determined by comparing the measured conductivity to the conductivity calculated using the self-diffusion constants (D_+ and D_-) determined from PFG NMR (Table 6.2). The measured conductivity is about half that of the calculated ideal conductivity. The conductivity calculated from PFG NMR does not account for any neutral pairs or clusters which do not contribute to

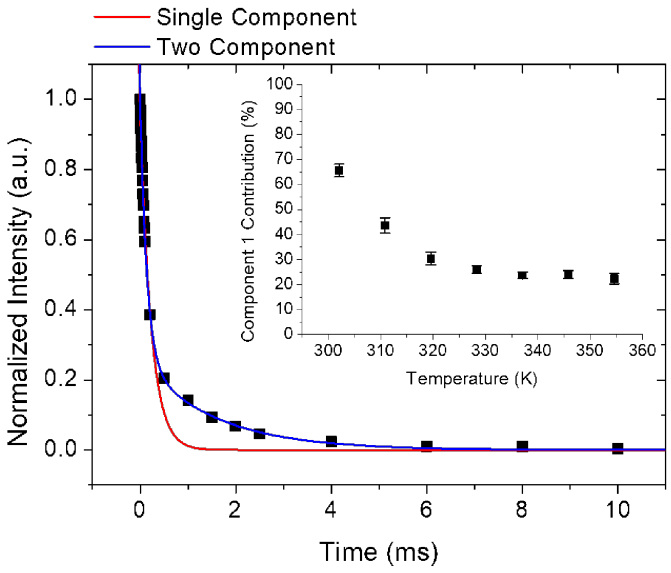

Figure 6.6: $T_{1\rho}$ decay curve measured at 55.2 °C for amide-free polymer requires a two component fit, highlighting the existence of at least two Li envronments. Temperature dependence of component 1 contribution is shown in the inset. NMR collected and analyzed by Dr. Peter Richardson.

the conductivity. It is not possible to speculate whether the loss of the ions is solely from the Li^+, $TFSI^-$ or likely a combination of both. However, since the difference is similar for both polymers it is fair to assume that the observed increase in transference number is reliable. The diffusion constants, transference numbers, calculated conductivity arising from the cation (σ_+), anion (σ_-) and total calculated and measured conductivities are summarized in Table 6.2 for both polymers.

The Li^+ t_+ may increase further at room temperature, matching the stronger conductivity improvement of the amide-free polymer seen in Figure 6.4. The t_+ can be estimated at room temperature by assuming that the self-diffusion values undergo Arrhenius-type behavior. The extrapolated t_+ at 25°C are 54.8 % and 25.0 % for the amide-free (0.3 Li:monomer) and amide-containing (0.1 Li:monomer) polymer respectively.

NMR spin-lattice relaxation time in the rotating frame of reference ($T_{1\rho}$) reveals at least two distinct Li environments exist in both polymers (Figure 6.6). $T_{1\rho}$ is sensitive to multiple environments when they present distinguishable differences in dynamics; the Li^+ in the polymer thus exists in a faster-diffusing and slower-diffusing environment. Since these two sites are present in both the amide-free and amide-containing polymers they may correspond to Li^+ bound to the imidazole (slower component) and 'free' Li^+ (faster component). The exact nature of the 'free' Li^+ cannot be determined from these measurements. The measured self-diffusion constants discussed above are thus a weighted average of the two sites. From these relaxation measurements it is possible to determine not only the $T_{1\rho}$ of each site but also the intensity correlating to the distribution of the two Li^+ sites. The contribution from component 1 (the faster diffusing of the two sites, determined from the relavtive activation energies) is observed to decrease with increasing temperature (Figure 6.6, inset).

6.5 Conclusion

In conclusion, we have shown that the ionic conductivity of polymer electrolytes can be improved by orders of magnitude through rational polymer design. The removal of the hydrogen-bonding and Li^+-coordinating amide functionality in a metal−ligand coordination polymer enabled a 100-fold increase in room-temperature total ionic conductivity and a doubling of the Li^+ transference number. These results emphasize the large gains that can be made in electrolyte performance through the targeted removal of detrimental functional groups. Further improvements in electrolytes based on metal−ligand coordination can be expected through choice of ligand moiety, as heterocycles offer tunability of their electronic and steric properties that can readily be

exploited in structure-function relationship studies in the future.

Chapter 7

Data Visualization and Statistical Learning for Polymer Electrolyte Design

7.1 Abstract

Visualization and statistical regression of compiled datasets can provide unique insights that cannot be gained from individual material system studies. Herein, we describe the curation and analysis of a database of published polymer electrolyte conductivity performance. We focus on solid, dry polymer electrolytes without additives. Data was manually extracted from the literature and manipulated for visualization and statistical regression. It was found that individual features, other than activation energy, are poor predictors of conductivity performance in the wide range of polymer chemistries, lithium-based salts, and salt concentrations examined. The Meyer-Neldel rule stipulating a strong correlation between conductivity prefactor and activation en-

ergy is shown to hold universally for both Arrhenius and VFT representations. Statistical regression techniques were employed to extract the most important features relevant in determing conductivity in polymer electrolytes – these include polymer molecular weight, glass transition temperature, existence of electronegative heteroatoms in a monomer, and anion size. It is emphasized that the ability to use statistical regression techniques on such a dataset is signficantly hampered by the lack of many processing and structural parameters that may be relevant to ionic conductivity performance, and the models trained herein can not be used for prediction of novel polymer electrolytes.

7.2 Introduction

Significant research effort over the past half-century has focused on the improvement of ionic conductivity performance of solid polymer electrolytes.[32, 164, 241] Solid polymer electrolytes show potential as safer, more mechanically robust, and more chemically stable alternatives to organic liquid electrolytes currently used in electrochemical energy storage devices. However, their conductivity performance is at least an order of magnitude below the required target for practical applications.[2] While many reviews have been published on various classes of polymer electrolytes, there is a lack of large-scale analysis of published data to extract fundamental understanding and design predictions.

There are, of course, many detailed studies of specific polymer electrolyte families describing design criteria, but it is unclear whether those parameters hold over a broader range of polymer electrolytes. For example, in Chapter 5, we describe the importance of low polymer T_g and intermediate ligand density in optimizing ionic conductivity in imidazole side-chain grafted polysiloxanes.[215] However, other studies

have compared polymers with low and high T_g and shown that the T_g is less important than other chemical features of the polymer.[224, 242] Thus, while detailed studies across a single polymer series are important for determining design rules within a certain class of materials (*i.e.* single polymer chemistry, single salt identity, single set of processing conditions, etc.), it is possible that a study across a broader range of polymer electrolyte materials could reveal design rules or insights that are hard to see when looking at only specific systems.

Data visualization and machine learning have recently gained popularity in materials science for improving understanding and predicting new compounds in a variety of applications ranging from thermoelectrics,[243–245] to inorganic battery materials,[246–250] to electronic materials,[251–253] to functional materials.[254–256] Polymers have also been the subject of recent data-driven techniques, including the prediction of polymer glass transition temperature, T_g,[257–259] exploration of new polymer electrolytes,[260, 261] and prediction of gas diffusion in membranes.[262] Data visualization alone can be immensely powerful, both to extract trends in aggregate data that may have been missed in smaller studies, as well as to highlight important gaps in published literature that should be corrected.[263–265] The addition of machine or statistical learning techniques can aid in situations where more complicated relationships exist between descriptors and the quantity of interest; in such cases simpler visualizations that are accessible to humans do not readily show trends.[266]

While data mining, visualization and machine learning are powerful, they also have limitations in their applicability to materials research in its current state. The first is the difficulty of data extraction – this is currently a rather manual process for many materials studies, as data exists in figure and publication form rather than in pre-existing databases. While natural language processing will no doubt aid in future efforts, cur-

rent studies generally rely on manual extraction and require domain knowledge to parse important features from each study. Data quality can also restrict the impact of data mining efforts; many studies do not report all relevant processing parameters, materials characteristics, and measurement conditions.[267] The limited size of many of the datasets that can be manually extracted also creates issues related to questions of data reproducibility, as it is more challenging to spot clear outliers in sparse datasets. A small number of entries and a large number of possible descriptors can also significantly impede machine or statistical learning techniques, which can suffer from severe over-fitting either due to the small size of the dataset or the lack of relevant descriptors reported in the original studies.

In spite of these limitations, data visualization and simple statistical analysis can still provide insight into the state and future direction of solid polymer electrolytes. We therefore set out to curate a database of polymer electrolytes for the visualization and statistical learning of features that may be important predictors of ionic conductivity performance. This study is limited to solid polymer electrolytes without solvent or other additives, and includes a database compiled from 65 papers with 655 entries. While the dataset includes a mix of crystalline and amorphous systems, with a wide range of polymer chemistries and some varying polymer architectures (i.e. linear versus branched), it does not cover block copolymers, electrolytes with additives, or single-ion conductors. The scope is thus limited to lithium-based polymer + salt systems.

We find that no single parameter, other than activation energy, adequately correlates with ionic conductivity performance over the entire range of polymers compiled in this study. While some correlations exist for specific chemical identities, such as T_g in a range of carbonate-ether copolymers, most polymer families do not actually show strong trends with any of the features previously predicted to influence conductivity be-

havior. Meanwhile, the strong correlation between conductivity and activation energy can be explained due to the universality of the previously-reported Meyer-Neldel rule, or compensation effect.[268–270] Statistical regression techniques reveal that the most important features for the prediction of conductivity are polymer molecular weight (MW), glass transition temperature (T_g), existence of electronegative heteroatoms in a monomer, and anion size. However, these features are not determinant, since the removal of the two most important features (MW and T_g) still allows for adequate performance prediction. Furthermore, efforts to limit data leakage in statistical learning by grouping the entries by polymer and anion identity results in poor model performance, and illustrates the difficulty in using such models for the prediction of previously unexplored polymer electrolytes. This underscores the general interdependence of features and complexity of polymer electrolyte conductivity prediction.

7.3 Methods

The data used for this work was manually extracted from the literature. Papers were selected from two major reviews,[32, 241] as well as from additional literature searches. Data was restricted to solid polymer electrolytes without additives, where the reported conductivity and characterization did not immediately look suspect. Random copolymers were included, but block copolymers were excluded due to the existence of additional factors complicating conductivity response, such as the possiblity for self-assembly into more complex morphologies. The literature provides a wide range of conductivity performance, but is likely skewed towards specific materials classes (e.g. many more studies on ether-based polymers than other polymers). Attempts were made to keep the distribution of polymer chemistries as even as possible, though over

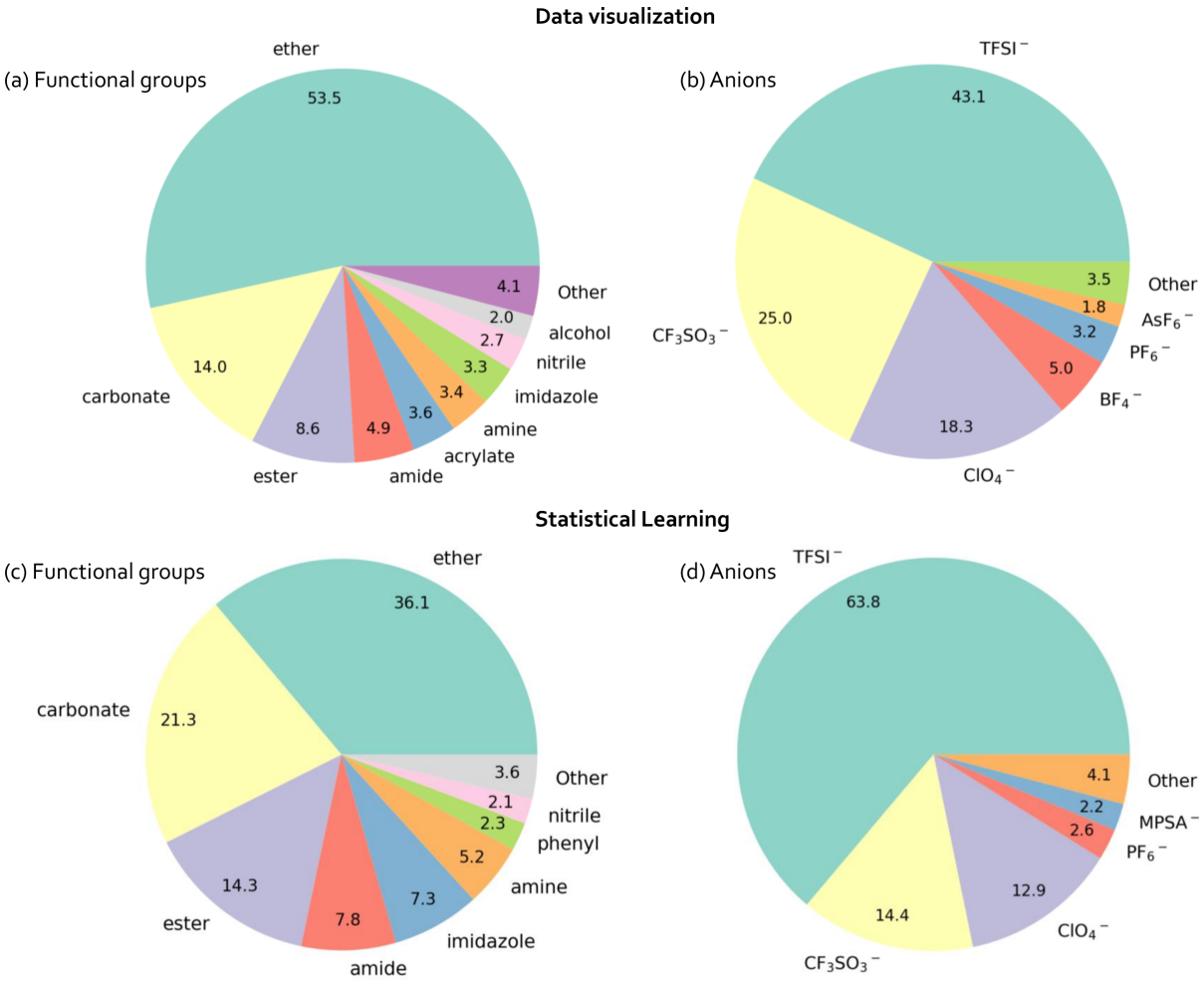

Figure 7.1: Distribution of polymeric functional groups and anions in entries included for visualization data and statistical learning data. (a) Functional groups extracted in this study include ethers, carbonates, esters, amides, and others. (b) Many Li-based salts were studied, with the highest prevalence for $TFSI^-$ and $CF_3SO_3^-$. (c) Entries extracted for statistical regression shift the distribution of functional groups to lower ether contents. (d) Upon dataset trimming for statistical regression, the prevalence of $TFSI^-$ anions increased.

half of all polymers examined here incorporated ether functional groups; the fraction of entries for the various functional groups and Li salt identities is shown in Figure 7.1.

Conductivity values and T_g values presented in figures were extracted using WebPlotDigitizer.[271] Additional descriptors, such as polymer molecular weight, processing conditions and salt concentrations were extracted from the text, tables or figures. For procedures with multiple drying or processing steps, the most rigorous (highest vacuum or temperature) processing step was included. When no drying vacuum was mentioned, it was assumed that no vacuum was used. For electrolyte concentration series where some T_g values were provided but others were omitted, the T_g versus salt concentration data was interpolated to extract approximate T_g values for intermediate salt concentrations. Electrolyte conductivity as a function of temperature data was fit to Arrhenius (Equation 7.1) and VFT conductivity functions. For VFT fitting, two methods were used – the first kept T_0 as a fit parameter (Equation 7.2), while the second set T_0 to $T_g - 50$, when T_g was provided (Equation 7.3).

$$\sigma = A \exp\left(\frac{-E_a}{k_B T}\right) \tag{7.1}$$

$$\sigma = A T^{-\frac{1}{2}} \exp\left(\frac{-B}{T - T_0}\right) \tag{7.2}$$

$$\sigma = A T^{-\frac{1}{2}} \exp\left(\frac{-B}{T - T_g + 50}\right) \tag{7.3}$$

After data retrieval, Python scripts were developed to clean and organize the data for visualization and statistical regression. An approximate polymer molecular weight was extracted as an additional column which was either the number-averaged molec-

ular weight (M_n), when provided, or the weight-averaged molecular weight when M_n was not provided; if no molecular weight was provided, the column was left blank. The solvent used for the processing steps was listed by its boiling point. In addition to the features extracted from the publications, chemical descriptors were calculated based on the polymer and anion identity. The MORDRED library[272] was used to calculate polymer and anion descriptors after manual input of the monomer and anion structure in SMILES format. BigSMILES notation has been suggested for use with polymer systems,[273] but is not yet compatible with Python libraries such as MORDRED and was therefore not used in this study. For some monomer structures, manual correction of number of hydrogen bond donors and acid groups was necessary due to the implicit addition of hydrogens to dangling bonds (e.g. C-O becomes C-OH). For the PF_6^- anion, many MORDRED ExtendedTopochemicalAtom parameters were not calculable because the bonding count to the central atom is greater than 4; for these values, the average of that column for all the other anions was substituted. Only a subset of the full list of chemical descriptors were calculated using MORDRED; those parameters that are expected to most influence physical and electronic structure were included. A list of the descriptors manually collected and used for visualization can be found in Table 7.1; the subclasses of descriptors calculated using the MORDRED library are Polarizability, HydrogenBond, RotatableBond, VdwVolumeABC, Weight, AcidBase, AtomCount, ExtendedTopochemicalAtom, and KappaShapeIndex.

The data was then visualized using MatPlotLib[274] and Seaborn in Python, as well as using Plotly and Dash as a webpage.[275] The webpage includes pages for visualization of data trends, conductivity plotting, a view of the correlation matrix of the descriptors used in the statistical regression portion of the study, and links to the curated dataset as well as the original paper DOIs. This webpage is accessible to the

Polymer characteristics	Processing/Performance characteristics	Salt characteristics
Polymer functional groups	Conductivities at 0 °C to 125 °C	Anion identity
Polymer	Li^+ t_+	salt concentration
SMILES comonomer 1	VFT/Arrhenius prefactors	(Li:functional group)
SMILES comonomer 2	VFT/Arrhenius activation energies	
Comonomer percentage	Li^+ diffusion coefficient	
T_g	viscosity	
T_g w/out salt	storage modulus	
is crystalline?	young's modulus	
T_m	solvent used	
M_n or M_w	drying temp	
Đ	drying vacuum	
chain architecture		

Table 7.1: List of manually collected descriptors.

larger community for additional exploration of dataset trends.

After visualization, the dataset was pruned further for statistical regression analysis. Ordinal categorical features such as crystallinity and vacuum strength used for the drying procedure were converted into sequential numbers, while chain architecture was converted to arrays using one-hot encoding. When no explicit electrolyte drying temperature was provided, 25 °C was assumed; when no drying time was provided, a nominal time of 8 h was entered for the dataset used for statistical learning.

Many features were dropped from the initial data set to optimize for a maximum number of entries while still including the most relevant features expected to contribute to conductivity performance. This feature selection was necessary since many entries had missing values for many features. Dataset manipulation and regression techniques were implemented in Python using the Scikit-Learn library. [276] After removing all entries with missing values, the dataset was split into a training and a test set, with 20% of the entries (55 entries) in the test set. Highly correlated features (with a correlation

> 0.99) were dropped from the features list, after which recursive feature elimination on the training data using a random forest algorithm and 5-fold cross-validation further reduced the number of features to an optimized amount. The final dataset used for statistical regression had 271 entries and 37 features. The target property for prediction was chosen as the base-10 logarithm of the total ionic conductivity at 60 °C, as this was the temperature at which the most entries recorded conductivity (389 entries from the original 655, or 60% reporting). The reduction from 389 to 271 entries is due to other missing features such as T_g and approximate molecular weight.

We then used machine learning models implemented in SK-Learn to explore feature importances in predicting conductivity performance. A pipeline was constructed for data manipulation and fitting – this includes standardizing then normalizing the data before fitting the data with the appropriate regression model. A simple dummy regressor was compared to ridge regression, random forest regression, gradient boosting regression and extra trees regression models. These models were chosen as they enable extraction of feature importances. Grid search and 5-fold cross-validation were used on the training data to optimize model hyper-parameters for each algorithm, taking care to set the random state for reproducible cross-validation splits for each algorithm. Mean squared error was used as the scoring criterion. The hyperparameters were tuned using grid search to select the best parameters for each algorithm.[276]

Once the hyperparameters were selected, the different algorithms were compared against each other, again using 5-fold cross-validation. Averaged mean squared error, averaged mean absolute error and averaged R^2 were all evaluated as scoring criteria. All algorithms were then re-trained on the entire training dataset and the top 10 most important features were compared between the models. Lastly, the trained random forest model, which provided the best performance on the cross-validated training data,

was evaluated on the test dataset.

In addition to a randomized dataset splitting into test, train and validation sets, grouped splitting was also attempted using Scikit-Learn's GroupShuffleSplit and GroupKFold. This splitting eliminates any data leakage between the train and validation or test sets for the groupings that were selected. Groupings were done by polymer type, as well as polymer+anion, which elimiates the possibility of that electrolyte combination occurring in both the training and validation/test datasets just at a different salt concentration or different processing conditions. Feature reduction using correlations and recursive feature elimination, pipeline construction, model hyperparameter tuning, and model fitting was repeated as before except with the additional constraint of using grouped splits for train-test split and cross-validation. Performances were compared between models, but were too low to motivate future model exploration.

7.4 Results and Discussion

The goal of this study is to explore trends in conductivity performance over the vast array of published work on solid polymer electrolytes. Through a combination of data mining, visualization, and statistical regression techniques, we have attempted to extract the most important features and predictors of ionic conductivity in additive-free polymer electrolyte systems. The work-flow followed in this study is shown in Figure 7.2. We began by selecting publications containing solid polymer electrolyte conductivity data, with an attempt to explore the performance from a representative range of polymers/functional groups found in the literature. After manual data extraction, the dataset was cleaned using Python, and additional descriptors for polymer and anion identity were calculated using the MORDRED library.[272] The full dataset was used

for manual and web-assisted visualization of trends, while a smaller cleaned data set with the removal of rows and columns containing empty values was used for subsequent statistical regression analysis.

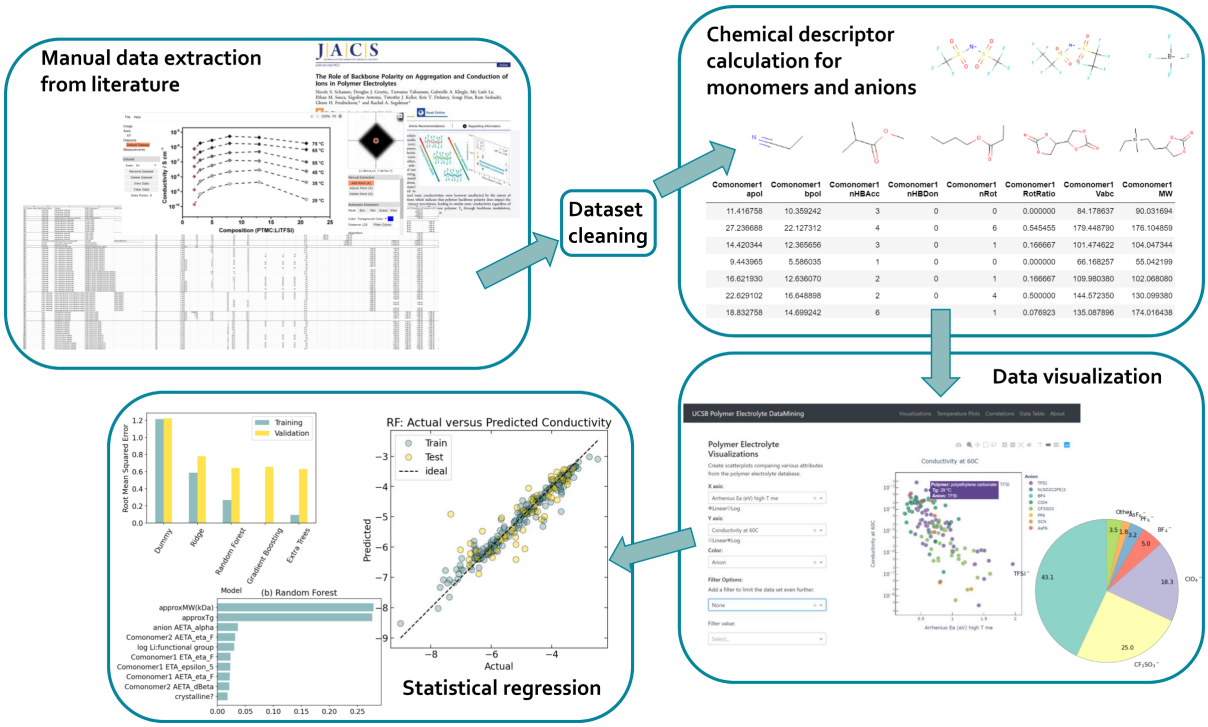

Comonomer1 apol	Comonomer1 bpol	Comonomer1 nHBAcc	Comonomer1 nHBDon	Comonomer1 nRot	Comonomer1 RotRatio	Comonomer1 Vabc	Comonomer1 MW
11.416758	10.359242	3	0	0	0.000000	84.178637	90.031694
27.236688	22.127312	4	0	6	0.545455	179.448790	176.104859
14.420344	12.365656	3	0	1	0.166667	101.474622	104.047344
9.443965	5.586035	1	0	0	0.000000	66.168257	55.042199
16.621930	12.636070	2	0	1	0.166667	109.980380	102.068080
22.629102	16.648898	2	0	4	0.500000	144.572350	130.099380
18.832758	14.699242	6		1	0.076923	135.087896	174.016438

Figure 7.2: The visualization study included manual extraction of data from relevant literature, calculation of relevant chemical descriptors, manual visualization using Python and a custom webpage, and statistical regression implemented using the Python scikit-learn library.

A large number of papers have been published on polymer electrolytes since the discovery of the ion-conducting properties of poly(ethylene oxide) in the late 1970s.[3] These studies range from fundamental explorations of the mechanisms of ionic conductivity, to more applied efforts to increase conductivity performance to relevant levels for application. As such, a wide range of polymer materials, lithium-based salts, additives and processing techniques have been studied. In an effort to limit the scope of this data mining study to a subsection that is feasible for manual collection, we

have decided to focus specifically on polymer-salt electrolytes *without* additives such as plasticizers, ionic liquids or inorganic fillers. This approach explores fundamental ion transport mechanisms in polymers – once additives are mixed into the polymer electrolyte, ion transport mechanisms can alter substantially, reducing the ability to draw cohesive conclusions from a single subset of studies.

For this study, 655 conductivity samples from 78 polymers and 65 papers were selected from reviews and primary literature for data extraction and examination. Trimming the dataset for statistical learning reduced these numbers to 271 entries from 50 polymers. Figure 7.1 shows the distribution of polymer classes and anions of the data examined in this study for data visualization (a,b) and statistical learning (c,d). Some polymers contained more than one functional group, either due to co-polymerization or because the monomer contained multiple functional groups – the visualizations here show the percentages for each functional group, such that polymers with multiple functional groups will contribute to each functional group percentage. For data visualization, functional groups listed in the 'Other' category include phosphazene (14 entries, 1.64%), phenyl (12 entries, 1.41%), sulfonyl (5 entries, 0.59%) and carbonyl (4 entries, 0.47%). The anions included in the 'Other' category include $MPSA^-$ (6 entries, 0.92%), $AlCl_4^-$ (6 entries, 0.92%), $N(SO_2C_2F_5)^-$ (4 entries, 0.61%), I^- (4 entries, 0.61%), SCN^- (2 entries, 0.31%) and FSI^- (1 entry, 0.15%).

Trimming the dataset for statistical learning led to an improvement in the distribution of functional groups, but weighted the anion choice heavily towards $TFSI^-$ (see Figure 7.1c,d). For statistical learning, functional groups listed in the 'Other' category include acrylates (6 entries, 1.56%), alcohols (4 entries, 1.04%), and carbonyls(4 entries, 1.04%). The anions listed in the 'Other' category include $N(SO_2C_2F_5)^-$ (4 entries, 1.48%), BF_4^- (4 entries, 1.48%), SCN^- (2 entries, 0.74%) and FSI^- (1 entry, 0.37%).

While this imbalance may lead to difficulties in the prediction capability for statistical learning models, this is unavoidable due to the lack of complete literature data for many publications.

Data quality and completeness is a continuous concern in scientific research, and was an issue for many of the manuscripts examined for data extraction for this study. In both older and more recent literature, instances of missing processing parameters (polymer-salt mixing solvent, drying procedures, etc.), polymer properties (molecular weight, dispersity), and electrolyte properties (glass transition temperature, lithium transport number) were prevalent and limited the scope of the current study. This is a commonly-discussed issue in materials data-mining and machine learning studies, where the ability to draw conclusions based on published data is hindered by the limited knowledge of the large number of factors that can affect material performance.[257, 267] To balance data completeness and overall data quantity, all data was included for the manual visualization component of the study, while a subset of relevant features were selected for statistical learning. Further, the low overall quantity of data, relative to fields where statistical regression and machine learning have been traditionally applied, prevents easy visualization of outliers. In this work, an attempt was made to filter studies with questionable data quality (i.e. lack of reasonable drying conditions for polymers, suspect impedance spectroscopy curves, etc.), but more work should be done in carefully and systematically characterizing processing parameters for polymer electrolytes in order to validate and explore the conclusions presented here.

7.4.1 Data visualizations

The large body of fundamental studies on polymer ion transport mechanisms suggests some key features that are likely to show predictive trends in ionic conductiv-

ity performance. These include the polymer electrolyte glass transition temperature (T_g),[26, 39, 42] conductivity activation energy,[43] anion size and electrostatic interaction with the Li^+,[277, 278] polymer dielectric constant,[37, 105, 161–163, 170] and salt concentration.[4, 60, 279] These features have been compiled (where possible) for all data extracted from the literature, and each feature is plotted against the electrolyte ionic conductivity at 60 °C in Figure 7.3. While some features show reasonable correlation to the ionic conductivity (e.g. Arrhenius activation energy, E_a), all features still show significant scatter in conductivity performance. That is, for a single value of T_g, E_a or other feature, the reported ionic conductivities still vary by multiple orders of magnitude. This underscores the difficulty of extracting a single feature or electrolyte descriptor that can be used to predict or explain conductivity performance.

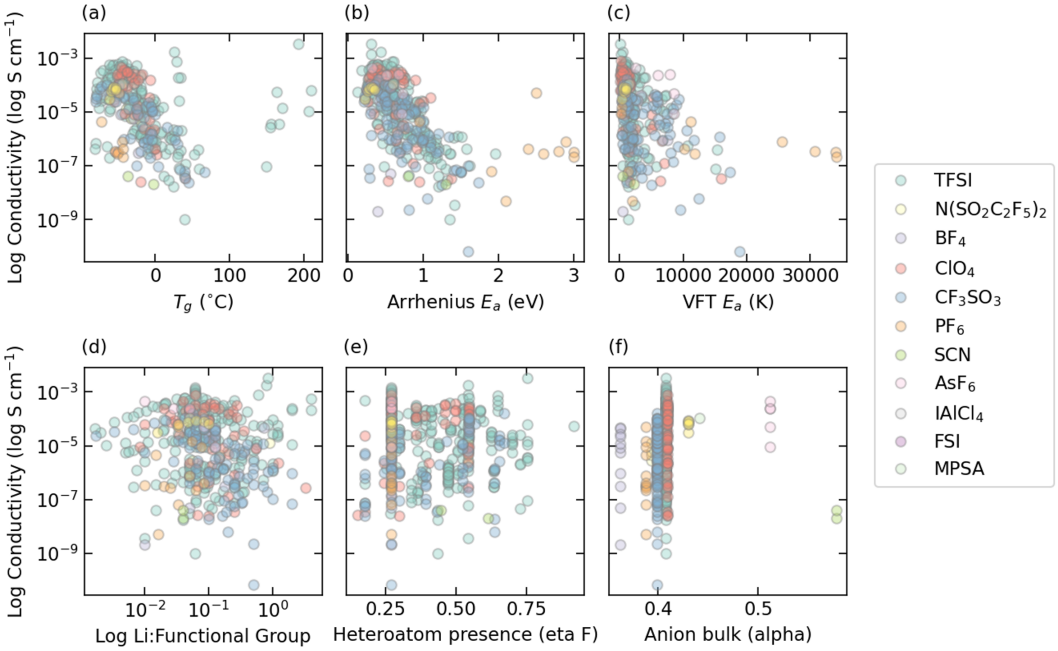

Figure 7.3: Scatter plots showing the lack of correlation between most features and the total ionic conductivity at 60 °C. Some correlation exists for T_g and activation energy (E_a).

To aid in the data visualization procedure, a website was constructed that enables

interactive data analysis (Figure 7.4, *website link*). The visualizations page allows a user to plot any two features against each other to explore possible trends and correlations. Further manipulation is available through color, as well as through specific filter drop-down menus that allow a user to limit the scope of the plotted data to a specific polymer family, publication DOI, salt identity, etc. The ability to explore trends from a specific feature in a sub-set of the extracted data aids in forming an understanding of possible correlations within a polymer family, etc., that might not translate across the entire spectrum of studied polymer electrolytes. Additional pages in the site allow a user to explore the raw conductivity data (with the ability to plot the data in Arrhenius, VFT, and temperature formats), feature correlations, and links to access the compiled data spreadsheets and original papers referenced in this study.

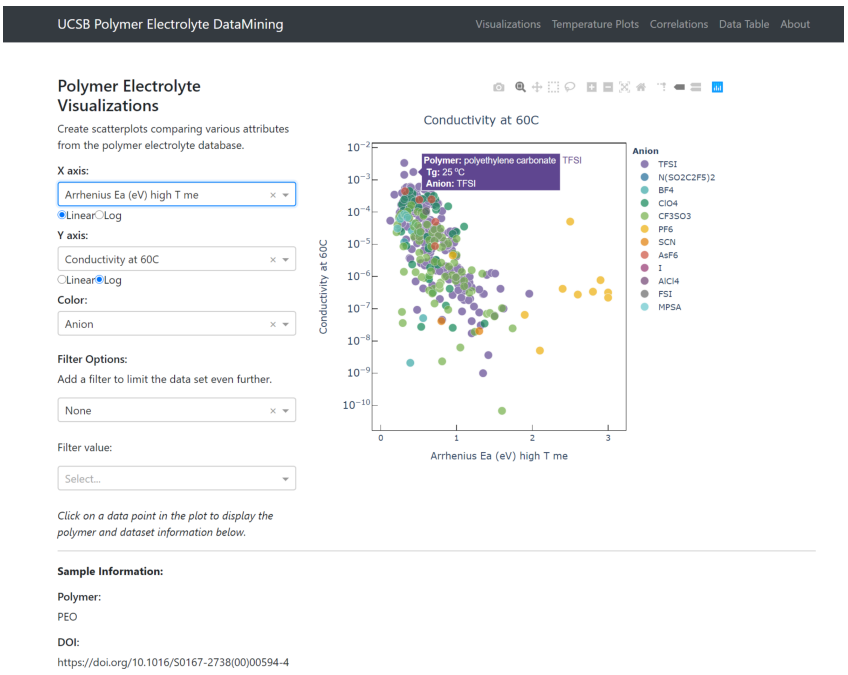

Figure 7.4: Screenshot of website created for interactive visualizations, temperature plotting, feature correlations, and access to the curated data spreadsheet and literature DOIs.

A combination of domain-specific knowledge (i.e. hypotheses of which features

might be important) along with the interactive interface of the created website allows for the exploration of features known or expected to influence ionic conductivity performance in solid polymer electrolytes.

A commonly discussed polymer characteristic that is expected to influence conductivity performance is polymer T_g.[26, 39, 42, 43, 215] From a fundamental perspective, the local polymer segmental relaxation/re-arrangement time rather than the bulk T_g is expected to govern ion mobility by affecting ion hopping rates through rubbery polymer electrolyte.[43] However, many studies use T_g as a proxy for more local dynamics due to the generally strong correlation between the polymer T_g and segmental relaxation dynamics. Individual studies on polymers ranging from polyethers [278] to siloxane-grafted imidazoles (Chapter 5) have shown that a lower polymer T_g generally improves the ionic conductivity. In fact, this is a common design strategy cited in the literature in the search for higher-performance polymer electrolytes.[32, 164]

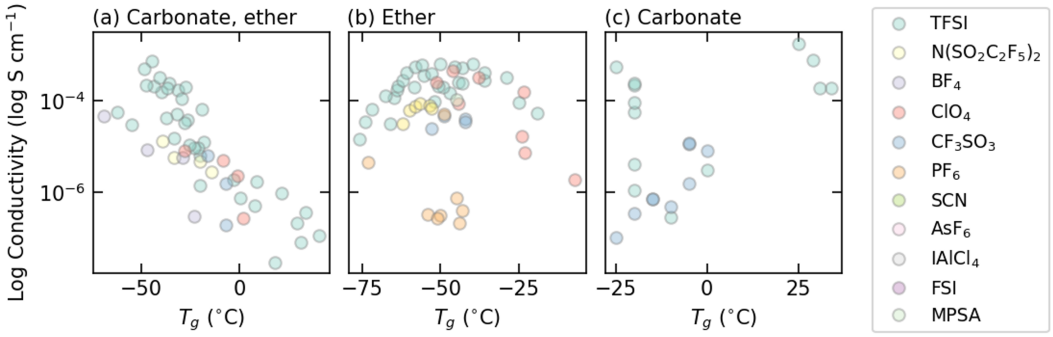

Figure 7.5: T_g is not a good predictor for ionic conductivity for all polymer classes; (a) while a lower T_g leads to higher conductivities for polymers with carbonate and ether functional groups, there is no trend for (b) pure polyethers, and a slightly positive trend for (c) pure polycarbonates.

As Figures 7.5a-c show, the glass transition temperature is not the sole indicator of ionic conductivity performance in most polymer electrolyte classes. Copolymers based on carbonate and ether functional groups seem to show a clear trend with T_g, while

the more general class of purely ether-based polymers shows no clear trend with T_g. Interestingly, polymers with only carbonate functional groups even seemed to show slight reversal of the expected conductivity trend with T_g, though the limited data for this family makes drawing broad conclusions challenging. The ether and carbonate polymer families are more likely to be semi-crystalline, which might play a role in the importance and applicability of T_g as a metric. It is also possible that differences in processing parameters (e.g. solvent identity, drying time, measurement conditions) is affecting the reproducibility of trends seen in individual studies. However, the lack of a clear universal trend in conductivity with polymer T_g also underscores the difficulty in attempting to find proxies for fundamental parameters expected to control ionic conductivity.

It is also relevant to note that some classes of polymer electrolytes, especially those with high T_gs and rigid backbones, are expected to follow a more solid-like conductivity mechanism in which local re-arrangements are less important, and ions hop through pre-existing pathways in the rigid structure.[32, 43, 157, 280] While such a mechanism is not expected for most polymers reported here, the possibility for conductivity mechanisms spanning these two extremes is also important to consider. Intermediate mechanisms of ion transport can be described by dynamic percolation theory,[226–229] in which both the ion hopping and segmental re-arrangement timescales are relevant to consider. In the first extreme, ion hopping is much faster than segmental re-arrangement, and a solid-like conduction mechanism is observed. The other extreme results in a liquid-like mechanism, where segmental re-arrangements dominate the conduction behavior. The continuum between these two extremes suggests that perhaps both segmental re-arrangements – possibly explained by T_g – *and* ion hopping – governed by functional group identity, polymer structure, etc. – are important

for conductivity performance.

Anion identity has also been suggested to correlate with conductivity performance in individual polymer studies,[277, 278] but does not provide a strong prediction of ionic conductivity in the aggregated data set (Figure 7.3f). While anion identity plays a role in enabling salt dissociation within the polymer, other factors such as polymer polarity, cation solvation ability, salt concentration, and ion aggregation also can affect ion mobility. This underscores the realization that many features work in concert to influence ionic conductivity, resulting in sometimes limited information gained from a single descriptor.

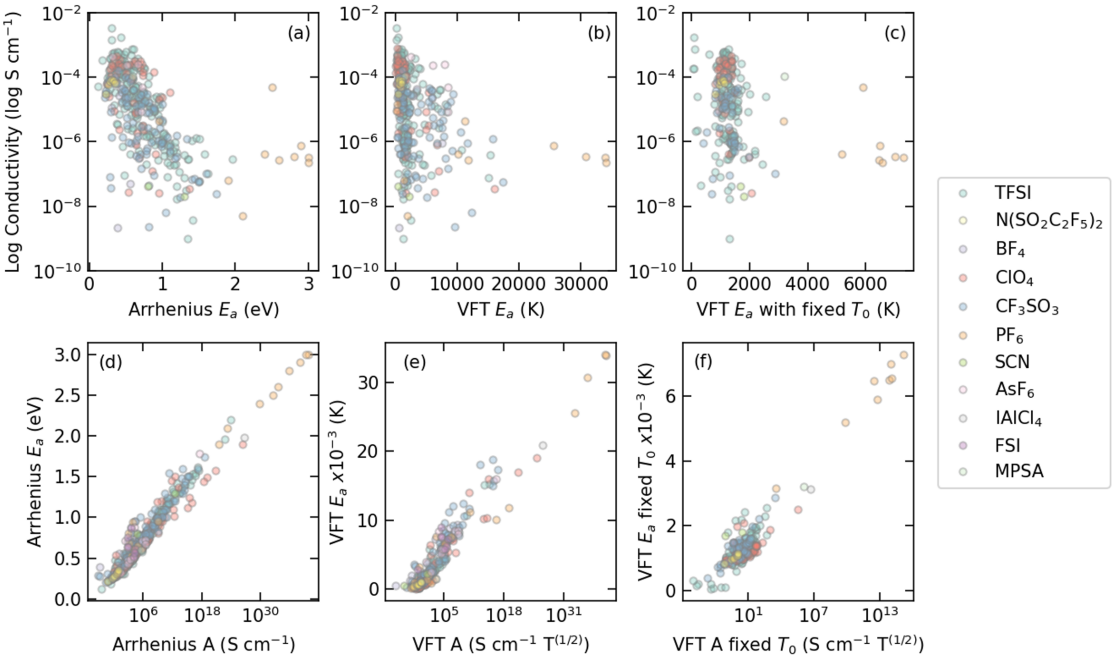

Figure 7.6: (a) Arrhenius (b) VFT with freely-varying T_0 and (c) VFT with $T_0 = T_g - 50$ activation energies correlate somewhat with ionic conductivity, though outliers and data spread exist. (d-f) In general, both Arrhenius and VFT activation energies correlate strongly with their conductivity pre-factors, confirming the generaltiy of the Meyer-Neldel rule.

The activation energies extracted from conductivity-*vs*-temperature plots for the

various collected data suggests a correlation between the Arrhenius activation energy and the conductivity, with a much weaker trend for VFT-based pseudo-activation energies (Figure 7.6a-c). Activation energy represents an estimate of the hopping barrier for ion mobility through the polymer matrix. Thus, it is perhaps unsurprising that a lower energy barrier for motion generally results in higher overall conductivity performance. What is surprising, is that the Arrhenius E_a provides a stronger correlation than the pseudo-activation energy obtained from VFT fits. Most polymer electrolyte performance extracted in this study was better represented in VFT format compared to Arrhenius. However, since the conductivity of most samples is measured over a relatively small temperature range, Arrhenius and VFT fits are generally not widely variant from each other, which could explain the relatively strong trend between Arrhenius activation energy and conductivity. Nevertheless, the VFT activation energy parameter exhibited a larger spread in values obtained through the fitting program, and does not provide as clear of a trend in conductivity performance. One possible explanation is the increase in free fitting parameters for a full VFT equation, resulting in greater uncertainty of the obtained fit values.[268] It is also possible that the more exact fit provided by the VFT equation captures experimental error inherent across the spread of publications, while the Arrhenius fitting essentially smoothes out uncertainty and error.

The strong correlation between activation energy and Arrhenius or VFT pre-factor was also confirmed to hold over the entire range of polymers examined in this study (Figure 7.6d-f). Known as the Meyer-Neldel rule, isokinetic relationship, or compensation effect,[268–270, 281] this correlation has been examined for activated processes in a number of inorganic and organic materials, including poly(ethylene oxide) following Arrhenius temperature dependence,[281] and single-ion conducting polymers with

VFT behavior.[268] It was already suggested in 1990 that the Meyer-Neldel rule should be a very general result for all systems with large activation energy. Indeed, visualizations of these correlations over such a wide range of polymer families, salt identities and salt concentrations emphasizes the universality of this correlation effect for both Arrhenius and VFT conductivity equations. The E_a versus prefactor plot for Arrhenius fits shows that chemical environment (e.g. solvation functional group, anion identity, etc.) does not appreciably affect the slope of the correlation. The microscopic understanding of this correlation has been described in terms of the connection between activated hopping energy (enthalpy) and the number of pathways that are available for hopping (entropy).[269, 281] This seems to hold similarly for all polymer electrolytes examined here.

The visualization results discussed above emphasize the difficulty in determining universal predictors for conductivity performance in additive-free solid polymer electrolytes. While we have discussed a few of the likely important features in the text above, we emphasize that additional features describing anion and polymer properties (including un-characterized or un-reported features such as ion aggregation structure) are likely to play a role in determining conductivity performance. For those descriptors that are documented, we now turn towards statistical regression techniques to extract more complex relationships between the various features and the total conductivity performance.

7.4.2 Statistical regression analysis

Statistical regression and machine learning present appealing opportunities to uncover trends and connections in datasets that are not immediately apparent to humans. This is generally the case when many of the possibly important features do not seem

to strongly correlate with the property of interest (*e.g.* conductivity), as was discussed above. A general trade-off exists between model prediction capability and interpretability; simple models are easily interpretable but often do not achieve the same prediction capability compared to more complex models.[266] Since the goal of the statistical regression implementation in this instance is to extract important descriptors, relatively simple regression models were chosen.

Many features that were included in the manual visualization portion of the study were dropped for the statistical regression. Most were dropped due to lack of data for many of the polymer entries. However, we also chose to drop the activation energy and prefactor terms from Arrhenius or VFT fits. Due to the strong correlation between the activation energy and conductivity prefactor, once one of the two parameters is known, the other is easily estimated (see discussion above and Figure 7.6d-f). These two parameters are the only values needed to calculate conductivity at any temperature using the Arrhenius or VFT equations. In effect, the activation energy fully describes the conductivity at any temperature. We therefore chose to remove these features from the statistical regression to avoid data leakage between the features and the target prediction value, the ionic conductivity. Highly correlated features (with correlation factors above 0.99) were also removed from the feature list to improve the interpretability of feature importances. Lastly, recursive feature elimination was used to optimize the total number of features used during learning, in an attempt to reduce the propensity for overfitting.

While a Random Forest (RF) regression model provided the best fitting performance compared to Ridge, Gradient Boosting (GB) and Extra Trees (ET) regression models, all models exhibited signs of overfitting. Figure 7.7 and Table 7.3 show the averaged 5-fold cross-validation root mean squared errors, mean absolute errors, and R^2 for the

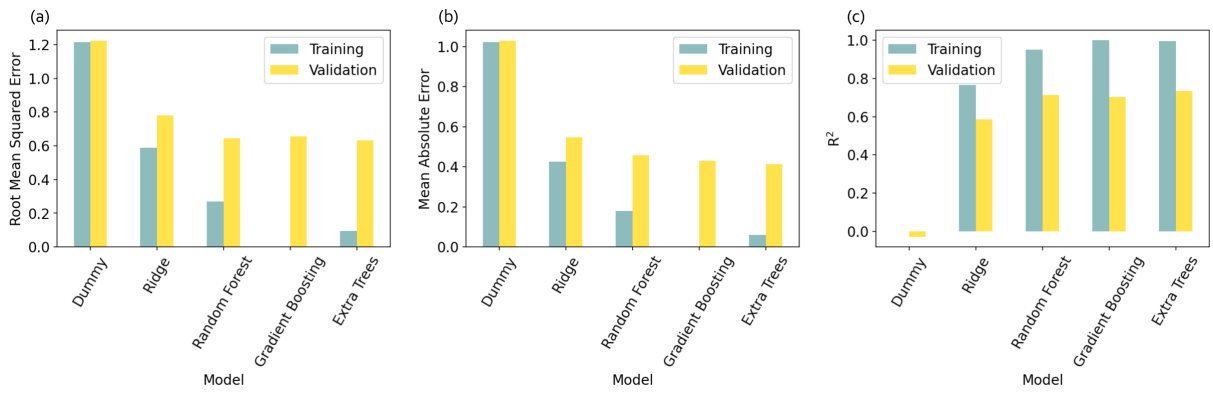

Figure 7.7: (a) Root mean squared error (b) mean absolute error and (c) R^2 performance metrics comparisons for dummy, ridge, random forest, gradient boosting and extra trees regression using 5-fold cross-validation. All statistical regressions perform better than the dummy regression, with random forest performing best on the validation sets in all metrics.

different models compared to a dummy regressor model where the mean conductivity value is always chosen. The optimized hyperparameters are listed in Table 7.2. All models show significant improvements in fitting performance over the dummy model, with RF regression consistently having the best performance for the validation set using each scoring metric. The linear nature of ridge regression seems to limit its ability to adequately learn from the training data, with much lower R^2 and higher errors compared to the nonlinear tree algorithms. All models show worse performance on the validation sets compared to the training sets, suggesting overfitting is an issue. This is most significant for the GB and ET regression models. It is interesting to note, however, that the performance of the models on the same cross-validated training set did not significantly improve after elimination of highly correlated features, or after the recursive feature elimination. This suggests that rather than there being too many features, the issue with overfitting arises either from a lack of appropriate features, or from the small dataset size which results in a higher impact of possible outliers. General noise in the conductivity performance data thus likely plays a large role in the

Model	Parameters
Ridge	$\alpha = 0.01$
Random Forest	*max depth* $= 10$
	n estimators $= 50$
Gradient Boosting	*max depth* $= 6$
	n estimators $= 500$
Extra Trees	*max depth* $= 10$
	n estimators $= 500$

Table 7.2: Hyperparameters optimized for each model

ability to create highly robust statistical models.

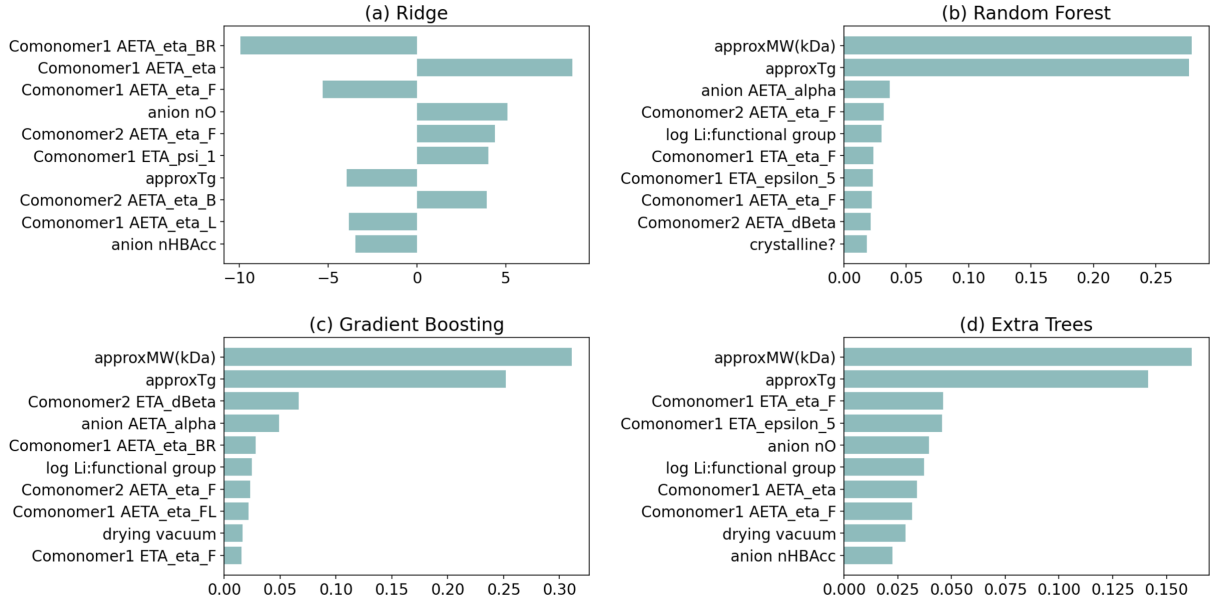

Figure 7.8: Top ten electrolyte features extracted from trained (a) ridge (b) random forest (c) gradient boosting and (d) extra trees regression models. All tree-based models rank approximate T_g and polymer approximate molecular weight highest, followed by salt concentration, monomer characteristics such as the presence of heteroatoms, and anion molecular bulk ('alpha').

All regression models show similar features to be most important at predicting conductivity performance, with the higest variance in features seen in the Ridge regression model. Figure 7.8 shows the top 10 most important features selected by each model after optimization and training on the entire training dataset.

Metric	Dummy	Ridge	Random Forest	Gradient Boosting	Extra Trees
Train					
RMS Error	1.22	0.59	0.27	0.0003	0.1
Mean Absolute Error	1.02	0.43	0.18	0.0003	0.06
R^2	0	0.77	0.95	1	0.99
Validation					
RMS Error	1.22	0.78	0.64	0.66	0.63
Mean Absolute Error	1.03	0.55	0.46	0.43	0.41
R^2	-0.03	0.59	0.71	0.7	0.73
Dropped MW, T_g		Ridge	Random Forest		
Train					
RMS Error		0.76	0.29		
Mean Absolute Error		0.57	0.20		
R^2		0.61	0.94		
Validation					
RMS Error		0.92	0.68		
Mean Absolute Error		0.67	0.47		
R^2		0.42	0.69		

Table 7.3: Cross-validated performance of all tested models

In all tree-based models, the top two most important features are the approximate molecular weight and the approximate T_g of the polymer. The approximate T_g uses the T_g of the electrolyte, where provided, and otherwise substitutes the T_g of the pure polymer without salt added. Based on the discussion above, this is expected to be a good indicator of performance for some functional groups, while for others the trend was less clear. However, the previous analysis was using *only* T_g as a predictor, while in the regression models T_g is one of multiple features that is aggregated to predict performance. Almost equally important is the approximate molecular weight of the polymer electrolyte, which is the number-averaged molecular weight where provided, and otherwise the weight-averaged molecular weight. Previous studies have suggested molecular weight is an important factor for oligomeric systems, while it ceases to be important above a threshold value.[282] This was attributed to the link between polymer molecular weight and T_g at low molecular weights. However, the approximate molecular weight and ionic conductivity for the entire aggregate data shows only very weak correlation (Figure 7.9), suggesting that this feature is only important when combined with additional features within the regression models. Interestingly, ridge regression does not suggest polymer MW is one of the most important features, though it does extract the negative correlation between ionic conductivity and T_g.

Salt concentration is also a common feature shared in the tree-based trained models, again suggesting that in conjunction with polymer T_g and molecular weight, it can play an important role in conductivity performance. Again, ridge regression does not rank this feature in the top 10; there, it is feature 16. Nevertheless, ridge regression provides a positive (though relatively weak) correlation between salt concentration and ionic conductivity. Many studies exploring the role of salt concentration at relatively low concentrations have shown that conductivity is nonmonotonic with salt concen-

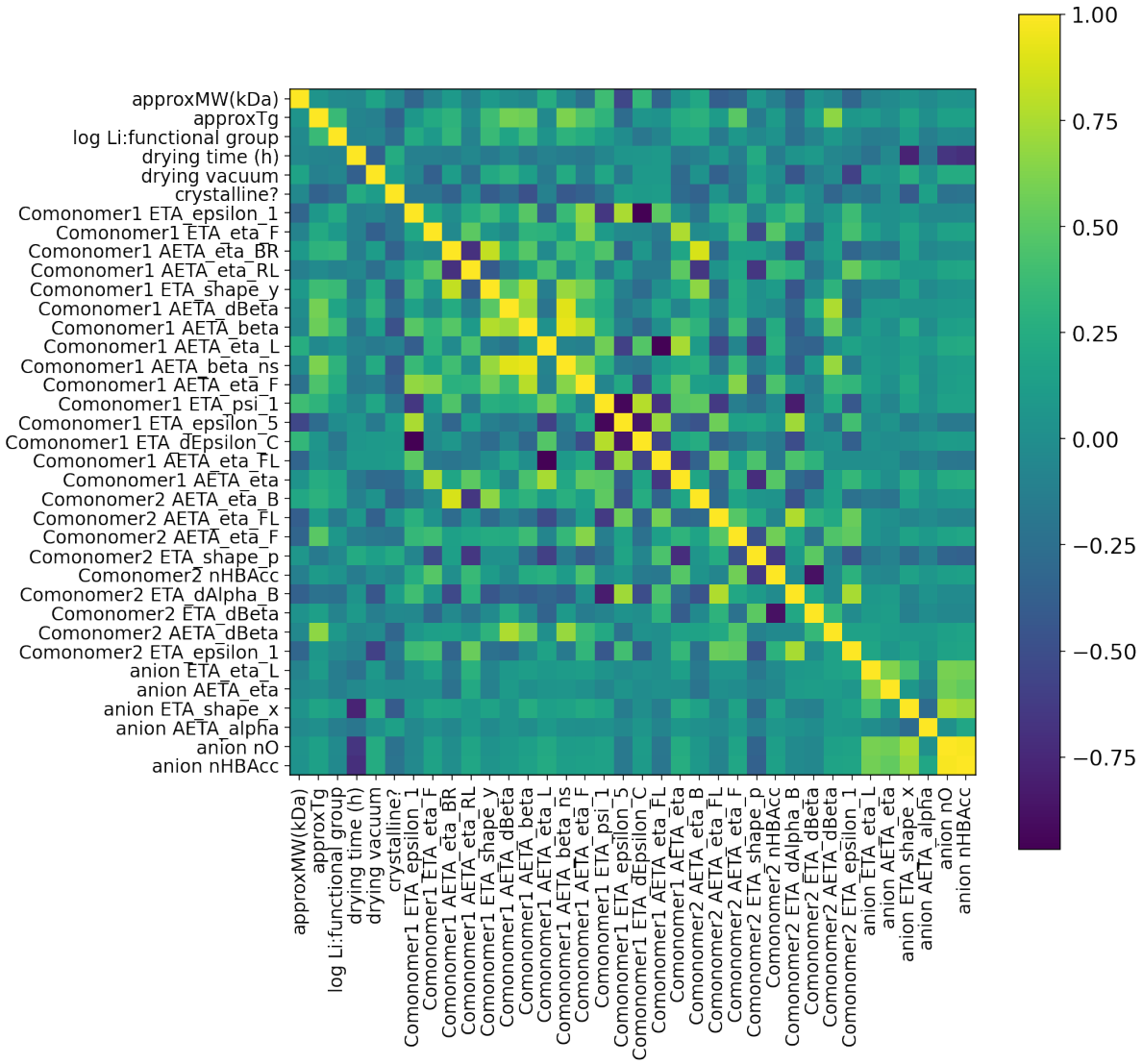

Figure 7.9: A correlation matrix of the 37 features used for statistical regression show generally weak correlations, though some monomer features are still correlated with each other, possibly slightly affecting feature importance rankings.

tration, reaching a maximum at intermediate salt concentration.[4, 213] At higher salt concentrations (e.g. over 50 wt%), another improvement in conductivity seems to occur;[32] the sign of the coefficient for ridge regression possibly emphasizes the higher overall conductivities seen at very high salt concentrations.

Monomer features also contribute to the ionic conductivity performance, and include measures of monomer complexity and presence of electronegative heteroatoms. Monomer complexity is captured through the branching coefficient ('eta BR'), measure of unsaturation ('dBeta'), and connectivity of the molecular graph ('eta'); the negative branching coefficient in ridge regression suggests less complex monomers tend to perform better. Heteroatom presence is captured through a functionality index denoting the presence of heteroatoms ('eta F'), a measure of the count of electronegative atoms in the polymer ('epsilon 5'), and a measure of hydrogen bonding or polar surface area of the monomer ('psi 1').[283, 284] Heteroatoms play an important role in salt dissociation, ion solvation and ionic conduction, and thus it is unsurprising that they dominate the monomer feature importance. However, the importance of heteroatom optimization for improved Li^+, rather than total, conductivity is not determined here because the performance metric observed in this study is total ionic conductivity.

For important anion characteristics, the measure of anion molecular bulk ('alpha'), oxygen atom count ('nO') and number of hydrogen bonding acceptors ('nHBAcc') all seem somewhat important in determing ionic conductivity. Individual studies have shown that larger anions (e.g. $TFSI^-$) dissociate more readily and result in higher ionic conductivity compared to smaller anions (e.g. ClO_4^-);[285] while the general aggregate data does not show a strong trend in conductivity versus ion identity, statistical regression confirms anion size importance on conductivity performance.

The true importance of some of the top features (averaged T_g and averaged molec-

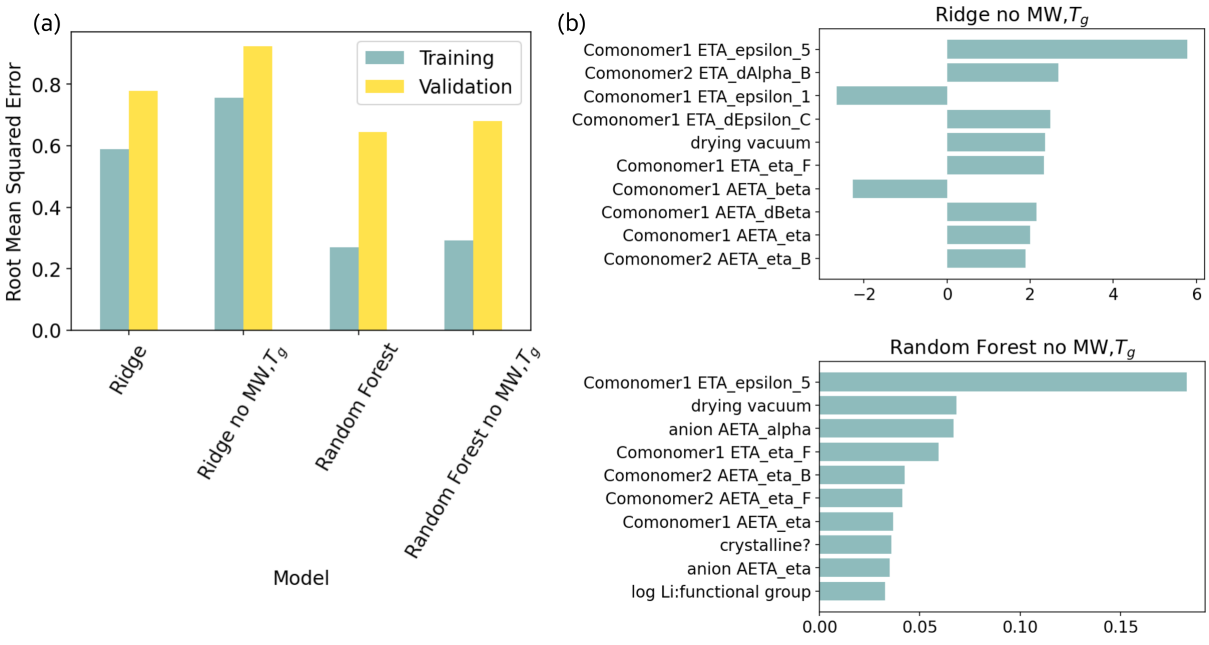

Figure 7.10: Re-training the ridge and random forest regression models after the removal of the T_g and molecular weight features leads to a small increase in root mean squared error (a), and a slight reshuffling of most important features (b), though the trends remain the same.

ular weight) is somewhat low, as can be seen by re-training ridge and RF regression models on datasets that have those features removed. The 5-fold cross-validated errors are compared to the original errors of all models in Figure 7.10a. Tabular values are given in Table 7.3. While the mean validation errors do increase, the increase is rather small, implying that other electrolyte features provide reasonably identical predictive capability. The top features still include monomer features emphasizing electronegative atom count ('epsilon 5') and heteroatom presence count ('eta F'), as well as anion molecular bulk ('alpha'), but also emphasizes drying vacuum as a processing parameter (see Figure 7.10b). It is likely that the existing correlation between the remaining features and the approximate T_g and molecualr weight is enough to provide reasonably similar predictive capabilities. This is likely caused by artifacts in feature correlations that arise in small datasets.

Notably, the ordering and importance of specific features on ionic conductivity seems to be somewhat model-dependent, and the omission of the top features does not appreciably affect model performance, underscoring the complexity and interdependence of the many features used as predictors in this study. This may be partly be explained by correlations within calculated monomer features, as well as within the calculated anion features (Figure 7.9), though trained models with and without highly correlated features showed similar predictive performance.

When models are trained without polymer-anion groupings preventing leakage between test and train, the prediction capability of the best-performing random forest regression algorithm is reasonably high, as can be seen from a plot of predicted versus actual conductivity performance of the training and final test data sets (Figure 7.11). The R^2, root mean squared error and mean absolute error are 0.74, 0.55 and 0.38, suggesting that on average the test data was predicted to 5x the actual conductivity

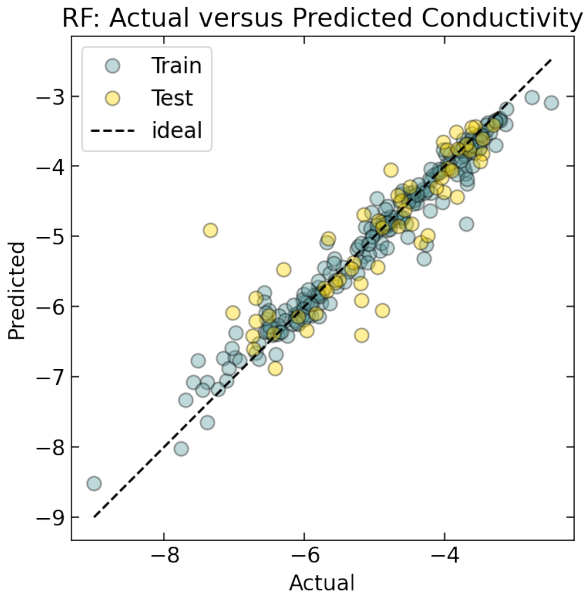

Figure 7.11: Prediction of conductivity performance can be best visualized by plotting actual versus predicted conductivity for both the training data and test data for the optimized random forest regression model. Most data falls within half an order of magnitude of the expected values, with a few outliers.

value. There are a few outliers within the data shown in Figure 7.11, but this error is within expected noise of conductivity measurements given the widely varying processing parameters and data quality that could not be accounted for in the data analysis due to lack of publication information.

Critically, however, once the dataset splitting between train, validation and test is done by grouped polymer-anion entries, model performance drops precipitously, underscoring the inability of the models to predict polymer electrolyte performance for polymer-anion combinations that they have not previously seen during training. Recursive feature elimination in this case removes all but seven features to use for model training – these are approximate T_g, approximate molecular weight, the log10 of lithium to functional group ratio (salt concentration), comonomer 2 measure of heteroatoms ('eta F'), comonomer 2 molecular graph complexity ('eta RL'), comonomer

Metric	Dummy	Ridge	Random Forest	Gradient Boosting	Extra Trees
Train					
Root Mean Squared Error	1.12	0.80	0.24	0.11	0.14
Mean Absolute Error	0.94	0.62	0.17	0.08	0.09
R^2	0	0.49	0.95	0.99	0.99
Validation					
Root Mean Squared Error	1.13	0.92	0.89	0.89	0.83
Mean Absolute Error	0.94	0.72	0.65	0.67	0.62
R^2	-0.02	0.32	0.37	0.36	0.44

Table 7.4: Cross-validated performance of all tested models when implementing polymer-anion grouped train-validation-test splitting.

2 measure of electronegative atom count ('epsilon 1'), and anion number of hydrogen bond acceptors. The model performances are shown in Table 7.4. The averaged R^2 fits for the validation sets are all less than 0.5, indicating poor predictive capability. Thus, while models perform reasonably well at understanding and predicting performance when the polymer and anion identity is not changed between the training and validation sets, once the validation set has significantly different characteristics compared to the training set, the models explored here struggle to recover predictive understanding. This suggests that perhaps the learnings obtained from a subset of polymer-anion combinations do not apply to other polymers or anions, and aligns well with the visualization results presented in Figure 7.5, where the T_g–conductivity trends of different polymer families can vary widely. The low performance of the models trained on grouped data emphasizes that such models should not be used to predict new polymer chemistries that are not related to those polymer-anion electrolyte combinations explored within the training data.

7.5 Conclusions

The analysis of aggregated data from the literature provides insight both into the applicability of design rules across a large range of polymer classes, as well as into the difficulties and uncertainties associated with data quality and quantity. While studies on individual polymer families show correlations between T_g, anion size, and ionic conductivity, the aggregated data has much weaker trends in most features known or expected to control ion conduction. Open-access web-based visualization will enable additional trends to be explored by us and other researchers. In the meantime, statistical learning on the aggregated data corroborates the importance of features such as T_g, monomer electronegative atom count, and anion size. However, the models explored here are highly susceptible to overfitting, and show only small reductions in performance when the two most important features are left out. This suggests a highly correlated network of features from which no single feature dominates the landscape. Additionally, constraining train-validation-test splittings to occur along polymer-anion groups results in poor model performance, emphasizing that the prediction and design of novel high performance polymer electrolytes is a challenging task that is not captured by the simple models or range of features explored in this study. Because of the relative lack of trends in existing databases, it is possible that other features such as processing metrics that are not commonly reported may be important in controlling ionic conductivity in these polymer systems. Future work in the field of polymer electrolytes must therefore focus on data qualtiy and completeness.

Chapter 8

Conclusion and Outlook

The field of ion-transporting polymers is highly active, with rich research detailing both fundamental understanding of ion motion and ion-polymer interactions, as well as more applied research exploring performance improvements for applications. This dissertation spans both fundamental and applied aspects of polymer electrolytes, beginning with mechanistic studies of the interplay between polymer mechanics and ionic conductivity in metal−ligand systems (Chapters 2 and 3), and transitioning towards design principles that can be used to improve conductivity performance (Chapters 4, 5 and 6). Metal-ligand coordinating polymers were previously explored for their self-healing and tunable mechanical characteristics, but had been overlooked as potential ion conductors. We therefore began by identifying key design criteria for metal−ligand ion-conducting polymers, exploring the fundamental connections between ion identity, ion mobility and polymer mechanics. Importantly, we emphasized the ability for multivalent cations to contribute to the ionic conductivity even while their individual

Reproduced in part with permission from [164]: N. S. Schauser, R. Seshadri, and R. A. Segalman. Multivalent Ion Conduction in Solid Polymer Systems. *Mol. Syst. Des. Eng.*, 4, 263 (2019). DOI: 10.1039/c8me00096d Copyright 2019 Royal Society of Chemistry.

mobility is lower than a monovalent cation, due to the higher valency of the ion.

A key question for polymer electrolyte design is how to achieve high ion concentration while concurrently increasing mono- or multivalent ion mobility. This requires controlling salt dissociation separately from ion mobility within the polymer matrix. Traditional polymer electrolyte design does not decouple these two factors, as the species within the polymer that improve salt dissociation also bind tightly to the cation. Ion concentration is controlled by both the choice of counterion as well as by the polymer dielectric environment, while ion mobility depends on the identity of the cation and the design of the coordinating ligand. Increasing ion mobility requires improving the frequency of ion exchange between coordination sites in a polymer matrix, which is especially challenging for multifunctional ions which interact with multiple sites within a polymer at once. The use of metal−ligand coordination polymers enables some of these factors to be decoupled, as shown in Chapter 4.

The complexity of the synthetic considerations as discussed in Chapters 4, 5, 6 and 7 illustrates the challenge in the directed design of mono- and multivalent conducting polymer electrolytes. A majority of the polymer electrolyte literature focuses on ether-based polymers, though a growing number of studies on alternative chemistries exist and illustate that polymer chemistries less dependent on ether solvation chemistry provide differing mechanisms for ion conduction and thus different design rules.[32, 164] Opportunities exist for computational studies to screen for promising candidates for multivalent conduction by identifying systems for which ion-polymer interactions are labile, and aggregation is low or solvation structures enable percolated networks for ion transport (as shown in Chapter 4). The lability of metal-polymer interactions can be tuned by using different coordinating groups whose geometry or strength of interaction may increase the kinetics of ligand exchange − this is emphasized as a promising

route towards future conductivity performance improvements for metal−ligand polymer electrolytes. While ligand exchange kinetics have been measured for a variety of divalent species and small-molecule ligands in aqueous solution, such trends may not translate to dry polymer systems[55] since exchange in aqueous solution is typically dominated by water molecules (see discussion in Chapter 3).[5] Hard-soft acid-base theory can be used as a predictor for the binding strength of multivalent cations to various potential ligands, although factors including the ligand-field stabilization energy are important for transition metal complexes. An understanding of ion transport mechanism can also be gained from a look at the activation energy (E_a) for ionic conductivity as a function of temperature; most polymers follow a VFT temperature-dependence above their T_g and Arrhenius behavior below T_g. Higher E_a suggests more hindered ion motion, as discussed in Chapter 7. Still, few polymer studies calculate E_a; improved reporting and analysis of the E_a of ion transport for mono- and multivalent systems could shed light on favorable polymer chemistries for cation transport.

Multivalent metal−ligand coordinating polymer electrolytes present opportunities for mechanical property enhancement compared to their monovalent counterparts. As we show in Chapter 3, the inclusion of multivalent metal−ligand coordination interactions within a polymer matrix presents significant enhancement of bulk mechanical properties, with minimal effects on the total ionic conductivity.[5] However, further work in such systems must be performed to identify the extent of cation mobility in a system where it also acts as a dynamic cross-linker. The ability for some cations, such as Ni^{2+} or Fe^{3+}, to dramatically enhance mechanical properties could also be used orthogonally, with the addition of those cations for the sole purpose of enhancing polymer mechanics while the ions of interest (e.g. Li^{+}, Mg^{2+}, or Zn^{2+}) are added separately for ionic conductivity. Further opportunities exist in the realm of block copolymers, both

in terms of conventional block copolymers with salt addition and single-ion work. The synthetic strategies mentioned above can be employed for the ion-containing block, while an inert block is added for mechanical stability.

An ongoing issue in the field of polymer electrolytes is the difficulty in measuring the cation contribution to conductivity, which is the relevant metric for many applications. To determine the efficacy of synthetic strategies in improving cation mobility, it must be possible to accurately measure the contribution of multivalent cations to the measured total conductivity. Transference number measurements using traditional techniques are extremely variable, likely because the underlying assumptions of ideal electrolytes with dissociated ions are not valid for most polymer electrolytes. In this dissertation, we have chosen to focus on NMR pulsed-field-gradient techniques as an initial estimate for ion mobility. This technique is not without its own limitations, however, especially for many of the multivalent ions due to their paramagnetic nature. Emerging techniques pioneered in other research groups should provide additional opportunities for studying these materials.[57, 58, 61, 62] The crucial issue of transference number measurements should not be taken lightly by the community, and additional research efforts must focus on expanding the toolkit for probing cation conductivity contributions.

Improving cation contribution to the conductivity can be achieved in multiple ways – in this dissertation we show one route towards tuning Li^+ t_+, namely removing functional groups that can exhibit unintended binding sites for cation entrapment (Chapter 6). The design of a tunable polymer platform requires the incorporation of linkages for polymer functionalization; we show that these linkages can play a critical role in affecting both polymer T_g and cation mobility through unintended ion binding. The removal of the amide linkage for our imidazole-grafted siloxane electrolytes improved

room-temperature ionic conductivity by 2 orders of magnitude, and approximately doubled Li^+ t_+ from 0.24 to 0.46.

It is also possible to design polymers in which the solvating groups primarily interact with the anion rather than cation species through the addition of either Lewis-acidic moieties into the polymer[239, 286] or other groups that preferentially solvate specific anions, such as fluorination of the polymer backbone to sequester fluorinated anions.[277] A PEO-based network with boroxine ring crosslinkers acts as an anion trap and increases Li^+ transference numbers to 0.75 for bulky salts such as $LiCF_3SO_3$ and $LiBF_4$, with additional improvement to 0.88 for LiCl.[287] Similar studies were performed for borate ester networks mixed with Mg^{2+} salts with perchlorate, triflate and $TFSI^-$ anions.[288, 289] Ionic conductivities on the order of $10^{-5}\,S\,cm^{-1}$ were measured at room temperature, and transference numbers ranged from 0.20 to 0.51 with smaller anions showing better transference numbers but lower conductivity at equivalent temperatures. Increasing the concentration of anion traps also increases the transference number. The transference number measurements were performed using DC polarization without adjustment for interfacial resistance changes over time and could thus be inaccurate, though the general trends between the studied anions and boron concentrations should still hold. Further work in this area could provide promising performance improvements for multivalent polymer electrolytes.

Identifying the connectivity of solvation sites through the polymer can also play a large role in screening for polymer candidates. One such study performed for Li-polyether conductors was influential in determining that the reason for the high conductivity of PEO over other polyethers and esters was due to the high percolation of solvation sites in PEO which result in more facile Li^+ transport.[138] This ambitious study highlights the complexity of designing a polymer electrolyte from the ground up; specif-

ically, the effects of segmental dynamics, solvation strength, and solvation connectivity interact synergistically to determine ultimate conductivity. Thus, electrolyte design cannot solely focus on the incorporation of labile coordinating moieties, high dielectric constant and high segmental dynamics, but must also consider polymer architecture and its effect on the proximity of neighboring solvation sites for ion transport. On the other hand, we have shown that the side-chain-grafted metal−ligand electrolytes studied in this dissertation seem to all exhibit percolating ionic domains, enabling decoupling of backbone design from ligand considerations (Chapter 4). This is a possible route for simplifying electrolyte design considerations, and enabling step-wise improvements in design features and performance, as exhibited in this thesis (see Chapters 5 and 6). Characterizing similar solvation trends for alternative polymer chemistries and architectures would enable screening for possible candidates before investing significant synthetic effort.

There is also the option to circumvent transference number measurement questions completely through the design of single-ion conductors. Significant effort in the field of single-ion conductors has focused on lithium,[290] while very few studies have focused on multivalent single-ion conducting polymers.[142, 291] For monovalent systems, it is known that improving cation mobility through dissociation from the anion is critical for enhancing conductivity,[292] as is reducing the glass transition temperature of the polymer. It is currently common practice to tether a $TFSI^-$ anion to a polystyrene-based backbone, though work on lower T_g backbones has been reported,[293, 294] as has the use of different tethered anions such as sulfonates[174] or borates.[295, 296] The more delocalized the anion, the higher the conductivity due to improved cation mobility;[292] thus sulfonates or carboxylates are not a great choice and result in lower conductivities,[297, 298] while the use of delocalized tethered anions has en-

abled ionic conductivities on the order of 10^{-4} S cm^{-1} at 90 °C.[292] The addition of a small molecule complex containing boron ($BF_3.OEt_2$) enabled improved dissociation of Li^+ from a carbonate anion-tethered polymer due to preferential boron-anion interactions.[298] A recent review summarizes advances and future opportunities for lithium-based single-ion conductors.[290] Similar concepts can be applied for multivalent systems, with the additional caveat that dynamic ionic crosslinking between cations and anions from multiple chains may play an important role in polymer segmental dynamics. The incorporation of solvating groups within the polymer that can preferentially interact with the cation species to enhance dissociation but enable mobility will be critical, as will the proximity between anion and solvating groups.[297]

The complex nature of the design criteria described above and explored in this dissertation highlights the importance of data reporting and complete characterization. Most publications on polymer electrolytes focus on total ionic conductivity measurements, without providing full details of polymer characteristics, processing conditions, structural (e.g. ion aggregation) considerations, or transport measurements. This creates significant challenges in extracting unifying trends from the large body of work that has been performed on even just Li^+-conducting polymer electrolytes, as is explored in Chapter 7. We therefore emphasize the need for more complete reporting in publications.

Finally, the design rules for mono- and multivalent polymer electrolytes explored within this dissertation present hope for improved polymer electrolyte performance by revealing that metal−ligand coordination polymers enable the decoupling of many of the properties previously shown to be intimately linked. The model system designed and explored in this thesis presents a starting point for conductivity improvements; while the individual performance metrics for the polymers in this work are lower than

necessary for applications, they set the groundwork for future performance improvements that could be achieved by tuning ligand chemistry, backbone identity, polymer architecture and, possibly, additives.

Bibliography

[1] J.-M. Tarascon and M. Armand. Issues and Challenges Facing Rechargeable Lithium Batteries. *Nature*, 414, 359 (2001).

[2] J. B. Goodenough and Y. Kim. Challenges for Rechargeable Li Batteries. *Chem. Mater.*, 22, 587 (2010).

[3] D. E. Fenton, J. M. Parker, and P. V. Wright. Complexes of Alkali Metal Ions with Poly(ethylene Oxide). *Polymer (Guildf).*, 14, 589 (1973).

[4] G. E. Sanoja, N. S. Schauser, J. M. Bartels, C. M. Evans, M. E. Helgeson, R. Seshadri, and R. A. Segalman. Ion Transport in Dynamic Polymer Networks Based on Metal–Ligand Coordination: Effect of Cross-Linker Concentration. *Macromolecules*, 51, 2017 (2018).

[5] N. S. Schauser, G. E. Sanoja, J. M. Bartels, S. K. Jain, J. G. Hu, S. Han, L. M. Walker, M. E. Helgeson, R. Seshadri, and R. A. Segalman. Decoupling Bulk Mechanics and Mono- and Multivalent Ion Transport in Polymers Based on Metal-Ligand Coordination. *Chem. Mater.*, 30(16), 5759 (2018).

[6] M. Guo, M. Zhang, D. He, J. Hu, X. Wang, C. Gong, X. Xie, and Z. Xue. Comb-like Solid Polymer Electrolyte Based on Polyethylene glycol-Grafted Sulfonated Polyether ether ketone. *Electrochim. Acta*, 255, 396 (2017).

[7] J. Ping, H. Pan, P. Hou, M.-Y. Zhang, X. Wang, C. Wang, J. Chen, D. Wu, Z. Shen, and X.-H. Fan. Solid Polymer Electrolytes with Excellent High-Temperature Properties Based on Brush Block Copolymers Having Rigid Side Chains. *ACS Appl. Mater. Interfaces*, 9, 6130 (2017).

[8] G. Zardalidis, A. Pipertzis, G. Mountrichas, S. Pispas, M. Mezger, and G. Floudas. Effect of Polymer Architecture on the Ionic Conductivity. Densely Grafted Poly(ethylene oxide) Brushes Doped with LiTf. *Macromolecules*, 49, 2679 (2016).

[9] M. K. Stowe, P. Liu, and G. L. Baker. Star Poly(ethylene oxide) as a Low Temperature Electrolyte and Crystallization Inhibitor. *Chem. Mater.*, 17, 6555 (2005).

[10] M. Singh, O. Odusanya, G. M. Wilmes, H. B. Eitouni, E. D. Gomez, A. J. Patel, V. L. Chen, J. Park, P. Fragouli, H. Iatrou, N. Hadjichristidis, D. Cookson, and N. P. Balsara. Effect of Molecular Weight on the Mechanical and Electrical Properties of Block Copolymer Electrolytes. *Macromolecules*, 40, 4578 (2007).

[11] A. Panday, S. Mullin, E. D. Gomez, N. Wanakule, V. L. Chen, A. Hexemer, J. Pople, and N. P. Balsara. Effect of Molecular Weight and Salt Concentration on Conductivity of Block Copolymer Electrolytes. *Macromolecules*, 42, 4632 (2009).

[12] T. H. Epps, T. S. Bailey, R. Waletzko, and F. S. Bates. Phase Behavior and Block Sequence Effects in Lithium Perchlorate-Doped Poly(isoprene-b-styrene-b-ethylene oxide) and Poly(styrene-b-isoprene-b-ethylene oxide) Triblock Copolymers. *Macromolecules*, 36, 2873 (2003).

[13] T. Fujinami, A. Tokimune, M. A. Mehta, D. F. Shriver, and G. C. Rawsky. Siloxyaluminate Polymers with High Li+ Ion Conductivity. *Chem. Mater.*, 9, 2236 (1997).

[14] R. Khurana, J. L. Schaefer, L. A. Archer, and G. W. Coates. Suppression of Lithium Dendrite Growth Using Cross-Linked Polyethylene/Poly(ethylene oxide) Electrolytes: A New Approach for Practical Lithium-Metal Polymer Batteries. *J. Am. Chem. Soc.*, 136, 7395 (2014).

[15] C.-X. Zu and H. Li. Thermodynamic Analysis on Energy Densities of Batteries. *Energy Environ. Sci.*, 4, 2614 (2011).

[16] C. Monroe and J. Newman. The Impact of Elastic Deformation on Deposition Kinetics at Lithium/Polymer Interfaces. *J. Electrochem. Soc.*, 152, A396 (2005).

[17] P. G. Bruce, S. A. Freunberger, L. J. Hardwick, and J. M. Tarascon. LiO2 and LiS Batteries with High Energy Storage (2012). doi: 10.1038/nmat3191.

[18] K. M. Abraham and Z. Jiang. A Polymer Electrolyte-Based Rechargeable Lithium/Oxygen Battery. *J. Electrochem. Soc.*, 143(1) (1996).

[19] J. Muldoon, C. B. Bucur, and T. Gregory. Quest for Nonaqueous Multivalent Secondary Batteries: Magnesium and Beyond. *Chem. Rev.*, 114, 11683 (2014).

[20] C. B. Bucur. Confession of a Magnesium Battery. *J. Phys. Chem. Lett.*, 6, 3578 (2015).

[21] C. Xu, B. Li, H. Du, and F. Kang. Energetic Zinc Ion Chemistry: The Rechargeable Zinc Ion Battery. *Angew. Chemie Int. Ed.*, 51, 933 (2012).

[22] H. Kim, G. Jeong, Y.-U. Kim, J.-H. Kim, C.-M. Park, and H.-J. Sohn. Metallic Anodes for Next Generation Secondary Batteries. *Chem. Soc. Rev.*, 42, 9011 (2013).

[23] Z. Rong, R. Malik, P. Canepa, G. S. Gautam, M. Liu, A. Jain, K. A. Persson, and G. Ceder. Materials Design Rules for Multivalent Ion Mobility in Intercalation Structures. *Chem. Mater.*, 27, 6016 (2015).

[24] P. Saha, M. Kanchan Datta, O. I. Velikokhatnyi, A. Manivannan, D. Alman, and P. N. Kumta. Rechargeable Magnesium Battery: Current Status and Key Challenges for the Future. *Prog. Mater. Sci.*, 66, 1 (2014).

[25] D. Aurbach, Y. Gofer, Z. Lu, A. Schechter, O. Chusid, H. Gizbar, Y. Cohen, V. Ashkenazi, M. Moshkovich, R. Turgeman, and E. Levi. A Short Review on the Comparison Between Li Battery Systems and Rechargeable Magnesium Battery Technology. *J. Power Sources*, 97, 28 (2001).

[26] M. A. Ratner and D. F. Shriver. Ion Transport in Solvent-Free Polymers. *Chem. Rev.*, 88, 109 (1988).

[27] D. T. Hallinan and N. P. Balsara. Polymer Electrolytes. *Annu. Rev. Mater. Res.*, 43, 503 (2013).

[28] M. Park, X. Zhang, M. Chung, G. B. Less, and A. M. Sastry. A review of conduction phenomena in Li-ion batteries. *J. Power Sources*, 195, 7904 (2010).

[29] M. Doyle, T. F. Fuller, and J. Newman. The Importance of the Lithium Ion Transference Number in Lithium/Polymer Cells. *Electrochim. Acta*, 39, 2073 (1994).

[30] A. Ab Aziz and Y. Tominaga. Magnesium Ion-Conductive Poly(ethylene carbonate) Electrolytes. *Ionics (Kiel).*, 303 (2018).

[31] K. Kimura, J. Motomatsu, and Y. Tominaga. Correlation between Solvation Structure and Ion-Conductive Behavior of Concentrated Poly(ethylene carbonate)-Based Electrolytes. *J. Phys. Chem. C*, 120, 12385 (2016).

[32] J. Mindemark, M. J. Lacey, T. Bowden, and D. Brandell. Beyond PEO - Alternative Host Materials for Li+-Conducting Solid Polymer Electrolytes. *Prog. Polym. Sci.*, 81, 114 (2018).

[33] J. S. Newman and K. E. Thomas-Alyea. *Electrochemical systems*. J. Wiley (2004). ISBN 9780471477563.

[34] I. Nakamura. Ion Solvation in Polymer Blends and Block Copolymer Melts: Effects of Chain Length and Connectivity on the Reorganization of Dipoles. *J. Phys. Chem. B*, 118, 5787 (2014).

[35] L. Liu and I. Nakamura. Solvation Energy of Ions in Polymers: Effects of Chain Length and Connectivity on Saturated Dipoles near Ions. *J. Phys. Chem. B*, 121, 3142 (2017).

[36] B. L. Papke, R. Dupon, M. A. Ratner, and D. F. Shriver. Ion-Pairing in Polyether Solid Electrolytes and its Influence on Ion Transport. *Solid State Ionics*, 5, 685 (1981).

[37] B. K. Wheatle, J. R. Keith, S. Mogurampelly, N. A. Lynd, and V. Ganesan. Influence of Dielectric Constant on Ionic Transport in Polyether- Based Electrolytes. *ACS Macro Lett.*, 6, 1362 (2017).

[38] L. M. Hall, M. J. Stevens, and A. L. Frischknecht. Effect of Polymer Architecture and Ionic Aggregation on the Scattering Peak in Model Ionomers. *Phys. Rev. Lett.*, 106, 127801 (2011).

[39] K. S. I. Mongcopa, M. Tyagi, J. P. Mailoa, G. Samsonidze, B. Kozinsky, S. A. Mullin, D. A. Gribble, H. Watanabe, and N. P. Balsara. Relationship between Segmental Dynamics Measured by Quasi-Elastic Neutron Scattering and Conductivity in Polymer Electrolytes. *ACS Macro Lett.*, 7, 504 (2018).

[40] A. Maitra and A. Heuer. Cation Transport in Polymer Electrolytes: A Microscopic Approach. *Phys. Rev. Lett.*, 98, 227802 (2007).

[41] J. C. Dyre, P. Maass, B. Roling, and D. L. Sidebottom. Fundamental Questions Relating to Ion Conduction in Disordered Solids. *Reports Prog. Phys.*, 72, 046501 (2009).

[42] V. Ganesan, V. Pyramitsyn, C. Bertoni, and M. Shah. Mechanisms Underlying Ion Transport in Lamellar Block Copolymer Membranes. *ACS Macro Lett.*, 1, 513 (2012).

[43] V. Bocharova and A. P. Sokolov. Perspectives for Polymer Electrolytes: A View from Fundamentals of Ionic Conductivity. *Macromolecules* (2020).

[44] F. Kremer and A. Schoenhals, editors. *Broadband Dielectric Spectroscopy*. Springer-Verlag, Heidelberg (2003).

[45] A. von Hippel. *Dielectrics and Waves*. Artech House, Boston (1995).

[46] E. Gileadi. *Physical Electrochemistry: Fundamentals, Techniques and Applications*. Wiley-VCH (2013).

[47] M. Lacey. Transport and Transference in Battery Electrolytes.

[48] Q. Zheng, D. M. Pesko, B. M. Savoie, K. Timachova, A. L. Hasan, M. C. Smith, T. F. Miller, G. W. Coates, and N. P. Balsara. Optimizing Ion Transport in Polyether-Based Electrolytes for Lithium Batteries. *Macromolecules*, 51, 2847 (2018).

[49] D. M. Pesko, K. Timachova, R. Bhattacharya, M. C. Smith, I. Villaluenga, J. Newman, and N. P. Balsara. Negative Transference Numbers in Poly(ethylene oxide)-Based Electrolytes. *J. Electrochem. Soc.*, 164, E3569 (2017).

[50] M. Doyle and J. Newman. Analysis of Transference Number Measurements Based on the Potentiastatic Polarization of Solid Polymer Electrolytes. *J. Electrochem. Soc.*, 142, 3465 (1995).

[51] P. G. Bruce and C. A. Vincent. Effect of Ion Association on Transport in Polymer Electrolytes. *Faraday Discuss. Chem. Soc.*, 88, 43 (1989).

[52] P. G. Bruce and C. A. Vincent. Steady State Current Flow in Solid Binary Electrolyte Cells. *J. Electroanal. Chem.*, 225, 1 (1987).

[53] S. Passerini, R. Curini, and B. Scrosati. Characterization of Poly(ethylene Oxide) Copper Salt Polymer Electrolytes. *Appl. Phys. A*, 49, 425 (1989).

[54] P. G. Bruce, F. Krok, and C. A. Vincent. Preparation and Characterisation of PEO-Hg(ClO4)2 Complexes and Some Thoughts on Ion Transport in Polymer Electrolytes. *Solid State Ionics*, 27, 81 (1988).

[55] A. F. Cotton and G. Wilkinson. *Advanced Inorganic Chemistry*. John Wiley & Sons, Singapore, 5 edition (1988).

[56] K. M. Anilkumar, B. Jinisha, M. Manoj, and S. Jayalekshmi. Poly(ethylene oxide) (PEO) – Poly(vinyl pyrrolidone) (PVP) Blend Polymer Based Solid Electrolyte Membranes for Developing Solid State Magnesium Ion Cells. *Eur. Polym. J.*, 89, 249 (2017).

[57] N. P. Balsara and J. Newman. Relationship between Steady-State Current in Symmetric Cells and Transference Number of Electrolytes Comprising Univalent and Multivalent Ions. *J. Electrochem. Soc.*, 162, A2720 (2015).

[58] Y. Ma, M. Doyle, T. F. Fuller, M. M. Doeff, L. C. De Jonghe, and J. Newman. The Measurement of a Complete Set of Transport Properties for a Concentrated Solid Polymer Electrolyte Solution. *J. Electrochem. Soc.*, 142, 1859 (1995).

[59] W. Gorecki, M. Jeannin, E. Belorizky, C. Roux, and M. Armand. Physical Properties of Solid Polymer Electrolyte PEO(LiTFSI) Complexes. *J. Phys. Condens. Matter*, 7, 6823 (1995).

[60] K. Timachova, H. Watanabe, and N. P. Balsara. Effect of Molecular Weight and Salt Concentration on Ion Transport and the Transference Number in Polymer Electrolytes. *Macromolecules*, 48, 7882 (2015).

[61] C. S. Johnson and Q. He. Electrophoretic Nuclear Magnetic Resonance. *Adv. Magn. Opt. Reson. Magn.*, 13, 131 (1989).

[62] M. Gouverneur, F. Schmidt, and M. Schoenhoff. Negative Effective Li Transference Numbers in Li Salt/Ionic Liquid Misctures: Does Li Drift in the "Wrong" Direction? *Phys. Chem. Chem. Phys.*, 20, 7470 (2018).

[63] L. Leibler, J. M. Rubinstein, and R. H. Colby. Dynamics of Reversible Networks. *Macromolecules*, 24, 4701 (1991).

[64] F. Tanaka and S. F. Edwards. Viscoelastic Properties of Physically Crosslinked Networks. 1. Transient Network Theory. *Macromolecules*, 25, 1516 (1992).

[65] Q. Chen, G. J. Tudryn, and R. H. Colby. Ionomer Dynamics and the Sticky Rouse Model. *J. Rheol. (N. Y. N. Y).*, 57, 1441 (2013).

[66] M. Doi and S. F. Edwards. *The Theory of Polymer Dynamics*. Clarendon Press (1988).

[67] M. Rubinstein and A. N. Semenov. Dynamics of Entangled Solutions of Associating Polymers. *Macromolecules*, 34, 1058 (2001).

[68] S. C. Grindy, M. Lenz, and N. Holten-Andersen. Engineering Elasticity and Relaxation Time in Metal-Coordinate Cross-Linked Hydrogels. *Macromolecules*, 49, 8306 (2016).

[69] D. Mozhdehi, J. A. Neal, S. C. Grindy, Y. Cordeau, S. Ayala, N. Holten-Andersen, and Z. Guan. Tuning Dynamic Mechanical Response in Metallopolymer Networks through Simultaneous Control of Structural and Temporal Properties of the Networks. *Macromolecules*, 49(17), 6310 (2016).

[70] S. Tang and B. D. Olsen. Relaxation Processes in Supramolecular Metallogels Based on Histidine-Nickel Coordination Bonds. *Macromolecules*, 49, 9163 (2016).

[71] D. E. Fullenkamp, L. He, D. G. Barrett, W. R. Burghardt, and P. B. Messersmith. Mussel-Inspired Histidine-Based Transient Network Metal Coordination Hydrogels. *Macromolecules*, 46, 1167 (2013).

[72] R. Groote, B. M. Szyja, E. A. Pidko, E. J. M. Hensen, and R. P. Sijbesma. Unfolding and Mechanochemical Scission of Supramolecular Polymers Containing a MetalÀLigand Coordination Bond. *Macromolecules*, 44, 9187 (2011).

[73] E. Filippidi, T. R. Cristiani, C. D. Eisenbach, J. H. Waite, J. N. Israelachvili, B. Kollbe Ahn, and M. T. Valentine. Toughening Elastomers Using Mussel- Inspired Iron-Catechol Complexes. *Science (80-.).*, 358, 502 (2017).

[74] J. M. G. Cowie and K. Sadaghianizadeh. Effect of Crosslinking on the A.C. Conductivity of Poly(3,6,9,12-tetraoxatridec-1-ene)/Lithium Perchlorate Mixtures. *Polymer (Guildf).*, 30, 509 (1989).

[75] D. Mozhdehi, S. Ayala, O. R. Cromwell, and Z. Guan. Self-Healing Multiphase Polymers via Dynamic Metal-Ligand Interactions. *J. Am. Chem. Soc.*, 136, 16128 (2014).

[76] S. C. Grindy, R. Learsch, D. Mozhdehi, J. Cheng, D. G. Barrett, Z. Guan, P. B. Messersmith, and N. Holten-Andersen. Control of Hierarchical Polymer Mechanics with Bioinspired Metal-Coordination Dynamics. *Nat. Mater.*, 14, 1210 (2015).

[77] J. H. Jung, J. H. Lee, J. R. Silverman, and G. John. Coordination Polymer Gels with Important Environmental and Biological Applications. *Chem. Soc. Rev.*, 42(3), 924 (2013).

[78] P. Cordier, F. Tournilhac, C. Soulié-Ziakovic, and L. Leibler. Self-Healing and Thermoreversible Rubber from Supramolecular Assembly. *Nature*, 451, 977 (2008).

[79] M. Guo, L. M. Pitet, H. M. Wyss, M. Vos, P. Y. W. Dankers, and E. W. Meijer. Tough Stimuli-Responsive Supramolecular Hydrogels with Hydrogen-Bonding Network Junctions. *J. Am. Chem. Soc.*, 136, 6969 (2014).

[80] J. N. Hunt, K. E. Feldman, N. A. Lynd, J. Deek, L. M. Campos, J. M. Spruell, B. M. Hernandez, E. J. Kramer, and C. J. Hawker. Tunable, High Modulus Hydrogels Driven by Ionic Coacervation. *Adv. Mater.*, 23, 2327 (2011).

[81] M. Lemmers, J. Sprakel, I. K. Voets, J. van der Gucht, and M. A. Cohen Stuart. Multiresponsive Reversible Gels Based on Charge-Driven Assembly. *Angew. Chemie Int. Ed.*, 49, 708 (2010).

[82] N. Holten-Andersen, M. J. Harrington, H. Birkedal, B. P. Lee, P. B. Messersmith, K. Y. Lee, and J. H. Waite. pH-Induced Metal-Ligand Cross-Links Inspired by Mussel Yield Self-Healing Polymer Networks with Near-Covalent Elastic Moduli. *Proc. Natl. Acad. Sci. U. S. A.*, 108, 2651 (2011).

[83] W. C. Yount, D. M. Loveless, and S. L. Craig. Strong Means Slow: Dynamic Contributions to the Bulk Mechanical Properties of Supramolecular Networks. *Angew. Chemie Int. Ed.*, 44, 2746 (2005).

[84] E. A. Appel, F. Beidermann, U. Rauwald, S. T. Jones, J. M. Zayed, and O. A. Scherman. Supramolecular Cr with oss-Linked Networks via Host-Guest Complexation with Cucurbit[8]uril. *J. Am. Chem. Soc.*, 132, 14251 (2010).

[85] A. Harada, R. Kobayashi, Y. Takashima, A. Hashidzume, and H. Yamaguchi. Macroscopic Self-Assembly through Molecular Recognition. *Nat. Chem.*, 3, 34 (2011).

[86] P. Alexandridis, J. F. Holzwarth, and T. A. Hatton. Micellization of Poly(ethylene oxide)-Poly(propylene oxide)-Poly(ethylene oxide) Triblock Copolymers in Aqueous Solutions: Thermodynamics of Copolymer Association. *Macromolecules*, 27, 2414 (1994).

[87] W. A. Petka, J. L. Harden, K. P. McGrath, D. Wirtz, and D. A. Tirrell. Reversible Hydrogels from Self-Assembling Artificial Proteins. *Science (80-.).*, 281, 389 (1998).

[88] M. S. Green and A. V. Tobolsky. A New Approach to the Theory of Relaxing Polymeric Media. *J. Chem. Phys.*, 12, 80 (1946).

[89] C. Wang, H. Wu, Z. Chen, M. T. McDowell, Y. Cui, and Z. Bao. Self-Healing Chemistry Enables the Stable Operation of Silicon Microparticle Anodes for High-Energy Lithium-Ion Batteries. *Nat. Chem.*, 5, 1042 (2013).

[90] R. Stadler. Transient networks by hydrogen bond interactions in polybutadiene-melts. In *Perm. Transient Networks*, pages 140–145. Steinkopff, Darmstadt (1987).

[91] R. Langer and D. A. Tirrell. Designing Materials for Biology and Medicine. *Nature*, 428, 487 (2004).

[92] K. A. Williams, D. R. Dreyer, and C. W. Bielawski. The Underlying Chemistry of Self-Healing Materials. *MRS Bull.*, 33, 759 (2008).

[93] J.-Y. Sun, X. Zhao, W. R. K. Illeperuma, O. Chaudhuri, K. H. Oh, D. J. Mooney, J. J. Vlassak, and Z. Suo. Highly Stretchable and Tough Hydrogels. *Nature*, 489, 133 (2012).

[94] C. Creton. 50th Anniversary Perspective: Networks and Gels: Soft but Dynamic and Tough. *Macromolecules*, 50, 8297 (2017).

[95] W. C. Yount, D. M. Loveless, and S. L. Craig. Small-Molecule Dynamics and Mechanisms Underlying the Macroscopic Mechanical Properties of Coordinatively Cross-Linked Polymer Networks. *J. Am. Chem. Soc.*, 127, 14488 (2005).

[96] W. Shen, J. A. Kornfield, and D. A. Tirrell. Dynamic Properties of Artificial Protein Hydrogels Assembled through Aggregation of Leucine Zipper Peptide Domains. *Macromolecules*, 40, 689 (2007).

[97] D. D. McKinnon, D. W. Domaille, J. N. Cha, and K. S. Anseth. Bis-Aliphatic Hydrazone-Linked Hydrogels Form Most Rapidly at Physiological pH: Identifying the Origin of Hydrogel Properties with Small Molecule Kinetic Studies. *Chem. Mater.*, 26, 2382 (2014).

[98] R. Wang, M. K. Sing, R. K. Avery, B. S. Souza, M. Kim, and B. D. Olsen. Classical Challenges in the Physical Chemistry of Polymer Networks and the Design of New Materials. *Acc. Chem. Res.*, 49, 2786 (2016).

[99] T. F. Miller, Z. G. Wang, G. W. Coates, and N. P. Balsara. Designing Polymer Electrolytes for Safe and High Capacity Rechargeable Lithium Batteries. *Acc. Chem. Res.*, 50, 590 (2017).

[100] W. M. Deen. *Analysis of Transport Phenomena*. Oxford University Press, 2 edition (2012).

[101] J. E. Letter and R. B. Jordan. Kinetic Study of the Complexing of Nickel(II) by Imidazole, Histidine, and Histidine Methyl Ester. *Inorg. Chem.*, 10, 2692 (1971).

[102] R. J. Sundberg and R. Bruce Martin. Interactions of Histidine and Other Imidazole Derivatives with Transition Metal Ions in Chemical and Biological Systems. *Chem. Rev.*, 74, 471 (1974).

[103] H. Ohno and K. Ito. Room-Temperature Molten Salt Polymers as a Matrix for Fast Ion Conduction. *Chem. Lett.*, 27, 751 (1998).

[104] D. Salas de la Cruz, M. D. Green, Y. Ye, Y. A. Elabd, T. E. Long, and K. I. Winey. Correlating Backbone-to-Backbone Distance to Ionic Conductivity in Amorphous Polymerized Ionic Liquids. *J. Polym. Sci. Part B Polym. Phys.*, 50, 338 (2012).

[105] U. H. Choi, Y. Ye, D. Salas De La Cruz, W. Liu, K. I. Winey, Y. A. Elabd, J. Runt, and R. H. Colby. Dielectric and Viscoelastic Responses of Imidazolium-Based Ionomers with Different Counterions and Side Chain Lengths. *Macromolecules*, 47, 777 (2014).

[106] J. R. Sangoro, C. Iacob, A. L. Agapov, Y. Wang, S. Berdzinski, H. Rexhausen, V. Strehmel, C. Friedrich, A. P. Sokolov, and F. Kremer. Decoupling of Ionic Conductivity from Structural Dynamics in Polymerized Ionic Liquids. *Soft Matter*, 10, 3536 (2014).

[107] Z. Wojnarowska, J. Knapik, M. Diaz, A. Ortiz, I. Ortiz, and M. Paluch. Conductivity Mechanism in Polymerized Imidazolium-Based Protic Ionic Liquid [HSO3-BVIm][OTf]: Dielectric Relaxation Studies. *Macromolecules*, 47, 4056 (2014).

[108] C. M. Evans, C. R. Bridges, G. E. Sanoja, J. Bartels, and R. A. Segalman. Role of Tethered Ion Placement on Polymerized Ionic Liquid Structure and Conductivity: Pendant versus Backbone Charge Placement. *ACS Macro Lett.*, 5, 925 (2016).

[109] J. Bartels, G. E. Sanoja, C. M. Evans, R. A. Segalman, and M. E. Helgeson. Decoupling Mechanical and Conductive Dynamics of Polymeric Ionic Liquids via a Trivalent Anion Additive. *Macromolecules*, 50, 8979 (2017).

[110] C. M. Evans, G. E. Sanoja, B. C. Popere, and R. A. Segalman. Anhydrous Proton Transport in Polymerized Ionic Liquid Block Copolymers: Roles of Block Length, Ionic Content, and Confinement. *Macromolecules*, 49, 395 (2016).

[111] G. E. Sanoja, B. C. Popere, B. S. Beckingham, C. M. Evans, N. A. Lynd, and R. A. Segalman. Structure-Conductivity Relationships of Block Copolymer Membranes Based on Hydrated Protic Polymerized Ionic Liquids: Effect of Domain Spacing. *Macromolecules*, 49, 2216 (2016).

[112] Y. Schneider, M. A. Modestino, B. L. McCulloch, M. L. Hoarfrost, R. W. Hess, and R. A. Segalman. Ionic Conduction in Nanostructured Membranes Based on Polymerized Protic Ionic Liquids. *Macromolecules*, 46, 1543 (2013).

[113] M. Kar, B. Winther-Jensen, M. Forsyth, and D. R. MacFarlane. Chelating Ionic Liquids for Reversible Zinc Electrochemistry. *Phys. Chem. Chem. Phys.*, 15, 7191 (2013).

[114] C. M. Bates and F. Bates. 50th Anniversary Perspective: Block Polymers-Pure Potential. *Macromolecules*, 50, 3 (2017).

[115] S. K. Kumar, B. C. Benicewicz, R. A. Vaia, and K. I. Winey. 50th Anniversary Perspective: Are Polymer Nanocomposites Practical for Applications? *Macromolecules*, 50, 714 (2017).

[116] P. Lundberg, N. A. Lynd, Y. Zhang, X. Zeng, D. V. Krogstad, T. Paffen, M. Malkoch, A. M. Nystrom, and C. J. Hawker. pH-Triggered Self-Assembly of Biocompatible Histamine-Functionalized Triblock Copolymers. *Soft Matter*, 9, 82 (2013).

[117] B. F. Lee, M. Wolffs, K. T. Delaney, J. K. Sprafke, F. A. Leibfarth, C. J. Hawker, and N. A. Lynd. Reactivity Ratios and Mechanistic Insight for Anionic Ring-Opening Copolymerization of Epoxides. *Macromolecules*, 45, 3722 (2012).

[118] J. P. Runt and J. J. Fitzgerald, editors. *Dielectric Spectroscopy of Polymeric Materials: Fundamentals and Applications*. American Chemical Society (1997). doi: 10.1021/JA975608V.

[119] L. Chen, M. Bos, P. D. J. Grootenhuis, A. Christenhusz, E. Hoogendam, D. N. Reinhoudt, and W. E. Van Der Linden. Stability Constants for Some Divalent Metal Ion/Crown Ether Complexes in Methanol Determined by Polarography and Conductometry. *Anal. Chim. Acta*, 201, 117 (1987).

[120] S. Tang, M. Wang, and B. D. Olsen. Anomalous Self-Diffusion and Sticky Rouse Dynamics in Associative Protein Hydrogels. *J. Am. Chem. Soc.*, 137, 3946 (2015).

[121] D. Xu and S. L. Craig. Scaling Laws in Supramolecular Polymer Networks. *Macromolecules*, 44(5465-5472) (2011).

[122] A. Eisenberg. Clustering of Ions in Organic Polymers. A Theoretical Approach. *Macromolecules*, 3, 147 (1970).

[123] P. Atkins. *Shriver and Atkins' Inorganic Chemistry*. Oxford University Press, New York, 4 edition (2006).

[124] S. Washiro, M. Yoshizawa, H. Nakajima, and H. Ohno. Highly Ion Conductive Flexible Films Composed of Network Polymers Based on Polymerizable Ionic Liquids. *Polymer (Guildf).*, 45, 1577 (2004).

[125] C. A. Angell. Dynamic Processes in Ionic Glasses. *Chem. Rev.*, 90, 523 (1990).

[126] P. J. Flory. *Principles of Polymer Chemistry*. Cornell University Press, Ithaca and London (1953).

[127] P.-G. de Gennes. *Scaling Concepts in Polymer Physics*. Cornell University Press, Ithaca and London (1979).

[128] M. Enke, D. Doehler, S. Bode, W. H. Binder, M. D. Hager, and U. S. Schubert. Intrinsic Self-Healing Polymers Based on Supramolecular Interactions: State of the Art and Future Directions. In M. D. Hager, S. van der Zwaag, and U. S. Schubert, editors, *Self-healing Mater.*, pages 59–112. Springer International Publishing (2016).

[129] M. J. Webber, E. A. Appel, E. W. Meijer, and R. Langer. Supramolecular Biomaterials. *Nat. Mater.*, 15, 13 (2016).

[130] A. M. Rosales and K. S. Anseth. The Design of Reversible Hydrogels to Capture Extracellular Matrix Dynamics. *Nat. Rev. Mater.*, 1, 15012 (2016).

[131] O. Chaudhuri, L. Gu, D. Klumpers, M. Darnell, S. A. Bencherif, J. C. Weaver, N. Huebsch, H.-P. Lee, E. Lippens, G. N. Duda, and D. J. Mooney. Hydrogels with Tunable Stress Relaxation Regulate Stem Cell Fate and Activity. *Nat. Mater.*, 15, 326 (2016).

[132] D. Chen, D. Wang, Y. Yang, Q. Huang, S. Zhu, and Z. Zheng. Self-Healing Materials for Next-Generation Energy Harvesting and Storage Devices. *Adv. Energy Mater.*, 7, 1700890 (2017).

[133] S. Burattini, B. W. Greenland, D. H. Merino, W. Weng, J. Seppala, H. M. Colquhoun, W. Hayes, M. E. Mackay, I. W. Hamley, and S. J. Rowan. A Healable Supramolecular Polymer Blend Based on Aromatic π-π Stacking and Hydrogen-Bonding Interactions. *J. Am. Chem. Soc.*, 132, 12051 (2010).

[134] R. J. Sheridan and C. N. Bowman. A Simple Relationship Relating Linear Viscoelastic Properties and Chemical Structure in a Model Diels-Alder Polymer Network. *Macromolecules*, 45, 7634 (2012).

[135] R. P. Sijbesma, F. H. Beijer, L. Brunsveld, B. J. B. Folmer, J. H. K. K. Hirschberg, R. F. M. Lnage, K. L. Lowe, Jimmy, and E. W. Meijer. Reversible Polymers Formed from Self-Complementary Monomers Using Quadruple Hydrogen Bonding. *Science (80-.).*, 278, 1601 (1997).

[136] K. E. Feldman, M. J. Kade, E. W. Meijer, C. J. Hawker, and E. J. Kramer. Model Transient Networks from Strongly Hydrogen-Bonded Polymers. *Macromolecules*, 42, 9072 (2009).

[137] T. Rossow, A. Habicht, and S. Seiffert. Relaxation and Dynamics in Transient Polymer Model Networks. *Macromolecules*, 47, 6473 (2014).

[138] M. A. Webb, Y. Jung, D. M. Pesko, B. M. Savoie, U. Yamamoto, G. W. Coates, N. P. Balsara, Z.-G. Wang, and T. F. Miller. Systematic Computational and Experimental Investigation of Lithium-Ion Transport Mechanisms in Polyester-Based Polymer Electrolytes. *ACS Cent. Sci.*, 1, 198 (2015).

[139] P. G. Bruce and C. A. Vincent. Polymer Electrolytes. *J. Chem. Soc. Faraday Trans.*, 89, 3187 (1993).

[140] G. C. Farrington and R. G. Linford. Poly(ethylene oxide) Electrolytes Containing Divalent Cations. In J. R. MacCallum and C. A. Vincent, editors, *Polym. Electrolyte Rev. II*, pages 255–284. Elsevier, London (1989).

[141] A. Lewandowski, I. Stepniak, and W. Grzybkowski. Copper Transport Properties in Polymer Electrolytes Based on Poly(ethylene Oxide) and Poly(acrylonitrile). *Solid State Ionics*, 143, 425 (2001).

[142] J. L. Thelen, S. Inceoglu, N. R. Venkatesan, N. G. Mackay, and N. P. Balsara. Relationship between Ion Dissociation, Melt Morphology, and Electrochemical Performance of Lithium and Magnesium Single-Ion Conducting Block Copolymers. *Macromolecules*, 49, 9139 (2016).

[143] J. Shi and C. A. Vincent. The Effect of Molecular Weight on Cation Mobility in Polymer Electrolytes. *Solid State Ionics*, 60, 11 (1993).

[144] O. Borodin and G. D. Smith. Mechanism of Ion Transport in Amorphous Poly(ethylene oxide)/ LiTFSI from Molecular Dynamics Simulations. *Macromolecules*, 39, 1620 (2006).

[145] J. P. Donoso, T. J. Bonagamba, H. C. Panepucci, L. N. Oliveira, W. Gorecki, C. Berthier, and M. Armand. Nuclear Magnetic Relaxation Study of Poly(ethylene oxide)–Lithium Salt Based Electrolytes. *J. Chem. Phys.*, 98(12), 10026 (1993).

[146] W. S. Young, W. F. Kuan, and T. H. Epps. Block Copolymer Electrolytes for Rechargeable Lithium Batteries. *J. Polym. Sci. Part B Polym. Phys.*, 52, 1 (2014).

[147] J. E. Weston and B. C. H. Steele. Effects of Inert Fillers on the Mechanical and Electrochemical Properties of Lithium Salt-Poly(Ethylene Oxide Polymer Electrolytes. *Solid State Ionics*, 7, 75 (1982).

[148] F. Croce, G. B. Appetecchi, L. Persi, and B. Scrosati. Nanocomposite Polymer Electrolytes for Lithium Batteries. *Nature*, 394, 456 (1998).

[149] H. Ben Youcef, O. Garcia-Calvo, N. Lago, S. Devaraj, and M. Armand. Cross-Linked Solid Polymer Electrolyte for All-Solid-State Rechargeable Lithium Batteries. *Electrochim. Acta*, 220, 587 (2016).

[150] M. Chintapalli, K. Timachova, K. R. Olson, S. J. Mecham, D. Devaux, J. M. DeSimone, and N. P. Balsara. Relationship between Conductivity, Ion Diffusion, and Transference Number in Perfluoropolyether Electrolytes. *Macromolecules*, 49, 3508 (2016).

[151] S. Arumugam, J. Shi, D. P. Tunstall, and C. A. Vincent. Cation and Anion Diffusion Coefficients in a Solid Polymer Electrolyte Measured by Pulsed-Field-Gradient Nuclear Magnetic Resonance. *J. Phys. Condens. Matter*, 5, 153 (1993).

[152] M. Appel and G. Fleischer. Investigation of the Chain Length Dependence of Self-Diffusion of Poly(dimethylsiloxane) and Poly-(ethylene oxide) in the Melt with Pulsed Field Gradient NMR. *Macromolecules*, 26, 5520 (1993).

[153] S. Bhattacharja, S. W. Smoot, and D. H. Whitmore. Cation and Anion Diffusion in the Amorphous Phase of the Polymer Electrolyte (PEO)8LiCF3SO 3. *Solid State lonics*, 18, 306 (1986).

[154] A. McAuley and J. Hill. Kinetics and Mechanism of Metal-ion Complex Formation in Solution. *Q. Rev. Chem. Soc.*, 23, 18 (1969).

[155] F. Basolo and R. G. Pearson. *Mechanisms of Inorganic Reactions: A Study of Metal Complexes in Solution*. John Wiley & Sons, New York, 2 edition (1967).

[156] R. Hooper, L. J. Lyons, M. K. Mapes, D. Schumacher, D. A. Moline, and R. West. Highly Conductive Siloxane Polymers. *Macromolecules*, 34, 931 (2001).

[157] Y. Wang, F. Fan, A. L. Agapov, X. Yu, K. Hong, J. Mays, and A. P. Sokolov. Design of Superionic Polymers - New Insights from Walden Plot Analysis. *Solid State Ionics*, 262, 782 (2014).

[158] R. Spindler and D. F. Shriver. Investigations of a Siloxane-Based Polymer Electrolyte Employing 13C, 29Si, 7Li, and 23Na Solid-State NMR Spectroscopy. *J. Am. Chem. Soc.*, 110, 3036 (1988).

[159] P. Johansson and P. Jacobsson. Rational Design of Electrolyte Components by Ab Initio Calculations. *J. Power Sources*, 153, 336 (2006).

[160] M. A. Webb, B. M. Savoie, Z.-G. Wang, and T. F. Miller III. Chemically Specific Dynamic Bond Percolation Model for Ion Transport in Polymer Electrolytes. *Macromolecules*, 48, 7346 (2015).

[161] K. P. Barteau. *Poly(Glycidyl Ether)-Based Battery Electrolytes: Correlating Polymer Properties to Ion Transport*. Ph.D. thesis, University of California, Santa Barbara (2015).

[162] E. W. Stacy, C. P. Gainaru, M. Gobet, Z. Wojnarowska, V. Bocharova, S. G. Greenbaum, and A. P. Sokolov. Fundamental Limitations of Ionic Conductivity in Polymerized Ionic Liquids. *Macromolecules*, 51, 8637 (2018).

[163] K. M. Diederichsen, K. D. Fong, R. C. Terrell, K. A. Persson, and B. D. McCloskey. Investigation of Solvent Type and Salt Addition in High Transference Number Nonaqueous Polyelectrolyte Solutions for Lithium Ion Batteries. *Macromolecules*, 51, 8761 (2018).

[164] N. S. Schauser, R. Seshadri, and R. A. Segalman. Multivalent Ion Conduction in Solid Polymer Systems. *Mol. Syst. Des. Eng.*, 4, 263 (2019).

[165] P. Johansson. First Principles Modelling of Amorphous Polymer Electrolytes: Li+-PEO, Li+-PEI and Li+-PES Complexes. *Polymer (Guildf).*, 42, 4367 (2001).

[166] L. M. Torell, P. Jacobsson, and G. Petersen. A Raman study of Ion Solvation and Association in Polymer Electrolytes. *Polym. Adv. Technol.*, 4, 152 (1993).

[167] L. R. Middleton and K. I. Winey. Nanoscale Aggregation in Acid- and Ion-Containing Polymers. *Annu. Rev. Chem. Biomol. Eng.*, 8, 499 (2017).

[168] Y. Ye, J.-H. Choi, K. I. Winey, and Y. A. Elabd. Polymerized Ionic Liquid Block and Random Copolymers: Effect of Weak Microphase Separation on Ion Transport. *Macromolecules*, 45, 7027 (2012).

[169] D. Brandell, P. Priimaegi, H. Kasemaegi, and A. Aabloo. Branched Polyethylene/Ooly(ethylene oxide) as a Host Matrix for Li-Ion Battery Electrolytes: A Molecular Dynamics Study. *Electrochim. Acta*, 57, 228 (2011).

[170] B. K. Wheatle, N. A. Lynd, and V. Ganesan. Effect of Polymer Polarity on Ion Transport: A Competition between Ion Aggregation and Polymer Segmental Dynamics. *ACS Macro Lett.*, 7, 1149 (2018).

[171] W. Wang, G. J. Tudryn, R. H. Colby, and K. I. Winey. Thermally Driven Ionic Aggregation in Poly(ethylene oxide)-Based Sulfonate Ionomers. *J. Am. Chem. Soc.*, 133, 10826 (2011).

[172] D. Fragiadakis, S. Dou, R. H. Colby, and J. Runt. Molecular Mobility and Li+ Conduction in Polyester Copolymer Ionomers Based on Poly(ethylene oxide). *J. Chem. Phys.*, 130, 064907 (2009).

[173] M. V. O'Reilly, H. Masser, D. R. King, P. C. Painter, R. H. Colby, K. I. Winey, and J. Runt. Ionic Aggregate Dissolution and Conduction in a Plasticized Single-Ion Polymer Conductor. *Polymer (Guildf).*, 59, 133 (2015).

[174] K. Sinha and J. Maranas. Does Ion Aggregation Impact Polymer Dynamics and Conductivity in PEO-Based Single Ion Conductors? *Macromolecules*, 47, 2718 (2014).

[175] Y. Cheng, J. Yang, J.-H. Hung, T. K. Patra, and D. S. Simmons. Design Rules for Highly Conductive Polymeric Ionic Liquids from Molecular Dynamics Simulations. *Macromolecules*, 51, 6630 (2018).

[176] Y. Chen, M. Thorn, S. Christensen, C. Versek, A. Poe, R. C. Hayward, M. T. Tuominen, and S. Thayumanavan. Enhancement of Anhydrous Proton Transport by Supramolecular nNnochannels in Comb Polymers. *Nat. Chem.*, 2, 503 (2010).

[177] E. B. Trigg and K. I. Winey. Nanoscale Layers in Polymers to Promote Ion Transport. *Mol. Syst. Des. Eng.*, 4, 252 (2019).

[178] Q. Zhao, C. Shen, K. P. Halloran, and C. M. Evans. Effect of Network Architecture and Linker Polarity on Ion Aggregation and Conductivity in Precise Polymerized Ionic Liquids. *ACS Macro Lett.*, 8, 658 (2019).

[179] L. J. Abbott and J. W. Lawson. Effects of Side Chain Length on Ionic Aggregation and Dynamics in Polymer Single-Ion Conductors. *Macromolecules*, 52, 7456 (2019).

[180] L. M. Hall, M. E. Seitz, K. I. Winey, K. L. Opper, K. B. Wagener, M. J. Stevens, and A. L. Frischknecht. Ionic Aggregate Structure in Ionomer Melts: Effect of Molecular Architecture on Aggregates and the Ionomer Peak. *J. Am. Chem. Soc.*, 134, 574 (2012).

[181] S. Yakovlev, X. Wang, P. Ercius, N. P. Balsara, and K. H. Downing. Direct Imaging of Nanoscale Acidic Clusters in a Polymer Electrolyte Membrane. *J. Am. Chem. Soc.*, 133, 20700 (2011).

[182] N. M. Benetatos, C. D. Chan, and K. I. Winey. Quantitative Morphology Study of Cu-Neutralized Poly(styrene-ran-methacrylic acid) Ionomers: STEM Imaging, X-ray Scattering, and Real-Space Structural Modeling. *Macromolecules*, 40, 1081 (2007).

[183] N. C. Zhou, C. D. Chan, and K. I. Winey. Reconciling STEM and X-ray Scattering Data To Determine the Nanoscale Ionic Aggregate Morphology in Sulfonated Polystyrene Ionomers. *Macromolecules*, 41, 6134 (2008).

[184] C. F. Buitrago, D. S. Bolintineanu, M. E. Seitz, K. L. Opper, K. B. Wagener, M. J. Stevens, A. L. Frischknecht, and K. I. Winey. Direct Comparisons of X-ray Scattering and Atomistic Molecular Dynamics Simulations for Precise Acid Copolymers and Ionomers. *Macromolecules*, 48, 1210 (2015).

[185] C. M. Roland, R. Casalini, P. Santangelo, M. Sekula, J. Ziolo, and M. Paluch. Chemical Structure and Local Segmental Dynamics in 1,2-Polybutadiene. *Macromolecules*, 36, 4954 (2003).

[186] J. Ilavsky. Nika Software for Two-Dimensional Data Reduction. *J. Appl. Crystallogr.*, 45, 324 (2012).

[187] SciAnalysis.

[188] S. Stoll and A. Schweiger. EasySpin, a Comprehensive Software Package for Spectral Simulation and Analysis in EPR. *J. Magn. Reson.*, 178, 42 (2006).

[189] J. M. Martin, W. Li, K. T. Delaney, and G. H. Fredrickson. Statistical Field Theory Description of Inhomogeneous Polarizable Soft Matter. *J. Chem. Phys.*, 145, 154104 (2016).

[190] D. J. Grzetic, K. T. Delaney, and G. H. Fredrickson. The Effective X Parameter in Polarizable Polymeric Systems: One-Loop Perturbation Theory and Field-Theoretic Simulations. *J. Chem. Phys.*, 148, 204903 (2018).

[191] D. J. Grzetic, K. T. Delaney, and G. H. Fredrickson. Contrasting Dielectric Properties of Electrolyte Solutions with Polar and Polarizable Solvents. *Phys. Rev. Lett.*, 122, 128007 (2019).

[192] D. J. Grzetic, K. T. Delaney, and G. H. Fredrickson. Field-Theoretic Study of Salt-Induced Order and Disorder in a Polarizable Diblock Copolymer. *ACS Macrom Lett.*, 8, 962 (2019).

[193] O. Duerr, W. Dieterich, and A. Nitzan. Coupled Ion and Network Dynamics in Polymer Electrolytes: Monte Carlo Study of a Lattice Model. *J. Chem. Phys.*, 121, 12732 (2004).

[194] J. Qin and J. J. de Pablo. Criticality and Connectivity in Macromolecular Charge Complexation. *Macromolecules*, 49, 8789 (2016).

[195] G. H. Fredrickson. *The Equilibrium Theory of Inhomogeneous Polymers*. Oxford University Press (2006).

[196] V. Ganesan and G. H. Fredrickson. Field-Theoretic Polymer Simulations. *Europhys. Lett.*, 55, 814 (2001).

[197] D. Duechs, K. T. Delaney, and G. H. Fredrickson. Multi-Species Exchange Model for Fully Fluctuating Polymer Field Theory Simulations. *J. Chem. Phys.*, 141, 174103 (2014).

[198] K. T. Delaney and G. H. Fredrickson. Recent Developments in Fully Fluctuating Field-Theoretic Simulations of Polymer Melts and Solutions. *J. Phys. Chem. B*, 120, 7615 (2016).

[199] B. Bennett, W. E. Antholine, V. M. D'souza, G. Chen, L. Ustinyuk, and R. C. Holz. Structurally Distinct Active Sites in the Copper(II)-Substituted Aminopeptidases from Aeromonas proteolytica and Escherichia coli. *J. Am. Chem. Soc.*, 124, 13025 (2002).

[200] S. Richert, I. Kuprov, M. D. Peeks, E. A. Suturina, J. Cremers, H. L. Anderson, and C. R. Timmel. Quantifying the Exchange Coupling in Linear Copper Porphyrin Oligomers. *Phys. Chem. Chem. Phys.*, 19, 16057 (2017).

[201] R. P. Bonomo, F. Riggi, and A. J. Di Bilio. EPR Reinvestigation of the Copper (II) -Imidazole System. *Inorg. Chem.*, 27, 2510 (1988).

[202] J. J. Shane, P. Hoefer, E. J. Reijerse, and E. de Boer. Hyperfine Sublevel Correlation Spectroscopy (HYSCORE) of Disordered Solids. *J. Magn. Reson.*, 99, 596 (1992).

[203] S. Stoll, C. Calle, G. Mitrikas, and A. Schweiger. Peak Suppression in ESEEM Spectra of Multinuclear Spin Systems. *J. Magn. Reson.*, 177, 93 (2005).

[204] J. McCracken, S. Pember, S. J. Benkovic, J. J. Villafranca, R. J. Miller, and J. Peisach. Electron Spin-Echo Studies of the Copper Binding Site in Phenylalanine Hydroxylase from Chromobacterium Violaceum. *J. Am. Chem. Soc.*, 110, 1069 (1988).

[205] F. Jiang, J. McCracken, and J. Peisach. Nuclear Quadrupole Interactions in Copper(II)-Diethylenetriamine-Substituted Imidazole Complexes and in Copper(II) Proteins. *J. Am. Chem. Soc.*, 112, 9035 (1990).

[206] F. Jiang, K. D. Karlin, and J. Peisach. An Electron Spin Echo Envelope Modulation (ESEEM) Study of Electron-Nuclear Hyperfine and Nuclear Quadrupole Interactions of dz2 Ground State Copper(II) Complexes with Substituted Imidazoles. *Inorg. Chem.*, 32, 2576 (1993).

[207] V. Kofman, O. Farver, I. Pecht, and D. Goldfarb. Two-Dimensional Pulsed EPR Spectroscopy of the Copper Protein Azurin. *J. Am. Chem. Soc.*, 118, 2576 (1996).

[208] R. Grommen, P. Manikandan, Y. Gao, T. Shane, J. J. Shane, R. A. Schoonheydt, B. M. Weckhuysen, and D. Goldfarb. Geometry and Framework Interactions of Zeolite-Encapsulated Copper(II)-Histidine Complexes. *J. Am. Chem. Soc.*, 122, 11488 (2000).

[209] A. T. Taguchi, P. J. O'Malley, C. A. Wraight, and S. A. Dikanov. Hyperfine and Nuclear Quadrupole Tensors of Nitrogen Donors in the QA Site of Bacterial Reaction Centers: Correlation of the Histidine Nd Tensors with Hydrogen Bond Strength. *J. Phys. Chem. B*, 118, 9225 (2014).

[210] H. Zhang and G. M. Geise. Modeling the Water Permeability and Water/Salt Selectivity Tradeoff in Polymer Membranes. *J. Memb. Sci.*, 520, 790 (2016).

[211] O. Borodin and G. D. Smith. Li+ Transport Mechanism in Oligo(Ethylene Oxide)s Compared to Carbonates. *J. Solution Chem.*, 36, 803 (2007).

[212] D. Diddens, A. Heuer, and O. Borodin. Understanding the Lithium Transport within a Rouse-Based Model for a PEO/LiTFSI Polymer Electrolyte. *Macromolecules*, 43, 2028 (2010).

[213] S. Lascaud, M. Perrier, A. Vallke, S. Besner, J. Prud'homme, and M. Armand. Phase Diagrams and Conductivity Behavior of Poly(ethylene oxide)-Molten Salt Rubbery Electrolytes. *Macromolecules*, 27, 7469 (1994).

[214] J.-C. Lai, X.-Y. Jia, D.-P. Wang, Y.-B. Deng, P. Zheng, C.-H. Li, J.-L. Zuo, and Z. Bao. Thermodynamically Stable Whilst Kinetically Labile Coordination Bonds Lead to Strong and Tough Self-Healing Polymers. *Nat. Commun.*, 10, 1164 (2019).

[215] N. S. Schauser, D. J. Grzetic, T. Tabassum, G. A. Kliegle, M. L. Le, E. M. Susca, S. Antoine, T. J. Keller, K. T. Delaney, S. Han, R. Seshadri, G. H. Fredrickson, and R. A. Segalman. The Role of Backbone Polarity on Aggregation and Conduction of Ions in Polymer Electrolytes. *J. Am. Chem. Soc.*, 142, 7055 (2020).

[216] J. C. Persson and P. Jannasch. Intrinsically Proton-Conducting Benzimidazole Units Tethered to Polysiloxanes. *Macromolecules*, 38, 3283 (2005).

[217] K. M. Abraham and M. Alamgir. Dimensionally Stable MEEP-Based Polymer Electrolytes and Solid-State Lithium Batteries. *Chem. Mater.*, 3, 339 (1991).

[218] N. Kobayashi, M. Uchiyama, K. Shigehara, and E. Tsuchida. Ionically High Conductive Solid Electrolytes Composed of Graft Copolymer-Lithium Salt Hybrids. *J. Phys. Chem.*, 89, 987 (1985).

[219] M. Morita, T. Fukumasa, M. Motoda, H. Tsutsumi, Y. Matsuda, T. Takahashi, and H. Ashitaka. Polarization Behavior of Lithium Electrode in Solid Electrolytes Consisting of a Poly(Ethylene Oxide)-Grafted Polymer. *J. Electrochem. Soc.*, 137, 3401 (1990).

[220] P. E. Trapa, Y.-Y. Won, S. C. Mui, E. A. Olivetti, B. Huang, D. R. Sadoway, A. M. Mayes, and S. Dallek. Rubbery Graft Copolymer Electrolytes for Solid-State, Thin-Film Lithium Batteries. *J. Electrochem. Soc.*, 152, A1 (2005).

[221] M. Bergman, A. Bergfelt, B. Sun, T. Bowden, D. Brandell, and P. Johansson. Graft Copolymer Electrolytes for High Temperature Li-Battery Applications, Using Poly(methyl methacrylate) Grafted Poly(ethylene glycol)methyl ether methacrylate and Lithium Bis(trifluoromethanesulfonimide). *Electrochim. Acta*, 175, 96 (2015).

[222] C. Karlsson and P. Jannasch. Highly Conductive Nonstoichiometric Protic Poly(ionic liquid) Electrolytes. *ACS Appl. Energy Mater.*, 2, 6841 (2019).

[223] S. Granados-Focil, R. C. Woudenberg, O. Yavuzcetin, M. T. Tuominen, and E. B. Coughlin. Water-Free Proton-Conducting Polysiloxanes: A Study on the Effect of Heterocycle Structure. *Macromolecules*, 40, 8708 (2007).

[224] D. M. Pesko, Y. Jung, A. L. Hasan, M. A. Webb, G. W. Coates, T. F. Miller III, and N. P. Balsara. Effect of Monomer Structure on Ionic Conductivity in a Systematic Set of Polyester Electrolytes. *Solid State Ionics*, 289, 118 (2016).

[225] A. L. Frischknecht, B. A. Paren, L. R. Middleton, J. P. Koski, J. D. Tarver, M. Tyagi, C. L. Soles, and K. I. Winey. Chain and Ion Dynamics in Precise Polyethylene Ionomers. *Macromolecules*, 52, 7939 (2019).

[226] S. D. Druger, A. Nitzan, and M. A. Ratner. Dynamic Bond Percolation Theory: A Microscopic Model for Diffusion in Dynamically Disordered Systems. I. Definition and One-Dimensional Case. *J. Chem. Phys*, 79, 3133 (1983).

[227] S. D. Druger, M. A. Ratner, and A. Nitzan. Polymeric Solid Electrolytes: Dynamic Bond Percolation and Free Volume Models for Diffusion. *Solid State Ionics*, 9, 1115 (1983).

[228] S. D. Druger, M. A. Ratner, and A. Nitzan. Generalized Hopping Model for Frequency-Dependent Transport in a Dynamically Disordered Medium, with Applications to Polymer Solid Electrolytes. *Phys. Rev. B*, 31, 3939 (1985).

[229] A. Nitzan and M. A. Ratner. Conduction in Polymers: Dynamic Disorder Transport. *J. Phys. Chem*, 98, 1765 (1994).

[230] S. Schoenauer, A. Buergy, J. Kreissl, and P. Schieberle. Structure/Odor Activity Studies on Aromatic Mercaptans and Their Cyclohexane Analogues Synthesized by Changing the Structural Motifs of Naturally Occurring Phenyl Alkanethiols. *J. Agric. Food Chem.*, 67, 2598 (2019).

[231] T. G. Fox and S. Loshaek. Influence of Molecular Weight and Degree of Crosslinking on the Specific Volume and Glass Temperature of Polymers. *J. Polym. Sci.*, 15, 371 (1955).

[232] H. Scher and R. Zallen. Critical Density in Percolation Processes. *J. Chem. Phys.*, 53, 3759 (1970).

[233] D. Bresser, S. Lyonnard, C. Iojoiu, L. Picard, and S. Passerini. Decoupling Segmental Relaxation and Ionic Conductivity for Lithium-Ion Polymer Electrolytes. *Mol. Syst. Des. Eng.*, 4, 779 (2019).

[234] C. Iacob, A. Matsumoto, M. Brennan, H. Liu, S. J. Paddison, O. Urakawa, T. Inoue, J. Sangoro, and J. Runt. Polymerized Ionic Liquids: Correlation of Ionic Conductivity with Nanoscale Morphology and Counterion Volume. *ACS Macro Lett.*, 6, 941 (2017).

[235] E. Quartarone and P. Mustarelli. Electrolytes for Solid-State Lithium Rechargeable Batteries: Recent Advances and Perspectives (2011). doi: 10.1039/c0cs00081g.

[236] A. Manthiram, X. Yu, and S. Wang. Lithium Battery Chemistries Enabled by Solid-State Electrolytes (2017). doi: 10.1038/natrevmats.2016.103.

[237] K. Pozyczka, M. Marzantowicz, J. R. Dygas, and F. Krok. Ionic Conductivity and Lithium Transference Number of Poly(ethylene oxide):LiTFSI System. *Electrochim. Acta*, 227, 127 (2017).

[238] Y.-L. Rao, A. Chortos, R. Pfattner, F. Lissel, Y.-C. Chiu, V. Feig, J. Xu, T. Kurosawa, X. Gu, C. Wang, M. He, J. W. Chung, and Z. Bao. Stretchable Self-Healing Polymeric Dielectrics Cross-Linked Through Metal-Ligand Coordination. *J. Am. Chem. Soc.*, 138, 6020 (2016).

[239] B. M. Savoie, M. A. Webb, and T. F. Miller. Enhancing Cation Diffusion and Suppressing Anion Diffusion via Lewis-Acidic Polymer Electrolytes. *J. Phys. Chem. Lett.*, 8, 641 (2017).

[240] K. Iizuka, K. Akahane, D. ichi Momoee, M. Nakazawa, T. Tanouchi, M. Kawamura, I. Ohyama, I. Kajiwara, Y. ichi Iguchi, T. Okada, K. Taniguchi, T. Miyamoto, and M. Hayashi. Highly Selective Inhibitors of Thromboxane Synthetase. 1. Imidazole Derivatives. *J. Med. Chem.*, 24, 1139 (1981).

[241] Z. Xue, D. He, and X. Xie. Poly(ethylene oxide)-Based Electrolytes for Lithium-Ion Batteries. *J. Mater. Chem. A*, 3, 19218 (2015).

[242] R. Tanaka, T. Fujita, H. Nishibayashi, and S. Saito. Ionic Conduction in Poly(ethylenimine)-and Poly(N-methylethylenimine)-Lithium Salt Systems. *Solid State Ionics*, 60, 119 (1993).

[243] T. Sparks, M. Gaultois, A. Oliynyk, J. Brgoch, and B. Meredig. Data Mining Our Way to the Next Generation of Thermoelectrics. *Scr. Mater.*, 111, 10 (2016).

[244] M. Gaultois, A. Oliynyk, A. Mar, T. Sparks, G. Mulholland, and B. Meredig. Perspective: Web-based Machine Learning Models for Real-Time Screening of Thermoelectric Materials Properties. *APL Mater.*, 4, 053213 (2016).

[245] A. Oliynyk, T. Sparks, M. Gaultois, L. Ghadbeigi, and A. Mar. Gd12Co5. 3Bi and Gd12Co5Bi, Crystalline Doppelganger with Low Thermal Conductivities. *Inorg. Chem.*, 55, 6625 (2016).

[246] A. D. Sendek, Q. Yang, E. D. Cubuk, K.-A. N. Duerloo, Y. Cui, and E. J. Reed. Holistic Computational Structure Screening of More Than 12000 Candidates for Solid Lithium-Ion Conductor Materials. *Energy Environ. Sci.*, 10, 306 (2017).

[247] Z. Ahmad, T. Xie, C. Maheshwari, J. C. Grossman, and V. Viswanathan. Machine Learning Enabled Computational Screening of Inorganic Solid Electrolytes for Suppression of Dendrite Formation in Lithium Metal Anodes. *ACS Cent. Sci.*, 4, 996 (2018).

[248] A. D. Sendek, E. D. Cubuk, E. R. Antoniuk, G. Cheon, Y. Cui, and E. J. Reed. Machine Learning-Assisted Discovery of Solid Li-Ion Conducting Materials. *Chem. Mater.*, 31, 342 (2019).

[249] N. S. Bobbitt and R. Q. Snurr. Molecular Modelling and Machine Learning for High-Throughput Screening of Metal-Organic Frameworks for Hydrogen Storage. *Mol. Simul.*, 45, 1069 (2019).

[250] G. H. Gu, J. Noh, I. Kim, and Y. Jung. Machine Learning for Renewable Energy Materials. *J. Mater. Chem. A*, 7, 17096 (2019).

[251] P. Balachandran, B. Kowalski, A. Sehirlioglu, and T. Lookman. Experimental Search for High-Temperature Ferroelectric Perovskites Guided by Two-Step Machine Learning. *Nat. Commun.*, 9, 1668 (2018).

[252] Y. Zhuo, A. Mansouri Tehrani, and J. Brgoch. Predicting the Band Gaps of Inorganic Solids by Machine Learning. *J. Phys. Chem. Lett.*, 9, 1668 (2018).

[253] Y. Zhuo, A. Tehrani, A. Oliynyk, A. Duke, and J. Brgoch. Identifying an Efficient, Thermally Robust Inorganic Phosphor Host via Machine Learning. *Nat. Commun.*, 9, 4377 (2018).

[254] B. Cao, L. Adutwum, A. Oliynyk, E. Luber, B. Olsen, A. Mar, and J. Buriak. How to Optimize Materials and Devices via Design of Experiments and Machine Learning: Demonstration Using Organic Photovoltaics. *ACS Nano*, 12, 7434 (2018).

[255] A. G. Kusne, T. Gao, A. Mehta, L. Ke, M. C. Nguyen, K.-M. Ho, V. Antropov, C.-Z. Want, M. J. Kramer, C. Long, and I. Takeuchi. On-the-Fly Machine-Learning for High-Throughput Experiments: Search for Rare-Earth-Free Permanent Magnets. *Sci. Rep.*, 4, 6367 (2015).

[256] G. Landrum, J. Penzotti, and S. Putta. Machine-Learning Models for Combinatorial Catalyst Discovery. *Meas. Sci. Technol.*, 16, 270 (2004).

[257] A. Jha, A. Chandrasekaran, C. Kim, and R. Ramprasad. Impact of Dataset Uncertainties on Machine Learning Model Predictions: the Example of Polymer Glass Transition Temperatures. *Model. Simul. Mater. Sci. Eng.*, 27, 024002 (2019).

[258] C. Kim, A. Chandrasekaran, A. Jha, and R. Ramprasad. Active-Learning and Materials Design: The Example of High Glass Transition Temperature Polymers. *MRS Commun.*, 9, 860 (2019).

[259] X. Yu. Support Vector Machine-Based QSPR for the Prediction of Glass Transition Temperatures of Polymers. *Fibers Polym.*, 11, 757 (2010).

[260] K. Hatakeyama-Sato, T. Tezuka, Y. Nishikitani, H. Nishide, K. Oyaizu, K. Hatakeyama-Sato, and K. Oyaizu. Synthesis of Lithium-ion Conducting Polymers Designed by Machine Learning-based Prediction and Screening. *Chem. Lett.*, 48, 130 (2019).

[261] K. Hatakeyama-Sato, T. Tezuka, M. Umeki, and K. Oyaizu. AI-Assisted Exploration of Superionic Glass-Type Li+ Conductors with Aromatic Structures. *J. Am. Chem. Soc.*, 142, 3301 (2020).

[262] G. Zhu, C. Kim, A. Chandrasekarn, J. D. Everett, R. Ramprasad, and R. P. Lively. Polymer Genome-Based Prediction of Gas Permeabilities in Polymers. *J. Polym. Eng.* (2020).

[263] R. Seshadri and T. D. Sparks. Perspective: Interactive Material Property Databases Through Aggregation of Literature Data. *APL Mater.*, 4, 053206 (2016).

[264] L. Ghadbeigi, J. K. Harada, B. R. Lettiere, and T. D. Sparks. Performance and Resource Considerations of Li-ion Battery Electrode Materials. *Energy Environ. Sci.*, 8, 1640 (2015).

[265] P. Gorai, D. Gao, B. Ortiz, S. Miller, S. A. Barnett, T. Mason, Q. Lv, V. Stevanovic, and E. S. Toberer. TE Design Lab: A Virtual Laboratory for Thermoelectric Material Design. *Comput. Mater. Sci.*, 112, 368 (2016).

[266] A. Y.-T. Wang, R. J. Murdock, S. K. Kauwe, A. O. Oliynyk, A. Gurlo, J. Brgoch, K. A. Persson, and T. D. Sparks. Machine Learning for Materials Scientists: An Introductory Guide toward Best Practices. *Chem. Mater.*, page acs.chemmater.0c01907 (2020).

[267] S. Kauwe, T. Rhone, T. Sparks, S. K. Kauwe, T. D. Rhone, and T. D. Sparks. Data-Driven Studies of Li-Ion-Battery Materials. *Crystals*, 9(1), 54 (2019).

[268] K. M. Diederichsen, H. G. Buss, and B. D. Mccloskey. The Compensation Effect in the Vogel-Tammann-Fulcher (VTF) Equation for Polymer-Based Electrolytes. *Macromolecules*, 50, 3831 (2017).

[269] A. Yelon and B. Movaghar. Microscopic Explanation of the Compensation (Meyer-Neldel) Rule. *Phys. Rev. Lett.*, 65, 618 (1990).

[270] J. C. Dyre. A Phenomenological Model for the Meyer-Neldel Rule. *J. Phys. C Solid State Phys.*, 19, 5655 (1986).

[271] A. Rohatgi. WebPlotDigitizer (2019).

[272] H. Moriwaki, Y.-S. Tian, N. Kawashita, and T. Takagi. Mordred: a Molecular Descriptor Calculator. *J. Cheminform.*, 10, 4 (2018).

[273] T. S. Lin, C. W. Coley, H. Mochigase, H. K. Beech, W. Wang, Z. Wang, E. Woods, S. L. Craig, J. A. Johnson, J. A. Kalow, K. F. Jensen, and B. D. Olsen. BigSMILES: A Structurally-Based Line Notation for Describing Macromolecules. *ACS Cent. Sci.*, 5, 1523 (2019).

[274] J. D. Hunter. Matplotlib: A 2D Graphics Environment. *Comput. Sci. Eng.*, 9, 90 (2007).

[275] P. T. Inc. Collaborative Data Science (2015).

[276] F. Pedregosa, G. Varoquaux, A. Gramfort, V. Michel, B. Thirion, O. Grisel, M. Blondel, P. Prettenhofer, R. Weiss, V. Dubourg, J. Vanderplas, A. Passos, D. Cournapeau, M. Brucher, M. Perrot, and E. Duchesnay. No Title. *J. Mach. Learn. Res.*, 12, 2825 (2011).

[277] D. B. Shah, K. R. Olson, A. Karny, S. J. Mecham, J. M. Desimone, and N. P. Balsara. Effect of Anion Size on Conductivity and Transference Number of Perfluoroether Electrolytes with Lithium Salts. *J. Electrochem. Soc.*, 164, A3511 (2017).

[278] P. M. Blonsky, D. F. Shriver, P. Austin, and H. R. Allcock. Complex Formation and Ionic Conductivity of Polyphosphazene Solid Electrolytes. *Solid State Ionics*, 18, 258 (1986).

[279] N. Shukla and A. K. Thakur. Role of Salt Concentration on Conductivity Optimization and Structural Phase Separation in a Solid Polymer Electrolyte Based on PMMA-LiClO4. *Ionics (Kiel).*, 15, 357 (2009).

[280] X. Wei and D. F. Shriver. Highly Conductive Polymer Electrolytes Containing Rigid Polymers. *Chem. Mater.*, 10, 2307 (1998).

[281] W. Wieczorek. Entropy Effects on Conductivity of the Blend-Based and Composite Polymer Solid Electrolytes. *Solid State Ionics*, 53-56, 1064 (1992).

[282] A. A. Teran, M. H. Tang, S. A. Mullin, and N. P. Balsara. Effect of Molecular Weight on Conductivity of Polymer Electrolytes. *Solid State Ionics*, 203, 18 (2011).

[283] K. Roy and G. Ghosh. QSTR with Extended Topochemical Atom Indices. 2. Fish Toxicity of Substituted Benzenes. *J. Chem. Inf. Comput. Sci.*, 44, 559 (2004).

[284] K. Roy and R. N. Das. QSTR with Extended Topochemical Atom (ETA) Indices. 16. Development of Predictive Classification and Regression Models for Toxicity of Ionic Liquids Towards Daphnia Magna. *J. Hazard. Mater.*, 254-255, 166 (2013).

[285] S. Wang, S. Jeung, and K. Min. The Effects of Anion Structure of Lithium Salts on the Properties of in-situ Polymerized Thermoplastic Polyurethane Electrolytes. *Polymer (Guildf).*, 51, 2864 (2010).

[286] P. Johansson and P. Jacobsson. Ab Initio Studies of Complexation of Anions to Neutral Species. *Electrochim. Acta*, 50, 3782 (2005).

[287] M. A. Mehta and T. Fujinami. Li+ Transference Number Enhancement in Polymer Electrolytes by Incorporation of Anion Trapping Boroxine Rings into the Polymer Host. *Chem. Lett.*, 26, 915 (1997).

[288] M. Saito, H. Ikuta, Y. Uchimoto, M. Wakihara, S. Yokoyama, T. Yabe, and M. Yamamoto. Interaction between the Lewis Acid Group of a Borate Ester and Various Anion Species in a Polymer Electrolyte Containing Mg Salt. *J. Phys. Chem. B*, 107, 11608 (2003).

[289] M. Saito, H. Ikuta, Y. Uchimoto, M. Wakihara, S. Yokoyama, T. Yabe, and M. Yamamoto. Investigation of the Effect of Lewis Acid on Ionic Conductivity of Polymer Electrolyte Containing Mg Salt. *J. Electrochem.*, 150, A726 (2003).

[290] H. Zhang, C. Li, M. Piszcz, E. Coya, T. Rojo, L. M. Rodriguez-Martinez, M. Armand, and Z. Zhou. Single Lithium-Ion Conducting Solid Polymer Electrolytes: Advances and Perspectives. *Chem. Soc. Rev.*, 46, 797 (2017).

[291] A. A. Rojas, K. Thakker, K. D. McEntush, S. Inceoglu, G. M. Stone, and N. P. Balsara. Dependence of Morphology, Shear Modulus, and Conductivity on the Composition of Lithiated and Magnesiated Single-Ion- Conducting Block Copolymer Electrolytes. *Macromolecules*, 50, 8765 (2017).

[292] Q. Ma, H. Zhang, C. Zhou, L. Zheng, P. Cheng, J. Nie, W. Feng, Y.-S. Hu, H. Li, X. Huang, L. Chen, M. Armand, and Z. Zhou. Single Lithium-Ion Conducting Polymer Electrolytes Based on a Super-Delocalized Polyanion. *Angew. Chemie Int. Ed.*, 55, 2521 (2016).

[293] S. Feng, D. Shi, F. Liu, L. Zheng, J. Nie, W. Feng, X. Huang, M. Armand, and Z. Zhou. Single Lithium-Ion Conducting Polymer Electrolytes Based on Poly[(4-styrenesulfonyl)(trifluoromethanesulfonyl)imide] Anions. *Electrochim. Acta*, 93, 254 (2013).

[294] L. Porcarelli, K. Manojkumar, H. Sardon, O. Llorente, A. S. Shaplov, K. Vijayakrishna, C. Gerbaldi, and D. Mecerreyes. Single Ion Conducting Polymer Electrolytes Based On Versatile Polyurethanes. *Electrochim. Acta*, 241, 526 (2017).

[295] Y. Zhang, W. Cai, R. Rohan, M. Pan, Y. Liu, X. Liu, C. Li, Y. Sun, and H. Cheng. Toward Ambient Temperature Operation with All-Solid-State Lithium Metal Batteries with a sp3 Boron-Based Solid Single Ion Conducting Polymer Electrolyte. *J. Power Sources*, 306, 152 (2016).

[296] W. Xu, M. D. Williams, and C. A. Angell. Novel Polyanionic Solid Electrolytes with Weak Coulomb Traps and Controllable Caps and Spacers. *Chem. Mater.*, 14, 401 (2002).

[297] S.-W. Ryu, P. E. Trapa, S. C. Olugebefola, J. A. Gonzalez-Leon, D. R. Sadoway, and A. M. Mayes. Effect of Counter Ion Placement on Conductivity in Single-Ion Conducting Block Copolymer Electrolytes. *J. Electrochem. Soc.*, 152, A158 (2005).

[298] T. Itoh, Y. Mitsuda, T. Ebina, T. Uno, and M. Kubo. Solid Polymer Electrolytes Composed of Polyanionic Lithium Salts and Polyethers. *J. Power Sources*, 189, 531 (2009).